FY06
Engineering Research and Technology Report

April 2007

Lawrence Livermore National Laboratory

UCRL-TR-227864

Acknowledgments

Scientific Editor
Camille Minichino

Graphic Designer
Irene J. Chan

Project Manager
Debbie A. Ortega

Production Staff
Jeffrey B. Bonivert
Lucy C. Dobson
Kathy J. McCullough

Cover:
Graphics representing projects from
Engineering's technology areas.

FY06
Engineering Research and Technology Report

April 2007

Lawrence Livermore National Laboratory

A Message from

Steven R. Patterson
Associate Director for Engineering

This report summarizes the core research, development, and technology accomplishments in Lawrence Livermore National Laboratory's Engineering Directorate for FY2006. These efforts exemplify Engineering's more than 50-year history of developing and applying the technologies needed to support the Laboratory's national security missions. A partner in every major program and project at the Laboratory throughout its existence, Engineering has prepared for this role with a skilled workforce and technical resources developed through both internal and external venues. These accomplishments embody Engineering's mission: "Enable program success today and ensure the Laboratory's vitality tomorrow."

Engineering's investment in technologies is carried out primarily through two internal programs: the Laboratory Directed Research and Development (LDRD) program and the technology base, or "Tech Base," program. LDRD is the vehicle for creating technologies and competencies that are cutting-edge, or require discovery-class research to be fully understood. Tech Base is used to prepare those technologies to be more broadly applicable to a variety of Laboratory needs. The term commonly used for Tech Base projects is "reduction to practice." Thus, LDRD reports have a strong research emphasis, while Tech Base reports document discipline-oriented, core competency activities.

This report combines the LDRD and Tech Base summaries into one volume, organized into six thematic technical areas: Engineering Modeling and Simulation; Measurement Technologies; Micro/Nano-Devices and Structures; Precision Engineering; Engineering Systems for Knowledge and Inference; and Energy Manipulation.

Engineering Modeling and Simulation efforts focus on the research, development, and deployment of computational technologies that provide the foundational capabilities to address most facets of Engineering's mission. Current activities range from fundamental advances to enable accurate modeling of full-scale DOE and DoD systems performing at their limits, to advances for treating photonic and microfluidic systems.

FY2006 LDRD projects encompassed coupling standard finite element analysis methods with "meshless" methods to address systems at and beyond failure; integration of electromagnetic forces with structural mechanics solutions; and nonlinear materials treatments for photonic systems. Tech Base projects included enhancements, verification, and validation of engineering simulation tools and capabilities; progress in visualization and data management tools; and extensions of our competence in structural damage analysis.

Measurement Technologies comprise activities in nondestructive characterization, metrology, sensors systems, and ultrafast technologies for advanced diagnostics. The advances in this area are essential for the future experimental needs in Inertial Confinement Fusion, High-Energy-Density Physics, Weapons and Department of Homeland Security programs.

FY2006 LDRD research featured transient recording extensions for streak cameras; investigations into terahertz systems for explosives detection; acoustic characterization of mesoscale objects; and research on the structure and properties of nanoporous materials. Tech Base projects included new capabilities for the fabrication of photonic integrated circuits; the implementation of a new transient sampling data recorder; ultra-wideband technology testbeds; computed tomography (CT) reconstruction tools; and tools to aid identification of defects in large CT data sets.

Micro/Nano-Devices and Structures encompasses technology efforts that fuel the commercial growth of microelectronics and sensors, while simultaneously customizing these technologies for unique, noncommercial applications that are mission-specific to LLNL and DOE. LLNL's R&D talent and unique fabrication facilities have enabled highly innovative and custom solutions to technology needs in Stockpile Monitoring and Stewardship, Homeland Security, and Intelligence.

FY2006 LDRD projects included novel capabilities to perform automated front-end processing of complex biological samples. Tech Base projects included the colocation of actuation MEMs with electronic packages; implementation of self-assembly structures through block copolymer nanolithography; and instantiation of new equipment capabilities for micro- and nano-fabrication.

Precision Engineering core technologies are the building blocks for the machines, systems, and processes that will be required for future Laboratory and DOE programs. These technologies help advance the Laboratory's high-precision capabilities in manufacturing, dimensional metrology, and assembly. Precision engineering is a multidisciplinary systems approach to achieve an order of magnitude greater accuracy than currently achievable.

FY2006 Tech Base projects included error budgeting and certification of dimensional metrology tools, and uncertainty analysis for inspection shop measurements.

Engineering Systems for Knowledge and Inference, an emerging focus area for Engineering as well as for the country at large, encompasses a wide variety of technologies. The goal is to generate new understanding or knowledge of situations, thereby allowing anticipation or prediction of possible outcomes. With this knowledge, a more comprehensive solution may be possible for problems as complex as the prediction of disease outbreaks or advance warning of terrorist threats.

FY2006 LDRD research included projects to determine the location and contents of atmospheric releases based on sensors in the field, and new research into decomposing extremely large semantic graphs. Tech Base efforts included a testbed to evaluate hierarchical clustering, and analysis tools and application of a previously developed image content engine to new inspection capabilities in optics.

Energy Manipulation, a long time focus that is receiving increased emphasis due to newly emerging applications, encompasses the fundamental understanding and technology deployment for many modern pulsed-power applications. This area has broad applications for magnetic flux compression generators and components for modern accelerators.

FY2006 LDRD research included research into the fundamental mechanisms responsible for flashover of insulators subject to microsecond pulses. Tech Base efforts involved capabilities to improve the switching performance of power MOSFETs, and solid-state replacements for ignitrons.

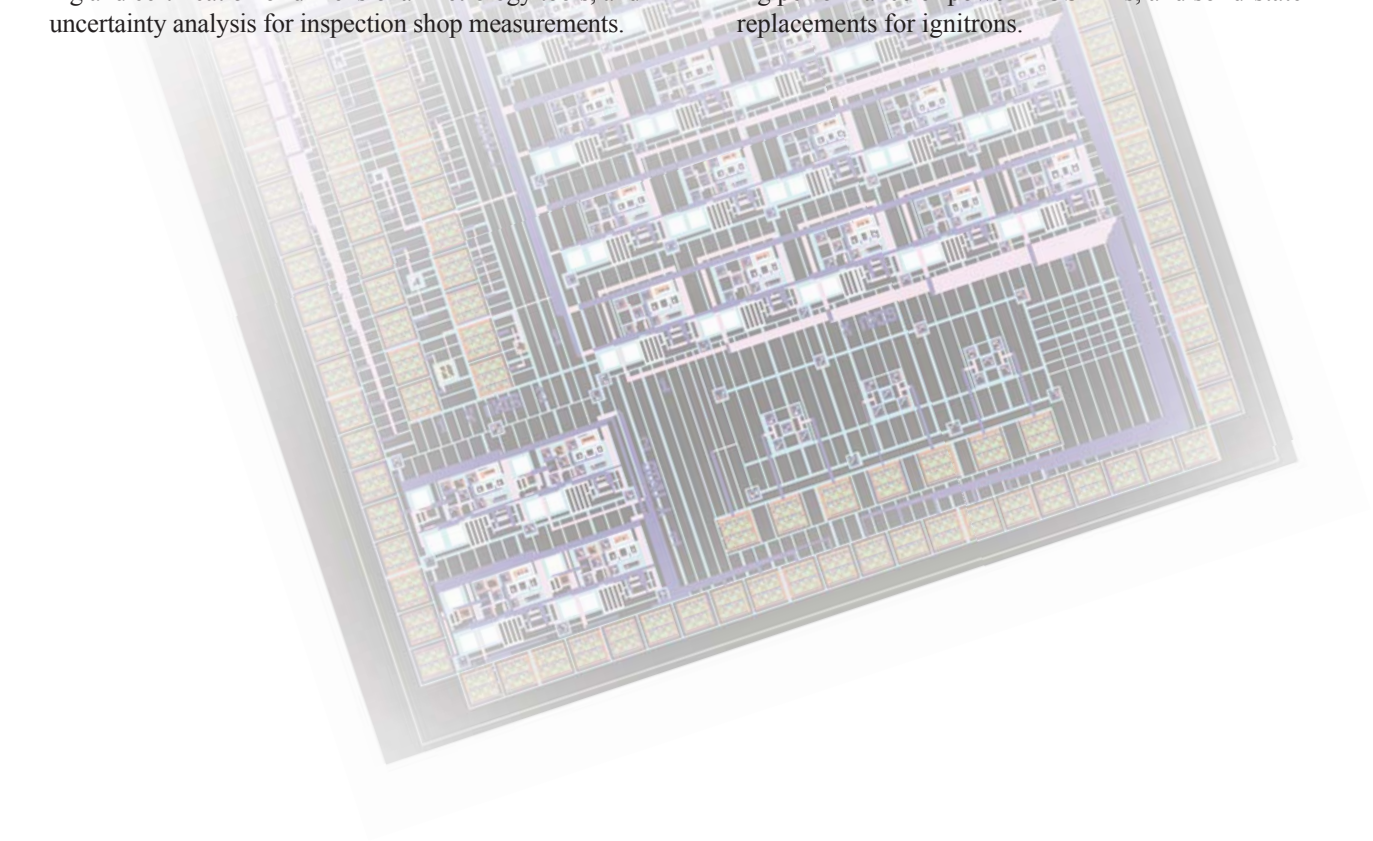

Contents

Measurement Technologies

Micro/Nano-Devices and Structures

Engineering Modeling and Simulation

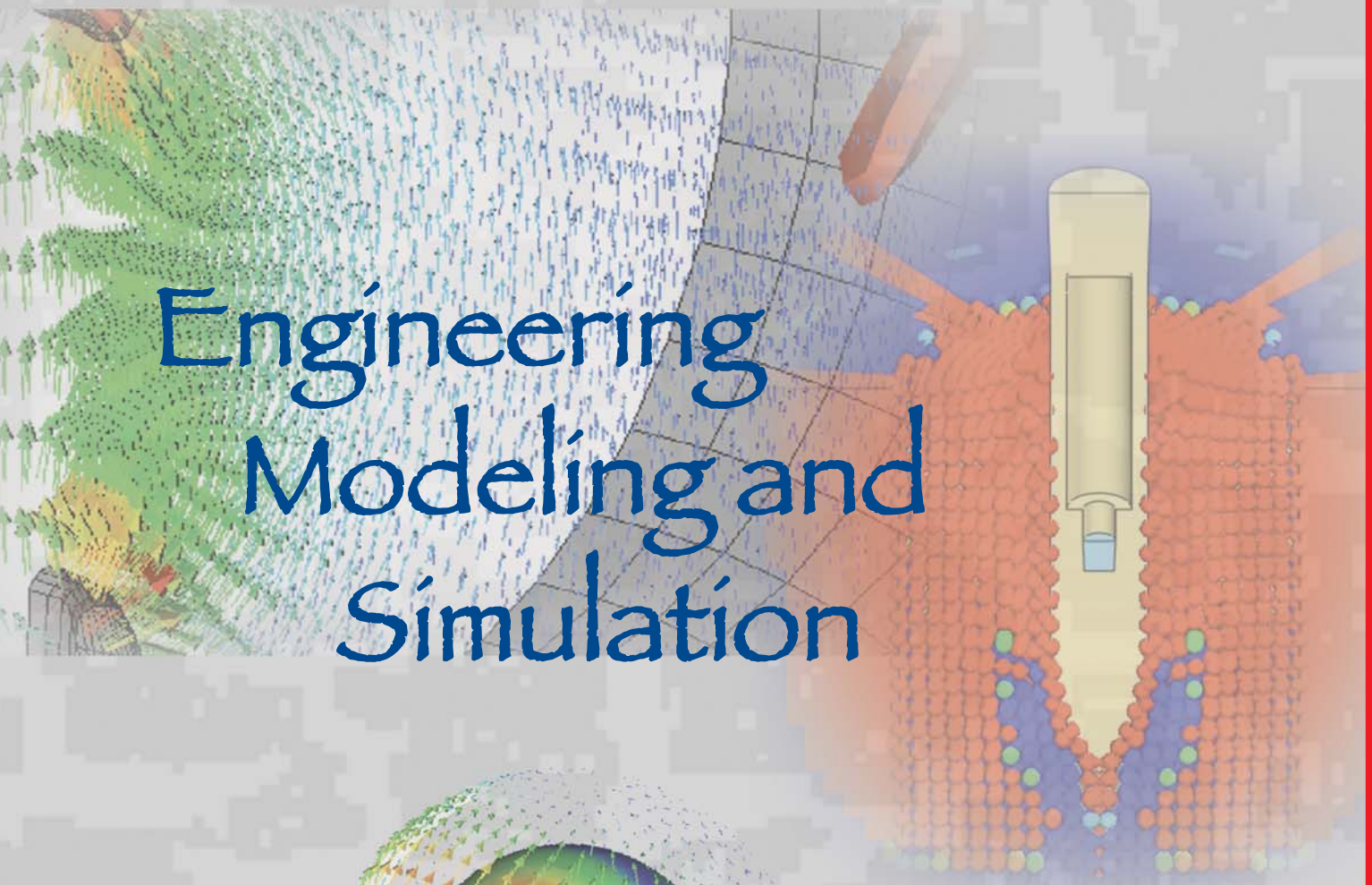

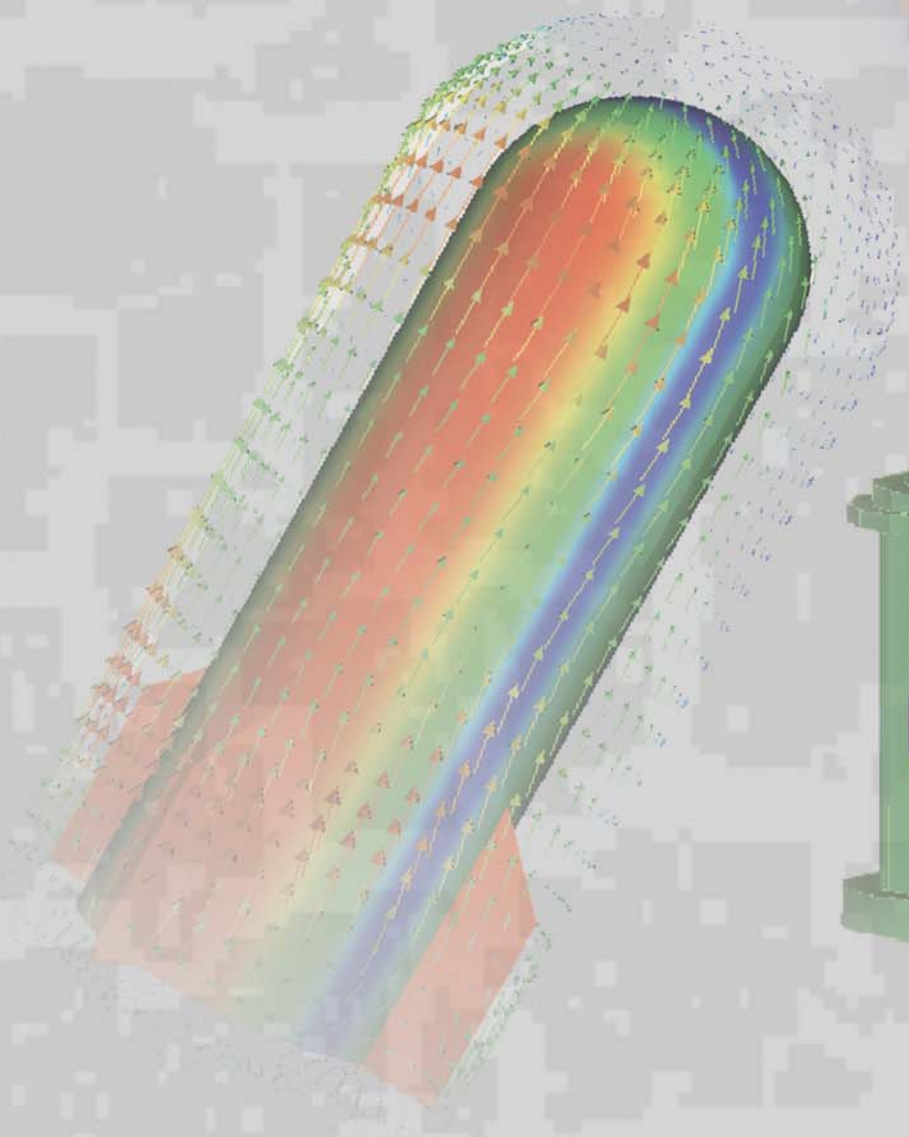

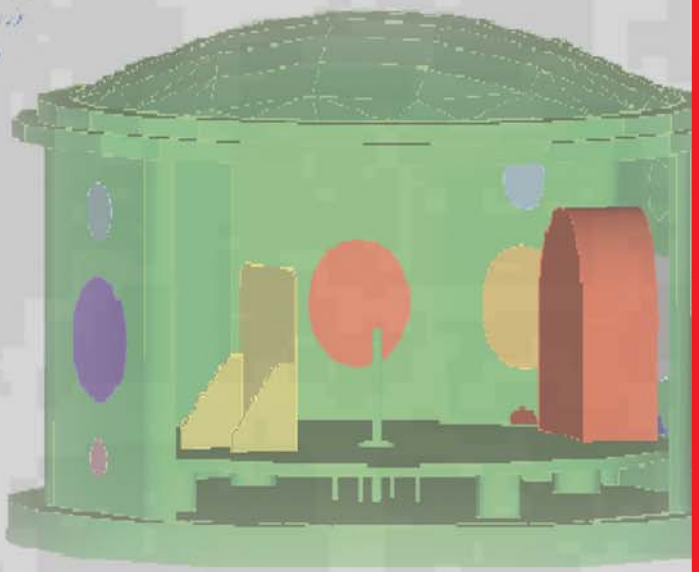

FY 06 Engineering Research and Technology Report

A New "Natural Neighbor" Meshless Method for Modeling Extreme Deformation and Failure

Michael A. Puso
(925) 422-8198
puso1@llnl.gov

The objective of this work is to develop a fully Lagrangian analysis approach based on "natural neighbor" discretization techniques to model extreme deformation and failure for analyses such as earth penetration and dam failure. In these problems, our standard Lagrangian finite element approach fails due to mesh tangling, whereas our Eulerian codes do not allow us to track particles and free surfaces to the degree necessary. Meshless particle methods such as smooth particle hydrodynamics (SPH) and element-free Galerkin (EFG) have been used for modeling such large deformations but have a variety of numerical problems that the new natural neighbor approach can potentially solve. To successfully use the new approach, issues such as numerical integration, time-step calculation, and adaptive point insertion are treated.

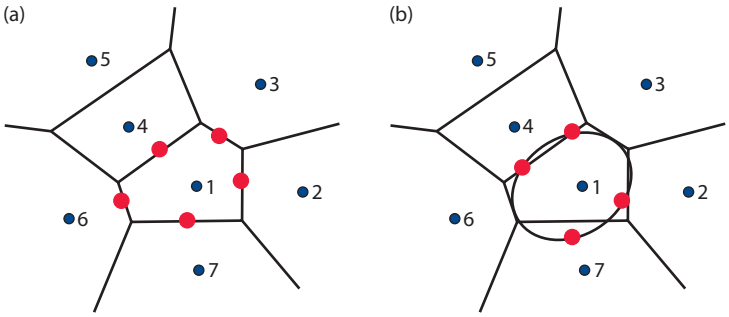

Figure 1. (a) Voronoi diagram formed about the cloud of points, used to compute natural neighbor shape functions and numerical integration. For example, nodal strains and stresses at 1 were computed using Gauss points (red) on the Voronoi cell. (b) Approximation of Voronoi cell using an ellipse. This requires only approximate calculation of the near neighbors.

Project Goals

The goal of this work is to develop a better meshless particle approach by overcoming the numerous problems inherent in these methods. In short, the new method should be more stable and accurate than the current meshless approaches. The new approach will provide an improved method for modeling extreme events such as earth penetration and dam failure. Furthermore, because it is meshless the approach can be used for applications where nondestructive evaluations are required, such as as-built weapons analysis and biomechanics. Overall, a much larger class of problems can then be solved.

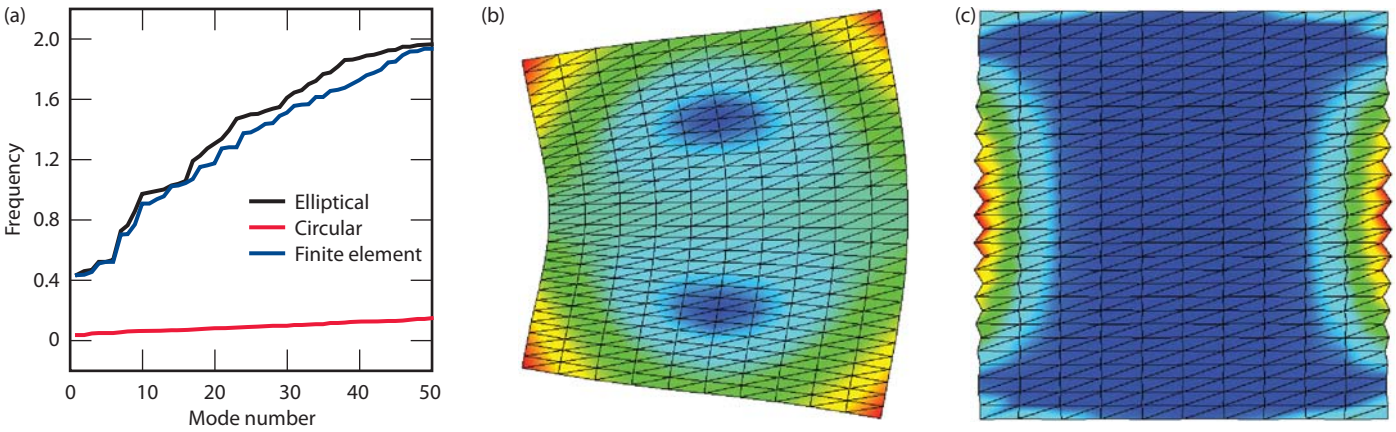

Figure 2. (a) Frequency vs. mode number for a 1-x-1 lattice of points with mesh spacing $h_x = 1$ and $h_y = 0.5$. The results using the natural neighbor based elliptical supports compare well with the finite element results. (b) First mode displacements using elliptical supports. (c) First mode displacement using circular supports.

Relevance to LLNL Mission

High-rate penetration dynamics has been identified as a challenge area in engineering and the new particle methods developed here directly apply to this area. Along with earth and armor penetration problems, vulnerability evaluation of infrastructure (*e.g.*, dams) can be analyzed. Furthermore, as-built x-ray tomography of NIF targets and *in-vivo* MRI imaging for biomechanics create "point clouds" and are good examples of where a meshless method could be exploited for expediting stress analyses.

FY2006 Accomplishments and Results

Our FY2005 implementation required the creation of a Voronoi diagram as shown in Fig. 1a. This was used to compute the natural neighbor shape functions and conforming cells for numerical integration. In FY2006 we simplified this approach such that nearest neighbors would have to be computed only approximately, as in Fig. 1b. In this approach, the smooth kernels would be elliptical and approximately fit Voronoi cells. Linear exactness of the resulting shape functions is provided by using a kernel correction. In fact, the elliptical kernels were also applied to other classical approaches in FY2006.

The natural neighbors are very important in providing locality (*i.e.*, tight supports) for the sake of efficiency and accuracy. We found that diagonalization of the mass matrix was valid only when the shape functions had tight support, as demonstrated in Fig. 2. Because the integration cells are no longer conforming, results are not as accurate as those using Voronoi cells when discretized points are not structured. To recover accuracy, a method for computing a correction term was developed (Fig. 3). Stabilization of the nodal integration is applied using the new cell approach. These new meshless methods were then applied to simulation of an earth penetrator (Fig. 4). Finally, new higher-order meshless integration approaches were developed for treating problems in electronic structure.

Related References

1. Puso, M. A., "A New Stabilized Nodal Integration Approach," *McMat Conference Proceedings*, 2005.
2. Puso, M. A., and J. Solberg, "A Formulation and Analysis of a Stabilized Nodally Integrated Tetrahedral," *International Journal for Numerical Methods in Engineering*, **67**, 6, pp. 841-867, 2006.
3. Puso, M. A., and J. S. Chen, "A New Stabilized Nodal Integration Approach," *Proceedings International Workshop Meshfree Methods*, 2005, in press.
4. Chen, J. S., and M. A. Puso, "Strain Smoothing for Stabilization and Regularization of Galerkin Meshfree Methods," *Proceedings International Workshop Meshfree Methods*, 2005, in press.
5. Chen, J. S., W. Hu, and M.A. Puso, "Orbital HP-Clouds and Higher Order SCNI for Solving Schrodinger Equation in Quantum Mechanics," *International Journal for Numerical Methods in Engineering*, in press.

FY2007 Proposed Work

Our major FY2007 goal is to validate the new methods and compare to more classical methods, *e.g.*, MLSPH, MLPG. Our main validation concern is earth penetration but we will be looking at other experimental results. If time permits, we will also use error indicators to do point insertion and conversion of finite elements into particles.

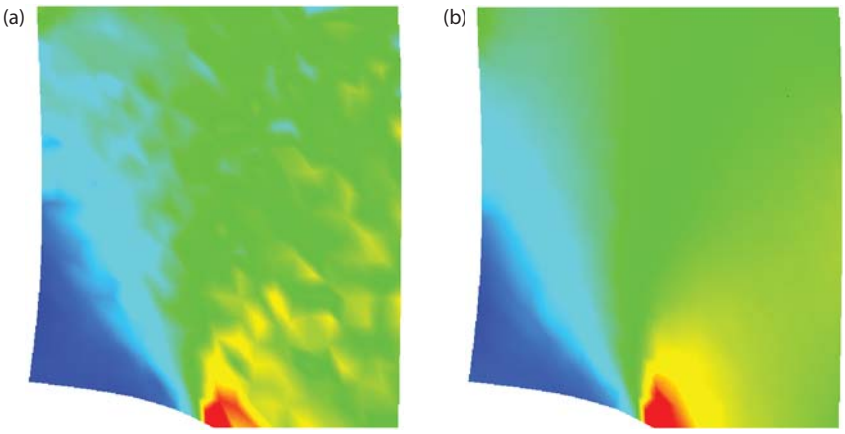

Figure 3. Simulation of mode one crack on a set of randomly discretized nodes. The stresses oscillate in (a) without correction but are very accurate with correction in (b).

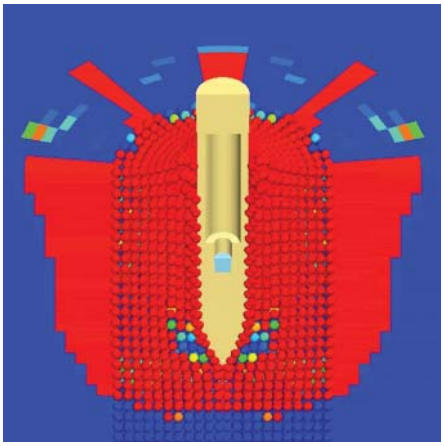

Figure 4. Simulation of earth penetrator. Meshless particles are located near the penetrator and finite elements at outer locations. The red denotes tensile failure.

Statistical Distribution of Material Properties and Improvements in DYNA3D

Jerry Lin
(925) 423-0907
lin5@llnl.gov

DYNA3D is one of the main explicit finite element analysis tools at LLNL for fast transient response of structures. This project funds DYNA3D enhancements through implementation of user-requested features, general technical support, document update and Software Quality Assurance (SQA) compliance for DYNA3D.

This project also supports Collaborator Program activities. The Collaborator Program grants access to selected licensed users to LLNL's computational mechanics/thermal codes in exchange for the collaborators' information and results. These collaborative parties include our sister laboratories, U.S. government agencies, and other institutions.

Project Goals

For FY2006, the planned tasks included the implementation of functionalities for various analytical needs, the addition of new result display capabilities, and continued compliance work on SQA and the Fortran90® standards.

Relevance to LLNL Mission

Many programs at LLNL require new DYNA3D functionalities and/or technical support to complete their missions. Some of these projects involve LLNL's collaboration with other institutions and federal agencies, such as the Las Alamos National Laboratory, Homeland Security, Bureau of Reclamation, U.S. Army Corps of Engineers, and the Naval Surface Warfare Center.

FY2006 Accomplishments and Results

Statistical distribution of material yield/failure strength was introduced to some of the material models. The inclusion of a distribution enables DYNA3D to simulate a manufactured product more realistically.

Figure 1. Strain pattern (solid color, except for small amount of data at upper right) of a biaxially loaded plate with no statistical distribution on the material failure strain.

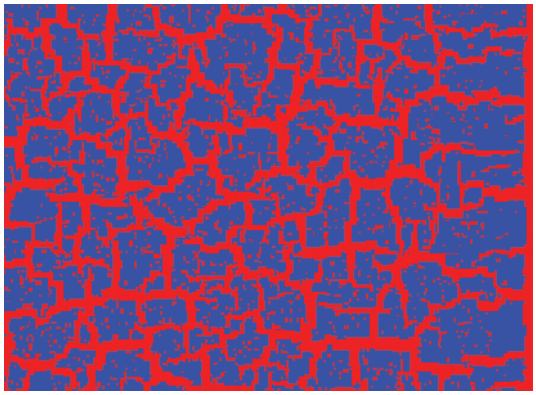

Figure 2. Strain pattern of a biaxially loaded plate with the Weibull statistical distribution on the material failure strain.

A biaxially loaded plate provides an example. The plate is made of an isotropic-elastic-plastic material with a user-assigned failure strain. A homogeneous plate is assumed in the first run, which results in a uniform strain pattern (solid color), as depicted in Fig.1. A Weibull distribution is applied to the failure strain in a subsequent run. The added distribution produces a clear fragmentation pattern, more representative for manufactured parts (Fig. 2).

Over the years, velocity overshoot and excessive "ringing" has been an issue in many computational analyses, especially in shockwave-related simulations. A self-adjusting viscosity model was implemented into DYNA3D to counter this difficulty. This new algorithm, in addition to the existing bulk viscosities, adds a complementary viscosity component at material points sustaining power dissipation.

A standard impacting bars problem is used to examine the algorithm's effectiveness. The simulation consists of two identical isotropic elastic bars, one at rest and the other with a unit initial velocity, undergoing an end-to-end impact. The velocity histories at the impact point of each individual bar are recorded for comparison. In Fig. 3, only the traditional bulk viscosity is applied, whereas in Fig. 4 the complementary viscosity is added. A smoother velocity record without overshoot and continuous ringing is evident in the latter case.

Other new features and improvements of note in DYNA3D include added failure mechanisms for selected material models, time-dependent gravity effect, streamlined restart and visualization capabilities for the quasi-static analysis phase, and additional result output for visualization.

FY2007 Proposed Work

We will continue our general technical support for DYNA3D users, and the ongoing modernization toward Fortran90®-compatible and SQA-compliance. We also plan to start or continue the following enhancements:

1. the integration of the surface class entities such as boundary conditions in output databases;
2. the computation and display of the kinematics of parts of an analysis model, such as the rotational velocities/accelerations of a part or a collection of parts; and
3. the implementation of a unified and consistent stiffness-proportional damping for all element types.

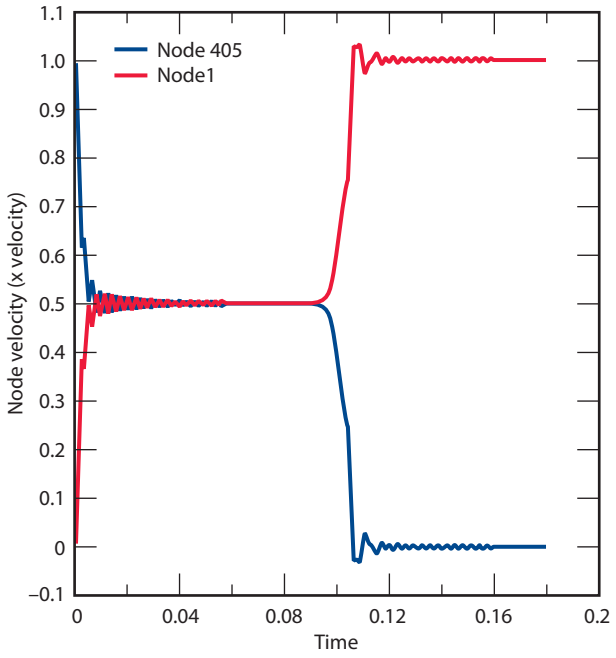

Figure 3. Velocity histories of impacting bars without the self-adjusting bulk viscosity.

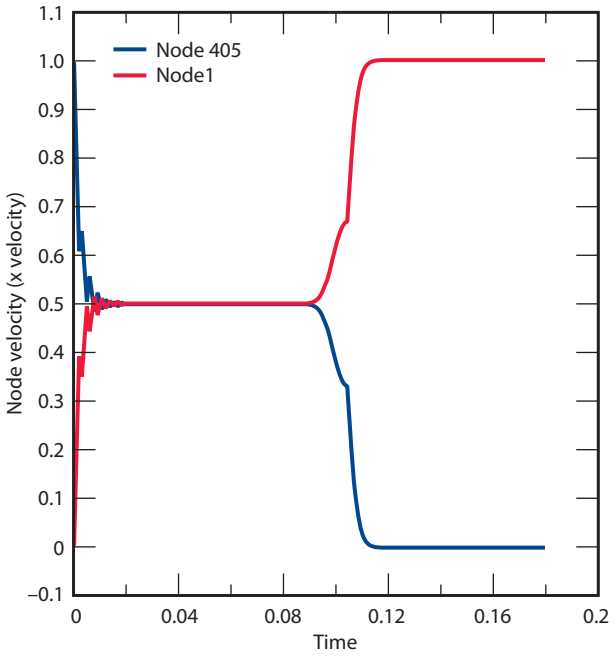

Figure 4. Velocity histories of impacting bars with the self-adjusting bulk viscosity.

Finite Element Analysis Visualization and Data Management

Elsie Pierce
(925) 422-4063
pierce5@llnl.gov

A key component of our project activities is its support for post-processing and visualization tools, which include the Griz finite element post-processor, a parallel file combiner tool called XmiliCS, and the Mili I/O Library. These tools are heavily used by analysts and engineers across LLNL and externally to post-process data from a variety of analysis codes, such as DYNA3D, ParaDyn, NIKE3D and Diablo.

Griz is our primary tool for visualizing finite element analysis results on 3-D unstructured grids. Griz calculates and displays derived variables for a variety of codes. Griz provides modern 3-D visualization techniques such as isocontours and isosurfaces, cutting planes, vector field display, and particle traces. Griz also incorporates the ability to animate all representations over time. XmiliCS is a utility for combining results from multiple processors that are generated by our large computing platforms. Mili provides the primary data path between analysis codes and Griz.

Project Goals

The primary goal of this effort is to provide on-going support for LLNL's post-processing tools. This includes efforts to add new capabilities to these tools for broad programmatic requirements.

Relevance to LLNL Mission

Post-processing tools such as Griz, XmiliCS, and Mili provide important user interfaces for our simulation capabilities and are critical elements in LLNL's simulation tool suite.

FY2006 Accomplishments and Results

We currently have many active users for Griz and Mili coming from programs at LLNL and also at LANL.

Figure 1. Original particle configuration at time=0.

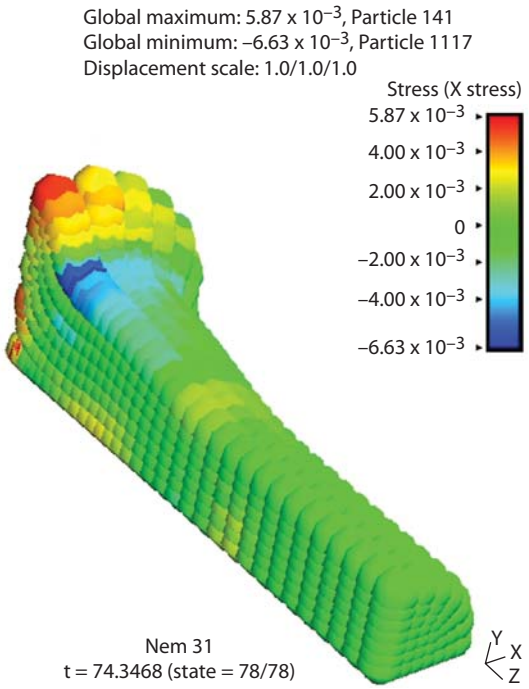

Figure 2. X Stress plot at time = 74.34 µs.

We made significant progress in adding the capability for Griz and Mili to manage and display surface objects. This is an essential step for facilitating the writing of boundary conditions and data onto surfaces from the analysis programs. To date the entire GUI implementation and database work has been completed, and released. We are in the process of getting the surface class capability used by our analysis codes.

This year we successfully ported Griz to new 64-bit Linux platforms. Griz performance seems quite good on these platforms, and there have been no problems with the multi-monitor displays. Such hardware configurations are becoming common for our analysts.

We added a new feature in Griz to provide a "rubber-band" (RB) zoom, as requested by several users. Using the RB zoom is much faster than the mouse zoom, since the latter requires a refresh (a wire frame redraw) at each cursor location change. This can amount to hundreds of updates to the display for a single zoom.

We continued to add new features in Griz to support advanced simulations of fragmentation and debris from hypervelocity impacts. This year we added the following new capabilities to support this study: 1) a capability to write out detailed tabular data for free-nodes; 2) the ability to plot time-history data for accumulated free-node velocity by material; and 3) a result for momentum.

Griz is now using an advanced regression testing system based on an LLNL tool called Tapestry, and weekly automated builds and tests are performed for all of our major platforms. This year we made additional enhancements to the Griz configuration and build system. We also implemented and released a new build system for the Mili Library.

In support of an investigation into future meshing techniques, we added a new capability in Griz to plot results for meshless or particle-based algorithms. These problems have no mesh, but an unstructured collection of nodes that carry result quantities. These problems are treated in Griz in much the same way that we treat problems with free-nodes, so much of the same work completed for hypervelocity impact applications was leveraged. All of the options available for free-nodes can also be applied to particles. Figures 1 and 2 are pictures taken from Griz that show stress plots for a rod that is represented with a field of particles. Figure 3 is a still from a movie that was produced to show the interaction of standard elements with particles.

We added a significant new capability to the Mili I/O Library that allows writing "non-state" at any point in the simulation. This was created as a general capability, but the first application is to support writing nodal mapping data in ParaDyn for multi-processor results.

We have completed the draft specification and project plan for an enhanced Mili I/O Library. The plan calls for a phased implementation with the first deliverable being a library that is based on more standardized I/O technology than currently in use. This enhancement should reduce future maintenance costs for Mili and provide an easier path for adding some complex features that have been requested by our users.

We continued to support the integration of Mili with the VisIt post-processor. This year we created a detailed list of features used in Griz to close the gap between VisIt and Griz capabilities. We worked with the VisIt team to enhance VisIt so that it can be used with Mili files generated from the heat-transfer code Topaz3D, meeting a new programmatic visualization requirement.

FY2007 Proposed Work

We will continue to provide support for our user base, currently numbering approximately three dozen active users at LLNL, LANL, and several other sites. We will continue our strategy of providing new features in Griz and Mili to meet specific programmatic requirements while building more long-term capabilities. For FY2007, the items that will have the most impact will be putting the new Qt-based GUI into production; providing a more robust I/O Library; and completing the enhancements to the VisIt Mili plug-in. Our long-term goal is to make a complete migration to VisIt for model visualization.

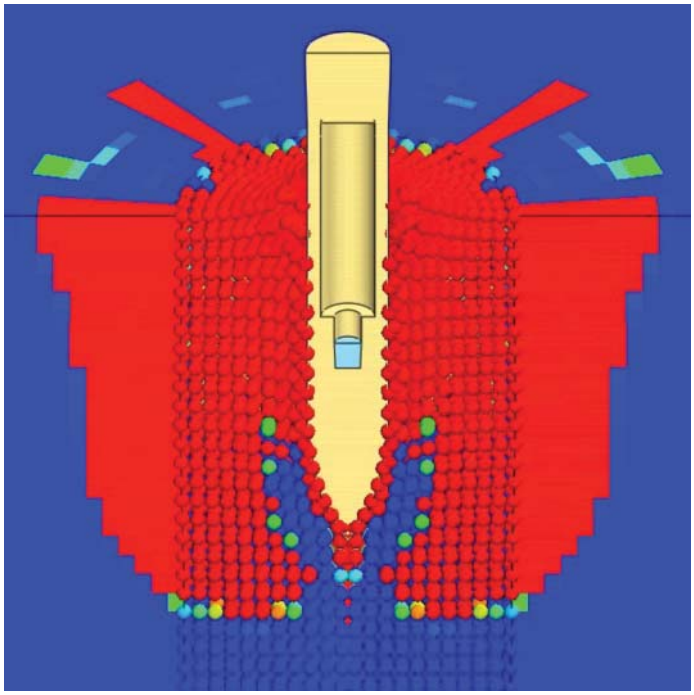

Figure 3. Rendering in Griz of standard elements and particles.

NIKE3D Support and Enhancement

Michael A. Puso
(925) 422-8198
puso1@llnl.gov

The objective of this work is to enhance, maintain, and support the implicit structural mechanics finite element code NIKE3D. New features are added to accommodate engineering analysis needs across multiple programs. Maintenance includes bug fixes and code porting to the new platforms available to engineering analysts. User support includes assisting analysts in model debugging and general analysis recommendations.

Project Goals

Code enhancement generates new features to meet our engineering community's user demands. Our goals to enhance NIKE3D included the following:

1. add new features to, and correct defects in, our mortar contact algorithms to enhance their production capabilities (details below);
2. add several additional features to material models and update the code's Users Manual; and
3. implement an 8-byte integer version of the WSMP direct linear equation solver to handle very large stiffness matrices; and interface NIKE3D to Intel's MKL library sparse direct solver for LINUX platform.

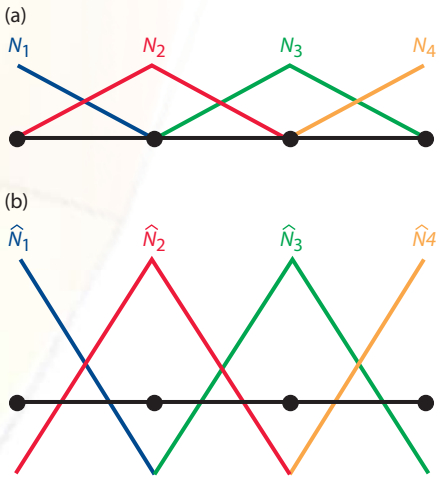

Figure 1. Shape functions used to approximate pressure on the boundary edge of a 2-D domain. (a) Standard mortar shape functions, N_A; (b) dual mortar shape functions, $\hat{N}_A$.

Relevance to LLNL Mission

Structural analysis is one of the most important functions of engineering and LLNL in-house maintenance for its suite of codes. NIKE3D, in particular, is a premier code for handling difficult nonlinear static structural analysis problems.

FY2006 Accomplishments and Results

The first production version of mortar contact in NIKE3D was made available at the end of FY2005. The first production work using the feature truly began in FY2006 and led to a number of related refinements.

1. Many contact problems have unintended initial interpenetration due to discrepancies in meshing non-matching curved surfaces. To treat these, a fast *nonlinear* algorithm to compute node relocations at problem initialization was implemented.
2. New diagnostics to display mortar contact activity (such as gap openings and slip) were added to help analysts diagnose models and solve problems.
3. We worked closely with analysts on large weapons problems to evaluate solution strategies. We compared different quasi-Newton nonlinear solution strategies, finding Broyden's method was often better than the default Broyden-Fletcher-Goldfarb-Shanno (BFGS) method.
4. We constructed 15 new QA problems specifically to test mortar contact.
5. We implemented the dual mortar approach into the production code for both mesh tying and contact.

So far, we have seen that the mortar segment-to-segment approach is able to solve defense-related problems more reliably and accurately and often faster (due to fewer iterations) than the classical node-on-surface approach. On the

other hand, we found that standard mortar contact increases the "bandwidth" of the global stiffness matrix. To rectify this, the dual mortar method originally created for mesh tying was implemented into the production code. Whereas the standard mortar contact method interpolates the contact pressures using the finite element "hat" functions, N_A, (Fig. 1a), the dual contact method uses discontinuous shape functions, $\hat{N}_A$, for the pressure (Fig. 1b) that diagonalize the slave side constraint equations, *i.e.*:

$$G_{AB} = \int \hat{N}_A N_B \, d\Gamma = \delta_{AB} \int N_A \, d\Gamma$$

This reduced problem size and matrix factorization times from 25% to 40% on many benchmark and production applications. Problem size is now often comparable to node-on-segment contact but still far more robust, as demonstrated in Fig. 2. Additional work was also performed on the higher-order mortar contact (10-node tets, 20- and 27-node bricks) bringing it closer to production status (Fig. 2).

Related References

1. Puso, M. A., and T. A. Laursen, "A Mortar Segment-To-Segment Frictional Contact Method for Large Deformations," *Computer Methods in Applied Mechanics and Engineering*, **193**, pp. 4891-4913, 2004.
2. Puso, M. A., and T. A. Laursen, "A Mortar Segment-to-Segment Contact Method for Large Deformation Solid Mechanics," *Computer Methods in Applied Mechanics and Engineering*, **193**, pp. 601-629, 2004.
3. Puso, M. A., "A 3D Mortar Method for Solid Mechanics," *International Journal for Numerical Methods in Engineering*, **59**, pp. 315-336, 2004.
4. Flemsch, B., M. A., Puso, and B. I. Wohlmuth,, "A New Dual Mortar Method for Curved Interfaces: 2D Elasticity," *International Journal for Numerical Methods in Engineering*, **63**, pp. 813-832, 2005.

FY2007 Proposed Work

1. Our current mortar contact implementation uses an N^2 search algorithm, the cost of which grows rapidly with surface size. Better and faster search algorithms will be implemented, *e.g.*, a bucket sort.
2. The BFGS algorithm does not effectively handle the evolving active contact constraints during nonlinear iterations within a time-step. Furthermore, the full Newton version of the mortar contact involves unsymmetrical stiffness matrices even for frictionless contact when the contact surfaces are not flat. Algorithms that perform secant updates such as BFGS, but better account for active constraints, will be investigated.

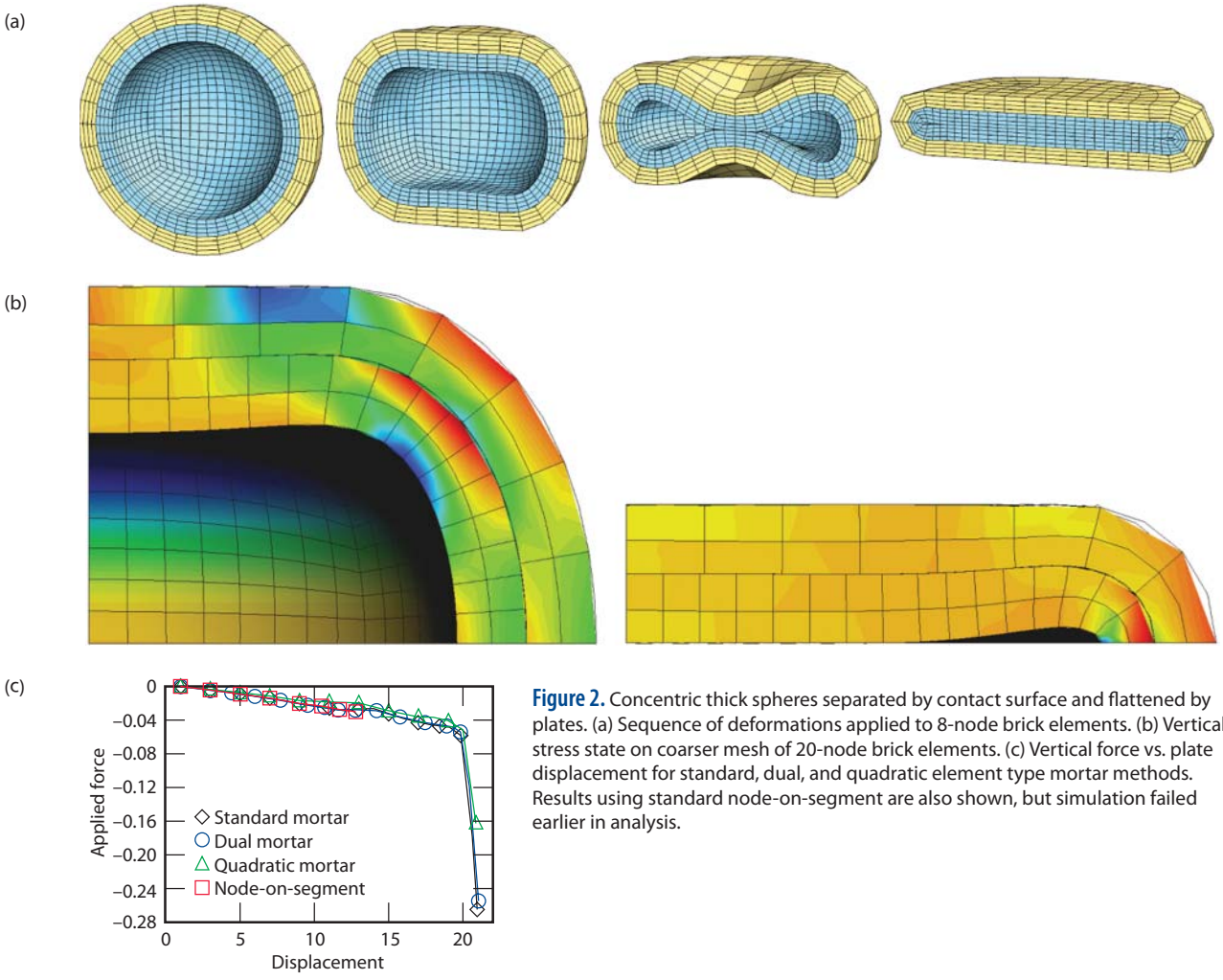

Figure 2. Concentric thick spheres separated by contact surface and flattened by plates. (a) Sequence of deformations applied to 8-node brick elements. (b) Vertical stress state on coarser mesh of 20-node brick elements. (c) Vertical force vs. plate displacement for standard, dual, and quadratic element type mortar methods. Results using standard node-on-segment are also shown, but simulation failed earlier in analysis.

Broadband Radiation and Scattering

Robert M. Sharpe
(925) 422-0581
sharpe1@llnl.gov

Electromagnetic phenomena are a central thread through much of modern engineering. There are two fundamental classes of applications: open region problems (where the energy propagates in unbounded space) and closed region problems (where the energy is guided by a waveguide structure or cavity).

This effort strives to enhance our computational electromagnetics (CEM) capability in broadband radiation and scattering in open regions. Broadband fields consist of energy with a robust spectrum, and include applications such as electromagnetic interference and electromagnetic compatibility noise analysis, broadband radar, and accelerator wakefield calculations.

LLNL analysis codes are limited by the accuracy of radiation boundary conditions (RBCs), which truncate space. We have developed improved RBCs by extending the perfectly matched layer (PML) approach to non-Cartesian meshes, and by developing discrete-time-domain, boundary-integral techniques that are compatible with high-accuracy, finite element methods and capable of arbitrary accuracy. These approaches have been compared to the traditional first-order absorbing boundary condition for a variety of radiation and scattering problems.

Project Goals

The ultimate deliverable is an enhanced CEM capability that can provide accurate and efficient computational solutions to broadband radiation and scattering problems. The algorithms for improved RBCs will be incorporated into LLNL's existing EMSolve code.

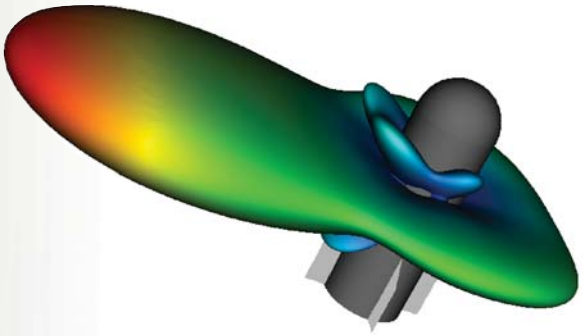

Figure 1. Scattered far-field generated by a broadside pulse hitting a rocket. The hybrid RBC was used to avoid the necessity of a huge air mesh.

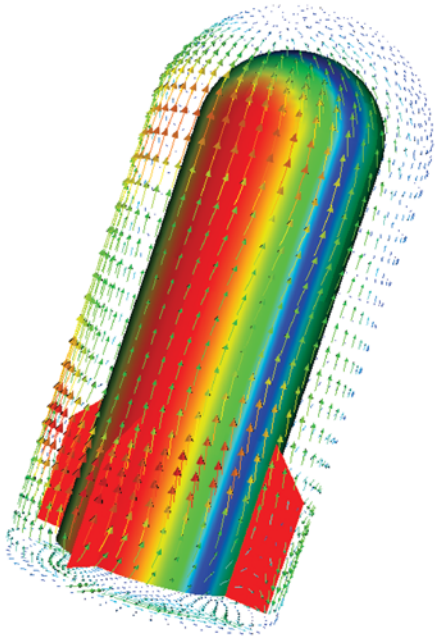

Figure 2. The electric field magnitude on the rocket surface and the equivalent vector currents produced by the hybrid RBC.

The result will be a 10- to 1000-fold improvement in the accuracy of simulations. Improved algorithms and our existing high-performance computer hardware will place LLNL's CEM activity among the top capabilities in the world. This research and the resulting capability will be documented in appropriate peer-reviewed publications.

Relevance to LLNL Mission

Electromagnetics is a truly ubiquitous discipline that touches virtually every major LLNL program. Our work supports the national security mission by reducing the time and money spent in building and testing existing programs. It will enable computer simulations for new devices and systems, performance analysis of systems critical to nonproliferation efforts, and the design of micropower impulse radar and other microwave systems.

FY2006 Accomplishments and Results

Figures 1 to 5 are samples of our FY2006 CEM work. We have completed the development of the parallel hybrid finite element boundary element code.

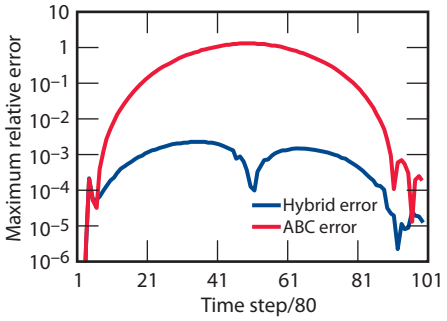

Figure 3. Pulsed Dipole Problem: the maximum relative error for the hybrid solution and the conventional ABC boundary condition solution as a function of time.

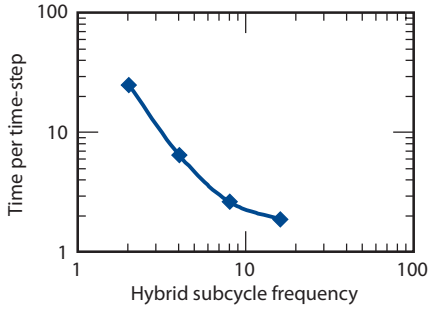

Figure 4. Pulsed Dipole Problem: computational cost per time-step for the hybrid method as the sub-cycling frequency changes.

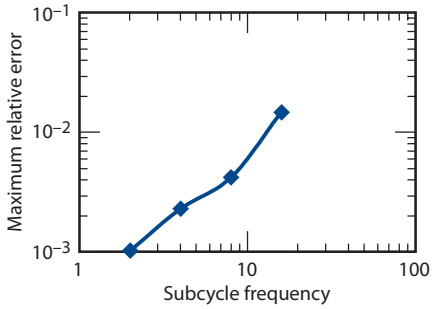

Figure 5. Pulsed Dipole Problem: maximum relative error behavior for the hybrid method as the sub-cycling frequency changes.

Several different formulations for RBCs are now available, including boundary conditions based on the electric field, magnetic field, or both at the boundary. A formulation using both the electric and magnetic fields was found to eliminate late-time stability issues due to interior resonances. We have collaborated with a professor at the University of Washington who is an expert on time-domain integral equations. It was found that the boundary element time-step could be different than the finite element time-step. By sub-cycling the boundary element computations at some multiple of the finite element time-step, large improvements in speed were observed, especially for very large meshes. This sub-cycling allows for a trade-off between speed and accuracy.

For a z-oriented pulsed dipole problem (with a known solution), we have achieved almost a 1000-fold increase in accuracy using our hybrid code (Fig. 3). The conventional Absorbing Boundary Condition (ABC) method fails to converge when applied on a spherical grid with a maximum radius of 1. In contrast, the hybrid solution shows good accuracy. Figures 4 and 5 show the behavior of our computation costs and error when sub-cycling of the hybrid boundary element calculation is applied.

Related Reference

Fasenfest, B., D. White, M. Stowell, R. Sharpe, N. Madsen, J. Rockway, N. J. Champagne, V. Jandhyala, and J. Pingenot, "A Hybrid FEM-BEM Unified Boundary Condition with Sub-Cycling for Electromagnetic Radiation," *IEEE Antennas and Propagation Society International Symposium*, Albuquerque, New Mexico, July 9-14, 2006.

Electro-Thermal-Mechanical Simulation Capability

Daniel White
(925) 422-9870
white37@llnl.gov

The purpose of this project is to research and develop numerical algorithms for 3-D electro-thermal-mechanical (ETM) simulations. LLNL has long been a world leader in the area of computational solid mechanics, and recently several solid mechanics codes have become "multiphysics" codes with the addition of fluid dynamics, heat transfer, and chemistry. However, these multiphysics codes do not incorporate the electromagnetics that is required for a coupled ETM simulation. There are numerous applications for an ETM simulation capability, such as explosively-driven magnetic flux compressors, electromagnetic launchers, inductive heating and mixing of metals, and MEMS. A robust ETM simulation capability will enable LLNL physicists and engineers to better support current DOE programs, and will prepare LLNL for some very exciting long-term DoD opportunities.

Project Goals

Our goal is to develop a novel simulation capability that is not available commercially or from the other national laboratories. We define a coupled ETM simulation as a simulation that solves, in a self-consistent manner, the equations of electromagnetics (primarily statics and diffusion), heat transfer (primarily conduction), and nonlinear mechanics (elastic-plastic deformation, and

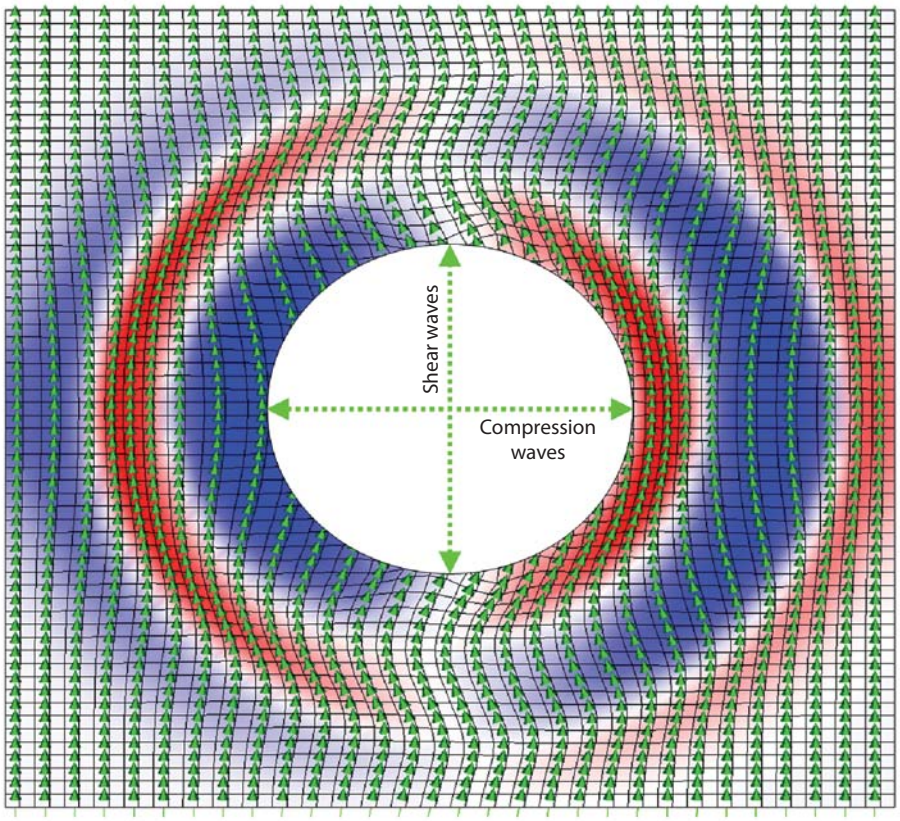

Figure 1. Simulation of Alfven waves (magnetic shear waves) using ALE3D. The simulation is of a small perturbation in the middle of the region; both Alfven waves and sound waves emanate from the perturbation. This is a snapshot of a time-dependent simulation, with the arrows depicting the direction of the magnetic field.

contact with friction). Our approach is to add electromagnetics to two existing mechanics codes, ALE3D and Diablo. ALE3D is a heavily used Arbitrary-Lagrangian-Eulerian hydrodynamics code; Diablo is an implicit Lagrangian thermal-mechanics code currently under development. Both codes are supported by Advanced Simulation and Computing (ASC). A finite element discretization will be used for the electromagnetics. In ALE3D the coupling of the electromagnetic equations, thermal equations, and mechanics equations will be done in an operator-split manner; in Diablo these equations will be solved in a self-consistent implicit Newton iteration.

Relevance to LLNL Mission

With this new capability, LLNL will have an unprecedented ability to simulate, design, and optimize ETM systems. This project is aligned with LLNL's core competency in Simulation Science and Engineering. It contributes to LLNL's mission to enhance/extend its simulation capabilities, and specifically addresses the need for simulation capability in the area of Energy Manipulation. This project complements on-going ASC work and will use ASC computers and software such as linear solver packages and visualization tools.

FY2006 Accomplishments and Results

Electromagnetics was incorporated into both the ALE3D and Diablo codes.

For ALE3D the key issue was advection of the electromagnetic flux density. We developed and implemented a novel divergence-preserving monotonic advection algorithm that works on unstructured meshes. This algorithm was verified by comparing computed results to canonical magnetohydrodynamic problems, to 2-D CALE simulations, and to previously published experimental results. In Fig. 1 we show a simulation of linear magnetohydrodynamic waves. This is a good test of the magnetic field advection algorithm. The computed wave velocity was compared to the analytical velocity, with $O(h^2)$ convergence.

For the Diablo task, the key issue was continuity of fields and currents across a sliding contact. A prototype penalty method for electromagnetic sliding contact has been developed and implemented, and the performance is being evaluated. We are also investigating an augmented Lagrange method for the electromagnetic sliding contact. A preliminary simulation result is shown in Fig. 2.

In addition, a novel Green's function method was developed for dealing with magnetic fields in the air. This method does not require a computational mesh of air regions, hence it significantly simplifies problem set-up (*i.e.*, meshing) for complicated problems. The challenge is that the Green's function method results in a dense matrix. We investigated low-rank QR compression of this matrix, resulting in an $O(n \log n)$ algorithm.

FY2007 Proposed Work

In FY2007 the emphasis will be on code verification and validation, and we will revisit the previously developed numerical algorithms to improve accuracy and efficiency as needed. We will simulate recent Office of Naval Research railgun experiments, which will allow us to validate the sliding electrical contact algorithms in Diablo. We have begun collaborating with several experimental pulse-power projects, and we will research methods to incorporate dielectric materials into the electric field update in order to address electric field breakdown issues that are relevant. Our initial approach is to solve an auxiliary partial differential equation involving the singular *curl-curl* operator. A recently developed multigrid algorithm will be used to solve the resulting system of equations.

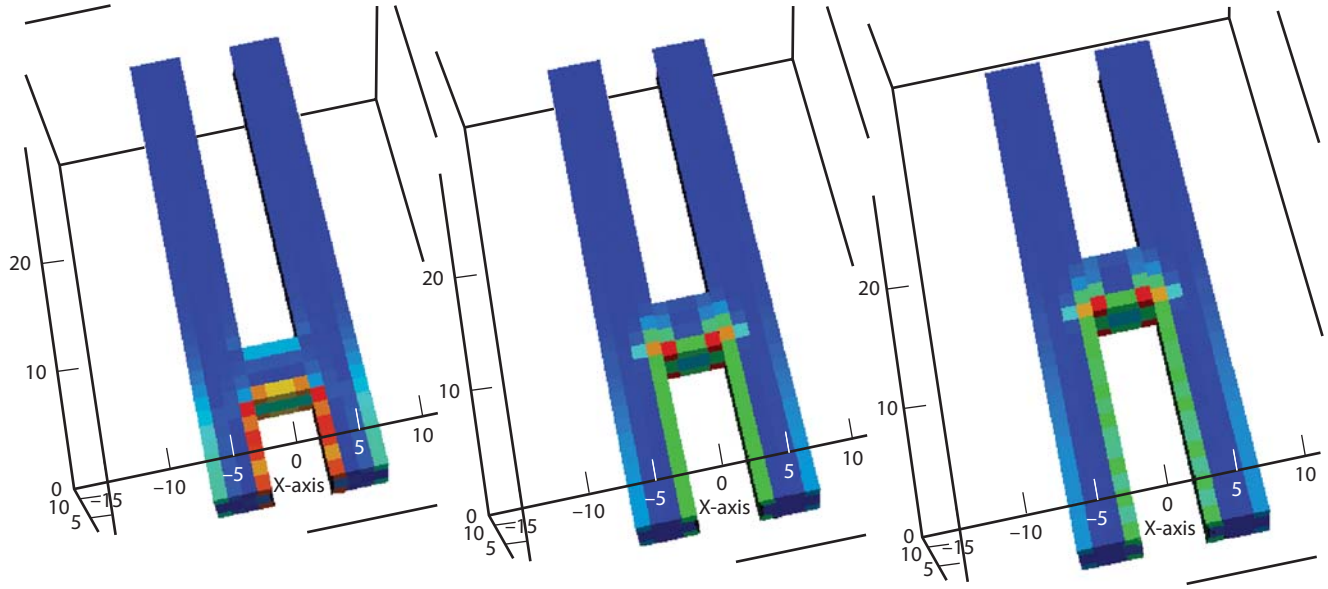

Figure 2. Sequence of snapshots of a preliminary sliding electrical contact simulation performed using the electromagnetics-enhanced Diablo code. The pseudocolor represents electric current density.

Computational Electromagnetics Implementation

Benjamin J. Fasenfest
(925) 423-6056
fasenfest1@llnl.gov

While improvements in commercial computational electromagnetic (CEM) tools are increasing every year, they lag academic advances by ten to twenty years. In addition, the major commercial CEM tools are not general enough to solve the unusual EM problems encountered in LLNL applications, nor are they ported to the latest massively parallel computers in use at LLNL. For these reasons and others, we have created in-house CEM tools such as EMSolve.

Recent projects in CEM have generated significant algorithms and prototype software in the areas of error estimators and improved radiating boundary conditions. Radiating boundary conditions provide a numerical termination of space for broadband radiation and scattering problems. LLNL's hybrid finite element boundary-element radiating boundary condition offers improved accuracy, as well as reduced sizes for the required finite element mesh. This technology has numerous applications, such as electromagnetic interference, broadband radar, and accelerator wakefield calculations. Error estimators provide a good approximation of the error in the solution of a finite element problem without requiring that the exact solution be known. By visualizing the error estimate throughout the problem, the mesh density or basis function order can be increased in areas with the largest error. This allows convergence to an accurate solution with many fewer mesh refinement iterations,

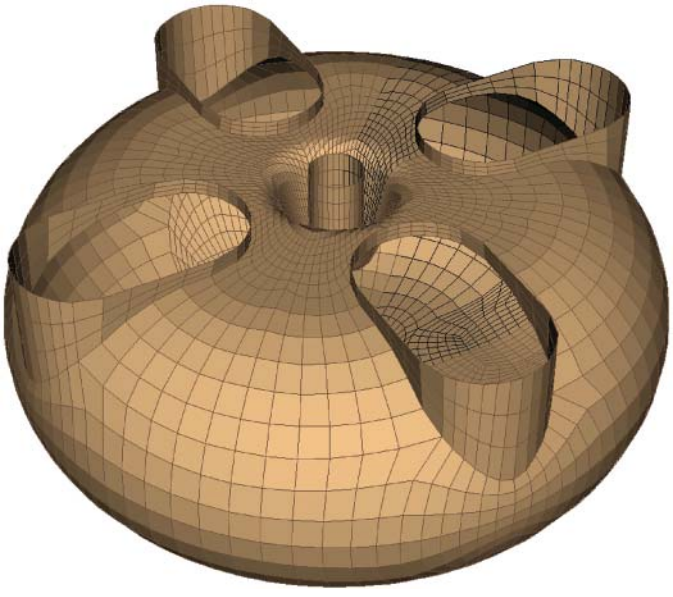

Figure 1. The inner surface of an accelerator induction cell. The round hole in the center is the beam tube. The four oblong holes connect this cell with its neighbor. The section of black mesh lines indicates the cutaway portion shown in Fig. 2.

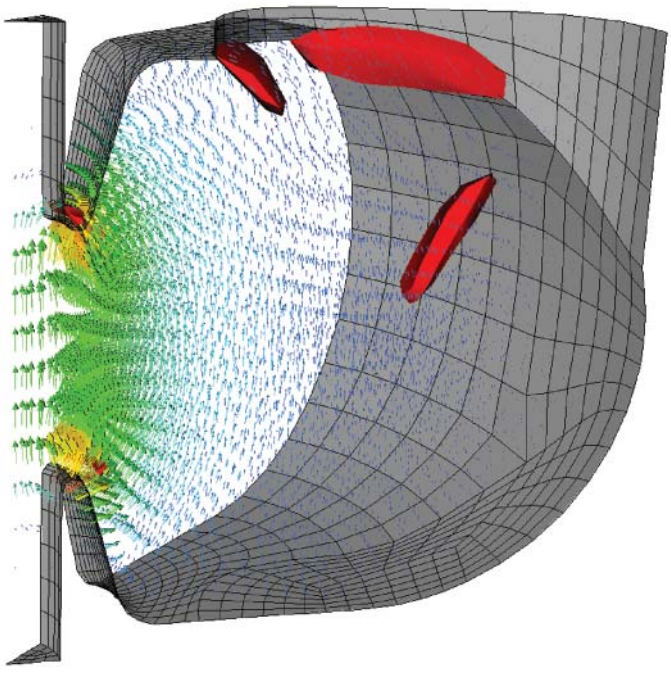

Figure 2. Cutaway image of an induction cell showing the first vector eigenmode of the cavity. The red lobes are areas identified by the residual error estimator as needing refinement. The two lobes near the top are located near a sharp edge in the surface of the mesh and the elements there are relatively coarse, so one would expect that refinement would be necessary. The third lobe was unexpected and on closer inspection it was found to contain poorly formed elements.

and the ability to produce more accurate solutions with less computing power.

This project focuses on fully integrating existing results into EMSolve to be used to solve real problems of interest. The algorithms and software need to be fully combined into the EMSolve framework and physics drivers, tested and verified in the new codes, and documented, so that they can be used easily. In addition, supporting features need to be added to the code to take advantage of the new improvements.

Project Goals

By the end of this project, significant upgrades to EMSolve functionality will be complete. Error estimators will be integrated within the EMSolve drivers for electromagnetic diffusion, and full-wave time- and frequency-domain EM. A full-wave time-domain radiating boundary condition will be implemented and tested for massively parallel simulations on LLNL's supercomputers. Supporting infrastructure, such as far-field patterns, radar cross-section, and plane-wave scattering formulations will be implemented. In addition, technical and user documentation will be created to assist in applying the new features. The implementation and documentation of these features will allow improved accuracy with fewer simulation iterations for LLNL's CEM work.

Relevance to LLNL Mission

Electromagnetics is a discipline that touches almost every major LLNL program. EMSolve is currently being used to support national security missions, the National Ignition Facility, and the Stockpile Stewardship program. The addition of new features to the EMSolve code, and their documentation, will allow for more accurate, faster results to be produced for these critical projects.

FY2006 Accomplishments and Results

The error estimators were integrated into the EMSolve codes, including time-domain and frequency-domain full-wave solvers, eigenvalue solvers, and magnetic diffusion solvers. Figures 1 and 2 show sample results generated by the error estimators. The speed of the error estimators was improved by about 60%, and their convergence for multi-material and higher-order problems was tested and verified.

A far-field output was added so that the broadband frequency-domain far-field and radar cross-section could be computed (Fig. 3). The hybrid radiating boundary condition was fully implemented within the EMSolve time-domain full-wave solver (Fig. 4). Its parallel efficiency and accuracy was tested and improved to allow scaling to very large numbers of processors. A scattered-field formulation was implemented to solve plane-wave scattering problems from composite structures.

In addition, the amount of code documentation was increased tremendously, both for the boundary-element and finite element portions of EMSolve. Several other improvements to EMSolve were made, including FORTRAN®-wrapping of the core computational library, consisting of hundreds of routines, improvements to the efficiency of integration rules, accurate memory usage computations, and the ability to define fields on a subset of the overall mesh.

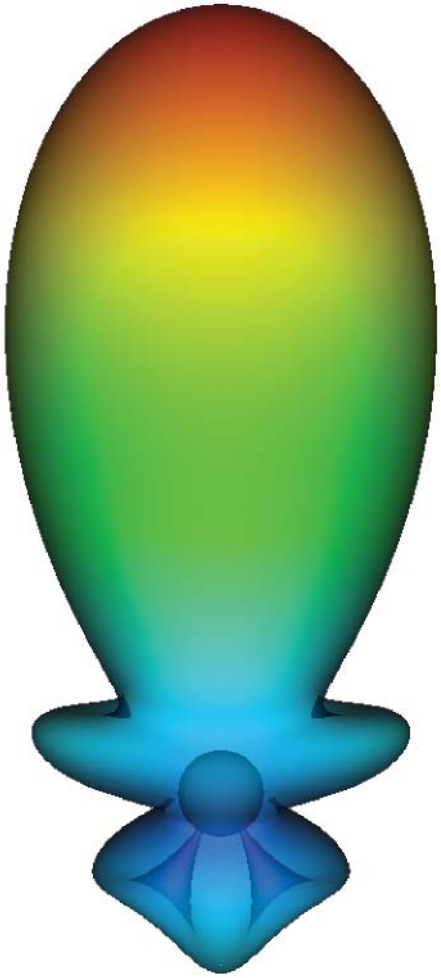

Figure 3. Far-field scattering produced by a four-wavelength dielectric sphere with a relative permittivity of 3.

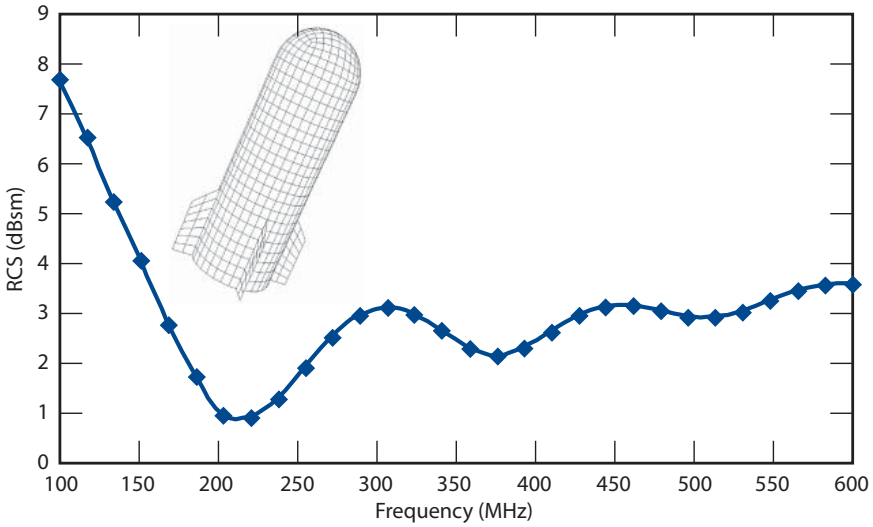

Figure 4. Broadband radar cross-section for a rocket. The radar cross-section determines how visible an object is to radar systems. The monostatic radar cross-section for a broadside pulse polarized along the rocket axis using the hybrid radiating boundary condition is displayed.

Three-Dimensional Vectorial Time-Domain Computational Photonics

Jeffrey S. Kallman
(925) 423-2447
kallman1@llnl.gov

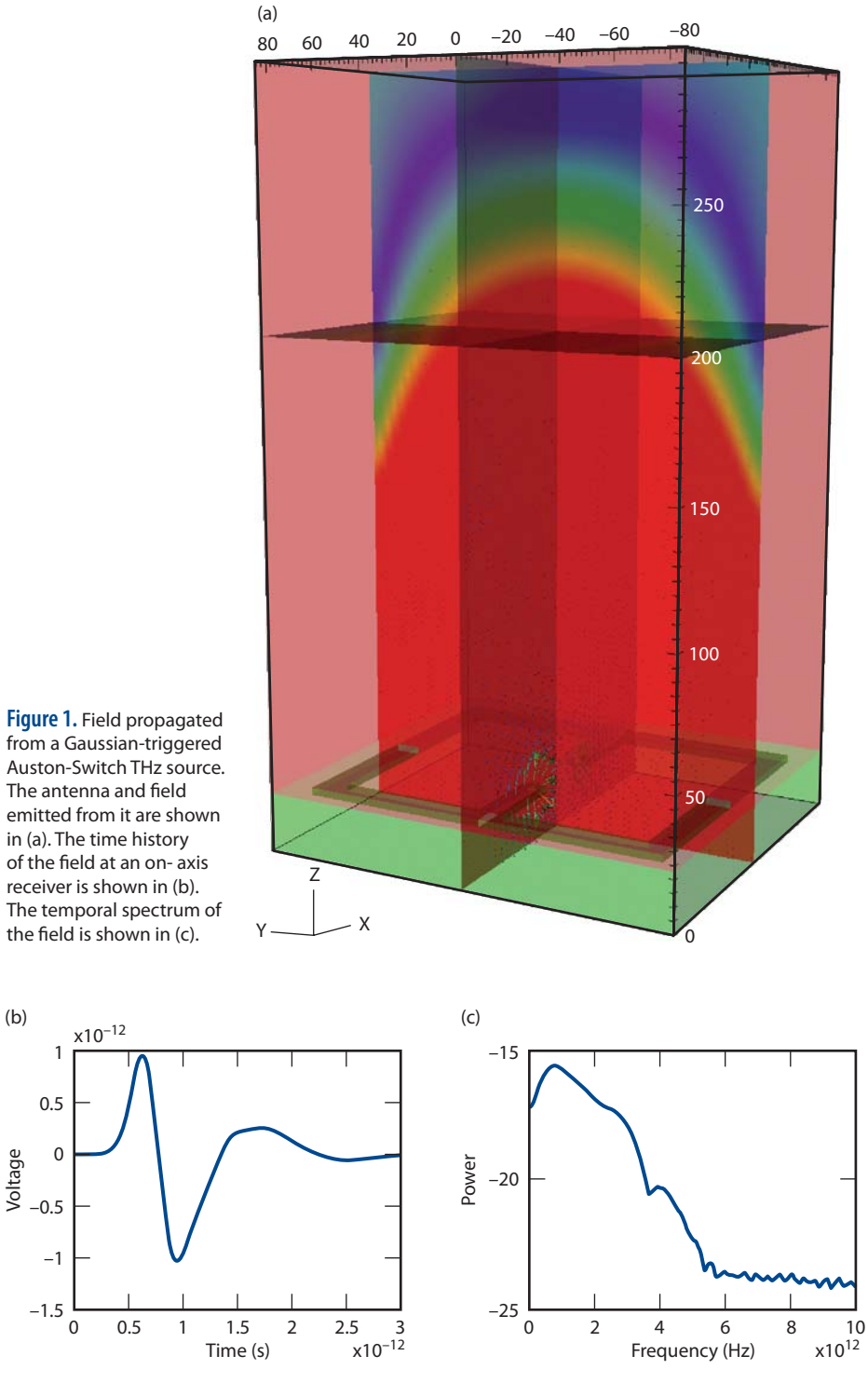

Figure 1. Field propagated from a Gaussian-triggered Auston-Switch THz source. The antenna and field emitted from it are shown in (a). The time history of the field at an on- axis receiver is shown in (b). The temporal spectrum of the field is shown in (c).

Customers with requirements for secure data transmission, computer networking, and high-bandwidth instrumentation are accentuating the need for photonic integrated circuit (PIC) technology. PICs will be the high-speed processing chips of the future and will impact both commercial and LLNL programmatic needs. Compact (LSI to VLSI), low-latency (sub-ps), wide-bandwidth (THz), ultrafast (100 Gb/s) miniaturized digital-logic, transmission, and sensor systems are potentially feasible. The design of novel integrated structures poses a considerable challenge, requiring models incorporating both microscopic and macroscopic physics.

Despite the strong photonic modeling capability at LLNL, new numerical methods are necessary as more complex photonic devices, materials, and configurations are devised. Three-dimensional time-domain (TD) design tools are fundamental to enabling and accelerating technologies for the realization of all-optical logic systems for data generation, transmission, manipulation, and detection. We have been doing the research necessary to create these new numerical methods.

Project Goals

We are filling the gap between existing modeling tools and those needed for LLNL missions by extending the state of the art in simulation for the design of 3-D PICs. We have defined challenges that must be addressed in our codes, such as models for optical gain and nonlinearities, as well as microscopic, nonuniform, inhomogeneous structures. Our tools leverage LLNL's expertise in computational electromagnetics (CEM) and photonics. We have developed models and algorithms for incorporation into a new generation of 3-D simulation tools. These tools

are general enough to be adapted to problems in many areas, and flexible enough to embrace the design of future mixed-signal systems as well as stand-alone systems in disparate regions of the EM spectrum.

Relevance to LLNL Mission

The ability to model complex 3-D photonic devices in the time domain is essential to LLNL for a broad range of applications. These include high-bandwidth instrumentation for NIF diagnostics; microsensors for weapon miniaturization within the DNT programs; encryption devices and circuits for secure communications for NHI surveillance applications; high-density optical interconnects for high-performance computing (core of the ASCI mission); and detection devices for homeland security.

FY2006 Accomplishments and Results

Most of our work has been concentrated in extending our two research codes: Quench3D and EMSolve. Quench3D is a narrow-bandwidth scalar beam-propagation-method code built for modeling large devices in which light propagates in a preferred direction. EMSolve is a vector time-domain code used for modeling small devices with either complicated geometries and/or no preferred direction for propagation. In support of both of these codes we have also been working on a program to generate accurate gain and absorption curves for semiconductor quantum wells as a function of quantum well structure, wavelength, and carrier density.

In the past year we spent time researching algorithms for incorporating a vector finite element beam-propagation solver and a finite element carrier-diffusion model into the Quench3D suite. The incorporation of vector finite elements into the BPM solver will allow us to model the dependence of gain on polarization in amplifier and laser structures. In addition we spent some time determining how the code should be parallelized.

We researched the algorithms necessary for incorporation of carrier diffusion and polarization models for 2- and 4-level absorption/gain in the EMSolve suite. We also performed research on submesh modeling of carrier effects in EMSolve. These codes can be used to efficiently examine power scaling in Auston-Switch-based THz sources and model Vertical Cavity Surface Emitting Lasers (VCSELs). Using the results of this research we were able to simulate the power scaling effects of Auston-Switch-based THz sources. Figures 1 to 3 illustrate the results of this work.

The quantum well modeling code work primarily involved researching extensions and corrections to the groundwork that had been laid in the summer of FY2005.

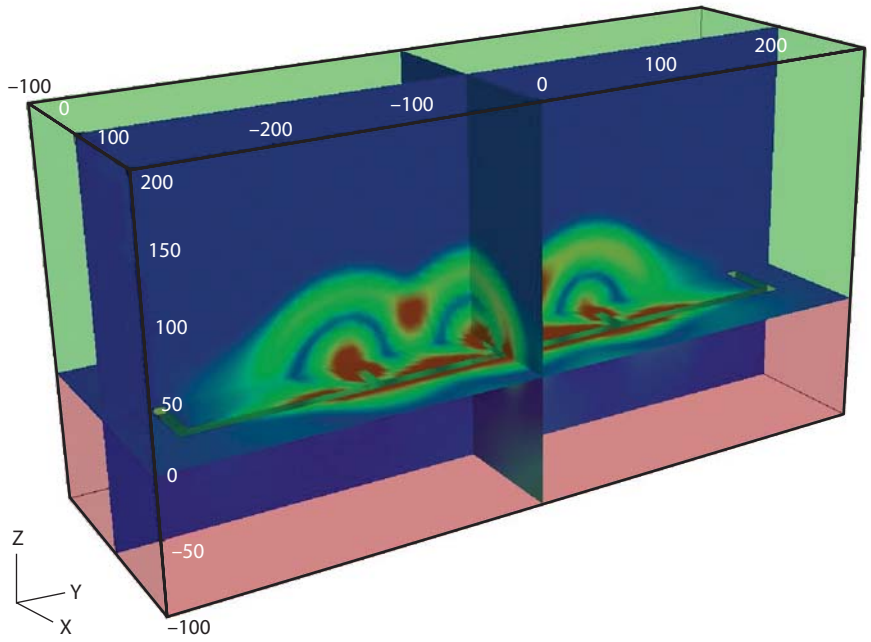

Figure 2. Field propagated from a trio of Gaussian-triggered Auston-Switch THz sources.

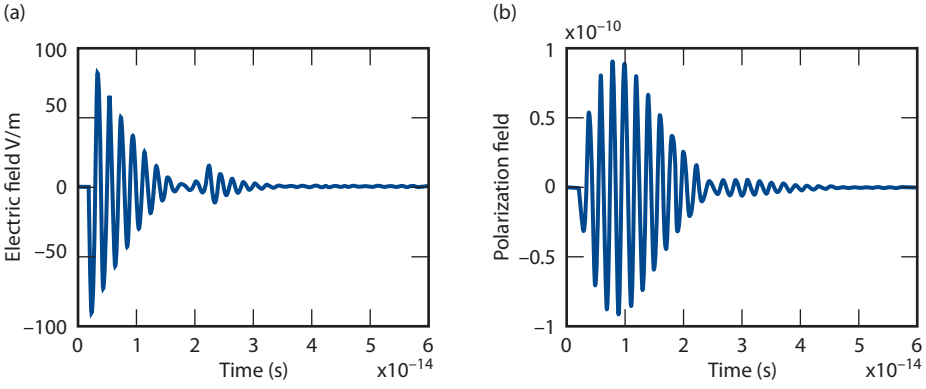

Figure 3. Electric field (a) and polarization (b) for a 2-level material illuminated by a beam of EM radiation. The polarization is computed using an auxiliary differential equation and is important in determining the gain and/or absorption in VCSEL simulations.

Related References

1. Bond, T. C., and J. S. Kallman, "Time-Domain Tools for the Investigation of Gain-Quenched Laser Logic," *International Semiconductor Device Research Symposium*, Washington, DC, December 10-12, 2003.
2. Koning, J. M., D. A. White, R. N. Rieben, and M. L. Stowell, "EMSolve: A Three Dimensional Time Domain Electromagnetic Solver," 5th *Biennial Tri-Lab Engineering Conference*, Albuquerque, New Mexico, October 21-23, 2003.
3. Koning, J. M., "Terahertz Photo-Conductive Antenna Array Power Scaling Simulations," *Proceedings IEEE APS*, pp. 2631-2634, 2006.

Usability Enhancements for 3-D Photonic Design Tools

Joseph Koning
(925) 422-3713
koning1@llnl.gov

A number of algorithms have been created to model novel and LLNL-specific devices. These algorithms were implemented in a suite of tools to model full 3-D, time-domain, nonlinear, photonics devices. This project was initiated to transition the suite of research codes to production codes, usable by a wider audience. The enhancements to the research codes will provide a set of packaged design tools that can be run on a variety of serial and parallel computers.

Project Goals

The capability for engineers to model novel 3-D photonic devices in the time domain requires usable and efficient simulation codes. The specific tasks of this project include the implementation of the existing algorithms, improving user interfaces, porting the codes to more common platforms, and running examples. The software that this team has written will be made widely available throughout LLNL on different computer architectures.

Relevance to LLNL Mission

Simulation is a core competency of LLNL, and this work enhances the ability of its engineers to model a broad class of devices. Potential users include the photonic designers in NIF (high speed diagnostics), DNT (weapons safe optical sensors), DHS (radiation sensing), NSA (gain quenched laser logic), NAI (fiber amplifiers), and PAT (components for the linac coherent light source).

FY2006 Accomplishments and Results

The existing algorithms have three main areas: enhancement of the full vectorial, 3-D time-domain code EMSolve; enhancement of the 3-D beam propagation quench suite of codes; and the creation of a code to model semiconductor physics.

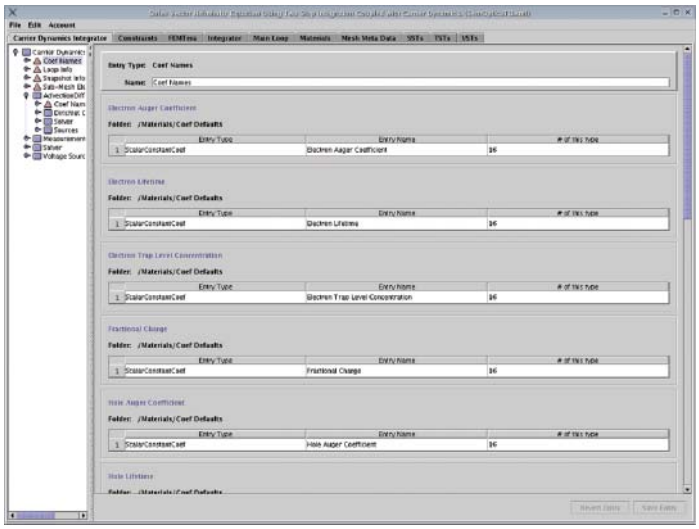

Figure 1. Configuration system. The EMSolve code uses an XML-based configuration system, which enables fast simulation configuration and easy integration of new code features. The GUI uses java for cross-platform portability.

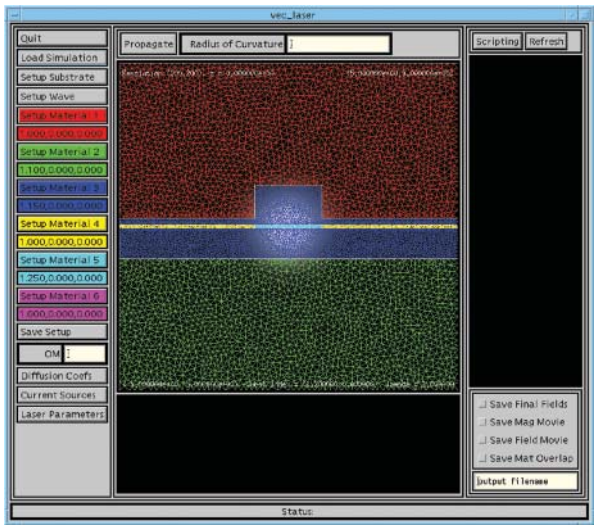

Figure 2. vec_laser GUI showing initial conditions for simulation of an optical amplifier. The mesh is shown in color and the input waveform is shown in grayscale.

The EMSolve code includes a number of enhancements to simulate photonic devices. A coupled carrier diffusion integrator/electrodynamics solver has been implemented for photonic integrated circuit simulations. In order to make this coupled system more efficient, a sub-mesh object was implemented to separate the carrier dynamics simulation grid from the full structure. In addition, efficient vector operations and finite element library optimizations were implemented, providing a 12x speed improvement. Figure 1 shows the configuration system. Adding a new component adds a tab to the configuration window. This advanced model was used to study THz photoconductive antennas.

In a separate integrator a polarization model was implemented using both 2- and 4-level absorption/gain models. These polarization models will be used to simulate 3-D vertical cavity, surface-emitting lasers (VCSELs).

The quench suite of codes has been augmented with a narrow bandwidth beam propagation method (BPM) code with coupled carrier diffusion called vec_laser. The GUI produced for this code is shown in Fig. 2. The vec_laser code has been parallelized and ported to run on Intel-based parallel machines.

In the Intermixed Quantum Well Physics modeling code the accomplishments for this year include implementation of Version 2 for calculation of complex permittivities in quantum wells using a quantum mechanics approach. Carrier induced effects are included: bandgap shrinkage is implicit in the calculation of electron wavefunctions using an iterative approach to solve Schroedinger-like and Poisson equations including many-body carrier effects, bandgap filling, and free-carrier absorption effects. Excitonic effects are also included. The potential distribution in the diffused well at quiescent state, the carrier density distribution formulation, the iterative formulation of quasi-Fermi levels, the interband absorption integrated with exciton saturation effects, and the integration limits have all been updated. Figure 3 shows the potential in a diffused quantum well for different diffusion lengths. Figure 4 shows the trend of absorption for a TE polarization in an AlGaAs/GaAs quantum well; with increasing carrier density saturation of the light-hole excitonic peak occurs.

Related References

1. Koning, J. M., "Terahertz Photo-Conductive Antenna Array Power Scaling Simulations," *Proceedings IEEE APS*, pp. 2631-2634, 2006.

2. Koning, J. M., D. A. White, R. N. Rieben, and M. L. Stowell, "EMSolve: A Three Dimensional Time Domain Electromagnetic Solver," *5th Biennial Tri-Lab Engineering Conference*, Albuquerque, New Mexico, October 21-23, 2003.

3. Bond, T. C., and J. S. Kallman, "Time-Domain Tools for the Investigation of Gain-Quenched Laser Logic," *International Semiconductor Device Research Symposium*, Washington, DC, December 10, 2003.

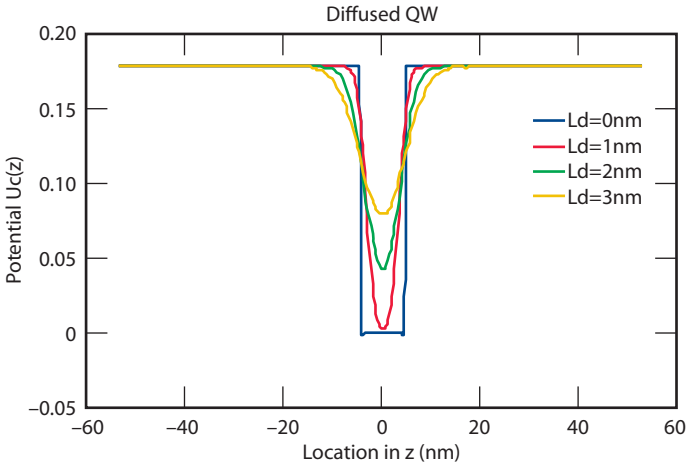

Figure 3. Potential distribution for the conduction band in a diffused quantum well for different diffusion lengths, Ld. The longer Ld, the smoother the transition from well to barrier and the wider the gap.

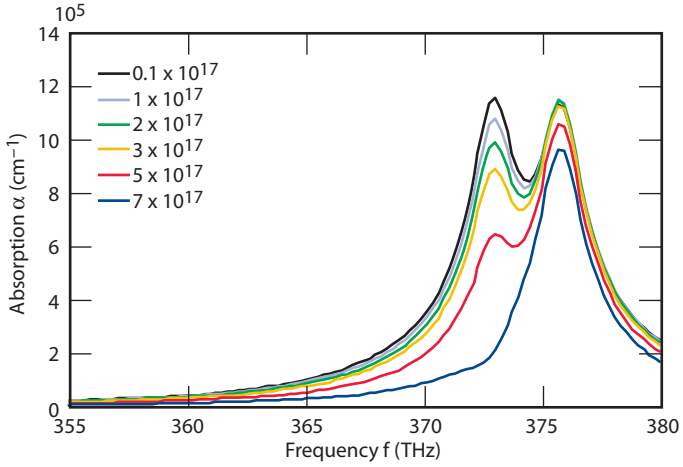

Figure 4. TE absorption in a 7-nm AlGaAs/GaAs well.

Laser Glass Damage: Computational Analysis of Mitigation Process

James S. Stölken
(925) 423-2234
stölken1@llnl.gov

Understanding and controlling the physical processes that cause laser-induced damage to optical components is crucial to the success of many high-energy-density experimental facilities, including LLNL's National Ignition Facility (NIF). Experimental and theoretical investigations of laser-damage in silica glass and KDP crystals are legion and are actively being pursued within the NIF Program. The insight garnered from experimental data is limited by the extremely short time-scale (~1 ns) of the damage events and the complex interplay between energy deposition and hydrodynamic response. A further complication is the stochastic nature of damage initiation, necessitating a *post priori* approach where the damage process must be deduced via forensic reconstruction.

Understanding laser-damage initiation and growth is just half of the problem. Creating an effective strategy to detect and mitigate laser damage is the essential second part. One promising process is to use long wavelength (CO_2) laser energy to excise/anneal the damage site. Key parameters to be optimized include the laser wavelength, intensity, pulse duration, and scan pattern in relation to the size and type of damage site. Both damage initiation/growth studies and mitigation process development could benefit from a high-fidelity predictive simulation capability that incorporates the essential ingredients of the laser-material interaction and the resulting coupled material response in experimentally relevant configurations.

We are addressing the technical challenges associated with energy deposition, dynamic material response, and the nature of the coupling between these two processes. Our approach is to adapt the current EM simulations capability within EMSolve to simulate the time, space, and material state dependence of the laser energy deposition process. The material's dynamic response is then simulated using advanced multi-phase equations of state (EOS) and failure models within the ALE3D multi-physics code. This also provides some facility to model damage initiation in silica, which would provide a self-consistent facility to establish initial conditions for mitigation studies.

Project Goals

The primary goal is to implement a capability to perform coupled EM simulations of laser energy deposition and subsequent material hydrodynamic response that includes the dependence of the energy deposition processes on local variations in state-dependent material properties. energy deposition (thermal transport) and hydrodynamic response (momentum transport). A secondary goal of the project is to determine how tightly-coupled the EM and hydro simulation schemes are for the deposition and the response. To accomplish these goals, specific objectives to enhance the hydro and EM simulation capabilities have been set.

The final objective is to couple the hydro and EM simulations to facilitate exploring how strongly this interaction must be implemented. The degree of coupling required to adequately simulate a given phenomenon is problem-dependent and greatly affects the computational costs and efficacy of the overall simulation methodology.

Our technical approach has been as follows.

1. Implement spatial and material state-dependent EM properties, such as the complex dielectric constant. Using a Lorenz-Lorentz formulism, we explicitly modeled the dependence of the material conductivity and permittivity upon density (Fig. 1). This same approach explicitly accounts for the laser energy frequency dependence, thereby facilitating the investigation of this important parameter in candidate mitigation processes. To improve the quality of the boundary conditions of the EM simulations and enhance their dynamic range, we adopted a scattered electric-field methodology (Fig. 2).
2. Adapt existing models of material deformation, phase transformations, and damage to simulate such processes under conditions relevant to laser damage in silica glass. We adopted a

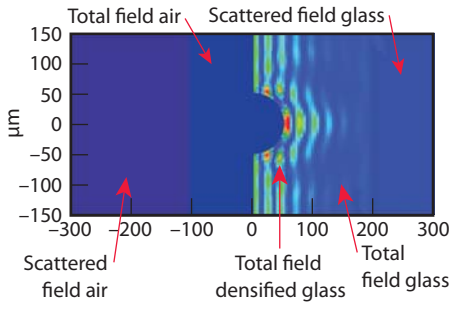

Figure 1. Simulated Joule heating in glass around an artificial defect with 20% greater permittivity and conductivity than the bulk glass.

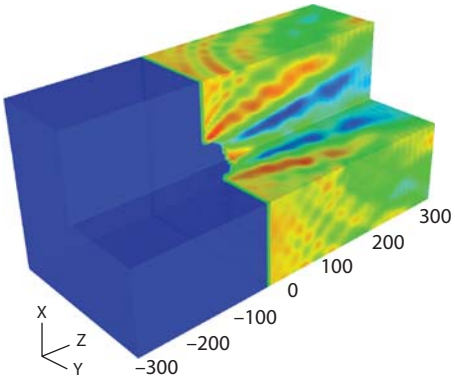

Figure 2. Three-dimensional rendering of laser heat deposition similar to that shown in Fig. 1. Energy deposition varies by a factor of one hundred from blue to red.

unified-creep model for the deformation of silica at high temperatures using material parameters consistent with a linear viscous solid and a temperature-dependent shear modulus. The two-phase EOS is based on combining two analytic forms for the low and high-pressure phases with an irreversible kinetic relation (Fig. 3).

3. As a first step, consider only a single material state variable: the material density. The material density plays a central role in both the hydrodynamic response and the energy deposition. Furthermore, under high-pressure loading, such as laser-induced shocks, the reference density of silica is modified, providing material "memory" of previous history such as glass damage.

A loosely coupled scheme is proposed to connect the hydrodynamic simulations (ALE3D) to the laser energy deposition simulations (EMSolve) via a file passing mechanism (Fig. 4). This approach leverages existing capabilities within ALE3D to specify spatially and temporally varying heat sources using an external file.

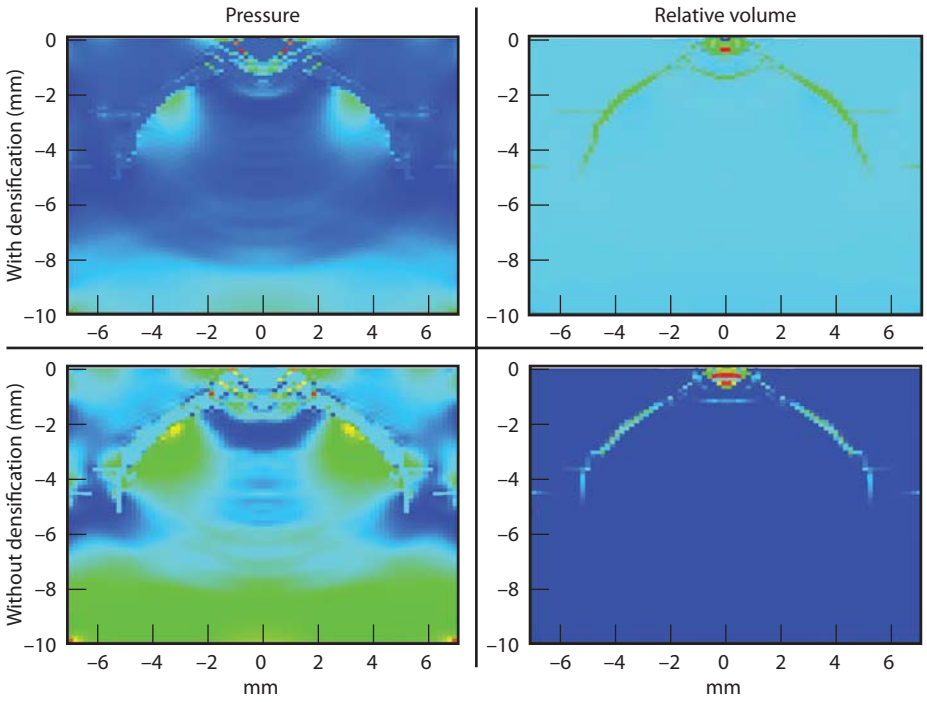

Figure 3. Residual pressure and relative volume following indentation of glass with a smooth circular punch. Cross-section views of a 3-D simulation showing the interplay of the damage model with EOS that (do)/(do not) capture the pressure-induced densification of silica glass.

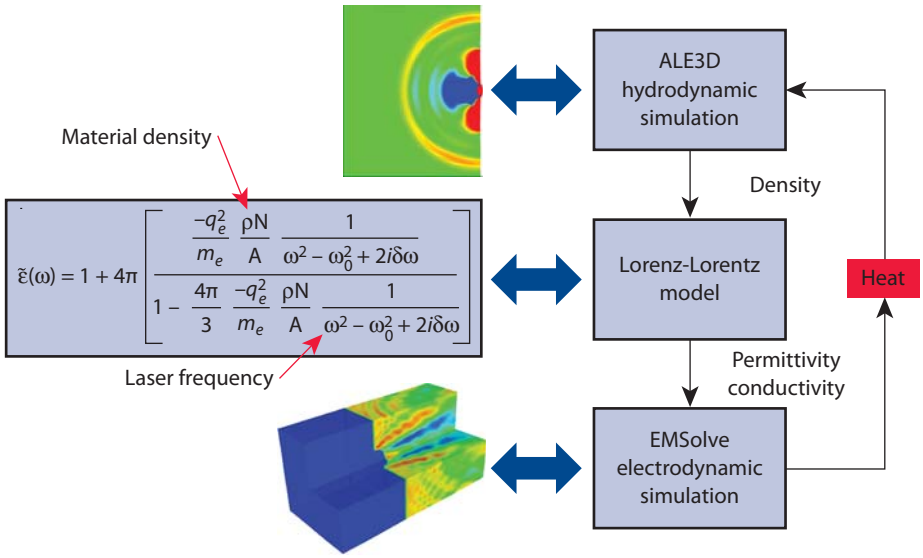

Figure 4. Loosely coupled scheme that includes the effects of laser frequency and material density.

Relevance to LLNL Mission

Leveraging current computational capabilities will place LLNL's Engineering Directorate in a key technical role for both process and facilities development.

FY2006 Accomplishments and Results

A two-phase EOS model has been adapted to account for the permanent densification of silica glass that occurs under high-pressure loading. Model parameters have been fit to the reference density, bulk modulus, and thermal expansion coefficients associated with both the high- and low-pressure phases. A simple model of brittle damage has been adapted to account for cracking under tensile loading, and has been successfully tested in conjunction with the above densification EOS model. A scattered electric field formulation has been implemented to improve the efficiency of the EM simulations. The capability to account for spatially varying permittivity and conductivity has been implemented. The dependence of the real and imaginary parts of the refractive index on material density and radiation wavelength has been accounted for in the framework of a Lorenz-Lorentz model and implemented in the EMSolve code.

FY2007 Proposed Work

We plan to couple the hydro and EM simulations via a file-sharing scheme by extending existing capabilities within the ALE3D software and adapting the EMSolve software to import and export the requisite files. We will also continue testing the new capabilities created in FY2006 and assess the efficacy of the coupling scheme on benchmark problems.

Simulation Capability for Nanoscale Manufacturing Using Block Copolymers

David Clague
(925) 424-9770
clague1@llnl.gov

This project focused on simulation capability for nanoscale manufacturing using block copolymers. The capabilities published in the literature enable prediction of the polymer combination and the ratio of polymers involved to achieve desired nanoscale features during melt solidification. Additionally, the length of the polymer blocks qualitatively influences the temperature and time necessary for the annealing process.

Project Goals

The goal of this project was to reduce to practice published, predictive block copolymers simulation capabilities to augment and guide experimental efforts to controllably form nanoscale features.

Relevance to LLNL Mission

Repeatable control of nanoscale features such as lithographic masks and 3-D structures is a critical capability gap at LLNL. This project will provide custom nanofabrication technology that will enable the transition and deployment of many nanoscale devices and technologies into the programs. This enabling capability will impact nanoscience and technology at LLNL, and aligns with competency goals in predictive simulation and micro-, meso- and nanoscale engineering, computational engineering, and mesoscale fabrication.

FY2006 Accomplishments and Results

We reduced to practice 2-D and 3-D Cahn-Hilliard-Cook (CHC) type

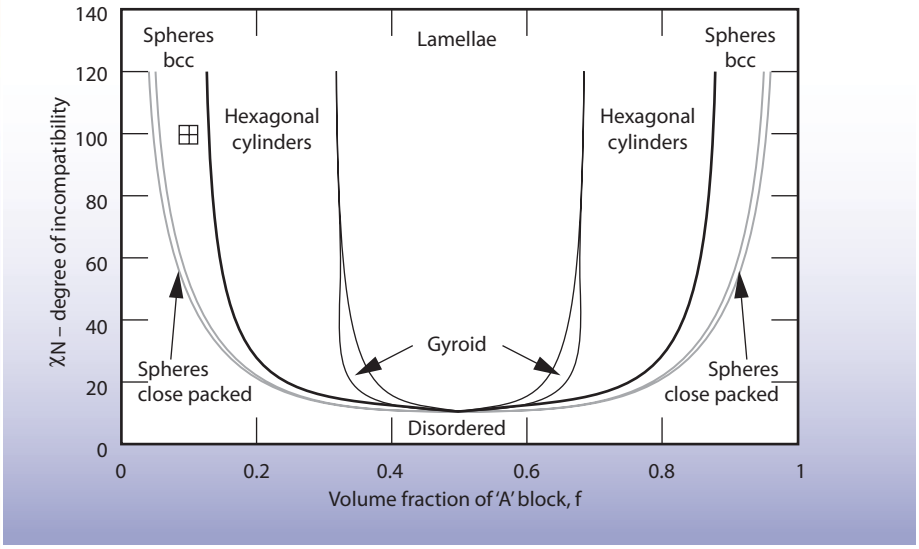

Figure 1. Phase diagram for polystyrene and PMMA, predicted using self-consistent mean field theory: χ is the Flory-Huggins parameter, which is a measure of block-block solubility; N is the degree of polymerization; and f is the number fraction of the reference polymer in the diblock.

models to predict nanophase formation in diblock copolymer systems. The models from the literature were reduced to both MatLab® scripts and Fortran90® simulation capabilities. The potential nanophases that can be predicted with the model include lamellae, cylinders, gyroids, and spheres (Fig. 1).

Two-dimensional results from this effort enabled elucidation of conditions that produced lamellae and cylindrical features. Additionally, through the literature, we were able to relate final features to real dimensions. When comparing predicted feature sizes with experiment, it was found that the simulation results were within 5% of the realized results. In Fig. 2, we show lamellae and cylindrical phase separations.

In addition to reduction to practice of the 2-D CHC model, a 3-D version of the capability was reduced to practice to enable prediction of 3-D effects and surface boundary conditions on nanoscale feature formation. Figure 3 shows the 3-D results for lamellae and spherical nanofeatures.

Using these newly available capabilities, simulation results have been collected to help guide block copolymer selection from commercial sources to achieve desired feature sizes.

Related References

1. Kielhorn, L., and M. Muthukumar, "Spinodal Decomposition of Symmetric Diblock Copolymer/Homopolymer Blends at the Lifshitz Point," *J. Chem. Phys.*, **110,** 8, 1999.

2. Chakrabarti, A., and R. Toral, "Late Stages of Spinodal Decomposition in Three-Dimensional Model System," *Phys. Rev. B,* **39,** 7, 1989.

3. Matsen, M. W., and F. S. Bates, "Unifying Weak- and Strong-Segregation Block Copolymer Theories," *Macromolecules,* **29,** 4, 1996.

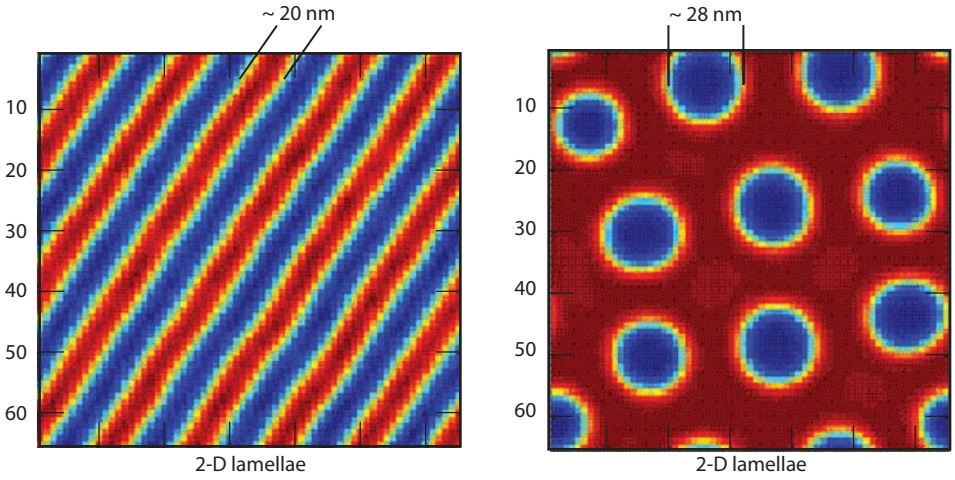

Figure 2. Predicted lamellae and cylindrical nanofeatures using 2-D CHC-like model for a polystyrene/PMMA diblock copolymer system. The volume fractions of the reference block were consistent with the phase diagram shown in Fig. 1. Results were in very good agreement with experiments.

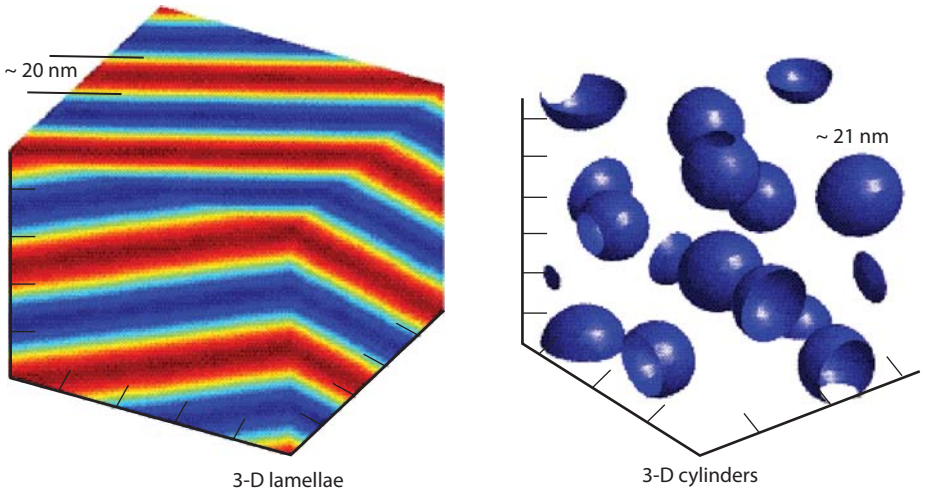

Figure 3. Predicted 3-D lamellae and spherical nanofeatures for a polystyrene/PMMA system. The average feature size is given on the images.

Sputtering Chamber and Capsule Thermal Modeling

Aaron Wemhoff
(925) 423-9839
wemhoff2@llnl.gov

The morphology of a thin film grown in a sputtering process has been shown to be heavily dependent upon the substrate temperature and the chamber conditions, as illustrated in the Thornton structure zone diagram in Fig. 1. Currently, measurements of the substrate temperature of spherical capsules in a sputtering process are extremely difficult due to the required motion of the capsule. Previous analyses for this process have involved a large number of approximations and simplifications, resulting in an uncertainty of +/- 70 ºC.

In this project, a predictive tool for the capsule temperature is investigated and applied as part of the Diablo multi-mechanics finite element code, nearly eliminating this uncertainty since the underlying mechanics of the system are captured by the code.

Project Goals

This project focuses on the full integration of all modes of heat transfer from the capsule to the surrounding chamber environment: gas adsorption, enclosure radiation, and wall-capsule contact. These modes of heat transfer are calculated using a standard finite element formulation, where the influence of each mode is designated via user-defined input variables. Furthermore, the influence of capsule motion on the aforementioned modes of heat transfer is automatically calculated at each capsule position.

Relevance to LLNL Mission

The structure of thin films is of vital importance to LLNL programs and areas of interest. Equally valuable are the addition of new features to the

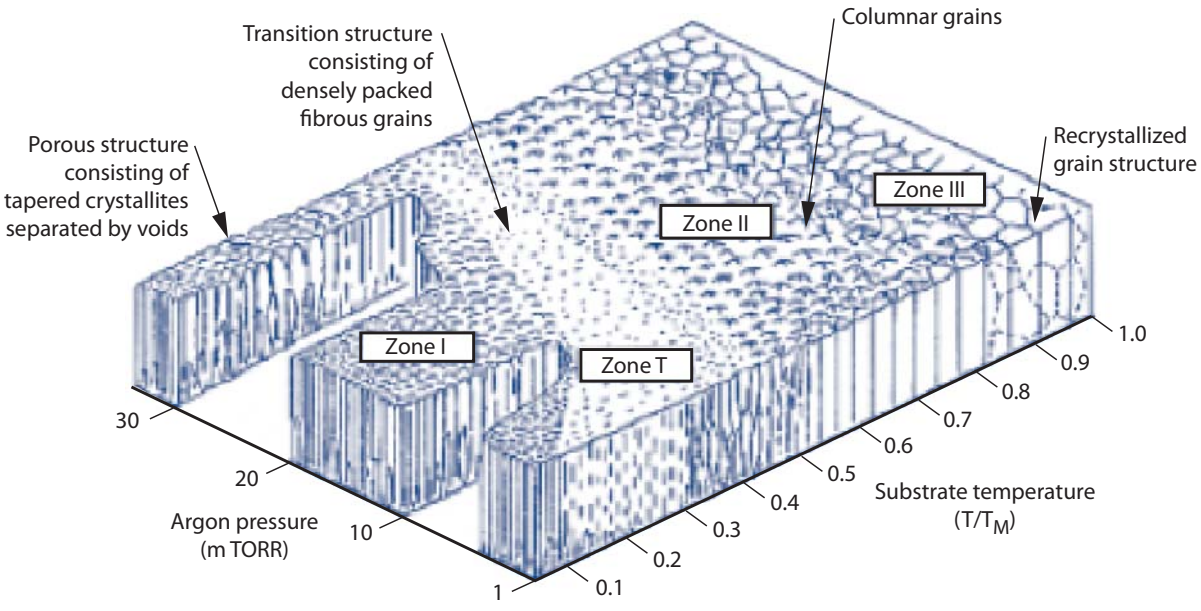

Figure 1. Thornton structure zone diagram.

Diablo code. The work performed in this project is part of a joint effort to improve the quality of sputtered films for NIF target preparation.

FY2006 Accomplishments and Results

A specialized Neumann boundary condition was added to Diablo. This module features a combination of thermal mechanics seen in the bulk node, contact, and convection algorithms. At each time-step the user-defined capsule position function allows for the automatic determination of the existence of contact, the location of contact along the chamber wall (if applicable), and the updated enclosure radiation view factor set.

View factors are efficiently calculated by projecting each facet of the chamber wall using spherical trigonometry, as seen in Fig. 2. The capsule temperature is calculated at each time-step using a standard lumped capacitance approach. The numerical approach and implementation was verified by comparing six test problems to known analytical solutions. In all cases the simulated capsule temperature agreed with the analytical solution within 0.3%.

A further test problem featured the change in capsule temperature history when the capsule was removed from the sputtering pan surface at specific times. Figure 3 shows that the change in heat loss is greatly reduced after this contact is removed, which is consistent with the reduction in heat transfer modes after the removal.

Related Reference

Thornton, J. A., "Influence of Apparatus Geometry and Deposition Conditions on the Structure and Topography of Thick Sputtered Coatings," *J. Vac. Sci. Technol.*, **11**, pp. 66-67, 1974.

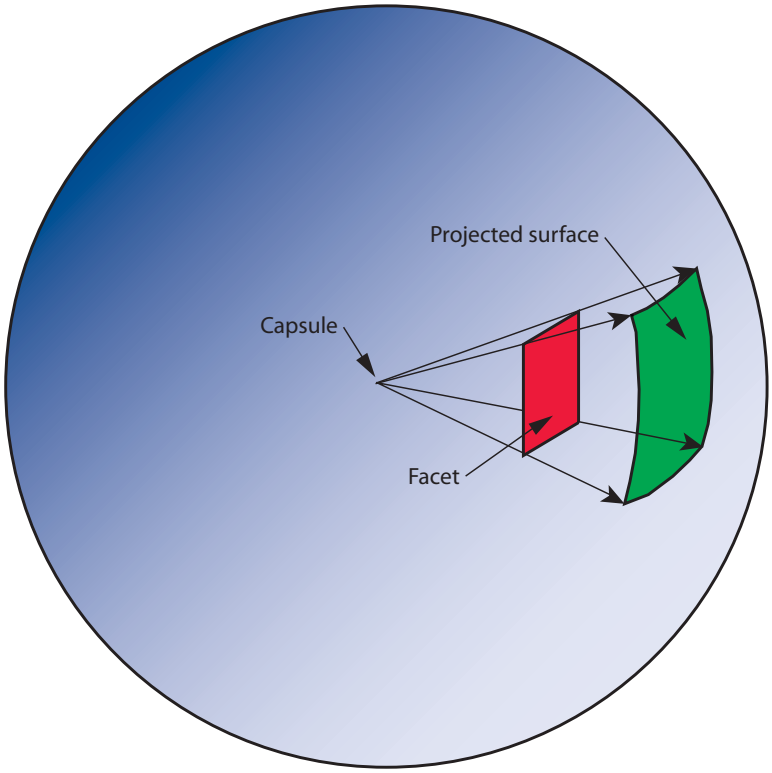

Figure 2. Projected surface used in determination of capsule-facet view factor.

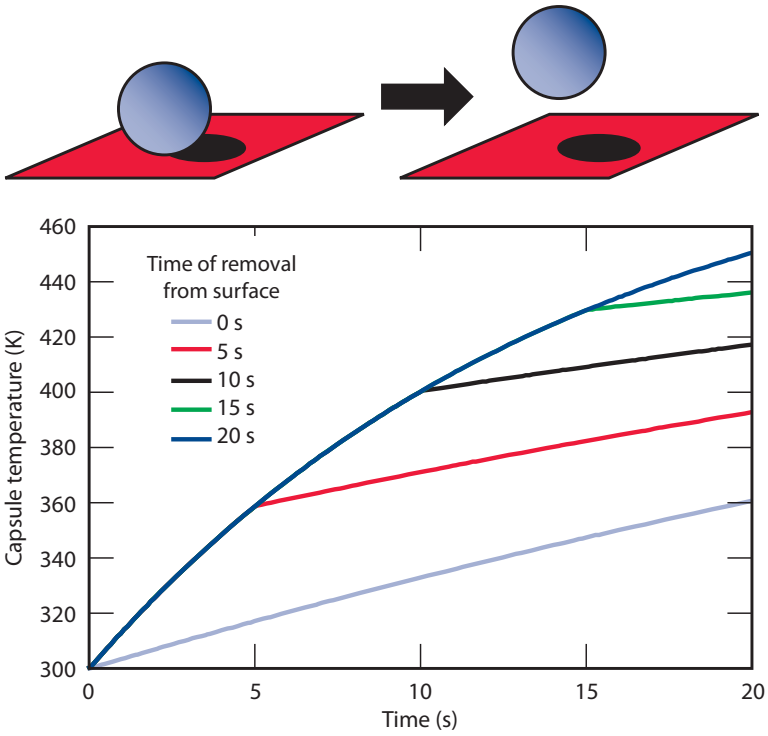

Figure 3. Temperature history of capsule for various durations of contact with the chamber wall surface.

Experimental Validation of Finite Element Codes for Nonlinear Seismic Simulations

Steven W. Alves
(925) 423-2391
alves6@llnl.gov

To further refine LLNL's abilities to simulate reinforced concrete structures subjected to seismic events, our computational codes and modeling approaches must be rigorously validated. Seismic excitations are long duration (~30 s), and large structures can require very large numbers of elements, so seismic simulations of reinforced concrete structures are computationally intensive. Using the homogenized rebar model implemented in DYNA3D/ParaDyn to approximate the reinforcing is attractive because of its efficiency in computation and mesh generation compared to explicitly modeling the rebar.

A series of shake table tests were performed on a full-scale seven-story slice of a reinforced concrete building using the NEES Large High-Performance Outdoor Shake Table (LHPOST) at the University of California, San Diego (UCSD) (see Fig. 1a). Results from the shake table experiment were provided so that the response of a finite element model of the structure could be compared to the experimental response.

Project Goals

The goal is to assess our capability to accurately model a full-scale reinforced concrete structure using a homogenized rebar/concrete model as implemented in the DYNA3D/ParaDyn codes.

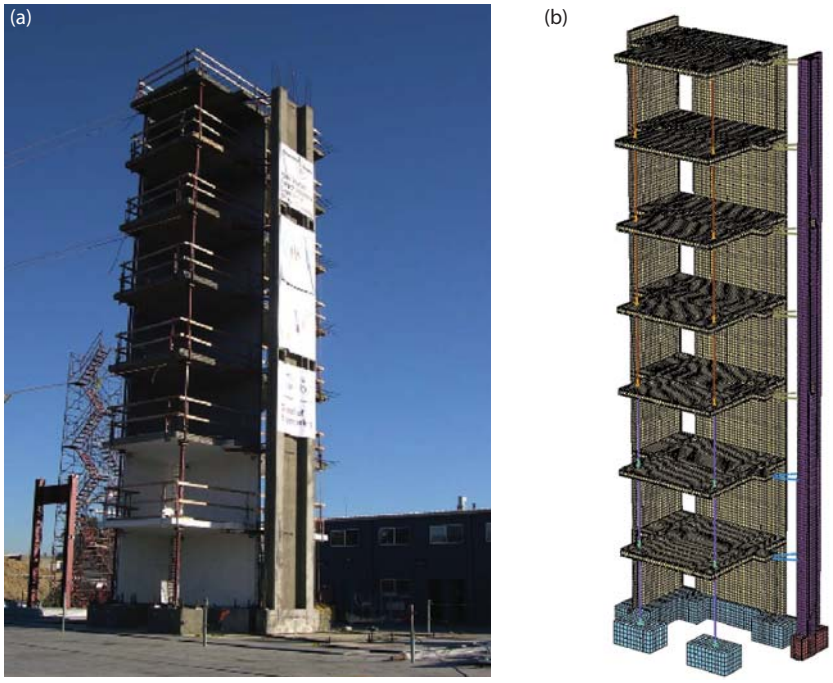

Figure 1. (a) Experimental structure; (b) half-symmetry finite element model.

Relevance to LLNL Mission

Simulation of the seismic response of reinforced concrete structures is of importance to LLNL's Nuclear Fuel Cycle and Reactor Program, the Global Nuclear Energy Partnership (GNEP), and the National Ignition Facility (NIF). In general, validating this capability allows LLNL to attract new projects in the area of seismic analysis. This project also promotes collaboration with UCSD.

FY2006 Accomplishments and Results

A version of the finite element model was first created for linear, static analysis in NIKE3D. From this analysis, natural frequencies and mode shapes of the structure were determined. The first mode of the structure is torsional, and the second mode is a first-order cantilever mode. The natural frequencies for the torsional and cantilever modes are 2.17 Hz and 2.65 Hz, respectively (see Fig. 2).

A more refined version of the model with enough discretization to capture the characteristics of the rebar was created for running dynamic analyses in ParaDyn. An instability was discovered in the homogenized rebar/concrete material model that prevented completion of the analysis of the four, successively stronger consecutive earthquakes. The instability arises out of a singularity in the formulation of the underlying concrete model, but the analysis up to the point where the instability occurs is uncontaminated.

The nonlinear analysis was completed for the entire first earthquake, which is the smallest ground motion, prior to the occurrence of the instability. The simulated roof displacement for this earthquake underestimates the measured roof displacement from the experiment by about a factor of 2; and the simulated displacement oscillates at a much higher frequency, indicating the model is too stiff (see Fig. 3). By comparing a test case of a wall modeled with homogenized rebar to a wall with explicitly modeled rebar, we verified that the homogenized rebar is not the cause of the high stiffness.

It is believed that the properties used in the model specify concrete that is too strong, that there may be mass that is not accounted for in the model, and that damping may be overestimated in the model. Perhaps most importantly, the concrete in the actual structure was probably already damaged to a significant degree from settling and low-amplitude white noise tests performed before the first earthquake motion was applied. This factor is not captured in the current model.

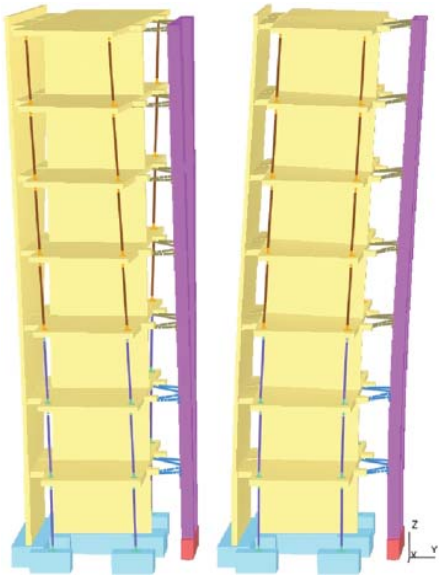

Figure 2. Left: torsional mode at 2.17 Hz; right: cantilever mode at 2.65 Hz.

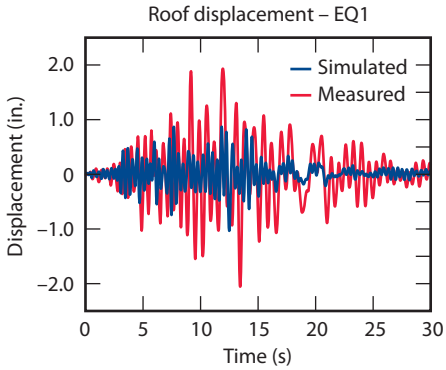

Figure 3. Comparison of simulated roof displacement to measured roof displacement.

FY2007 Proposed Work

We will work to better understand the singularity in the concrete model and determine how to deal with it. We will meet with UCSD faculty to identify discrepancies between the computational model and the test structure. We will then compare the simulated response from the updated model to the experimental results.

Structure and Properties of Nanoporous Materials

Anthony Van Buuren
(925) 423-5639
vanbuuren1@llnl.gov

Our goal is to quantify the microstructure of highly porous materials, and to determine how processing of the porous material relates to the structure, and ultimately to the mechanical behavior. We quantify structural changes with a combination of small-angle x-ray scattering (SAXS) and high-resolution x-ray tomography. We use finite element modeling, using the structures determined above, to study the effects of mechanical loading on the cell structures, and to map out relationships among processing, density, and strength. Synthesis and processing variables affect kinetics of nucleation, particle growth and the organization of the aerogel networks.

Project Goals

Our goals are to perform the following:

1) high-spatial-resolution SAXS and synchrotron radiation computed tomography (SRCT) measurements of the pore structure in metal-oxide aerogels and metal foams to quantify density, pore size, pore distribution, and the aspect ratios of the cell backbone as a function of preparation conditions;
2) extremely high-resolution diffraction imaging to determine the structure of the lattice of select, low-density metal-oxide foam to provide a basis for interpreting the SAXS data;
3) finite element modeling, using the structures determined in the first goal, to study the effects of mechanical loading on the cell structures, and to map out relationships among processing conditions, density, and strength; and
4) determination of the extent of any anisotropy in lattice architecture and improve spatial resolution to examine and characterize graded-density structure.

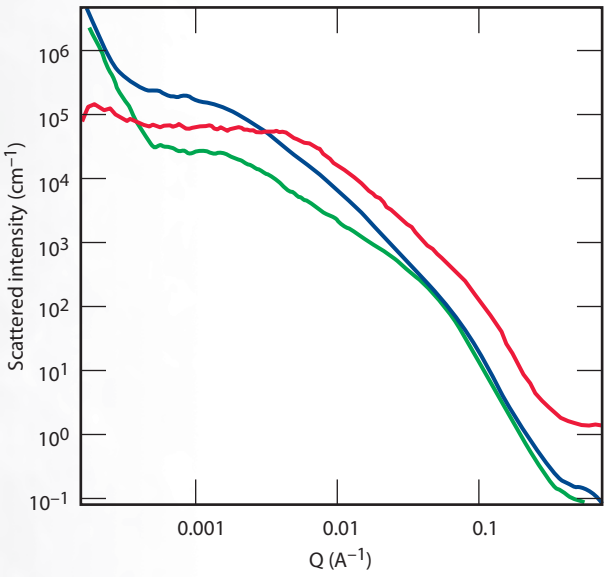

Figure 1. Plot of scattering intensity as a function of the wave vector over three orders of magnitude in Q: USAXS from 250 mg/cm^3 (red line), 100 mg/cm^3 (blue line), and 40 mg/cm^3 (green line) Ta_2O_5 aerogel.

Relevance to LLNL Mission

This program develops critical experimental technologies for many LLNL applications. A key deliverable will be the ability to predict the mechanical properties of nanoporous materials and characterize gradient-density foam microstructures for future laser targets.

FY2006 Accomplishments and Results

The ultra-small-angle x-ray scattering (USAXS) data shows that there are significant changes to the cell structure of metal-oxide foams as a function of preparation conditions and density. In Fig. 1 we show the scattering intensity as a function of wave vector, Q, for three different densities of Ta_2O_5 aerogel. We find that the smallest particles that define the strut width in the aerogel do not increase with density and are 3 to 4 nm for all densities. However, the correlation length decreases suggesting that strut length also decreases with increased density. In the USAXS, we see evidence for large (> 500 nm) voids in the aerogels with the lowest density.

We have also done *in-situ* measurements of structural changes in the Ta_2O_5 aerogel as a function of thermal cycling down to 100 K. At 100 K we find a decrease in correlation length consistent with a shrinkage in the network structure. Evidence for wetting was also observed.

In the Ta_2O_5 we did not observe a large fraction of unconnected dangling mass fragments, which is inconsistent with the percolation model. However, we did establish that, for the 100-mg/cm^3 Ta_2O_5 foam (Fig. 2), approximately 85 % of the mass was confined to the nodes, consistent with the formation of fractal clusters. The exponents of the modulus vs fraction power laws are 3.74. Correcting the scaling laws for the reduced apparent mass lowered the theoretical estimate to 1.7, consistent with bending. Our results provide the first experimental support for a diffusion limited cluster aggregation model for aerogel growth.

Related Reference

Kucheyev, S. O., M. Toth, T. F. Baumann, A. V. Hamza, J. Ilavsky, W. R. Knowles, B. L. Thiel, V. Tileli, A. van Buuren, Y. M. Wang, and T. M. Willey, "Structure of Low-Density Nanoporous Dielectrics Revealed By Low-Vacuum Electron Microscopy and Small-Angle X-Ray Scattering," accepted to *Langmuir* 2006.

FY2007 Proposed Work

In FY2007 we plan to make USAXS measurements to understand the effect of synthesis conditions on the change in structure; in particular, how synthesis conditions may affect the amount of mass at the nodal points in the aerogel.

In situ USAXS measurements will be conducted on aerogels at temperatures where nitrogen gas will condense in the aerogel matrix. How the aerogel wets in a cryogenic fluid is unknown, but it is required knowledge if these foams are to be used in laser targets.

The small angle results will provide the correlation length and beam thickness as a function of density and processing parameters. From these measurements, stochastic lattices will be generated for finite element simulations. Simulations will then provide the elastic constants of the material. In addition to providing the elastic constants of the foam, finite element simulation will be used to study thermo-elastic deformation.

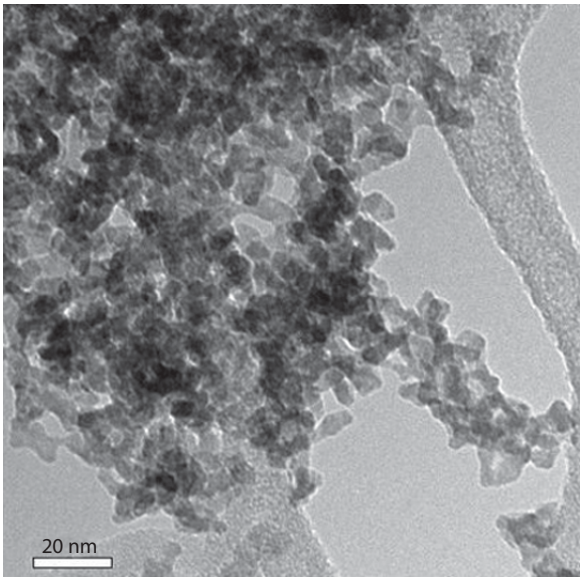

Figure 2. TEM image of a 100-mg/cm^3 Ta_2O_5 aerogel.

Enhanced Composite Modeling Tools

Andrew T. Anderson
(925) 423-9634
anderson1@llnl.gov

Composite materials are used in many advanced weapons systems and structures at LLNL. We have previously enhanced our ability to simulate structural response and progressive failure of composite systems in ALE3D by porting an existing composite constitutive model from DYNA3D (Model 22, the Fiber Composite with Damage Model) into ALE3D. This year, a more advanced model (DYNA3D Model 62, the Uni-Directional Elasto-Plastic Composite Model) has been implemented. The Uni-Directional Elasto-Plastic Composite Model has already been successfully used to analyze the response of a fiber wound composite pressure vessel. Verification and validation of the model's implementation in ALE3D has also been accomplished.

Project Goals

A variety of composite models have been described in the literature and implemented in other codes. Our initial goal was to select the models to be evaluated. In the next phase, the predictions of these models were compared with experimental data, either in their native code or in our initial implementation. Finally, we implemented an experimentally validated fiber composite material model into ALE3D.

Relevance to LLNL Mission

The improved fiber composite material models can be used in simulations (to failure) in the many LLNL programs, such as those for composite munitions, armor penetration, pressure vessels, and rocket motors. This effort also supports LLNL work-for-others programs. This project has been beneficial in supporting the composite modeling efforts within the DoD Joint Munition Program and the Focused Lethality Munition Program. This study supports LLNL's engineering core competency in high-rate mechanical deformation simulations of large complex structures by providing an enhanced capability to model composite structures with ALE3D.

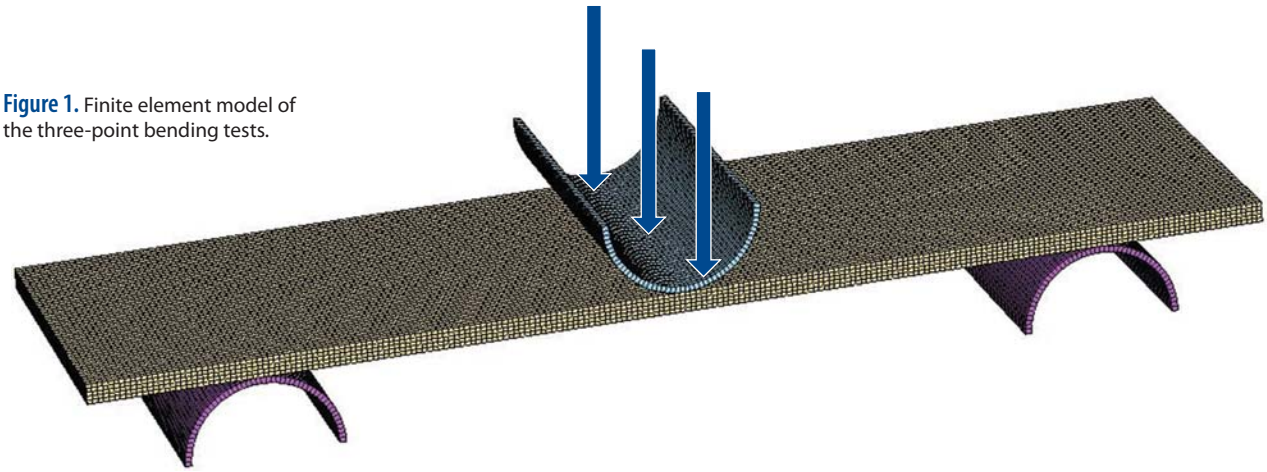

Figure 1. Finite element model of the three-point bending tests.

FY2006 Accomplishments and Results

After we completed a literature survey of available fiber composite models, we implemented two solid-element models into ALE3D that are already available in DYNA3D. The Fiber Composite with Damage Model, which requires a laminate material description for each element, and the Uni-Directional Elasto-Plastic Composite Model, which uses a ply-level description of the fiber composite, were determined to replicate all or most of the necessary material responses.

The validation process was initiated with DYNA3D using experimental data. The two solid-element composite models were used to predict the response of three-point bending in composite beams. The elastic response of the models was found to be acceptable, but the damage parameters needed additional refinement.

The Fiber Composite with Damage Model was implemented into ALE3D. An important part of this task was creating an algorithm to initialize and update material directions at the element level. The model was validated against the same three-point bending experiments that were modeled with the DYNA3D simulations, and the results were found to closely match the DYNA3D predictions.

Our results are illustrated in Figs. 1 to 4.

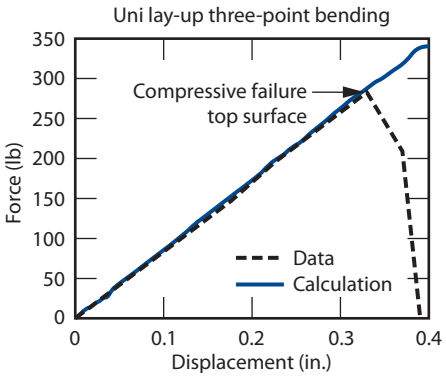

Figure 2. Verification of the laminate model using three-point bending data for uni-directional lay-up.

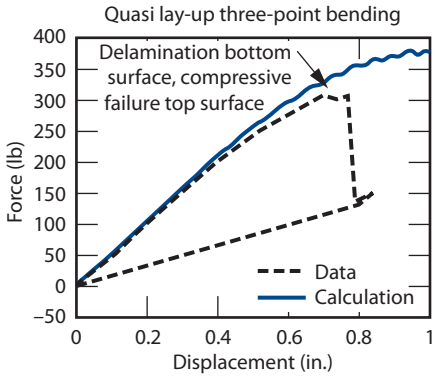

Figure 3. Verification of the laminate model using three-point bending data for quasi-isotropic lay-up.

FY2007 Proposed Work

The DYNA3D Uni-Directional Elasto-Plastic Composite Model will be ported to ALE3D. The failure algorithm from DYNA3D's Fiber Composite with Damage model will be added to the ported material model. The progressive failure algorithm could be altered during the validation phase. A list of the projected milestones follows:

1. implement existing DYNA3D solid-element composite mode into ALE3D;
2. streamline ability to output orthotropic data information with prescribed local volume elements (this data will enable the construct of a global/local composite modeling strategy that will facilitate higher fidelity);
3. incorporate a failure algorithm that includes matrix delamination, fiber tensile and fiber compressive failure;
4. use the model to predict dynamic impact and three-point bending responses;
5. perform relevant tests based on expected responses; and
6. compare tests to simulations and make modifications to models as necessary.

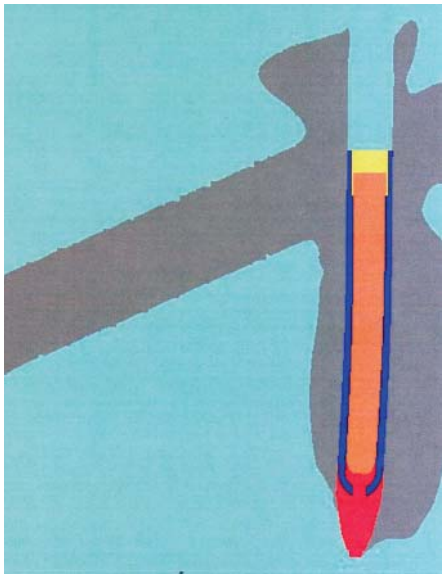

Figure 4. Modeling of composite-cased penetrator.

Modeling Forming Processes

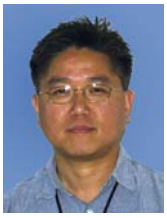

Moon Rhee
(925) 424-4990
rhee1@llnl.gov

The ability to model and optimize material manufacturing processes and predict resulting material properties is important where product performance, costs and/or waste reduction are concerns. DOE programs such as Reliable Replacement Warhead (RRW), Transformational Materials Initiative (TMI), and Responsive Infrastructure (RI) will rely on rapid prototyping of complex components. The goal of process modeling is to provide a simulation-based, rapid-design capability for efficient production of high quality parts with better control over the desired properties. Application of process tools will reduce trial and production costs and shorten the time from product conception to production. Detailed understanding of material response and product performance predictions can be achieved by combining robust finite element simulation tools from DOE's ASC program with advanced models of material properties.

Project Goals

The goal of this project is to demonstrate advanced material modeling capability for forming process simulation and to work with production laboratories toward validating the models. The capability will be valuable in the design and optimization of forming processes to achieve desired microstructures, properties, and performance characteristics.

Relevance to LLNL Mission

This effort will contribute to LLNL's role and core competency in numerical modeling and material response. The capability demonstrated in this project is supportive of other forming processes where geometric fidelity and control of material properties are critical.

FY2006 Accomplishments and Results

A material model for static recrystallization has been implemented into ALE3D for use in forming process

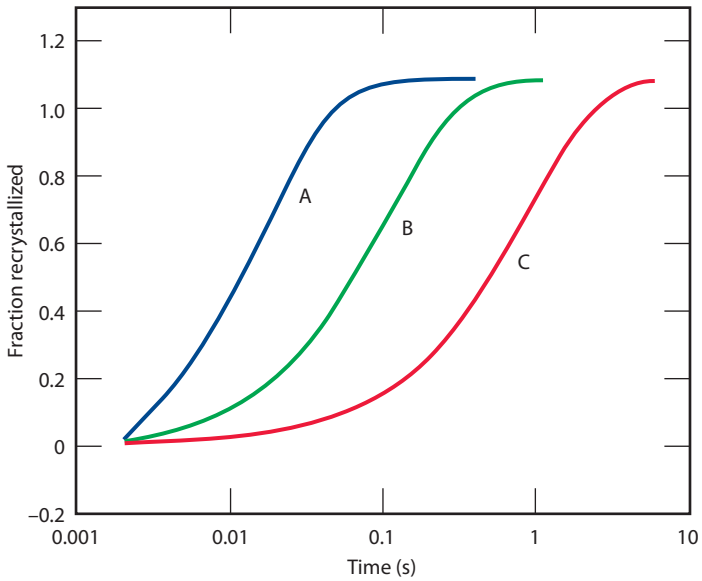

Figure 1. Recrystallized fraction plotted against time for aluminum. For A: $\dot{\varepsilon} = 10^{-7}\ s^{-1}$, $\varepsilon = 0.3$; for B: $\dot{\varepsilon} = 0.1\ s^{-1}$, $\varepsilon = 0.3$; and for C: $\dot{\varepsilon} = 10^{-7}\ s^{-1}$, $\varepsilon = 0.3$.

simulations. The model is based on microstructure parameters such as grain size; prior deformation that creates a forest dislocation structure; and the Zener-Hollomon parameter, which is a function of temperature and strain rate. The model accounts for the material strength reduction resulting from dissolution of the forest dislocation structure as the grains recrystallize. Figure 1 shows a typical range of fraction recrystallized as a function of time following deformation under various strain and strain rate conditions.

A rolling simulation of an aluminum slab was performed for validation, and a contour plot of recrystallized fraction at the end of the first pass is given in Fig. 2. The figure shows that the most recrystallized portion of the rolled slab is the offset from the top and bottom surfaces since the strain is higher at these locations. The variation in strength levels across the slab thickness results from a combination of increased strength due to strain hardening and strength reduction from recrystallization.

Also, demonstrations of shock processing simulations of porous materials were performed. A constrained-random void configuration model was constructed as shown in Fig. 3, where, under shock conditions, these voids collapse. The collapsing voids can significantly alter local stress fields, and at the same time the temperature can increase dramatically. The shock-processed material is subsequently deformed, so the effect of this prior processing on the material performance is of great importance. A series of simulations using different shock conditions, ranging from 10 GPa to 40 GPa, were carried out to demonstrate capability for constructing equation-of-state models for a porous material (Fig. 4). The figure reveals that different values of bulk modulus were observed, depending on the level of initial pressure conditions.

Related Reference

Bontcheva, N., and G. Petzov, "Microstructure Evolution During Metal Forming Process," *Computational Materials Science*, **28**, pp. 563-573, 2003.

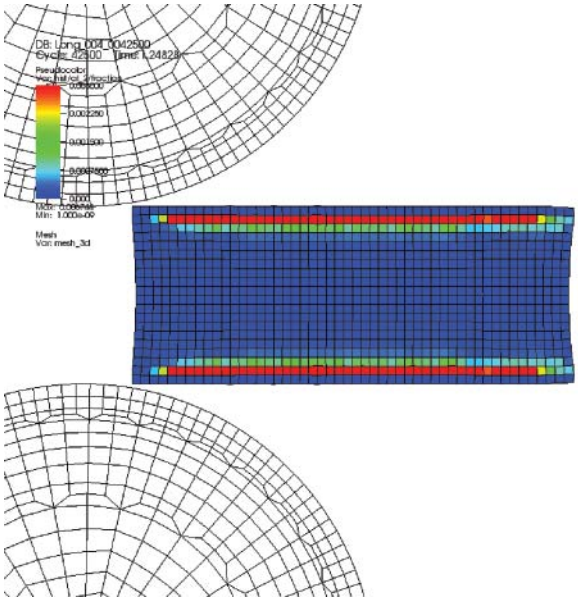

Figure 2. Hot rolling simulation of aluminum at 700 K. Red colors at the second element from the top and bottom surfaces indicate highest portion of recrystallization.

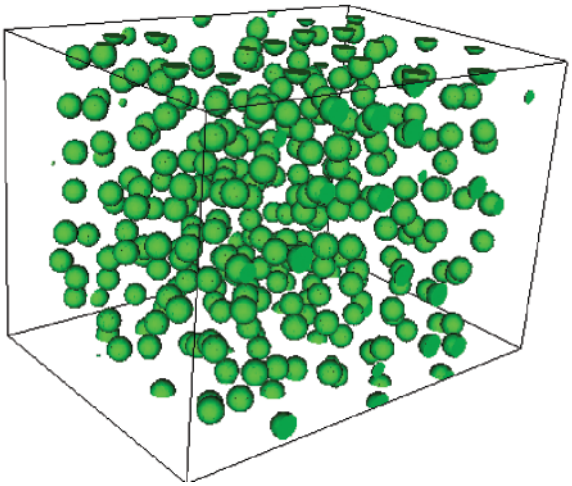

Figure 3. Constrained-random void distribution, 10 % void fraction.

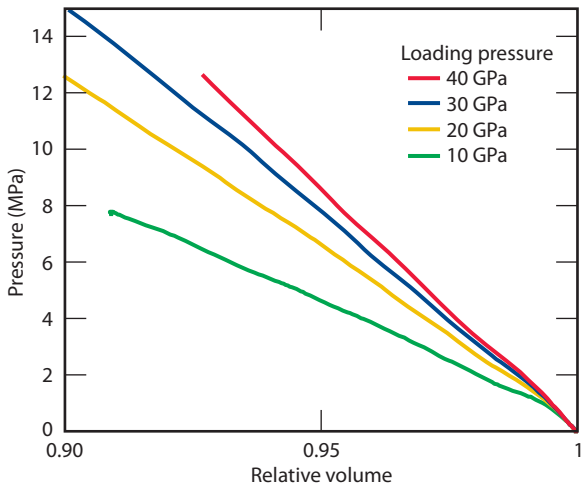

Figure 4. Elasticity pressure vs. relative volume for void configuration given in Fig. 3.

Multiscale Characterization of bcc Crystals Deformed to Large Extents of Strain

Jeffrey N. Florando
(925) 422-0698
florando1@llnl.gov

Experimental data are crucial in the process of constructing and validating the multiscale crystal plasticity models used in computer code simulations of materials deformed under extreme conditions, such as high strain rate, high pressure, and large extents of strain. The "6 Degrees of Freedom" (6DOF) experiment was designed specifically for this task and has provided data on the behavior of bcc crystals that may revolutionize the field.

Until now, the experimental data and simulation efforts have focused on relatively small extents of plastic deformation (0.5%). Both experiments and modeling must now be extended to large strain deformations on the order of tens of percent. At these larger extents of strain, the use of multiscale characterization tools can be improved to better understand the fundamental behavior.

Project Goals

The goal of this project is to develop large strain experiments that will provide the essential data to enhance the multiscale modeling capability through the validation of dislocation dynamics simulations and the development of continuum strength models. This work will increase LLNL's ability to develop predictive strength models for use in computer code simulations.

Relevance to LLNL Mission

Understanding and simulating the plastic, or non-reversible, deformation of body-centered cubic (bcc) metals, is a major component of LLNL's stockpile stewardship mission, and is applicable to future NIF experiments.

FY2006 Accomplishments and Results

Slip System Analysis. Previous years' accomplishments included incorporating a full-field 3-D image correlation strain measurement system into the 6DOF experiment. Sequential photos are compared to determine the local movement of spots. Unlike traditional testing techniques, the 6DOF experiment allows essentially unconstrained deformation of the crystal. This unique set-up, shown in Fig. 1, allows for an unprecedented examination of the deformation of single crystals, including the complete displacement gradient matrix. Using this technique, we have performed an analysis that calculates the activity of individual slip systems in a single crystal from the image correlation data. The results for zinc single crystals are that for a pristine sample only the primary system is active, as expected. However, for a cold-worked and annealed sample, the analysis shows the unexpected result that there is appreciable activity on the primary as well as other slip systems.

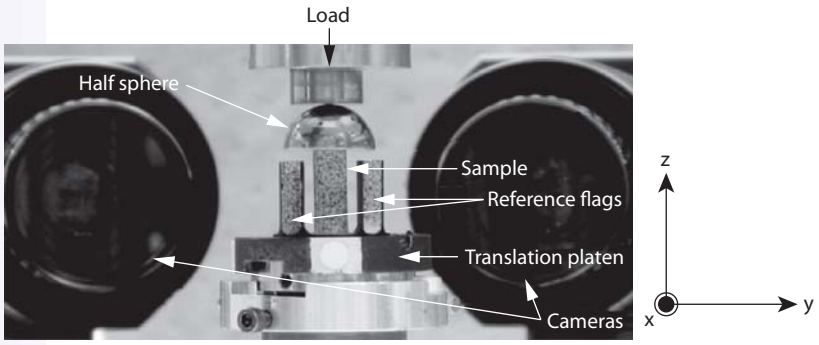

Figure 1. 6DOF set-up with the image correlations cameras.

Copper single crystals experiments. Experiments have been performed on copper single crystals that have also shown surprising results. The image correlation strain map (Fig. 2) shows slip along the primary (expected) and orthogonal to the primary slip system (unexpected). Using the image correlation data, analyses have been conducted that show that the slip is orthogonal and in some cases nearly equal in magnitude to the primary system. Additional experiments addressing the effect of fabrication and boundary conditions on the deformation behavior also show appreciable deformation orthogonal to the primary system. This behavior cannot be explained using traditional theories. In addition, orthogonal slip has been observed in hcp and bcc crystals, and therefore may be a general mechanism that can be applied to a large number of materials.

Characterization of the deformed material. Characterization of the deformed material, which is more definitive at larger strains, is essential to understanding the underlying deformation mechanisms in single crystal metals. One method of characterizing the deformed material is using the x-ray microdiffraction beamline at the Advanced Light Source (ALS) at LBL. The high-energy synchrotron light source allows subsurface dislocation structure to be analyzed. This technique can detect features over a larger area than is possible with Transmission Electron Microscopy (TEM). Copper single crystals, which show the orthogonal slip, have been characterized at ALS using x-ray microdiffraction. Figure 3, which is a map of the local rotations in the sample, shows band structures in the material that are 90º from each other. This result suggests that the local lattice rotations are related to the overall orthogonal structure seen in the image correlation strain maps.

Related References

1. Lassila, D. H., M. M. LeBlanc, and G. J. Kay, "Uniaxial Stress Deformation Experiments for Validation of 3-D Dislocation Dynamics Simulations," *J. Eng. Mat. Tech.*, **124**, p. 290, 2002.
2. LeBlanc, M. M., J. N. Florando, D. H. Lassila, T. Schmidt, and J. Tyson, II, "Image Correlation Applied to Single Crystal Plasticity Experiments and Comparison to Strain Gage Data," *Experimental Techniques*, **30**, 4, p. 33, 2006.

FY2007 Proposed Work

Further experiments and characterizations are needed to solidify the observation of orthogonal slip. Also, new theories and models, such as a dislocation dynamics simulation that takes into account local lattice rotations, need to be developed to account for this behavior.

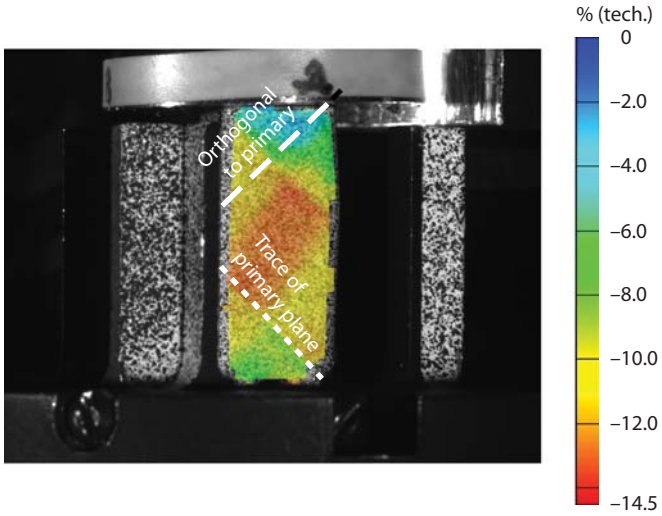

Figure 2. Axial strain map of copper single crystal overlaid onto the sample, showing deformation on the primary slip system and orthogonal to the primary system.

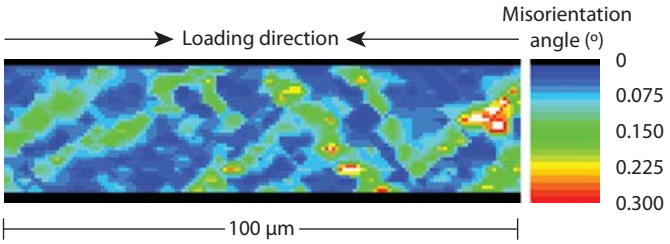

Figure 3. ALS results showing bands that are 90º from each other.

Temperature Capability for *In-Situ* TEM Nanostage

Mary LeBlanc
(925) 422-8954
leblanc2@llnl.gov

Nanomaterials are roughly defined as solids with characteristic dimensions that are 200 nm or less. The physical properties of nanomaterials are frequently very different from typical bulk properties. For example, some newly invented composite materials that incorporate nanomaterials in their structure have very high yield strength and excellent fracture toughness. In essence, it is the very small dimensions and concurrent high surface-area-to-volume ratio of the nanomaterials that give rise to these properties. It is important to be able to characterize the mechanical behavior of these materials under different temperature regimes, especially as nanomaterials and structures are used in various programmatic applications including laser targets, materials for weapons, and sensing elements.

Perhaps the most compelling application for the Transmission Electron Microscope (TEM) nanostage is to directly measure dislocation velocities, which are important material characteristics used in multiscale modeling. The nanostage also permits the direct observation of dislocation reactions and the resulting dislocation substructures, which can be used to validate dislocation dynamics simulations.

Project Goals

The goal of this project is to establish a new capability to experimentally measure the mechanical response of nanomaterials and structures in the TEM, over a range of temperature from 100 to 500 K. To accomplish this goal, a loading stage must be built that is compatible with the TEM, and a loading cartridge, which holds the nano-sized sample, must be fabricated to fit into the tip of the stage and transfer a continuously measured load onto the sample (see Fig. 1). The scope of the project is to establish and test the new capability, and provide documentation on the utility for future studies.

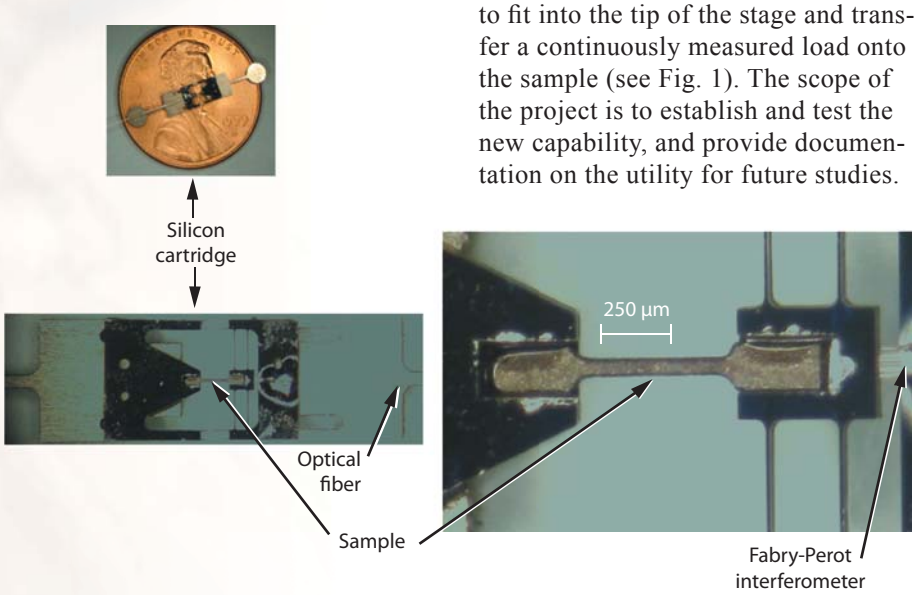

Figure 1. Photographs of the loading cartridge. Counterclockwise: the cartridge in relation to a penny; the complete cartridge; blow-up near the sample region. The sample has not yet been thinned to transparency.

Relevance to LLNL Mission

This project will add to the increasing number of capabilities LLNL will need to characterize and use nanomaterials and structures. Nanomaterials have the potential to play a key role in the development of sensors for programmatic applications.

The first use of this capability will be to quantify the dislocation velocity as a function of applied stress in single crystals. These dislocation mobility values have never been accurately measured, and are essential input for LLNL's multiscale modeling program.

FY2006 Accomplishments and Results

Sample Fabrication. Damage to the test sample during handling of the cartridge was an unexpected and significant obstacle during FY2006. In response, fixturing to hold the loading cartridge during Focused Ion Beam thinning of the sample was fabricated. The titanium frame for the cartridge was stiffened to reduce in-plane and out-of-plane bending, and an aluminum reinforcing plate was bonded to the cartridge to prevent damage during installation into the straining stage. Successful thinning of the test sample to electron transparency has since been demonstrated by our collaborator at LBL (Fig. 2).

Loading stage. The *in-situ* TEM straining stage has been fabricated, assembled, and tested (Fig. 3). It is sized to fit in LLNL's Philips 300 TEM. The tip of the stage is cooled by a cold finger that resides inside the microscope and is attached after the stage is inserted. Temperature measurements made in a vacuum chamber to simulate the microscope environment (Fig. 4) show that the loading cartridge temperature matches that of the tip.

Data acquisition. A PC-based data acquisition system has been assembled, and software written to capture the TEM image (either from the microscope camera or an external camera), and up to eight channels of other data, including load and temperature.

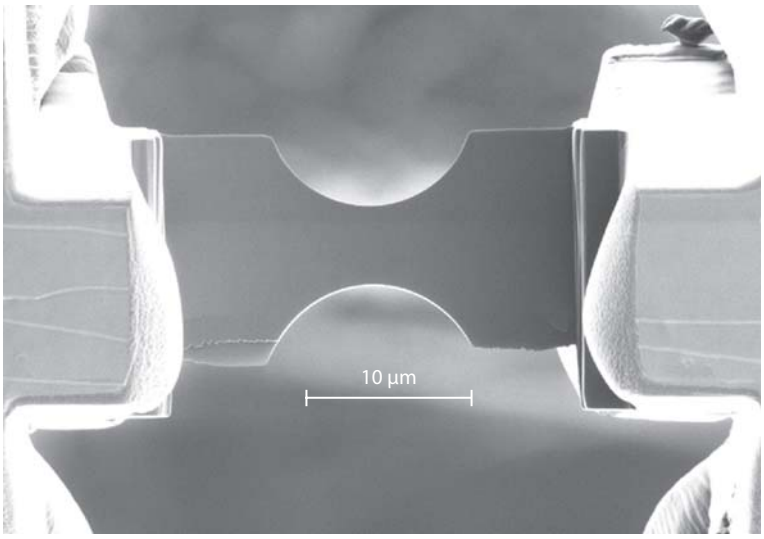

Figure 2. SEM photograph of the sample thinned to electron transparency. The cross-section is diamond shaped with the minimum thickness (1.6 µm) near the sample center.

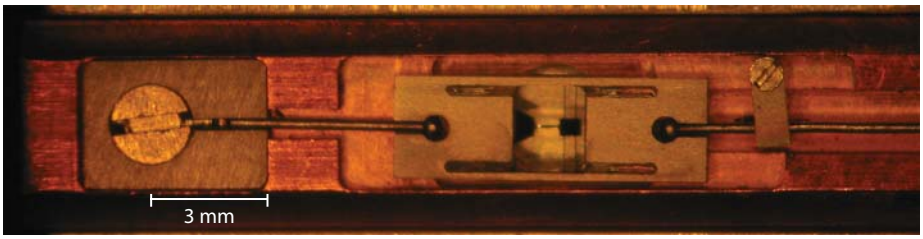

Figure 3. Close-up of the stage tip with a loading cartridge installed. The cartridge is in unloaded condition (loading wires slack) with the silicon side down.

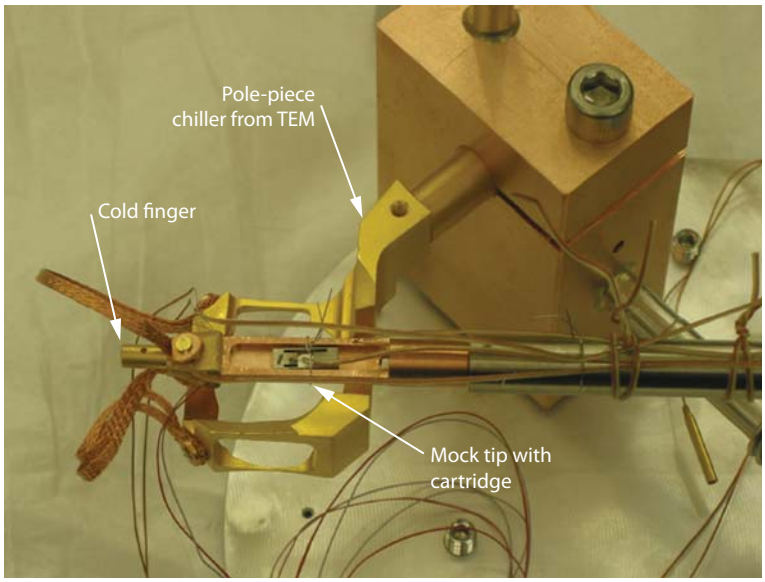

Figure 4. Photograph of the temperature conduction experiment. A mock tip was cooled using conduction from the LN-cooled pole-piece chiller through copper braid to the cold finger that attaches to the stage tip. The cartridge and tip were within 1 °C; the cold finger was 5° cooler.

EMP Simulation and Measurement Data Analysis in Support of Laser Experiments

Charles G. Brown, Jr.
(925) 423-4435
brown207@llnl.gov

Electromagnetic pulse (EMP) is generated at short-pulse laser facilities such as LLNL's Titan and Vulcan in England during target experiments. NIF also may produce EMP on target experiments. This project focused on learning how to perform simulations of electromagnetic (EM) fields due to electrons from laser/target interactions.

Project Goals

The overarching goal of this project is to simulate EMP due to electrons from laser/target interactions in the Titan short-pulse laser and to compare measurement results with the simulations. To accomplish the simulation task, we use EMSolve, an LLNL code that has been augmented with electron beam sources. Unlike most available codes, EMSolve's architecture allows seamless integration of user-created sources and boundary conditions.

Relevance to LLNL Mission

An understanding of the EMP in Titan, through simulation and analysis in this project, could be extrapolated to NIF to better mitigate EMP effects in NIF and other laser systems.

FY2006 Accomplishments and Results

During FY2006, we gained experience in performing simulations using the EMSolve processing chain, which consists of Cubit, EMSolve, and VisIt. Cubit is a meshing tool from Sandia National Laboratories that is used to construct models for EMSolve. VisIt is an LLNL code for visualizing simulation data.

One of the most difficult tasks we faced was creating CAD models appropriate for EM simulation from the original mechanical CAD files. The original Titan CAD model was far too detailed for direct transfer to EM simulation. In a

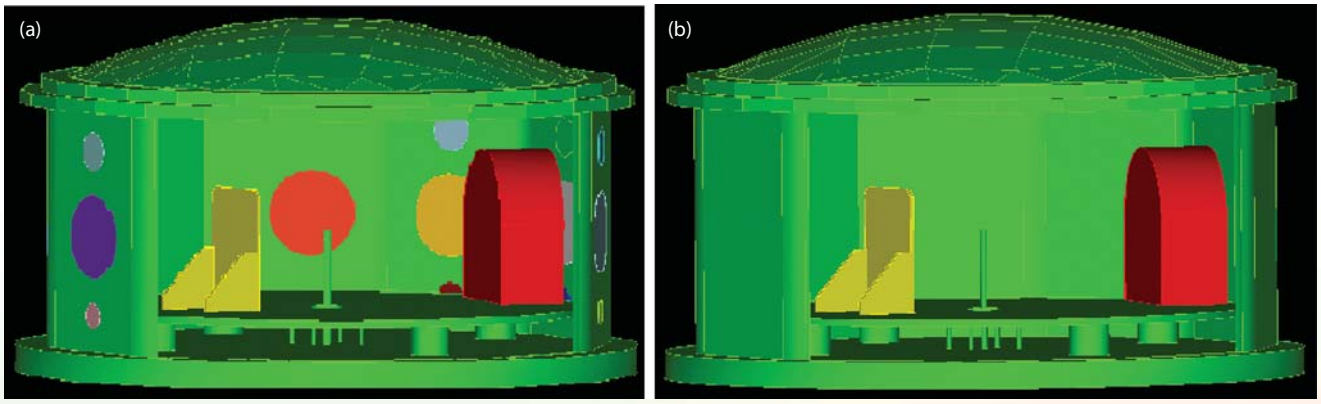

Figure 1. Simplified Titan model (a) with portholes, and (b) without portholes.

related effort, an experienced mechanical drafter removed features less than 1 in., such as bolt holes. We then further simplified the models using Cubit and Microwave Studio, a commercial EM solver. We started simply and added complexity. For example, we added simple versions of portholes (Fig. 1).

Further, we used a simple cylindrical geometry to learn how to use the EMSolve processing chain and to test the electron beam sources. We hope to write a simple EMSolve tutorial based on these examples. Figure 2 depicts the conical current source's current density and the resulting magnetic fields for one snapshot in time. The electric fields (not shown) have errors due to some aspects of the source that we are currently working to resolve.

Related Reference

Mead, M. J., *et al*., "Electromagnetic Pulse Generation within a Petawatt Laser Target Chamber," *Review of Scientific Instruments*, **75**, 10, pp. 4225-4227, October 2004.

FY2007 Proposed Work

Our FY2007 work will include improving our CAD models to perform more realistic simulations; continuing to learn to use EMSolve and working to improve its electron beam sources; assisting laser experiment teams in the measurement process to better understand the measurement systems; and working with signal processing experts to calibrate and analyze the data.

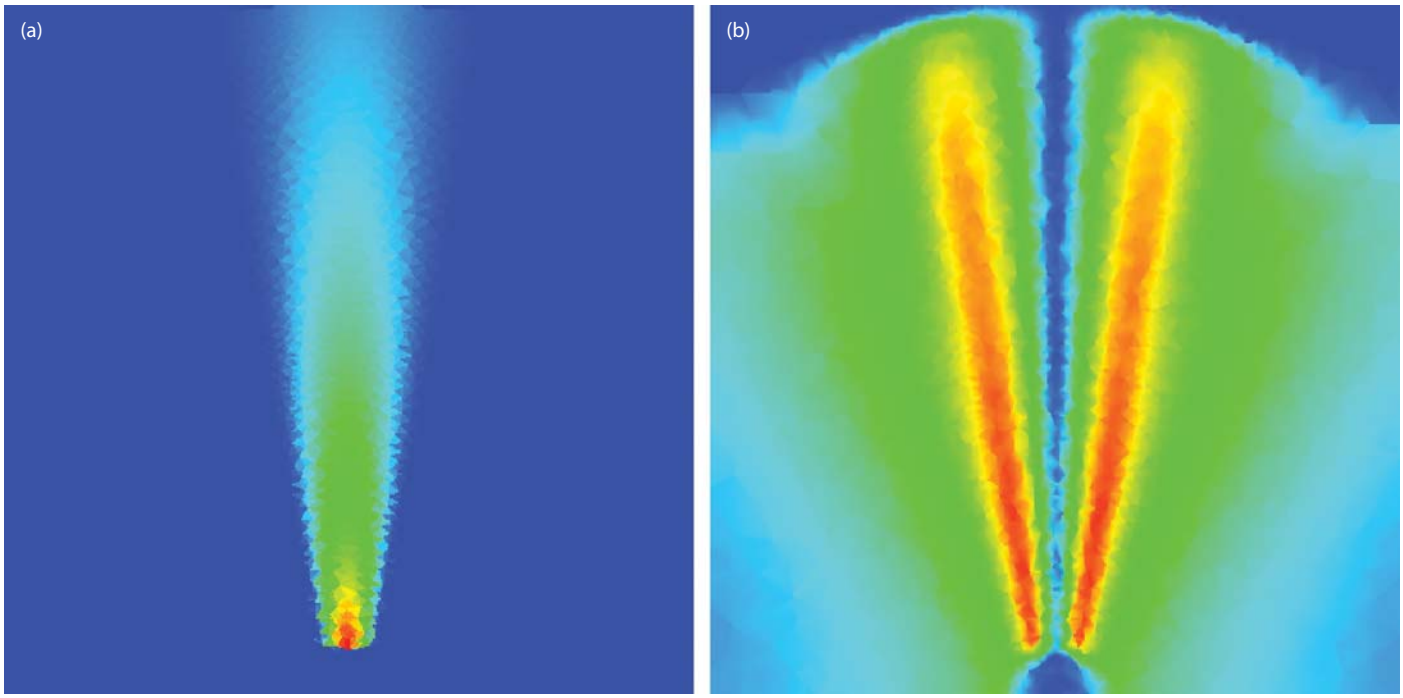

Figure 2. (a) Magnitude of current density of conical electron beam source. (b) Magnitude of resulting magnetic field.

Measurement Technologies

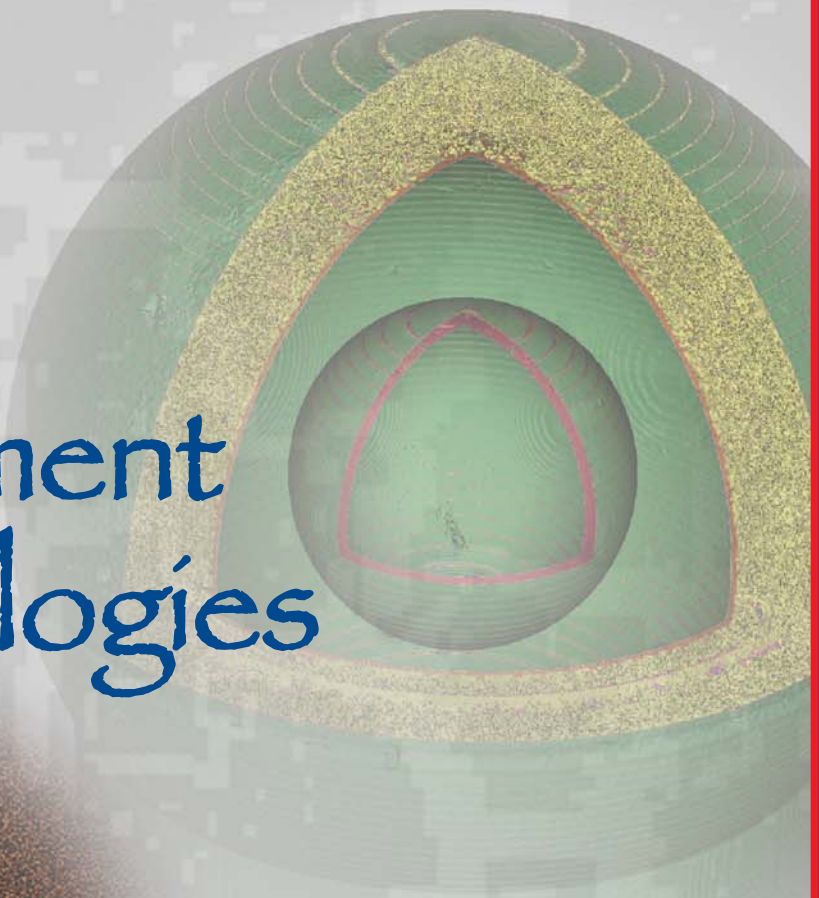

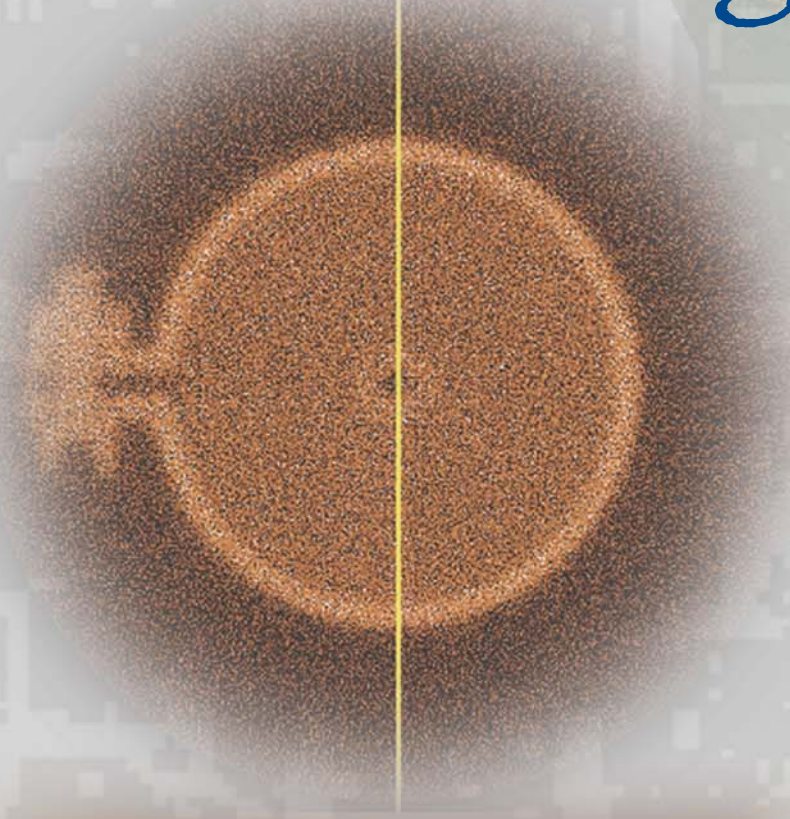

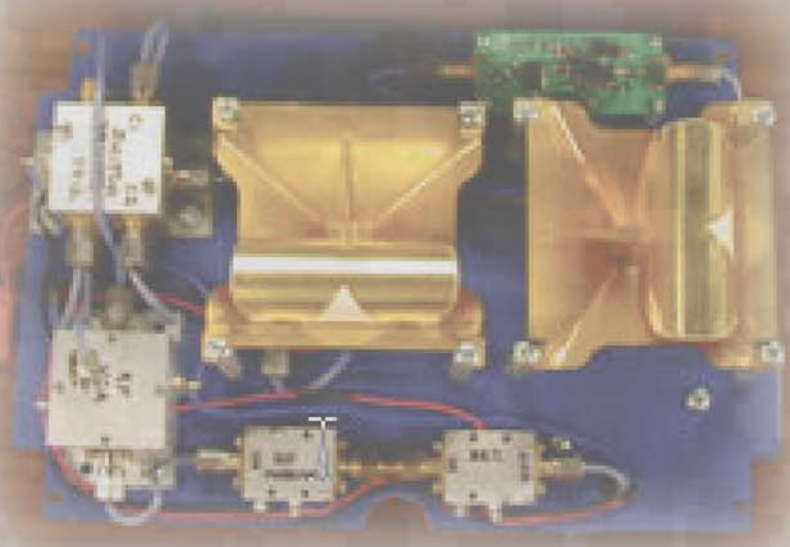

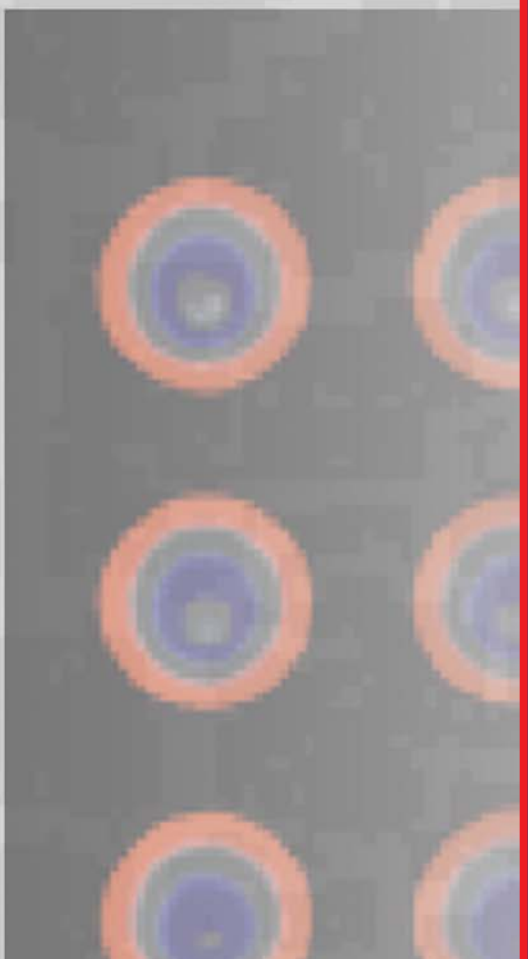

FY 06 Engineering Research and Technology Report

Standoff Explosives Detection Using THz Spectral Imaging

Robert J. Deri
(925) 424-5343
deri1@llnl.gov

Standoff detection of high-explosive (HE) material RDX (1,3,5-trinitro-1,3,5-triazacyclohexane) is a difficult technical problem due to its low vapor pressure (10 ppt). On the other hand, RDX is the one of the most widely available active ingredients in plastic explosives such as C-4 and Semtex-H, and is commonly used for improvised explosive devices (IEDs).

RDX-based HE exhibit a distinctive sub-THz signature near 800 GHz (Fig. 1) that distinguishes them from common background materials. Since THz radiation can penetrate common fabric concealants, and provides reasonable resolution for imaging applications, spectral imaging near 800 GHz may provide a solution to the RDX detection problem. This project aims to evaluate the suitability of near-THz multispectral imaging for reliable RDX screening of people at a safe ~30- to 50-m standoff distance.

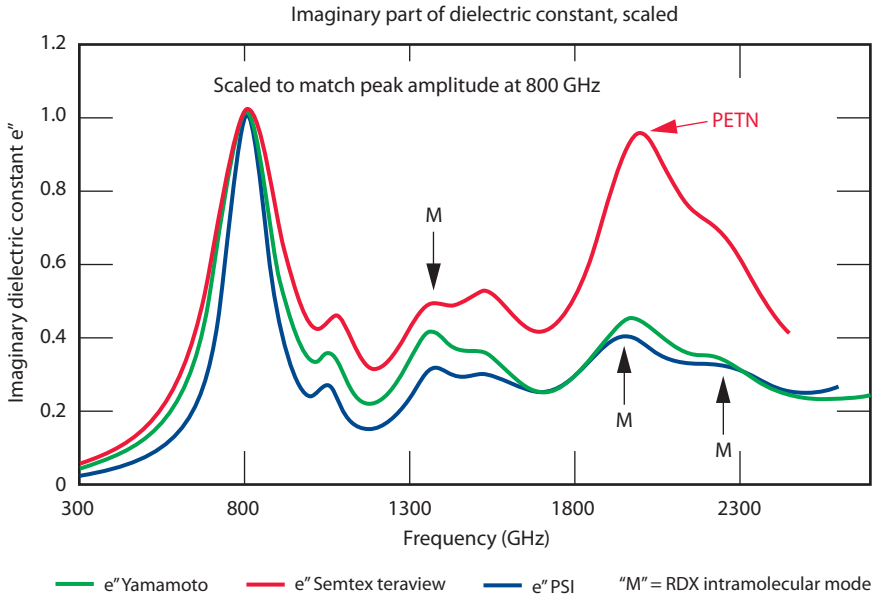

Figure 1. Spectra of several RDX-based high explosives (Green: C-4, Blue: RDX; Red: Semtex-H). RDX exhibits a peak at 800 GHz, which is common to all formulations. Additional resonances at higher frequencies are associated with the compound PETN.

Project Goals

The two major project goals are:

1. to assess the utility of THz spectral imaging for the detection of RDX-based explosives, by developing a systems concept, supporting multispectral detection algorithms, and simulating system behavior in the presence of atmospheric absorption, obscurant losses, and noise; and
2. to experimentally validate the overall system concept.

Our final goal is to demonstrate detection of RDX-based explosives at 30 to 50 m through a concealant, using multispectral imaging.

Relevance to LLNL Mission

Explosives detection that enables the interdiction of terrorists is an important capability for LLNL's missions in both national security and homeland security.

FY2006 Accomplishments and Results

In FY2006, we developed a systems concept and supporting algorithms for THz spectral imaging. In particular, we developed an approach for deconvolving the spectral modifications induced by atmospheric propagation. We simulated the performance of this system using atmospheric absorption data from HITRAN (a standard database of atmospheric absorption properties), and material parameters obtained from our own limited set of experiments and from data reported in the literature.

Our simulation results suggest that the proposed system can achieve standoff detection of bulk HE at safe standoff distances (~30 to 50 m), even when the explosive is concealed by a few layers of fabric. The results are obtained as sets of "receiver operation characteristic" curves, which show the probability that the system detects an explosive as a function of a system threshold setting. Ideally, the probability of detection should be high for explosives, and low for innocuous materials.

Representative results are shown in Fig. 2, for discrimination of C-4 against innocuous materials such as skin and lactose. This work was presented at a by-invitation-only NATO Workshop on explosives detection.

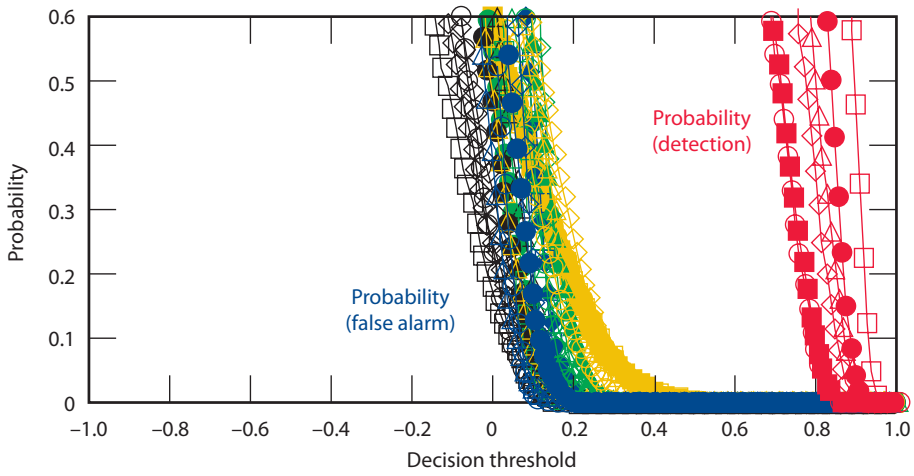

Figure 2. Receiver operating characteristic for 50-m standoff through a US Standard Atmosphere. The red curves show the probability of detection for different explosives (C-4, Semtex, RDX); the blue curves show the detection probability for innocuous materials (different scenarios and material types for skin and lactose). At threshold setting of 0.6, the curves indicate a high probability of explosives detection and low probability of false alarms for innocuous materials.

Related References

1. National Academy of Sciences, Existing and Potential Standoff Explosives Detection Techniques, National Academies Press, 2004.
2. Woolard, D. L., E. R. Brown, M. Pepper, and M. Kemp, "Terahertz Frequency Sensing and Imaging: A Time of Reckoning Future Applications?" *Proc. IEEE*, **93**, pp. 1722-1743, 2005.
3. Yamamoto, K., *et al.*, "Noninvasive Inspection of C-4 Explosive in Mails by Terahertz Time-Domain Spectroscopy," *Jap. J. Appl. Phys.*, **43**, L414, 2004.
4. Bjarnason, J. E., *et al.*, "Millimeter-Wave, Terahertz, and Mid-Infrared Transmission Through Common Clothing," *Appl. Phys. Lett.*, **85**, p. 519, 2004.

FY2007 Proposed Work

For FY2007 and FY2008 we propose to verify experimentally our recently developed algorithms for spectral detection of RDX in the presence of atmospheric losses and concealants. We will first explore near-THz (800 to 900 GHz) imaging at the necessary standoff distances. If results are favorable, we will extend the measurements to two lower frequency bands to obtain the required multispectral coverage.

Ultra-Wideband Technology Testbed

Carlos E. Romero
(925) 423-2830
romero29@llnl.gov

Ultra-wideband (UWB) systems emit extremely short electromagnetic pulses, where the pulse duration can range from tens of ps to 1 ns, corresponding to a spatial pulse width of 3 mm to 30 cm. Since the energy of the pulse is distributed across several GHz, the power spectral density is much lower in magnitude than a narrowband system. To a narrowband system, UWB signals appear below the noise floor, and are therefore very difficult to detect (Fig. 1). These characteristics, including their propagation through harsh multipath environments, enable the technology to be used in a wide range of applications from sensing to imaging to communications.

Project Goals

Our goal was to establish a uniform UWB testbed so that an accurate, repeatable, streamlined characterization of UWB RF components could be carried out in support of LLNL efforts.

Relevance to LLNL Mission

LLNL has been a pioneer in UWB technologies, ranging from Micropower Impulse Radar (MIR) to Transmit-Reference Communication (TRC) systems. Many of our programs have a need to characterize RF propagation.

FY2006 Accomplishments and Results

In FY2006, UWB systems were used for many LLNL projects and programs: to trigger active armor defense systems, measure extreme particle velocities, begin investigation into interior building visualization, track intrusions for cargo container security, and communicate in harsh urban and nautical environments.

All these activities have one thing in common, the need to characterize the RF propagation of existing and future

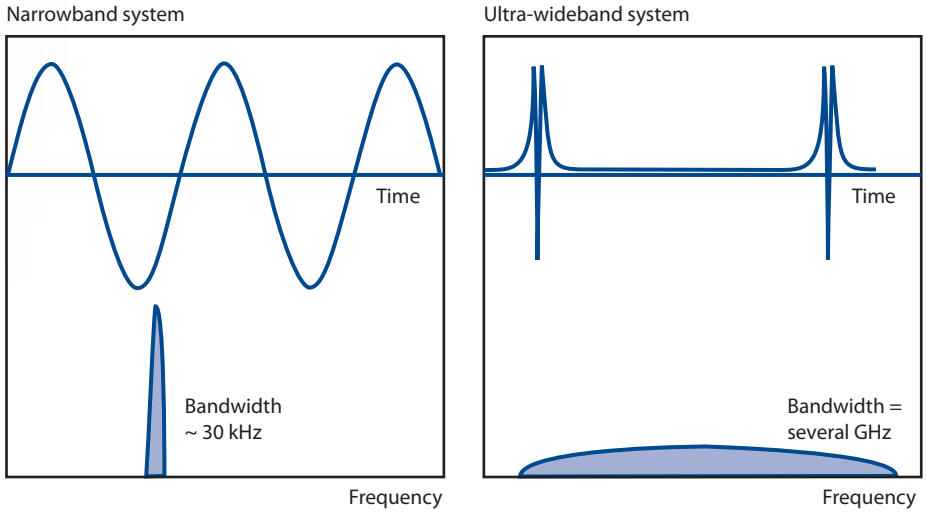

Figure 1. Narrowband vs. UWB in time and frequency domains.

systems. Of particular interest were antenna characterization (beam pattern, gain); transmitter characterization (pulse shape, bandwidth, noise floor); receiver characterization (bandwidth, noise floor); channel capacity; low probability of intercept and detection (LPI/D); resistance to jamming; performance in multipath channels; material penetration characteristics; and propagation physics.

As a result of this effort, a UWB test bed now exists at LLNL that can meet these needs.

Our UWB testbed room has been retrofitted so that radar absorbent material now lines the walls to produce a partial anechoic effect (Fig.2). A highly accurate, 3-axis gantry system permits reliable and repeatable experiments along the length and width of the room. This system is coupled with custom software to permit easy specification of trajectory paths, both by scripts and a drawing board (Fig.3). Test equipment such as oscilloscopes, spectrum analyzers, network analyzers, digitizers, and interval counters, has been consolidated into one location, along with LabView code to create a repository for data acquisition and storing. A database has been established and populated with the RF characterization of several standard UWB configured systems. A series of radar cross-section (RCS) targets have been acquired and manufactured to provide baseline performance information. Protocols are in place for ongoing and future characterization efforts.

This facility is available for use in RF characterization where a full anechoic chamber is not necessary. It is currently supporting a variety of projects.

Figure 2. UWB testbed built to produce a partial anechoic effect.

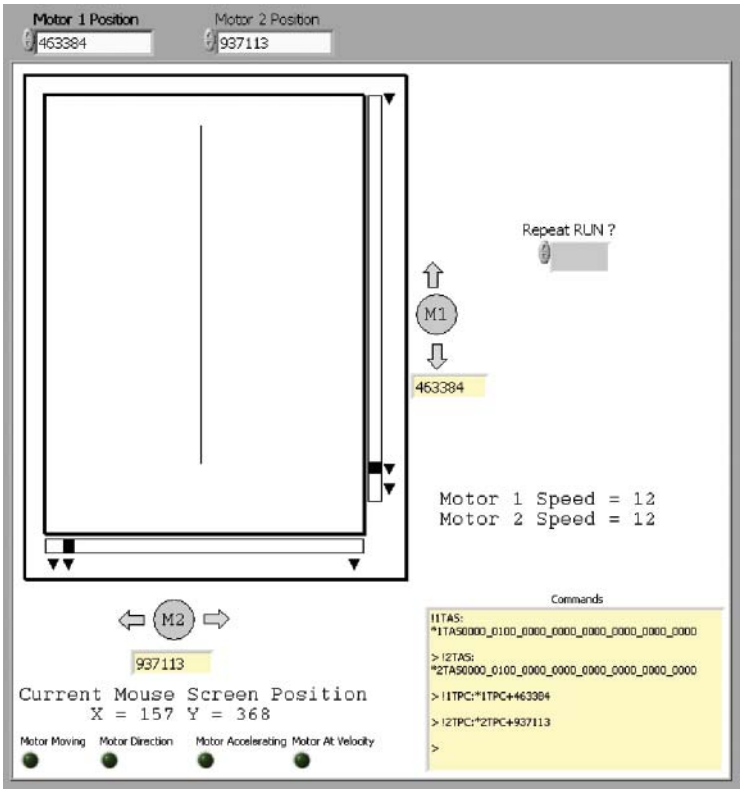

Figure 3. Three-axis gantry software graphical user interface.

Urban Tracking and Positioning System

Peter Haugen
(925) 422-0749
haugen2@llnl.gov

The Urban Tracking and Positioning System is a high-resolution urban tracking demonstration system similar to GPS but suitable for indoor use in locales such as buildings and caves. Indoor localization of radio devices is a daunting task due to the presence of severe multipath and low probability of a line-of-sight (LOS) signal between the transmitter and receiver. This harsh propagation environment for radio signals is due to the shadowing and reflections from walls and objects.

In FY2005 we built a set of high-accuracy ranging devices using ultra-wideband (UWB) RF signals and algorithms for position estimation. UWB signals are particularly suited for ranging because of their short duration, high-bandwidth pulses. Our ranging and positioning algorithms improve accuracy by addressing some of the known challenges in UWB localization. In FY2006 we expanded the capabilities of these units to support multiple masters and tag units operating in the same environment, offering true 3-D location capabilities to multiple receivers.

Project Goals

The goals of this project were to combine LLNL UWB radio hardware capable of collecting range measurements with LLNL software algorithms to perform the signal processing needed to recover the RF signatures in high-scattering environments. When combined, these technologies create a complete system capable of high-resolution geo-location in poor RF environments, such as urban areas or inside buildings, where traditional geo-location technologies such as GPS, are not available or do not yield sufficient accuracy.

Relevance to LLNL Mission

Several LLNL programs have an interest in the high strategic potential of urban tracking. Applications for high-accuracy systems for use in complex

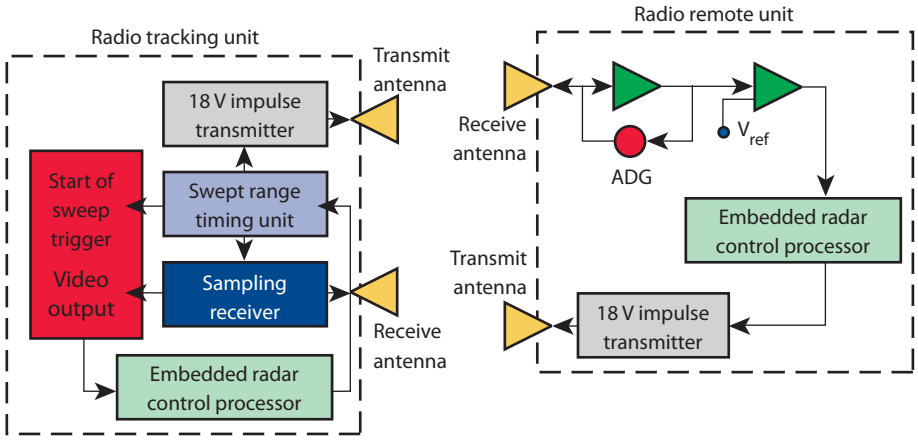

Figure 1. Block diagram of the round-trip TOF ranging pair, consisting of two units. The radio tracking unit sends a pulse to the remote unit, which replies with its own pulse. The main unit records the total round-trip TOF to extract the distance measurement.

urban environments is growing, and LLNL's established technology in MIR UWB radios and signal processing allows us to be at the cutting edge.

FY2006 Accomplishments and Results

In FY2006, we added the capability to support ranging and communication between multiple tracking and remote radio units, permitting the 3-D location of multiple units simultaneously. To accomplish this task we first added data-encoding capabilities into the UWB ranging transaction that the radios previously used. Then we uniquely identified the radar tracking and remote units so they can be addressed individually. Finally we implemented and embedded a Time Division Multiple Access (TDMA) protocol scheme so multiple units could co-exist in the same environment, without interfering with each other's ranging and communications transactions.

Figure 1 shows the updated hardware component diagrams; Fig. 2 shows their ranging transaction. For that transaction, the radio tracking unit sends an encoded pulse stream to the target radio remote unit. The remote unit receives the request and responds with its own uniquely encoded reply. The tracking unit receives and time-stamps the reply to find elapsed round-trip travel time, and thus distance. Distance measurements from multiple tracking radios can then be combined to compute a 3-D position estimation. A set of the complete remote and tracking hardware units can be seen in Fig. 3.

Using this completed system we have tested and documented the ranging performance in several harsh environments, supporting other LLNL projects, including the United States Coast Guard ships and subterranean caves.

Related References

1. Gezici, S., *et al.*, "Localization Via Ultra-Wideband Radios: A Look at Positioning Aspects for Future Sensor Networks," *IEEE Signal Processing Magazine*, **22**, 4, pp. 70 - 84, 2005.
2. Young, D., *et al.*, "Ultra-Wideband (UWB) Transmitter Location Using Time Difference of Arrival (TDOA) Techniques," *Conference Record of the Thirty-Seventh Asilomar Conference on Signals, Systems and Computers*, 2003.
3. Jourdan, D., *et al.*, "Monte Carlo Localization in Dense Multipath Environments Using UWB Ranging," *Proceedings of the IEEE Conference on UWB*, Zurich, Switzerland, 2005.
4. Lee, J., and A. Scholtz, "Ranging in a Dense Multipath Environment Using an UWB Radio Link," *IEEE Journal on Selected Areas in Communications*, **20**, 9, pp. 1677 - 1683, 2002.
5. Smith, J., and J. Abel, "Closed-Form Least-Squares Source Location Estimation from Range-Difference Measurements," *IEEE Transactions of Acoustics, Speech*, and *Signal Processing*, **ASSP-35**, 12, 1987.

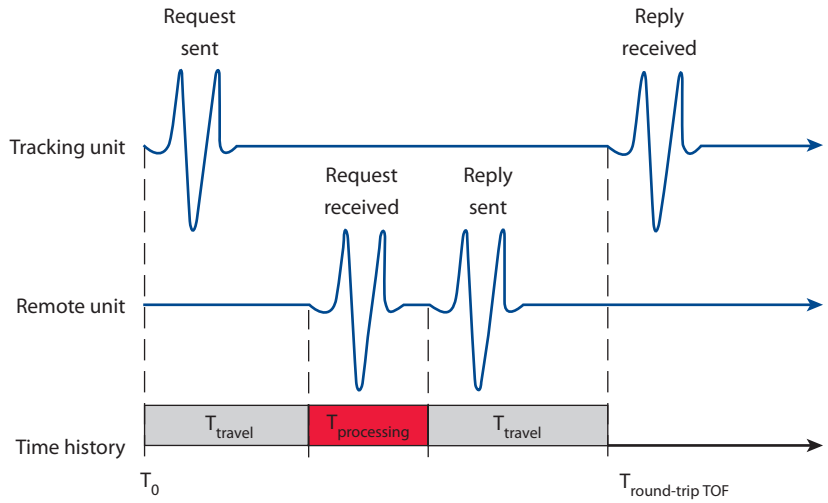

Figure 2. The round-trip TOF, consisting of travel time to and from the remote unit (approximately equal) and time spent in processing at the remote location (a known value we can subtract).

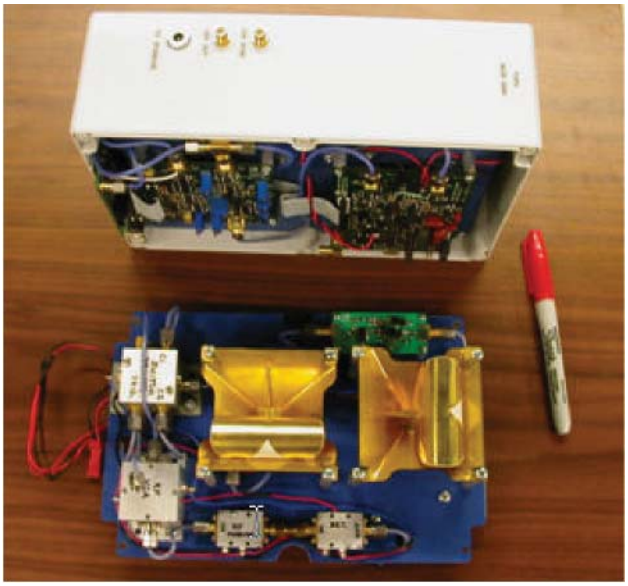

Figure 3. Completed UWB remote geo-location unit (top) and tracking radio (bottom).

Ultrasonic Techniques for Laser Optics Inspection

Michael J. Quarry
(925) 422-2427
quarry1@llnl.gov

This project applied two ultrasonic methods that could be subsequently deployed to inspect NIF optics either on- or off-line. One method used ultrasonic shear-wave, the other longitudinal-wave tomography. This project has constructed ultrasonic hardware that generated images of damage to the surface of optics using a set of multiple sensors that are applied to the outside edge of the optic. The system was built and demonstrated on glass with programmed defects and actual laser damage to assess detection capabilities and sizing abilities. The system is also portable, enabling field-testing of optics or other structures.

Project Goals

The goal is to detect and size laser damage on an optic with defects ranging in size from 0.1 to 10 mm or larger by generating acoustic images of a laser-damaged optic that are easily interpreted by those less familiar with acoustics.

Relevance to LLNL Mission

NIF will benefit from nondestructive methods that can assess damage to allow for timely replacement of critically damaged optics or surface refinishing of reuseable optics. The electronic switching technology and data acquisition interface is also being used on an Advanced Development and Production Technology (ADAPT) project for monitoring a weapon production process.

FY2006 Accomplishments and Results

We investigated the application of two ultrasonic techniques, 1-MHz longitudinal waves with tomographic reconstruction and 10-MHz horizontally-polarized shear waves, to image surface damage in NIF optics. To evaluate the techniques we used fused silica samples with programmed hemispherical machined pits with diameters ranging from 0.5 to 5 mm.

In FY2005, shear-wave experiments were performed on an optic with hemispherical defects machined into the surface. The shear wave technique is able to accurately image and size all the defects. In FY2006, the tomographic experiments were performed with a 32-element, 1-MHz linear array with point-like elements, generating a broad beam. The data was reconstructed with a time-reversed MUSIC (Multiple Signal Classification) detection algorithm.

A sample detection map shows 3- and 5-mm hemispherical flaws (Fig. 1). The tomographic approach was able to detect only defects greater than or equal to 3 mm diameter. The 1-MHz linear array was not able to produce waveforms with sufficient signal-to-noise to detect the smaller flaws. Based on these results,

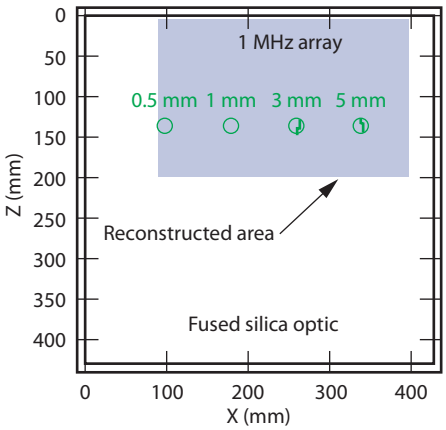

Figure 1. Tomographic detection map obtained from the 1-MHz array data overlaid on a schematic image of the defects, revealing the 3- and 5-mm hemispherical pits. The 0.5- and 1-mm pits were not detected.

the shear-wave technique was chosen for demonstration, test, and evaluation on a NIF fused-silica optic with laser damage created without vacuum loading conditions (Fig. 2a).

The shear-wave technique uses narrow, highly-directed beams. The outer edge of an optic can be covered with shear-wave transducers on all four sides. Each transducer transmits a pulse into the optic and any damage reflects the pulse back to the transmitter. The transducers are multiplexed, and the collected time waveforms are enveloped and replicated across the width of the element. Multiplying the data sets from all four sides produces a map of reflected amplitude to the fourth power, which results in an acoustic image of the surface of the optic.

Shear-wave data were collected on the fused-silica optic shown in Fig. 2a. The shear-wave technique was able to accurately detect, locate, and size laser damage from 0.5 to 8 mm in diameter. Figure 2b shows the 25.4-mm images of the surface of 0.5-, 1.5-, 7- and 8-mm damage sites. These are size ranges in which NIF has interest. Surface damage size can be directly measured on the image. Maximum depth correlates to maximum amplitude of the detecting waveform. The shear-wave data results in a monotonically increasing amplitude as a function of maximum depth, as shown in Fig. 3. Previous efforts with 5-MHz longitudinal data showed a non-monotonic relationship. A higher signal-to-noise ratio with virtually no effects of mode conversion or multiple echoes from the bottom surface was observed, compared to previous 5-MHz longitudinal acoustic data.

Related Reference

Martin, P., D. Chambers, and G. Thomas, "Experimental and Simulated Ultrasonic Characterization of Complex Damage in Fused Silica," *IEEE Transactions on Ultrasonics, Ferroelectrics, and Frequency Control*, **49**, 2, pp. 255-265, 2002.

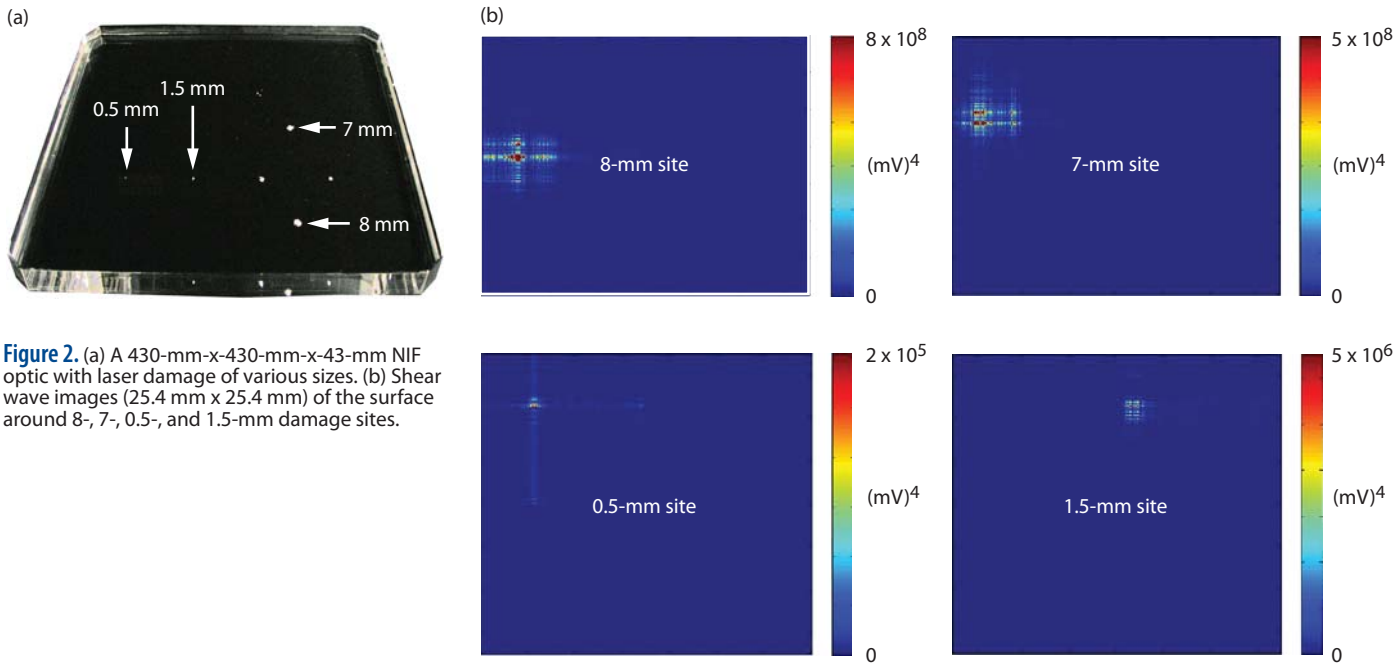

Figure 2. (a) A 430-mm-x-430-mm-x-43-mm NIF optic with laser damage of various sizes. (b) Shear wave images (25.4 mm x 25.4 mm) of the surface around 8-, 7-, 0.5-, and 1.5-mm damage sites.

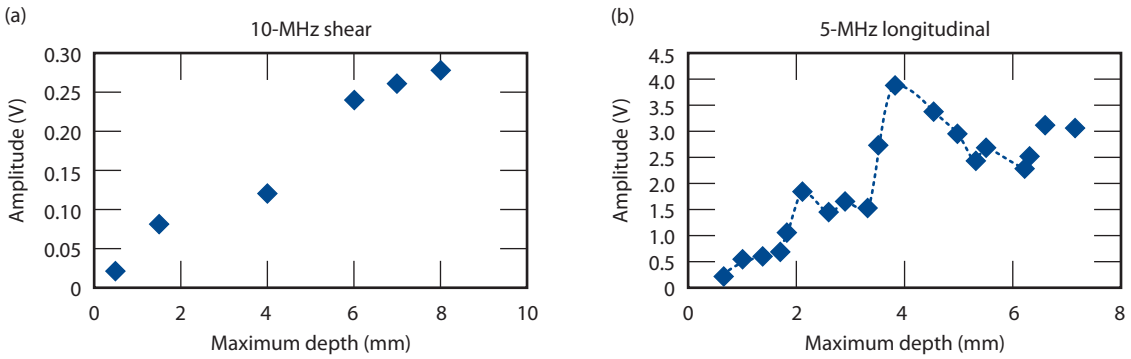

Figure 3. (a) Depiction of 10-MHz shear wave yielding a monotonic relationship with maximum laser damage depth, while (b) the 5-MHz longitudinal-wave data has a non-monotonic relationship. Data is from sample shown in Fig. 2(a).

Surface Acoustic Wave Microscopy of Optics

Michael J. Quarry
(925) 422-2427
quarry1@llnl.gov

We investigated the feasibility of surface acoustic wave microscopy to detect fine cracking in NIF optics. Cracks occur in the surface of NIF optics from the grinding of the surface, and subsequent polishing still leaves fine cracks. An Olympus UH-3 acoustic microscope was refurbished to enable surface acoustic wave microscopy from 200 MHz to 1 GHz on fused silica. The system uses high-frequency bulk and surface acoustic waves to characterize surfaces, near surfaces, and thin films. Feasibility studies were performed on polished fused silica.

Project Goals

The goal of the project is to show detection of fine cracking (1 to 15 μm) in the surface of a polished sample of fused silica over a 2-mm-x-2-mm area.

Relevance to LLNL Mission

Surface acoustic wave microscopy will enable the acoustic characterization of NIF optics without etching. Characterization of laser damage for mitigation purposes may also now be investigated. Mapping density gradients in JASPER projectiles is another possible LLNL application. Other applications include thin films, grain structure visualization, and observation of biological cells without staining.

FY2006 Accomplishments and Results

An Olympus UH-3 surface acoustic wave microscope was refurbished for operation. Two-hundred-MHz and 400-MHz acoustic lenses were found to be operational, while the 1-GHz lens was damaged. However, we have access to a 1-GHz lens through our relationship

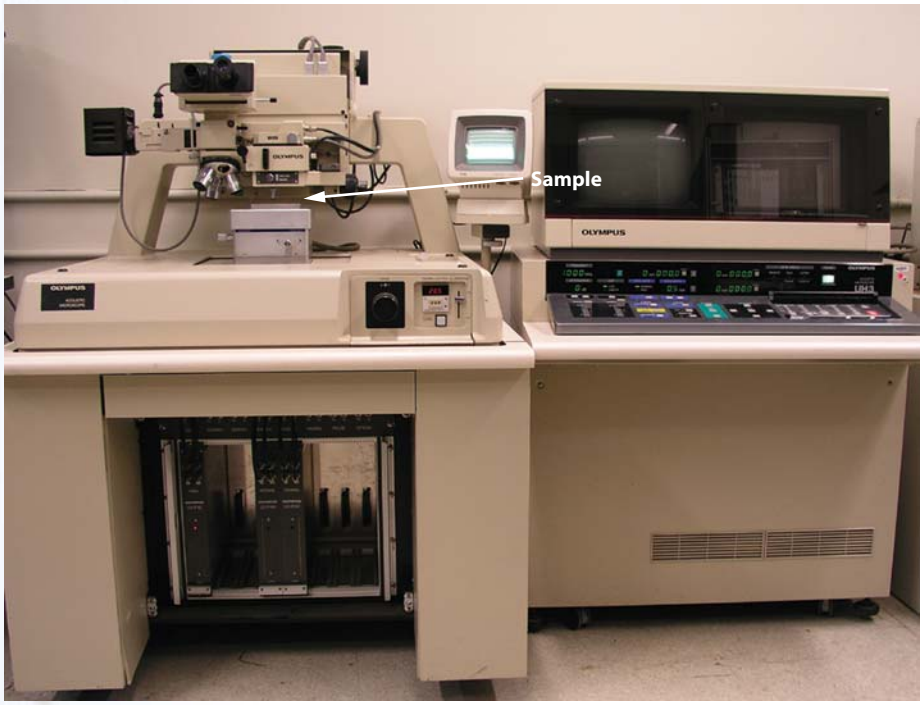

Figure 1. Olympus UH-3 acoustic microscope system.

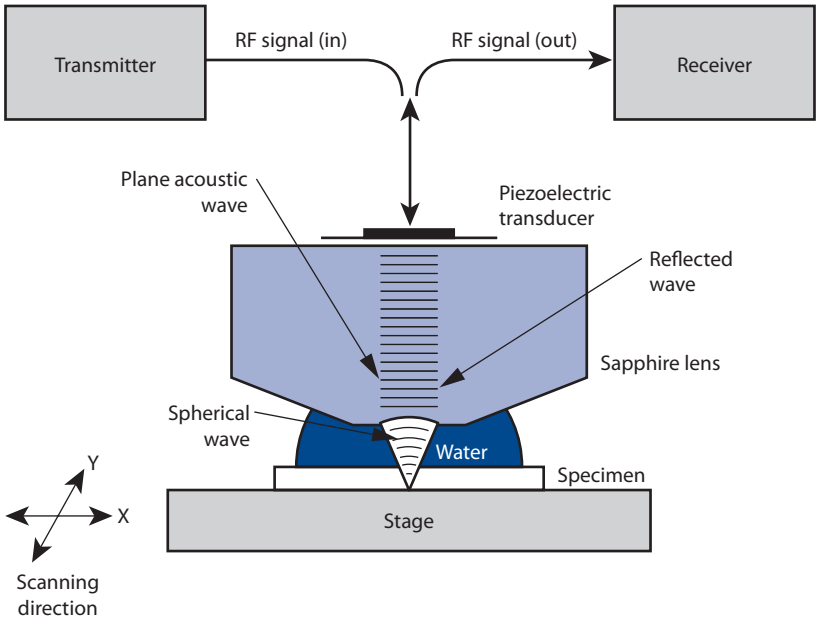

Figure 2. Diagram of the ZnO transducer and sapphire lens.

with Pennsylvania State University. At 1 GHz the lateral resolution of the system is 1 µm. The acoustic lens is designed with an F-number of 0.7 to optimize surface and near surface resolution.

Figure 1 shows a picture of the system. A sample is placed on the stage, and an acoustic lens is raster-scanned over the sample to obtain an image. A diagram of the transducer and lens is shown in Fig. 2. The transducer is driven by tens of cycles of a tone-burst generator. The burst travels down a sapphire buffer rod and is focused through the lens at or near the surface of the sample. A Rayleigh surface wave and the bulk waves interfere with each other. A peak detector captures the peak of the reflected energy. The scanning process takes about 10 s to form an image.

A fused silica Corning 7980 sample (Fig. 3) with grinding and polishing fractures was examined with the Olympus system. An area of 1 mm^2 was scanned in the position indicated in Fig. 3. The resultant image (Fig. 4a) shows many fine cracks. A zoomed-in image with an area of 0.25 mm^2 is also shown, in Fig. 4b. The crack lengths along the surface are about 10 µm using the scale on the image to measure across the crack. A similar image could be obtained without etching.

In the future, we will look at other applications for surface acoustic wave microscopy. One important problem is looking at gradient density structures including JASPER projectiles. We can also improve the technology with new lens and transducer designs. PZT is a much more efficient transduction material than the current ZnO. Frequency could be optimized with a tunable tone-burst generator.

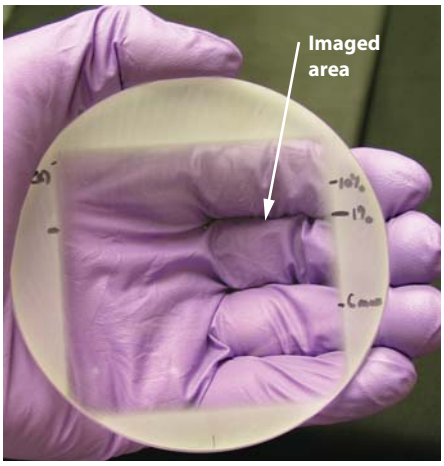

Figure 3. Polished fused silica sample. The area investigated with surface acoustic wave microscopy is indicated by the arrow.

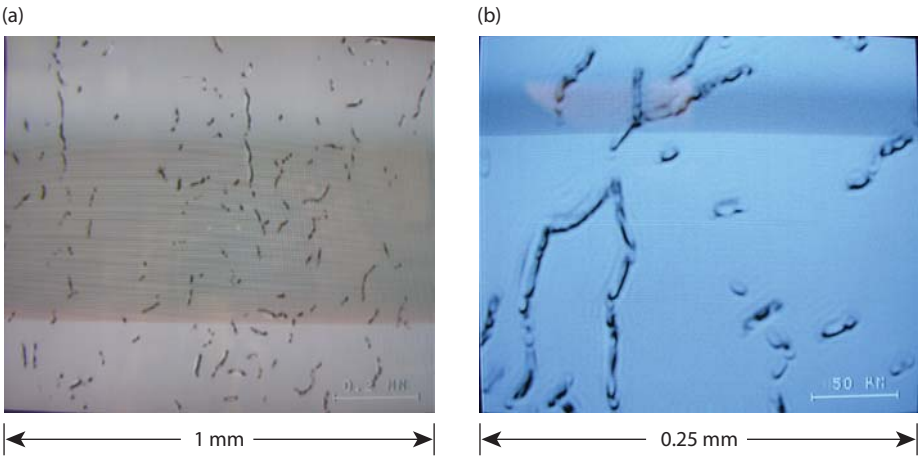

Figure 4. (a) Image of the surface of polished fused silica, showing surface fractures with a crack length of about 10 µm as measured using the scale on the image. (b) Enlargement of the same approximate area shown in Fig. 3.

Ultrafast Transient Recording Enhancements for Optical-Streak Cameras

Corey V. Bennett
(925) 422-9394
bennett27@llnl.gov

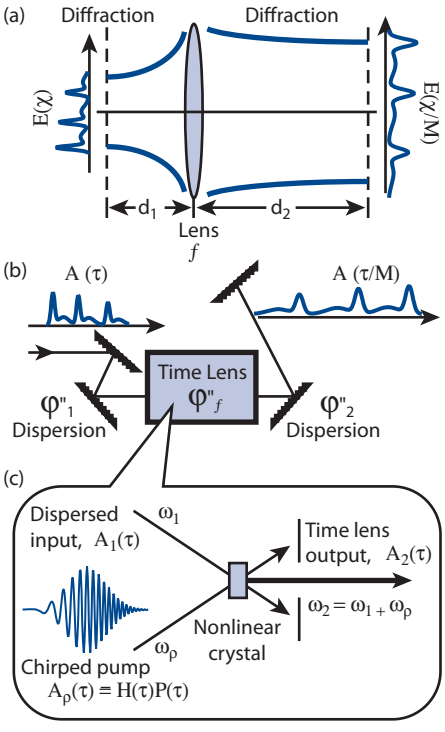

Figure 1. Comparison of (a) spatial and (b) temporal imaging systems. (c) A time lens is produced by mixing the input signal with a chirped optical pump pulse.

Several experiments at LLNL will require hard x-ray and neutron diagnostics with temporal resolution of ~1 ps and a high dynamic range, particularly those experiments involving ignition. The Linac Coherent Light Source (LCLS) at the Stanford Linear Accelerator Center (SLAC) will need to measure timing and pulse shapes of its 100-fs FWHM x-ray pulse. These measurement requirements are far beyond existing capabilities.

This is the final year of a three-year project that has developed a "time-microscope" front end for optical streak cameras, magnifying (temporally stretching) signals having ultrafast detail so that they can be recorded with slower speed instruments with a much higher fidelity. The system is compatible with a new class of ultrafast radiation detectors being developed, which produce a modulated optical carrier in response to ionizing radiation.

Project Goals

Our goal is to ensure delivery of the next-generation ultrafast diagnostics for experiments at LLNL's NIF and other facilities such as LCLS.

Temporal imaging is based on a space-time duality between how a beam of light spreads due to diffraction as it propagates in space and how pulses of light disperse as they propagate through dispersive media, such as grating systems or optical fiber (Fig. 1.) There is also a one-to-one analogy between the quadratic spatial phase modulation produced by a lens and imparting of a quadratic temporal phase (equivalent to a linear frequency chirp). We have chosen to implement a "time lens" through sum-frequency generation (SFG) of a broadband-chirped optical pump with the input signal in a nonlinear crystal because of the improved resolution it produces.

The system was designed using all guided wave technologies for compactness and robustness. Its fiber optic input accepts an ultrafast signal at a 1534-nm wavelength. Available component limitations required re-scoping the project to demonstrating temporal imaging with 33x temporal magnification (instead of 100x) and 100-ps record length (instead of 600 ps), although the original goals should still be possible after rebuilding certain component technology capabilities that industry no longer supports.

Additional goals include a resolution < 300 fs and a dynamic range > 100:1.

Relevance to LLNL Mission

The success of NIF is critical to LLNL's stockpile stewardship mission. Our project is focused on delivering the diagnostics needed for the critical experiments to carry out that mission.

FY2006 Accomplishments and Results

We've designed and implemented the temporal imaging system in Fig. 2 using specially designed fiber-optic dispersive delay lines in the input and time-lens pump generation arms of the systems. These arms also include optical filters and amplifier stages to improve the final signal to noise. The time lens uses sum-frequency mixing in a chirped-period periodically poled lithium niobate (chirped-PPLN) waveguide because of the high-efficiency broadband mixing that can be obtained. The final output dispersion is in a specially designed

chirped fiber Bragg grating because of the extremely large dispersion with low loss that can be obtained.

An input "ring down/up" test pattern was generated by passing a train of 2-ps FWHM pulses through a 2-x-2 50%:50% splitter and looping one output of the splitter back to an input with a delay nearly, but not exactly, equal to the repetition rate of the laser. This path delay difference could be set to place successively weaker pulses before or after a larger pulse passing directly through the splitter without looping back. Time delay could be set with 2.2-fs/step resolution of the controller. The time magnification was calibrated by making precise changes to the input and observing the magnified output change.

Figure 3 shows the time magnified output waveform recorded on a streak camera with the input delay between pulses set at 11.3 ps. The top scale is the actual time recorded on the streak camera and the bottom scale is the equivalent input time determined by dividing the output time by the observed –30.1x time magnification. A signal decay rate of 21.4%/pulse can be observed, which is consistent with losses in the test pattern set up. The dynamic range in this single shot measurement is nearly 1000:1, with an input temporal resolution of 1.8 ps. Better temporal resolution should be possible with additional adjustment of the system.

Related References

1. Bennett, C. V., and B. H. Kolner, "Upconversion Time Microscope Demonstrating 103x Magnification of Femtosecond Waveforms," *Optics Letters*, **24**, 11, pp. 783-785, June 1, 1999.

2. Bennett, C. V., and B. H. Kolner, "Principles of Parametric Temporal Imaging-Part I: System Configurations," *IEEE J. Quantum Electronics*, **36**, 4, pp. 430-437, April 2000.

3. Bennett, C. V., and B. H. Kolner, "Principles of Parametric Temporal Imaging-Part II: System Performance," *IEEE J. Quantum Electronics*, **36**, 6, pp. 649-655, June 2000.

4. Yang, S.-D., A. M. Weiner, K. R. Parameswaran, and M. M. Fejer, "400-Photon-Per-Pulse Ultrashort Pulse Autocorrelation Measurement with Aperiodically Poled Lithium Niobate Waveguides at 1.55 mm,"*Opt. Lett.*, **29**, pp. 2070-2072, 2004.

5. Durkin, M., M. Ibsen, M. J. Cole, and R. I. Laming, "l-m Long Continuously-Written Fibre Bragg Gratings for Combined 2nd and 3rd Order Dispersion Compensation," *Electronics Letters*, **33**, 22, pp. 1891-1893, 1997.

FY2007 Proposed Work

With outside funding, we are continuing this project. We are developing an optical frequency chirp diagnostic that is capable of recording the frequency chirp of each 100-ps pulse in a high-repetition rate (620 MHz) sequence of optical pulses. Signals will have over 300 GHz (to 1 THz) of bandwidth and can be positively or negatively chirped.

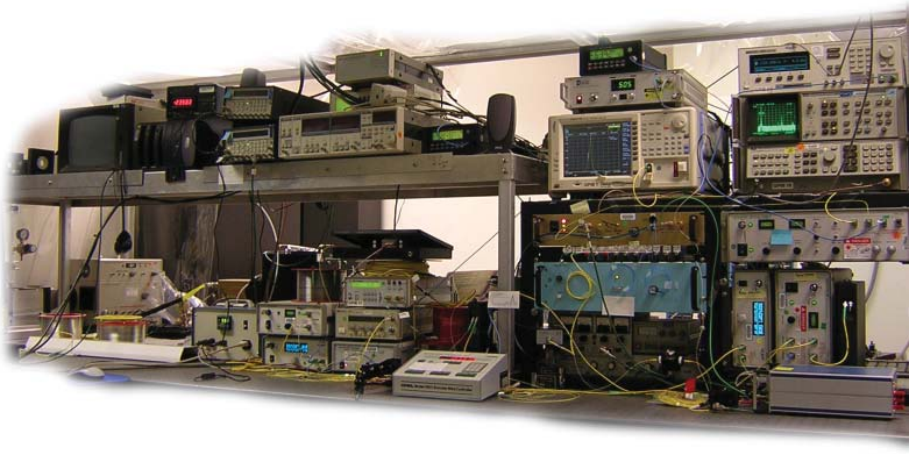

Figure 2. Photograph of the temporal imaging system.

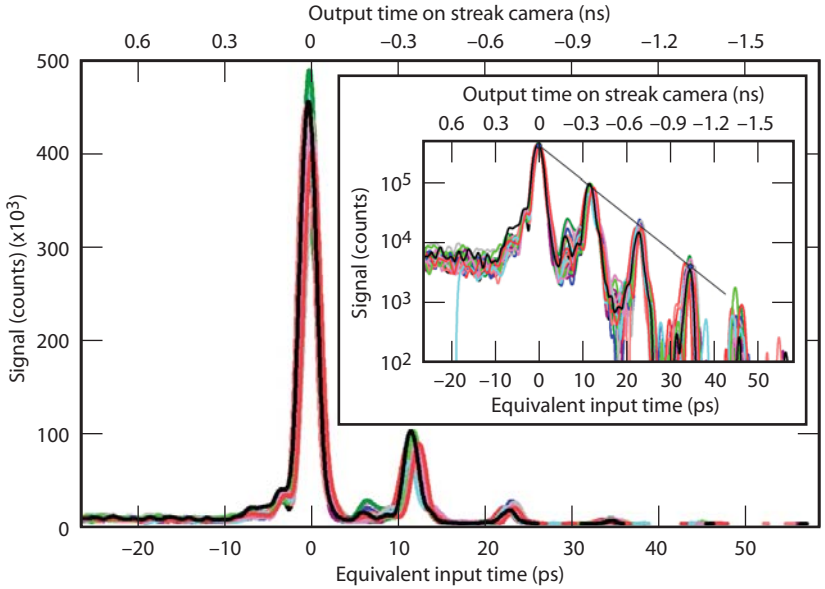

Figure 3. Many single-shot time magnified "ring down" patterns recorded on an optical streak camera. Inset log scale plot: the weak pulses are difficult to see on a linear scale but clearly show on the log scale plot.

Evaluation of Ultrafast Recording Technologies for Reduction to Practice

John E. Heebner
(925) 422-5474
heebner1@llnl.gov

This project addresses limitations of technologies presently used for single-shot, transient recording of ultrafast signals. Current instrumentation relies on high-bandwidth oscilloscopes, streak cameras, and Frequency Resolved Optical Gating (FROG) methods. The performance associated with these solutions is fundamentally limited and will fail to support upcoming programmatic requirements. The best candidate for achieving these requirements is a hybrid technology implementing 1) an all-optical sampler that routes serial signals into parallel channels at timescales approaching 1 ps, followed by 2) detection with an array of high-dynamic-range integrating detectors.

This strategy circumvents the limitations (Fig. 1) of current methods in an analogous manner to hybrid communication strategies involving both serial optical time division multiplexing (OTDM) and parallel wavelength division multiplexing (WDM) for the high-bandwidth transmission of information. Recent progress in nonlinear optics, driven by the new fast all-optical switching technologies for telecommunications applications, has achieved a critical maturity. However, the lack of obvious commercial applications for high-fidelity single-shot transient recording technologies has limited progress in this approach thus far.

Project Goals

We aim to conduct an initial scoping and exploration of a technology area that has high strategic potential for LLNL missions. Specifically, we seek to compare selected classes of integrated microphotonic devices that can be tailored to implement ultrafast nonlinear optical switching phenomena. We plan to construct a framework and supplementary modeling tools required to uncover the nonlinear optical materials, fabrication processes, and photonic architectures optimally suited to handle next-generation instrumentation requirements.

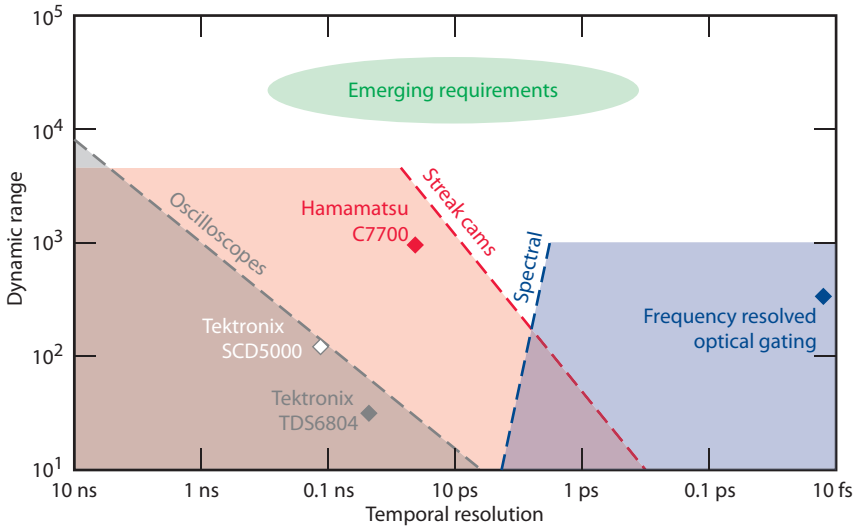

Figure 1. Parameter space (dynamic range vs. speed) of existing recording technologies and emerging LLNL HEDS/NIF requirements.

Relevance to LLNL Mission

The work directly addresses instrumentation performance gaps identified by LLNL. Specifically, future HEDS (high-energy-density science) experiments on NIF will demand transient recording technology possessing high temporal resolution (< 10 ps), high dynamic range (> 1000:1), and scalability to multichannel geometries. No existing recording technology satisfies these demanding requirements simultaneously.

The implementation of all-optical sampling mechanisms for ultra-high-fidelity transient recording represents a radical but promising departure from conventional recording technologies. The characterization of ultrashort laser pulses would benefit directly from this technology. Furthermore, when coupled with LLNL-pioneered radiation-to-optical encoding technology, a potential replacement for aging radiation–sensitive transient recording instrumentation is feasible.

FY2006 Accomplishments and Results

Nonlinear optical phenomena that result in the optically-induced modification of the refractive index of a solid-state material include (Fig. 2) the optical Kerr and Stark effects, the plasma effect, exciton screening, the bandfilling (Burstein-Moss) effect, and the bandgap shrinkage effect. All-optical switches that route a light signal in proportion to the intensity of a secondary (control) light source can be engineered from these phenomena through a variety of mechanisms. In practice however, due to the relatively weak nature of nonlinear optical interactions, nonlinear optical engineering lags nonlinear electrical engineering (*i.e.*, electronics) by some 50 years. Thus, applications of this promising technology with relevance to optical sampling are posed with the following challenges:

1. The subset of materials that display substantial nonlinear optical response and maintain compatibility with state-of-the-art integration technologies is limited primarily to III-V semiconductors.
2. The effective speed of the signal sampling will depend on the material response times (rise and recovery), inter-gate propagation delays, and structured resonance bandwidths.
3. The attainable dynamic range of the instrument will be further corrupted in practice by optical leakage and cross-talk at each of the sampling gates due to fabrication imperfections, control pulse instabilities, and control beam nonuniformities.

To address these challenges, a major component of our study consisted of the detailed investigation and identification of architectures that implement materials with high nonlinear figures of merit and compatibility with integration technologies for which LLNL carries strong expertise. We furthermore sought an all-optical sampling mechanism that displays a strong, ultrafast response, and is robust to the fabrication errors, pulse instabilities, and beam nonuniformities expected to be encountered in reasonably toleranced systems.

We down-selected from among multiple architectures to a deflection encoded geometry that implements bandfilling and plasma effects in III-V semiconductors. In direct analogy to electron-based oscilloscopes and streak cameras, the down-selected architecture deflects an optical beam onto a high-dynamic-range detector array or camera for subsequent recording.

Related References

1. Walden, R. H., "Analog-to-Digital Converter Survey and Analysis," *IEEE J. Sel. Area Comm.*, **17**, pp. 539-550, 1999.
2. Heebner, J. E., N. N. Lepeshkin, A. Schweinsberg, G. W. Wicks, R. W. Boyd, R. Grover, and P.-T. Ho, "Enhanced Linear and Nonlinear Optical Phase Response of AlGaAs Microring Resonators," *Optics Letters*, **29**, pp. 769 -771, 2004.
3. Lowry, M. E. *et al.*, "X-Ray Detection by Direct Modulation of an Optical Probe Beam-Radsensor: Progress on Development for Imaging Applications," *Rev. Sci. Instrum.*, **75**, pp. 3995-3997, 2004.

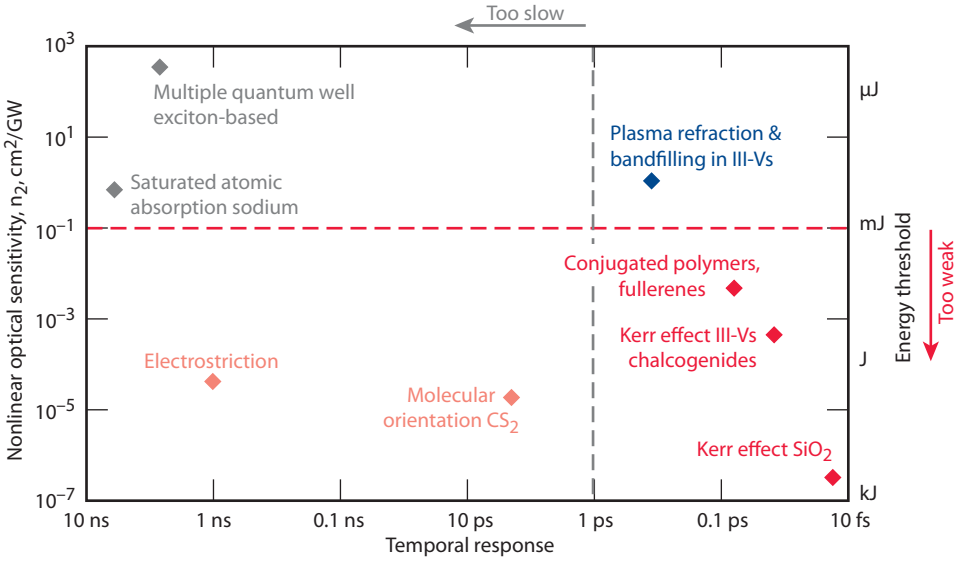

Figure 2. Parameter space (sensitivity vs. speed) of existing nonlinear optical sampling mechanisms in solid-state materials capable of modifying optical properties on a fast timescale.

Acoustic Characterization of Mesoscale Objects

Diane Chinn
(925) 423-5134
chinn3@llnl.gov

Mesoscience is an emerging area of science and engineering that focuses on the study of materials with dimensions, features, and structures that range from a few millimeters down to a few micrometers. Mesoscale objects typically have embedded features that require characterization with resolution on the order of a few micrometers. Mesoscale nondestructive characterization technologies are required that can 1) penetrate into or through a few millimeters of diverse materials; and 2) provide spatial resolutions of about a micrometer.

An acoustic technique is attractive because it offers high sensitivity to features such as thickness and interface quality that are important to mesoscale objects. In addition to the resolution requirements, many mesoscale objects require a non-contact technique to avoid damaging fragile surfaces.

Project Goals

This research will achieve micrometer resolution characterization by extending the range of laser-acoustic testing to GHz frequencies. Materials and the geometry of components used in most LLNL mesoscale objects necessitate the use of a non-contacting technique at frequencies from 100 MHz to 10 GHz. This frequency range is required to acoustically characterize features from 5 to 0.5 µm in size. In order to be applicable to mesoscale objects, the GHz acoustic waves must propagate sufficient distances into materials of interest. For LLNL applications, mesoscale structures are on the order of 25 to 200 µm thick.

Relevance to LLNL Mission

This work directly addresses metrology and characterization gaps of interest in LLNL's engineering focus areas, such as measurement technologies and nondestructive characterization. Of the different mesoscale characterization challenges at LLNL, the targets prepared

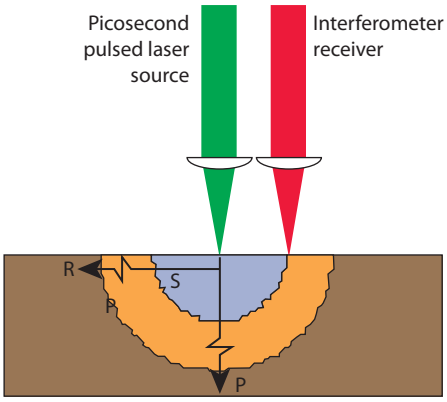

Surface (R), Shear (S), and longitudinal (P) waves generated

Figure 1. Schematic of laser ultrasound technology. Laser UT uses a pulsed laser as a source to generate acoustic waves and a laser interferometer to detect acoustic waves. The source and receiver can be on the same side (as shown) or on opposite sides of the object. The acoustic wave travels through the object before it is detected. Use of a pulsed laser gives temporal resolution to the detected signal.

for OMEGA and NIF are the most relevant. This proposal impacts the DNT, NIF, Engineering, and Chemistry and Materials Science Directorates through target fabrication and characterization.

FY2006 Accomplishments and Results

The primary research goal in the final year of this project is to understand GHz acoustic wave propagation and its potential for material characterization. Two major accomplishments in support of this goal are validation of laser-acoustic models with experimental data, and identification and validation of material attenuation modes in relation to material microstructure.

Theoretical and experimental waveforms for a 25-μm-thick gold foil taken with the configuration in Fig. 1 are shown in Fig. 2. The analytical model, which includes laser and material parameters, shows good agreement with measured data. Figure 3 shows the frequency dependence of the acoustic-wave attenuation in the gold foil. The quadratic relation to attenuation is characteristic of stochastic grain scattering where wavelength, λ, is proportional to the grain size. At 0.8 GHz in gold, λ = 4 μm. From micrographs of the gold, the grain size was confirmed to be approximately 4 μm. This finding demonstrates that GHz laser ultrasound can be a valuable tool in material characterization.

Related References

1. Chambers, D., D. Chinn, and R. Huber, "Optical Mapping of the Acoustic Output of a Focused Transducer," *Proceedings of the 147th Acoustical Society of America Meeting*, p. 2526, 2004.
2. Hebert, H., F. Vidal, F. Martin, J.-C. Kieffer, A. Nadeau, and T. W. Johnston, "Ultrasound Generated by a Femtosecond and a Picosecond Laser Pulse Near the Ablation Threshold," *J. Appl. Physics*, **98**, p. 033104, 2005.
3. Huber, R. H., D. J. Chinn, O. O. Balogun, and T. W. Murray, "High Frequency Laser-Based Ultrasound," *Review of Progress in Quantitative Nondestructive Evaluation*, pp. 218-224, August 2005.
4. Martz, H., and G. Albrecht, "Nondestructive Characterization Technologies For Metrology of Micro/Mesoscale Assemblies," *Proceedings of: Machines and Processes for Micro-scale and Meso-scale Fabrication, Metrology, and Assembly*, ASPE Winter Topical Meeting, pp. 131-141, 2003.
5. Scruby, C., Laser Ultrasonics: Techniques and Applications, Adam Hilger, New York, 1990.

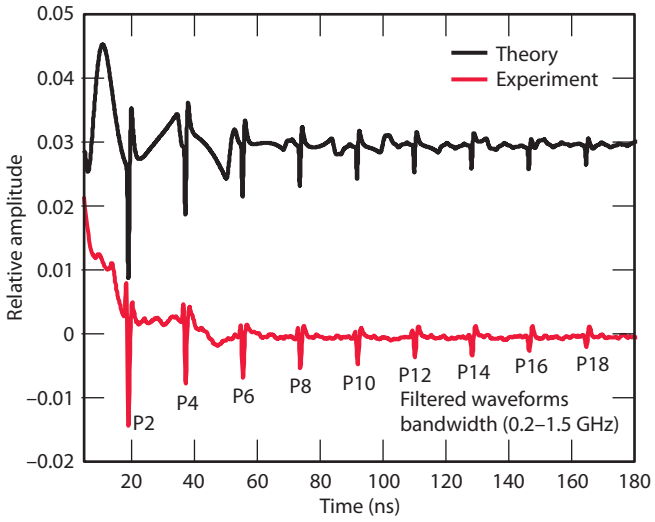

Figure 2. Using the configuration in Fig. 1, temporal signals from modeled (black) and measured (red) signals for a 25-μm-thick gold foil, show good correlation. Each peak in the signal represents an arrival of an acoustic wave at the epicentral location. The analytical model includes laser energy, spot size, and pulse width as well as optical, thermal, and mechanical properties of the material.

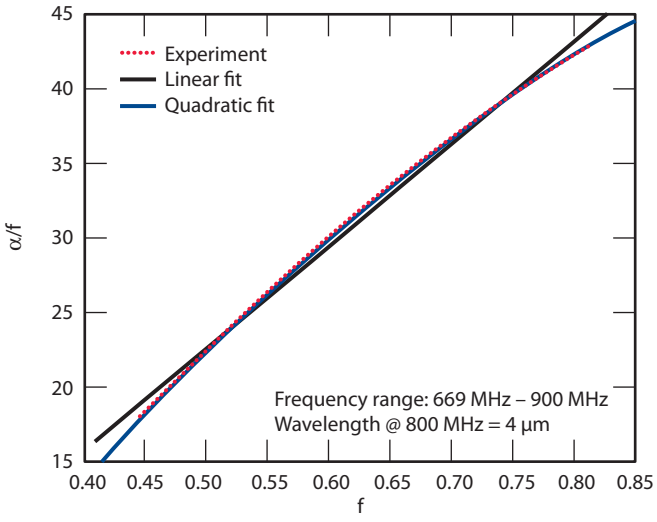

Figure 3. Frequency dependence of the acoustic-wave attenuation in the 25-μm gold foil. Acoustic attenuation of the wave propagation increases with the square of the frequency. This dependence is characteristic of stochastic grain scattering.

Application of Laser GHz Ultrasound to Mesoscale Materials

Robert Huber
(925) 424-2002
huber5@llnl.gov

Laser-based ultrasound offers non-contact nondestructive characterization for materials and structures. A state-of-the-art laser-based ultrasound system has been installed at LLNL and demonstrated on numerous mesoscale samples. Mesoscale (µm scale features and up to mm extent) materials and their characterization are of increasing importance at LLNL in many fields, including high-energy-density physics (HEDP) and other National Ignition Facility (NIF) targets, and medical applications for determination of tissue health.

Project Goals

The goal of this work was to set up a laboratory housing the state-of-the-art GHz laser-based ultrasound system and demonstrate its ability to characterize mesoscale materials.

Relevance to LLNL Mission

The National Ignition Facility is, and will continue to be, a major program at LLNL. This facility offers a unique capability for conducting fusion and other HEDP experiments. The targets required for these experiments will be some of the most complex ever devised, and characterizing these targets prior to testing them is critical to determining the success of the experiments. These targets are mesoscale structures and, as such, require new nondestructive characterization tools.

FY2006 Accomplishments and Results

A new laser-based ultrasound laboratory was set up to house the GHz laser-based ultrasound equipment (Fig.1). Numerous samples, including metal foils and samples with two layers

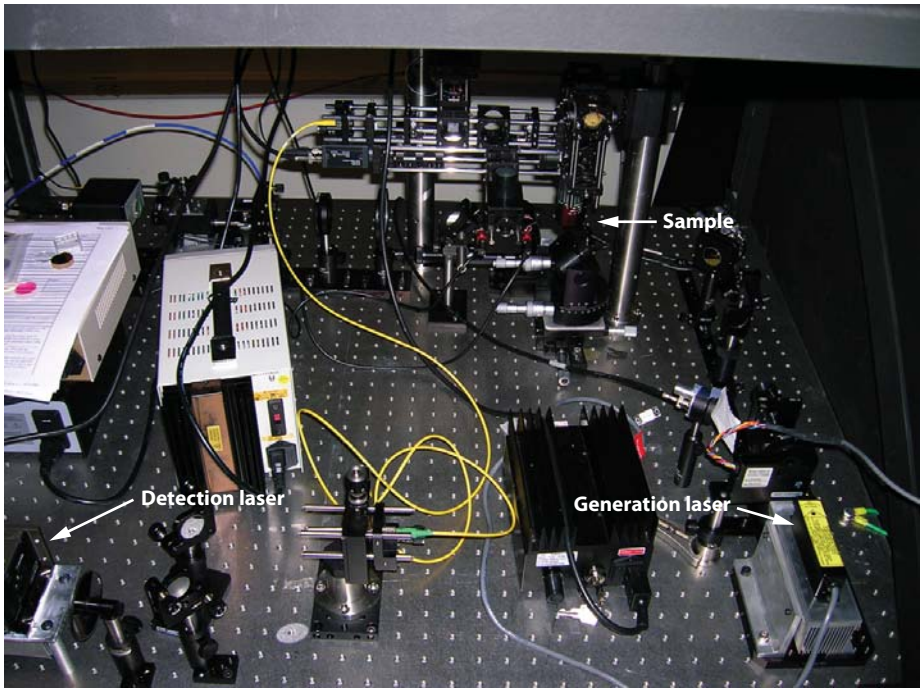

Figure 1. GHz laser-based ultrasound system.

were tested. Raw and filtered waveforms for a 25-µm-thick gold foil are shown in Fig. 2. Raw and filtered waveforms for a two-layer (Al-Cu) sample are provided in Fig. 3. The Al and Cu thicknesses were 63 µm and 35 µm, respectively. These tests demonstrated the system's high spatial resolution for thickness measurement as well as its ability to characterize bonds.

Ultrasound techniques are valuable for characterizing bonds. Translation stages were incorporated into the system to allow scanning of objects. Linear scans were performed, and work is proceeding to allow automated 2-D scans. Modifications were made to the system during the course of the year. These modifications are aimed at making the system more robust and user-friendly. It is anticipated that more modifications will be suggested as operators get more experience and think of ways to improve the system further.

Related References

1. Huber, H., D. J. Chinn, O. O. Balogun, and T. W. Murray, "High-Frequency Laser-Based Ultrasound," *Review of Progress in Quantitative Nondestructive Evaluation,* D. O. Thompson and D. E. Chimenti, Eds., American Institute of Physics, Melville, New York, pp. 218-224, 2005.

2. Martz, H. E., and G. F. Albrecht, "Nondestructive Characterization Technologies for Metrology of Micro/Mesoscale Assemblies," *Proceedings of: Machines and Processes for Micro-scale and Meso-scale Fabrication, Metrology, and Assembly,* ASPE Winter Topical Meeting, Gainesville, Florida, January 22-23, pp.131-141, 2003.

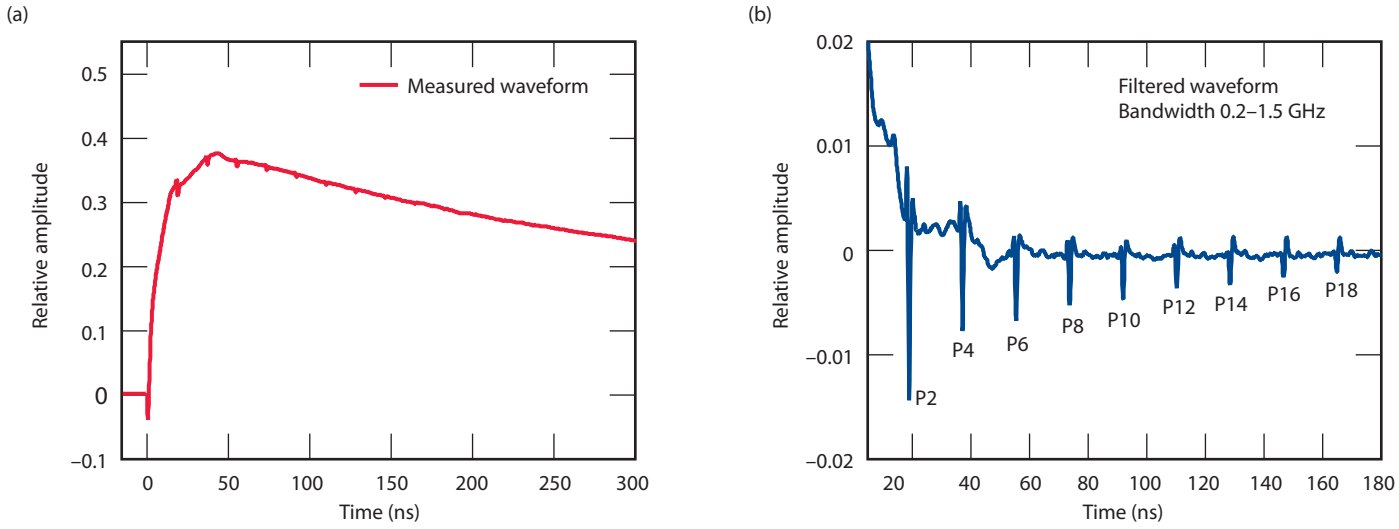

Figure 2. (a) Raw and (b) filtered waveforms on 25-mm-thick Au foil.

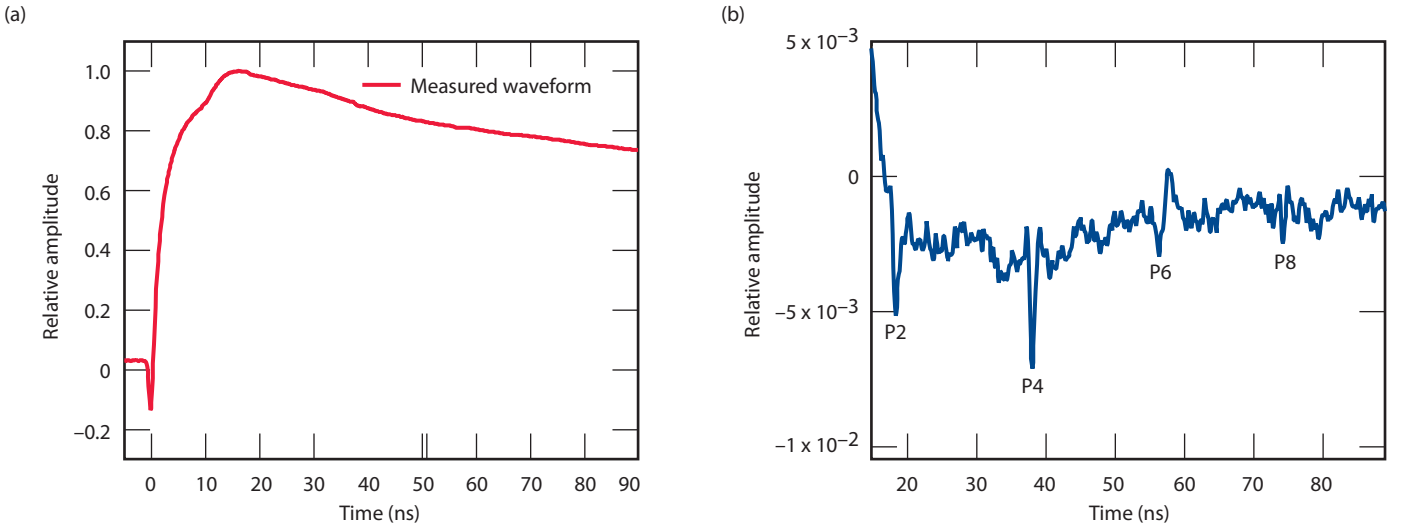

Figure 3. (a) Raw and (b) filtered waveforms on Al-Cu bonded sample.

VisIt for NDE: Real-Time Visualization for Large NDE Data Sets

John D. Sain
(925) 422-3409
sain1@llnl.gov

LLNL's Center for Nondestructive Characterization (CNDC) needs a tool to provide fast, real-time, 3-D visualization of feature metrology within very large data sets. Considerable resources have been spent increasing the spatial resolution and, therefore, the size of NDE data sets. Current data sets typically range in size from 4 GB (1 voxel) to 108 GB (27 voxels), and future data sets will be 2 TB (512 voxels). Visualization of such data is currently performed off-line and can take days or weeks to complete. VisIt is a real-time, 3-D visualization and quantitative analysis software tool that can use parallel processing machines on multiple platforms to visualize large data sets in seconds or minutes. We explored the capabilities of VisIt with the intent to facilitate its application to very large NDE data sets.

Project Goals

The project goals were to:

1. verify that features for NDE visualization are available in VisIt by operating on small computed tomography (CT) data sets;
2. test for limitations of visualization of large data sets;
3. write a graphical user interface or scripts incorporating visualization features relevant to NDE data; and
4. demonstrate VisIt to NDE users to stimulate interest and obtain feedback about desired features.

Relevance to LLNL Mission

The project addresses LLNL's need for non-contact dimensional metrology of millimeter-sized 3-D structures (HEDS and ICF target requirements), and highly improved imaging, processing, and analyzing methods that are applicable to large-size data sets ranging from terabytes to petabytes. The project also supports LLNL's engineering core competencies in nondestructive characterization and signal/image processing and control.

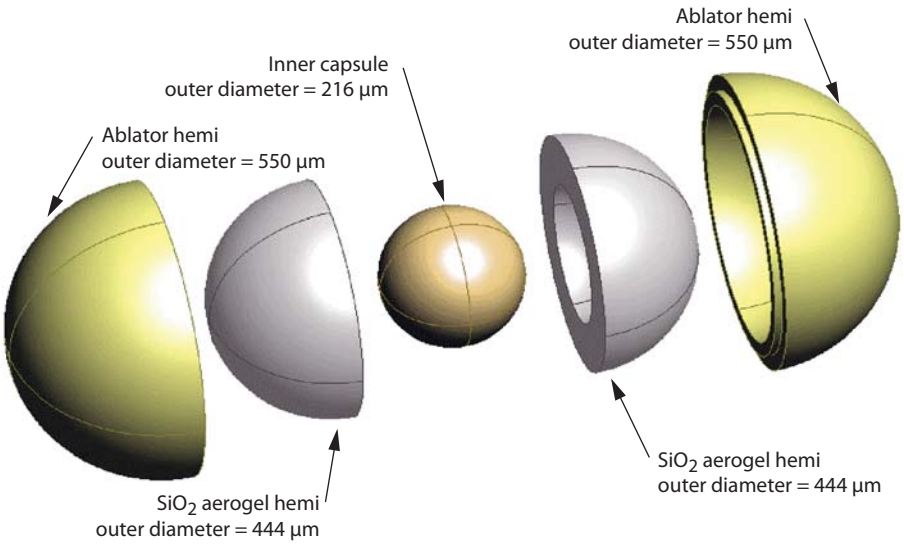

Figure 1. Schematic of the components that make up a double-shell target. The target consists of an inner shell (or capsule), a two-piece spherical aerogel intermediary shell, and a two-piece spherical outer shell. The three elements are concentric, with the aerogel shell acting as a spacer between the inner shell and outer shell. There are zero to a minimum number of air gaps in the final assembly.

FY2006 Accomplishments and Results

A Windows-based PC platform for VisIt was set up for NDE data. Several CT data sets (128^3 to $1{,}200^3$ voxels in size) were placed locally on the PC and remotely on the Livermore Computing (LC) OCF file system. Visualizations of both local and remote data were performed. Figure 1 is a schematic of components of a double-sided shell target. Figure 2 is a sample volume rendering of a 512^3-voxel data set. The processing time for larger data sets and/or more complex operations decreased when LC machines were used. VisIt contains many useful features for NDE data applications such as:

1. viewing 3-D objects from any angle;
2. slicing data sets with planes oriented in any direction;
3. manipulating threshold and opacity levels to view object features within the context of the whole data set;
4. extracting line-outs of data values; and
5. performing quantitative analyses.

Visualization of data is constrained by the number of processors scheduled, length of time required, and region of interest desired. No limitations were encountered in this project. For example, visualization of the $1{,}200^3$-voxel data set was done using 64 to 256 processors, and LC maintains several machines with between 1-K and 4-K processors and even one ("Blue Gene") with 128-K processors. Large numbers of processors can be scheduled for visualization and/or analysis.

Some sample scripts were written to implement desired calculations. For example, one measures object sphericity and another determines boundary surfaces between materials of different attenuation.

Some attractive features of VisIt are:

1. the ability to perform remote desktop visualization of data stored on LC OCF/SCF file systems;
2. visualization of multiple materials in a single view using opacity control;
3. real-time analysis of metrology information; and
4. comparative overlaying of CT data with data generated by other means.

Some desired features for VisIt are:

1. scripts for concentricity and wall thickness of nested spherical shells;
2. "fly-through" movies with opacity control; and
3. hierarchal data structures that permit high-resolution "close-ups" of subsets of coarsely-sampled data sets.

Related References

1. Childs, H., E. Brugger, K. Bonnell, J. Meredith, M. Miller, B. Whitlock, and N. Max, "A Contract Based System for Large Data Visualization," *Proceedings of IEEE Visualization*, 2005.

2. Brown, W. D., and H. E. Martz, Jr., "X-ray Digital Radiography and Computed Tomography of ICF and HEDP Materials, Subassemblies and Targets," *Digital Imaginig IX, An ASNT® Topical Conference*, Mashantucket, Connecticut, July 24-26, 2006.

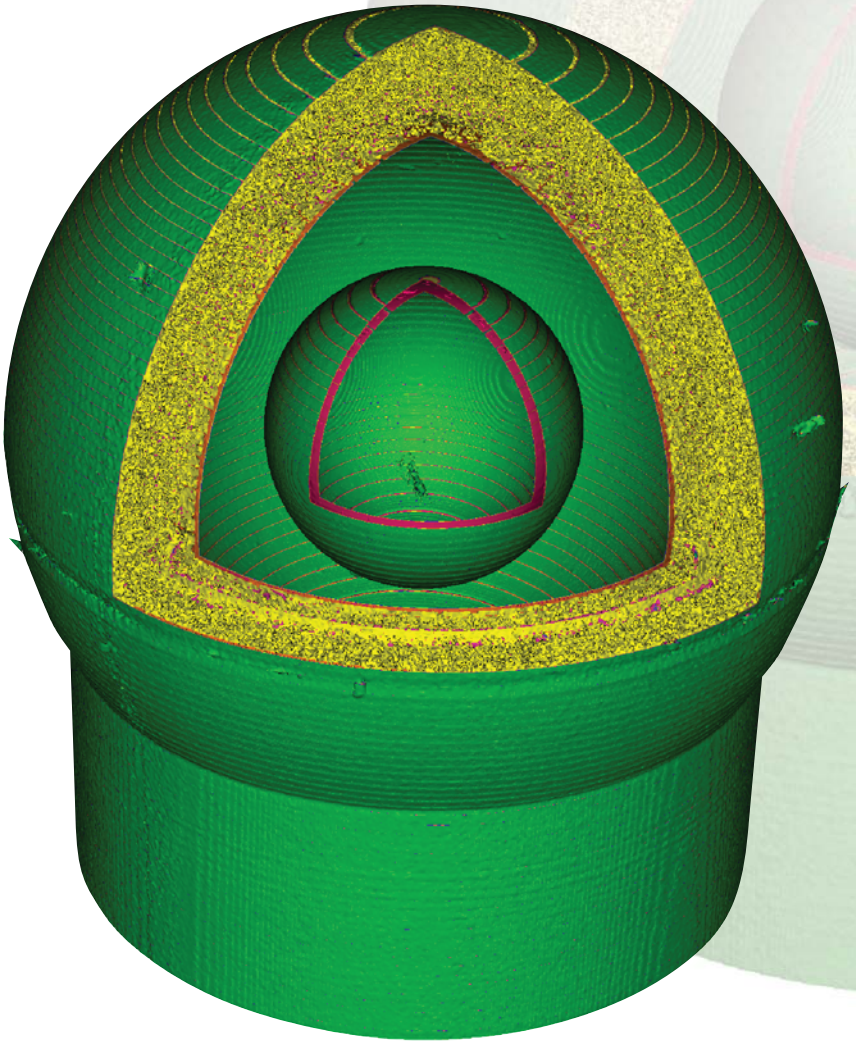

Figure 2. VisIt volume rendering of a real double-shell target (as depicted in Fig. 1) while still mounted on its manufacturing pedestal. The rendering is of a 512^3-voxel CT data set. The cutaway view provides a look inside both the inner and outer shells. The aerogel material has been removed from view via thresholding.

X-Ray System Characterization

William D. Brown
(925) 422-7933
brown197@llnl.gov

We are implementing a forward model for x-ray system response that will enable us to predict the capability of our systems and allow us to choose optimal system parameters. The system model will include four components of the x-ray systems: source, transport, x-ray scattering, and detector. The components will be used in conjunction with the LLNL HADES program to model the x-ray system.

Project Goals

The overall project goal is to model the four components of the micro-XCT Xradia system. For FY2006, we focused on modeling the 150-kV Hamamatsu microfocus x-ray source. In FY2007, we will work on models for transport, scatter, and detection.

Relevance to LLNL Mission

A forward model for system response will enable us to better perform experiments for DNT, NIF and NHI.

FY2006 Accomplishments and Results

Our approach included coding of spectral algorithms and comparison of the algorithms with known empirical results. The first task was to validate a National Bureau of Standards x-ray source code called "Tubdet." Tubdet was originally implemented at LLNL on a VAX and ported to the Macintosh II in Absoft FORTRAN®. The latter version was used to evaluate Tubdet's performance on selected spectra. Comparing Tubdet to experimental spectra showed an overemphasis of the low-energy continuum and characteristic lines in the

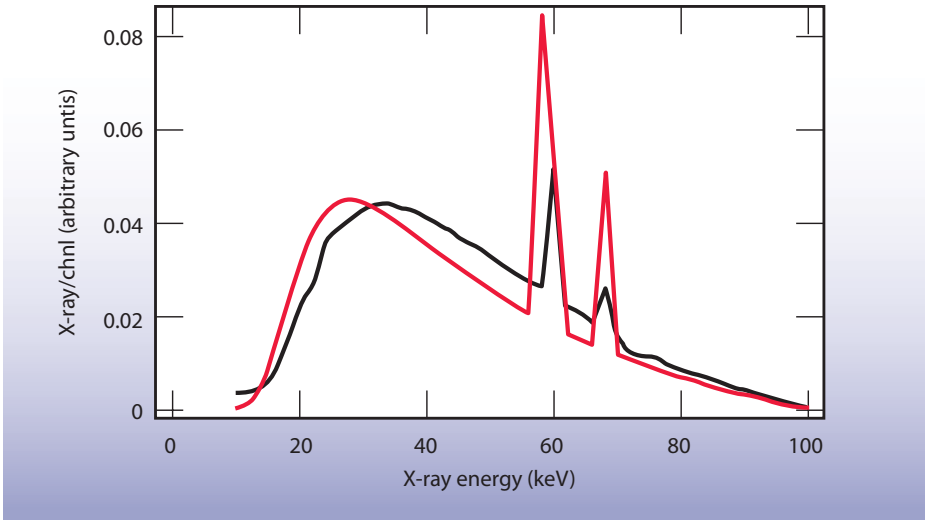

Figure 1. A Tubdet model spectrum (red) compared to an experimental spectrum. The overemphasis of low-energy continuum and very strong characteristic lines are typical of the Tubdet performance.

Tubdet-generated spectra. Figure 1 is a comparison of a Tubdet model spectrum and an experimental spectrum taken from a Toshiba x-ray tube head with 1.2-mm Al inherent filtration. Because of the poor match between the Tubdet model and the experimental data, Tubdet was determined not to be a good choice for modeling tube spectra.

We then changed our focus to two other models, Ebel and Finkelshtein. The names of the models refer to the first authors of the papers. Both models include separate descriptions of the generation of Brehmsstrahlung and characteristic lines within the material and the attenuation of the x-radiation on transport to the surface. We implemented the Brehmsstrahlung models of Ebel and Finkelshtein in Mathematica. Figures 2 and 3 show a comparison of the continuum models with the experimental data from a Machlett x-ray source. The model data has been filtered to match the attenuation of the 2.7-mm Al filtration of the Machlett tube. Both models appear to provide excellent spectral shapes for the continuum up to 120 kV.

Next, we focused our efforts on modeling the continuum with the characteristic lines of the spectra. Here we implemented the Ebel and Finkelshtein characteristic-line algorithms to generate the spectra. We compared the models with a selection of experimental data with differing characteristics lines (K and L), and anodes (Cu, Mo, W, and Au). Neither of the models consistently matched absolute intensity measurements. Model to experimental intensity ratios varied from 10% to 300% too high and the ratio of characteristics lines to the continuum varied by a factor of two.

Related References

1. Tao, G. Y., P. A. Pella, R. M. Rousseau, "NBSGSC—A FORTRAN Program for Quantitative X-Ray Fluorescence Analysis," NBS Technical Note 1213, April 1985.
2. Bhat, M., and J. Pattison, *et al.*, "Diagnostic X-Ray Spectra: A Comparison of Spectra Generated by Different Computational Methods with a Measured Spectrum," *Med. Phys.*, **25**, January 1998.
3. Ebel, H., "X-Ray Tube Spectra," *X-Ray Spectrometry*, **28**, pp. 255–266, 1999.
4. Finkelshtein, A. L., and T. O. Pavlova, "Calculation of X-Ray Tube Spectral Distributions," *X-Ray Spectrometry*, **28**, pp. 27–32, 1999.
5. Fewell, T. R., R. E. Shuping, and K. R. Hawkins, Handbook of Computed Tomography X-ray Spectra, Bureau of Radiological Health, U.S. Dept. of Health and Human Services, Rockville, Maryland, April 1981.

FY2007 Proposed Work

In FY2007, we will continue our work of modeling the source and begin work on a methodology to model the detector. The detector consists of a CsI scintillator mounted to a microscope objective. The scintillator/objective is optically coupled to a scientific grade charged-couple device. Each component of the detector will need to be modeled for an overall detector model. We will also include existing transport codes and x-ray scatter models to complete the model methodology for the four components. We will use HADES to generate an overall model of the system.

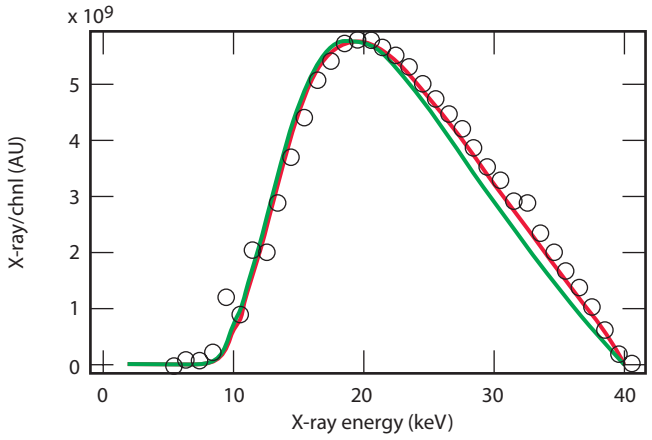

Figure 2. Measured spectra data (circles) compared to Ebel (red) and Finkelshtein (green) models at 40 kV. Measured data from Fewell handbook.

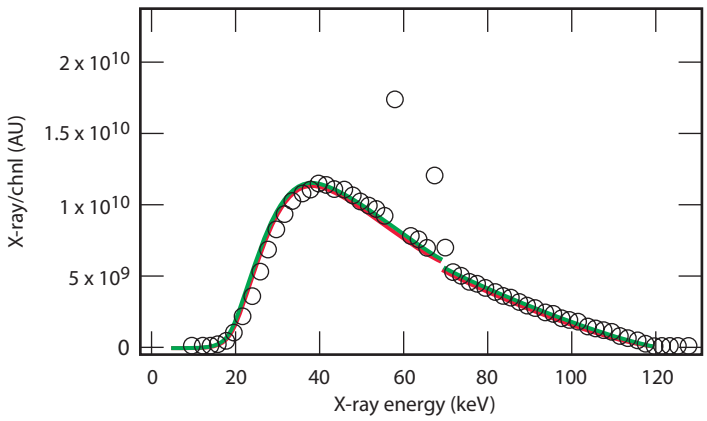

Figure 3. Measured spectra data (circles) compared to Ebel (red) and Finkelshtein (green) models at 120 kV. Measured data from Fewell handbook.

Computed Tomography Reconstruction Codes

John D. Sain
(925) 422-3409
sain1@llnl.gov

The code, CCG-LCONE (for constrained-conjugate gradient for large-angle cone beam), has been used in LLNL's nondestructive evaluation work for a number of years. Code documentation has been needed to provide users and programmers with a guide to its theory and structure. This report, originally authored by LLNL retiree Jessie A. Jackson, presents a summary of the code and its documentation.

Project Goals

This project was to document the code CCG-LCONE, an x-ray reconstruction tool.

Relevance to LLNL Mission

An expanded x-ray computed tomography (CT) reconstruction tool set will benefit several LLNL programs, including the study of explosive samples for DoD and DOE, high-energy-density physics for DNT, and surveillance of weapons components. Code documentation furthers this usefulness.

FY2006 Accomplishments and Results

We have completed the report, "CCG-LCONE, CT Reconstruction Code, User and Programmer's Guide," which documents the theory behind parts of the code and the structure of the code. It functions as both a user's guide and a programmer's guide.

CCG-LCONE is used to reconstruct objects from images acquired on cone-beam radiographic systems.

There are many CT techniques to create reconstructed objects. These methods consist of processing the projection data by filtering, scaling and/or

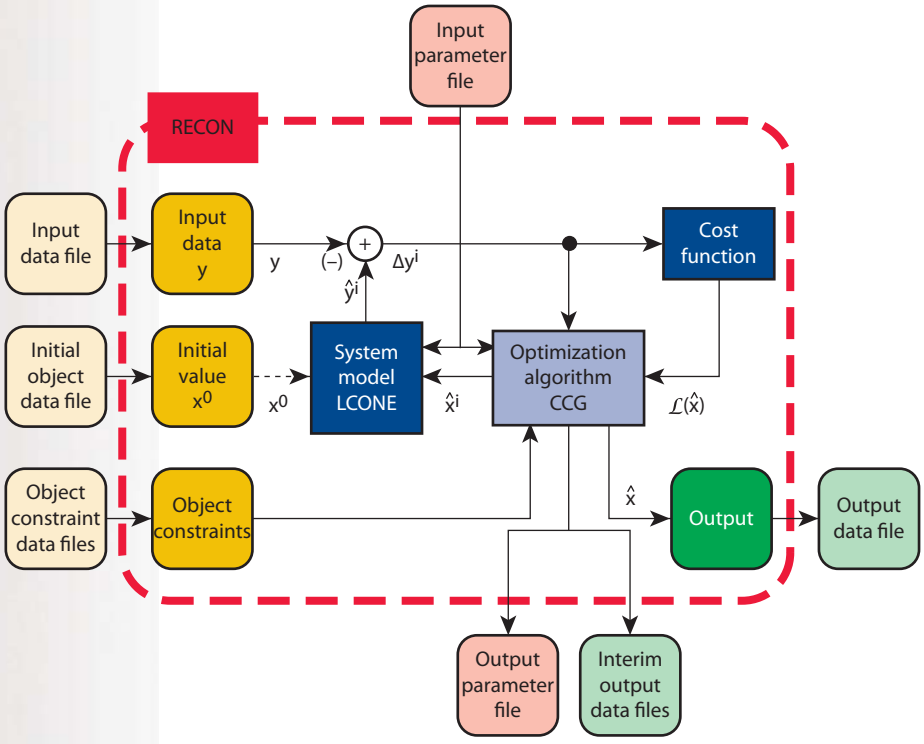

Figure 1. RECON-CCG-LCONE model.

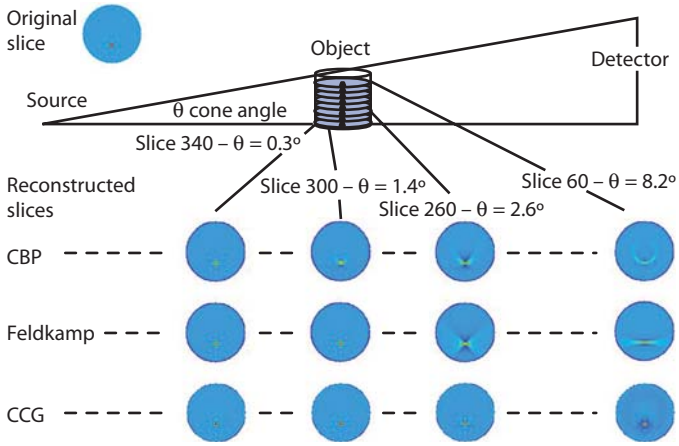

Figure 2. Large cone angle simulated cone-beam reconstruction comparison.

FFTs, and then essentially backprojecting and summing the data. These methods include Filtered Backprojection (FBP), Convoluted Backprojection (CBP), and the Feldkamp Algorithm. FBP and CBP are designed to work on systems with parallel and fan beams, respectively. These beams pass through only one slice of an object. Processing speeds for these methods are generally reasonable even for large detectors. Also the slices can be processed in parallel, further reducing the overall processing time.

Cone-beam systems are more complicated. In a cone-beam system the beam can pass through a number of object slices. FBP and CBP are not designed to work for this case. The Feldkamp algorithm was developed for cone-beam geometries. However, for the sake of speed and memory it makes certain simplifying assumptions, as a result it works reasonably well for small cone angles but it is less effective for larger cone angles.

To provide a method that would produce a more accurate reconstruction for large cone angles an iterative, optimization, cone-beam system was created. The Constrained Conjugate Gradient (CCG) method was selected as the optimization algorithm in combination with a least-squares cost function. A Linear Cone-Beam (LCONE) ray-path system model was created. In fact, a number of different ray-path models have been created in an effort to improve the processing speed. The latest ray-path model based on a polar coordinated system has proved quite effective.

A number of years ago LLNL's NDE staff developed a suite of reconstruction codes called RECON. Included in the system were routines for reading and writing parameter files, known as SCT files, and routines for reading and writing data files in the VIEW file format. CCG-LCONE was created within this system. Figure 1 shows the CCG_LCONE iterative optimization system within RECON.

CCG-LCONE has proved to be effective for cone-beam CT problems. Figure 2 shows a comparison of simulated results for different algorithms. At four different cone angles the reconstruction results are shown for CBP, Feldkamp and CCG-LCONE. CCG-LCONE obviously out performs CBP and Feldkamp.

CCG-LCONE is, however, slow and memory intensive, so it has been generally used only in special cases. One case where it has been effective is in neutron imaging. Neutrons produce noisy data, since they are heavy particles and cause a great deal of scattering. CCG-LCONE has been effective in processing this data, as shown in Fig. 3.

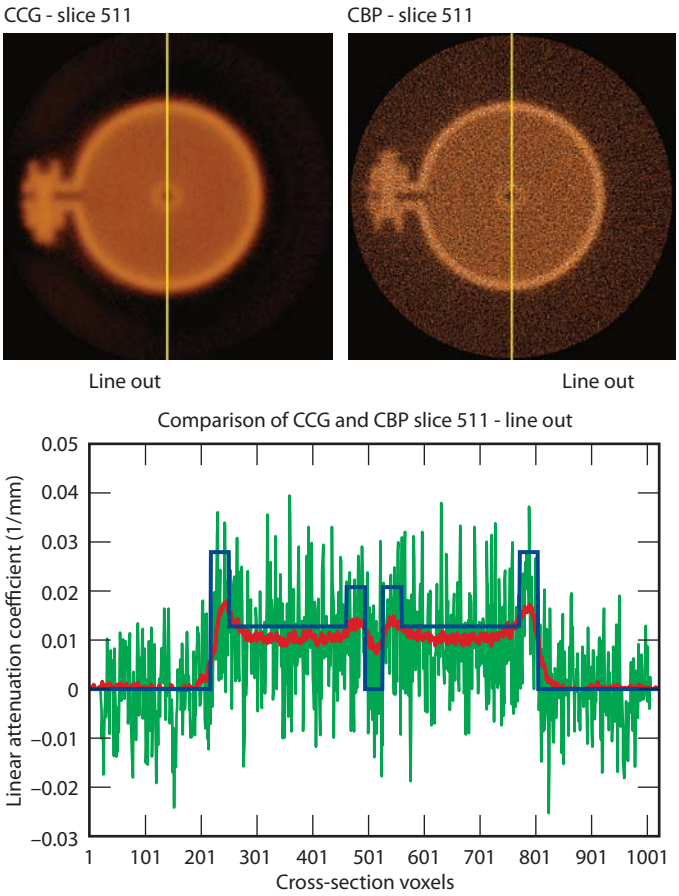

Figure 3. CCG-LCONE (red) and CBP (green) reconstruction comparison for neutron imaging.

Super-Resolution Algorithms for Ultrasonic NDE Imaging

Grace Clark
(925) 423-9759
clark9@llnl.gov

Generally, one of the major desired results from a nondestructive evaluation (NDE) test of a mechanical part is a segmented image or image cube showing the locations and physical characteristics of cracks, inclusions, voids, delaminations, ablations, and other flaws. A key NDE goal is to obtain images having the best possible spatio-temporal resolution. Unfortunately, the resolution of all ultrasonic measurements is severely limited by the inherent fundamental band-limited spectral transfer function of ultrasonic transducers, the uncertainty principle, and the diffraction limit. In the time domain, the transducer causes severe ringing that can limit resolution.

Previous studies have shown that this ringing can be mitigated by solving an ill-posed and ill-conditioned inverse problem. The solution uses several constraints to regularize the ill-posed problem. The algorithm consists of two steps: 1) Optimal Least Squares System Identification (Wiener) to estimate the impulse response of the material under test, given the available transducer bandwidth; and 2) Bandlimited Spectrum Extrapolation (BSE) using constrained analytic continuation to expand the available bandwidth and improve spatio-temporal resolution.

Project Goals

The goal of this project is to implement BSE in combination with the Wiener algorithm in a user-accessible form to provide an important new ultrasonics super-resolution software tool for NDE. We will 1) implement the super-resolution algorithms for processing signals (A-scans), images (B-scans), and 3-D volumes (multiple

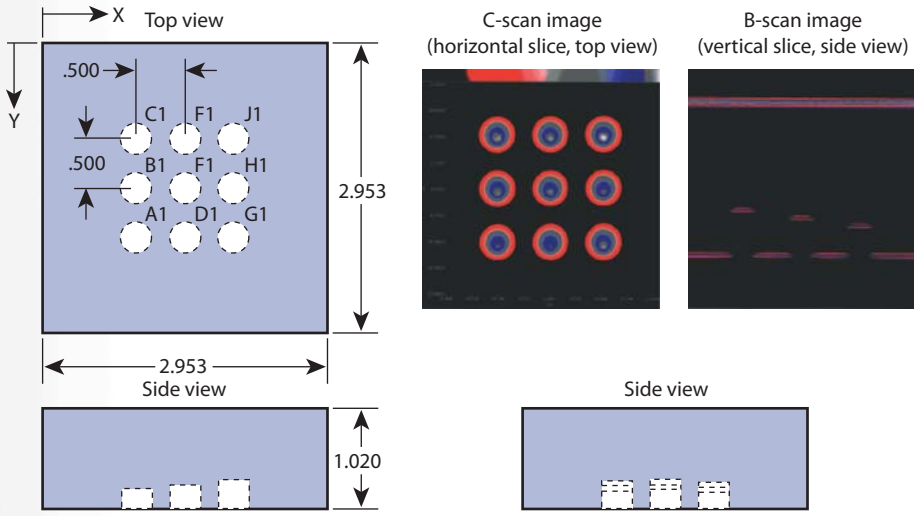

Figure 1. Line drawings (top and side views) and images of an Al block insonified with ultrasound in a water bath. The transducer was raster-scanned across the top surface in multi-monostatic mode. The drilled flat-bottom holes are apparent in the top and side views. Tape was placed over the back of the holes to prevent water from entering. The B-scan represents a vertical slice through the volume. The C-scan represents a horizontal slice through the volume. The B-scan shows the front surface of the Al block at the top, the top surface of the holes in the middle, and the back surface of the block at the bottom. It can be seen from the B-scan that the spatio-temporal resolution (multi-colored lines) is compromised by the transducer ringing.

B-scans); and 2) publish results of validation tests using simulated data and existing programmatic data.

Relevance to LLNL Mission

Resolution enhancement will directly benefit all LLNL programs that require ultrasonic imaging tests. Our project also has been useful in improving the results from time-domain reflectometry for a weapons program.

FY2006 Accomplishments and Results

This is the second year of a two-year project. All of the proposed deliverables have been produced:

1. a MATLAB implementation of the algorithms, complete with a Graphical User Interface (GUI);
2. algorithm validation tests with simulated signals;
3. algorithm validation tests with real programmatic data sets: a) an aluminum block containing known flat-bottom holes; b) a known "phantom" object consisting of concentric cylinders of various materials for sensor fusion studies with ultrasound and x-ray computed tomography; c) ultrasonic multi-monostatic data set for the Stanford Geophysical Exploration Project; d) electromagnetic time-domain reflectometry (TDR) signals for the stockpile stewardship project;
4. a report describing the algorithms, and user information for the software; and
5. technical papers describing the work.

Even greater benefit can be realized in applications in which the raw reflection wavelets are superimposed, as in thickness measurements for very thin layers; *i.e.*, adhesive thickness measurements. Here, the super-resolution algorithms can separate the reflections in time/distance.

An aluminum block (Fig. 1) with flat bottom holes is used to show the improvements obtained using the super-resolution algorithms. With respect to Fig. 2, the original data show low resolution, as the transducer ringing causes the surface edges to appear broad and unclear. The system identification (Wiener) results improve the resolution somewhat, but only within the limits of the transducer bandwidth. The Wiener plus BSE results show that the surface edges have been delineated clearly as sharp impulses. This is the desired resolution enhancement.

Related References

1. Clark, G. A., D. M. Tilly, and W. D. Cook, "Ultrasonic Signal/Image Restoration for Quantitative NDE," *NDT International*, **19**, 3, June 1986.

2. Papoulis, A., and C. Chamzas, "Improvement of Range Resolution by Spectral Extrapolation," *Ultrasonic Imaging* **1**, pp. 121-135, 1979.

3. Clark, G. A., and J. A. Jackson, "Super-Resolution Algorithms for Ultrasonic Nondestructive Evaluation Imagery," *4th Joint Meeting of the Acoustical Society of America and Acoustical Society of Japan*, Honolulu, Hawaii, November 28 – December 2, 2006.

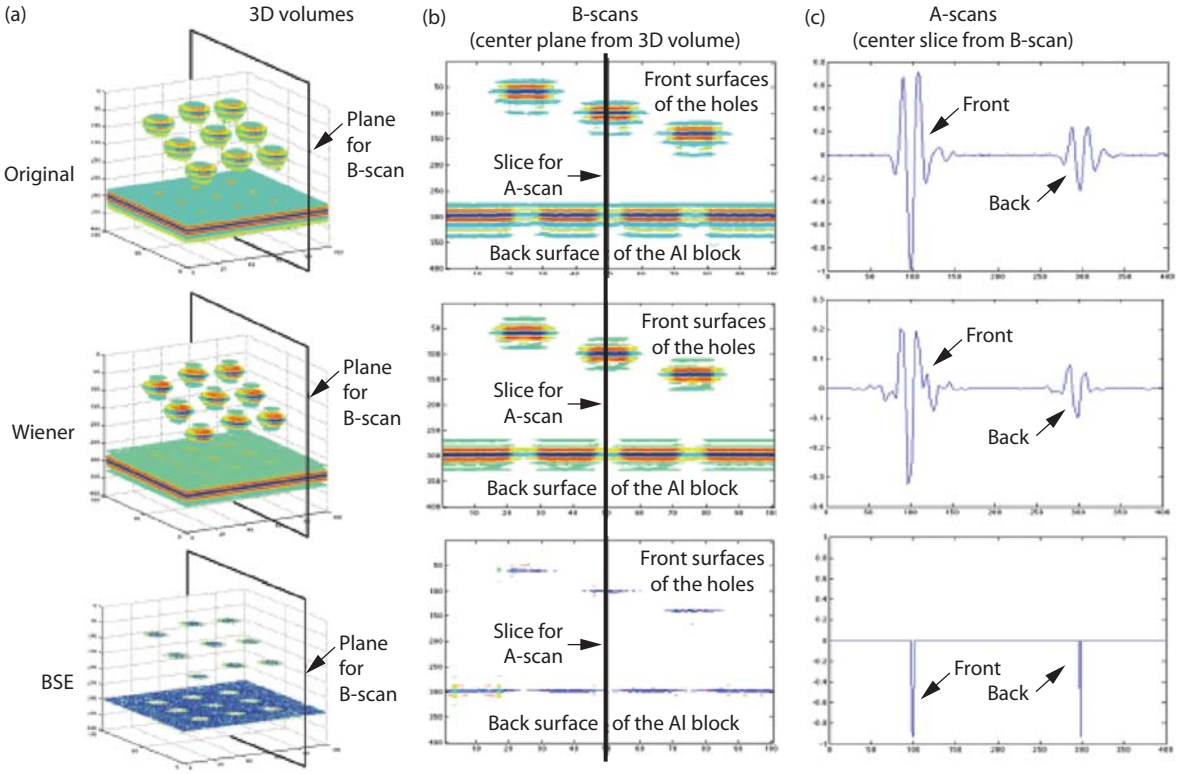

Figure 2. Processing results for experiments with the Al block in Fig. 1. Ultrasonic 3-D volume data are used. (a) Original (raw) 3-D volume, the system identification results (Wiener), and the Wiener plus BSE results. (b) Corresponding results for the B-scan (2-D vertical image (slice) depicted by the planes in (a). (c) Processing results for a single signal (A-scan) selected from the corresponding B-scans (b).

Defect Detection in Large CT Image Sets

Douglas N. Poland
(925) 422-4980
poland1@llnl.gov

This image analysis project is constructing a tool for performing computer-assisted detection of small voids in computed tomography (CT) data sets. The focus of year one is to identify candidate algorithms and demonstrate satisfactory performance on a test object. The test object is a tungsten ring with various holes on its inner circumference. The approaches being evaluated are mathematical morphology (MM) algorithms that operate on the CT datasets, model-based matching algorithms that operate on the sinograms (before reconstruction), and combinations of these two. In year two the focus will shift to implementing the proven algorithmic approach within a software platform with existing data management and visualization capabilities. Potential platforms include VisIt, ImageRec (currently used for reconstruction and analysis of programmatic CT data) and Image Content Engine (ICE).

Project Goals

The enhanced surveillance program requires CT datasets that are up to several thousand voxels on a side (*i.e.*, 8000 x 8000 x 8000). The current method of analysis requires a tomographer to view sequences of several thousand images, where each image occupies several computer screens at full resolution. The goal of this project is to create a tool that will reduce these datasets to a ranked set

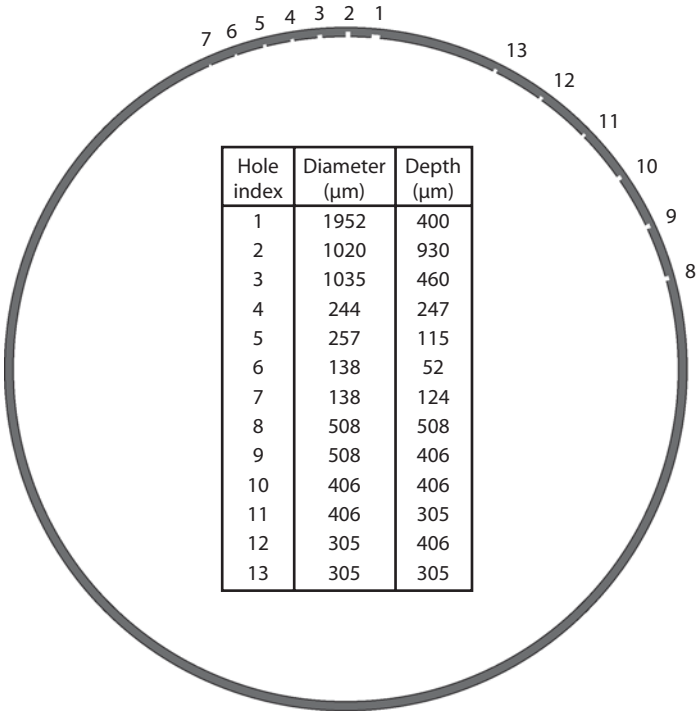

Hole index	Diameter (µm)	Depth (µm)
1	1952	400
2	1020	930
3	1035	460
4	244	247
5	257	115
6	138	52
7	138	124
8	508	508
9	508	406
10	406	406
11	406	305
12	305	406
13	305	305

Figure 1. Tungsten ring test object with 13 holes drilled into its inner surface. This cutaway sketch shows the hole locations, while the table lists their sizes. Note that in the images used for this work, holes #4 through #7 are very difficult to impossible to detect manually; they are not found by our algorithms.

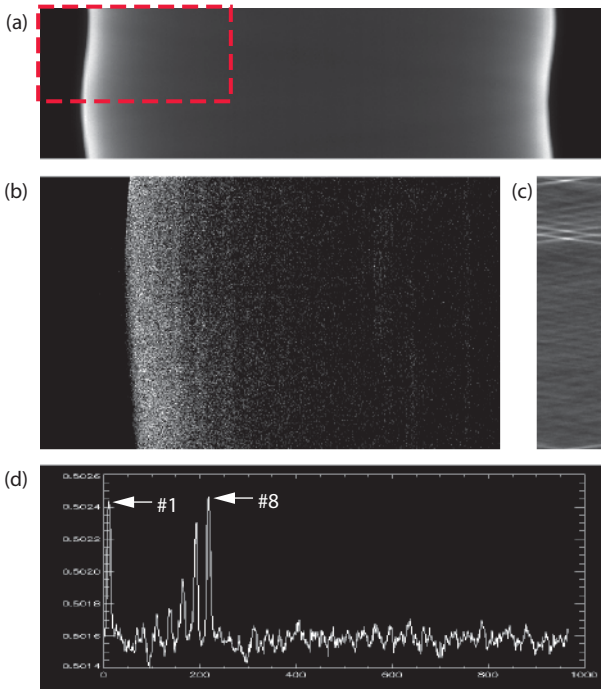

Figure 2. GDM/sinogram processing of tungsten ring. (a) Unprocessed sinogram (outlined segment is shown in (b) after processing). (b) Portion of processed sinogram. (c) Match surface output from GDM algorithm. Brightness corresponds to degree of match to sinusoid of a given phase and amplitude. (d) Final GDM output, with peaks corresponding to holes #1 and #8 labeled. To the left of #8 are seen the peaks corresponding to holes #9 through #13 (the latter disappearing into the noise).

of candidate voids that can be quickly validated or rejected by the tomographer and possibly even program personnel.

The enhanced surveillance program has produced a tungsten ring with surrogate defects drilled into it (Fig. 1) for use in studying the ability of their systems and analysts to detect this class of defects. Of the 13 holes in this ring, 9 (ranging from 305 to over 1000 µm) are well resolved by the CT system and are readily discernible in the processed CT data (the remaining 4 are less than 300 µm in diameter); one key success metric is that our algorithm must place these 9 voids at the top of our ranked list of candidate voids.

Relevance to LLNL Mission

This project will produce a tool that will increase the efficiency of enhanced surveillance program tomography analysts, allowing them to focus their attention on resolving ambiguous suspect voids (*i.e.*, voids less than 300 µm). This tool will provide a well characterized analytical package, ensuring uniform analysis of each region of these large data sets. This tool will also make these data sets more accessible to other technical staff, who may not be tomography experts, by performing necessary preprocessing and quickly guiding them to regions with suspect voids.

FY2006 Accomplishments and Results

CT scanning produces 2-D radiography projections and volumetric CT image data that can be viewed in many different ways. Our initial approach was to emulate a common strategy for leveraging these different data types: identify candidate voids in the CT data and then refer to the sinograms for corroboration. Sinograms are created by extracting a given row (elevation) from each radiograph in the sequence and stacking them, creating an image in which voids form a distinct sinusoid pattern due to the rotation of the object during imaging. We looked for these sinusoid patterns using the Gradient Direction Matching (GDM) algorithm created through the ICE, a powerful model-based matching tool (Fig. 2). This approach was attractive due to the success of GDM in similar problems and the fact that it does not require image reconstruction. The results reveal that this method was able to identify 8 holes, the smallest of these being #12 (305 µm x 406 µm).

Once the CT image reconstruction is performed, we looked for defects in either 2-D image slices or 3-D volumes. We searched for localized bright (inclusions) or dark (voids) regions indicative of defects in these data using MM filters and tophat reconstruction (Fig. 3). Based on max/min operations in a local neighborhood, MM filters are nonlinear, and use a shape sensitive "structure element." They can solve many problems not amenable to solution by classical linear filtering methods. The results reveal that this method was able to identify 9 holes, the smallest of these being #13 (305 µm x 305 µm).

Using both simulated and real data, we implemented and evaluated these approaches. We found that the MM/CT approach is more robust for these data sets due to the low sinogram SNR associated with small defects. The MM algorithm on 3-D CT data successfully ranks all 9 target holes (≥ 300 µm in diameter) in the tungsten ring dataset at the top of the candidate void list. This was accomplished with fewer false alarms than the sinogram processing, thus the initial finding is that MM processing alone is the most effective algorithm. There is still promise that GDM/sinogram analysis could be developed as a confirmatory tool for MM/CT, and that combining their results in this way could lead to a more robust and sensitive algorithm. This must be left for future work.

Related References

1. Paglieroni, D. W., W. G. Eppler and D. N. Poland, "Phase Sensitive Cueing for 3D Objects in Overhead Images," *SPIE Defense and Security Symposium: Signal Processing, Sensor Fusion and Target Recognition XIV, Proc. SPIE*, **5809**, pp. 431-442, Orlando Florida, March 2005.

2. Brase, J. M., D. W. Paglieroni, D. N. Poland, G. F. Weinert, C. W. Grant, A. S. Lopez, and S. Nikolaev, "Image Content Engine (ICE): A System for Fast Image Database Searches," *SPIE Defense and Security Symposium: Optics and Photonics in Global Homeland Security, Proc. SPIE*, **5781**, pp. 150-154, Orlando, Florida, March 2005.

3. Serra, J., Image Analysis and Mathematical Morphology, Academic Press, New York, New York, 1982.

FY2007 Proposed Work

We are in the process of quantifying the performance of the MM algorithm using real weapon component CT data, and will then implement automated parameter selection (*e.g.*, automated thresholding based on global and local statistics). The final steps will be algorithm integration and a report on future work.

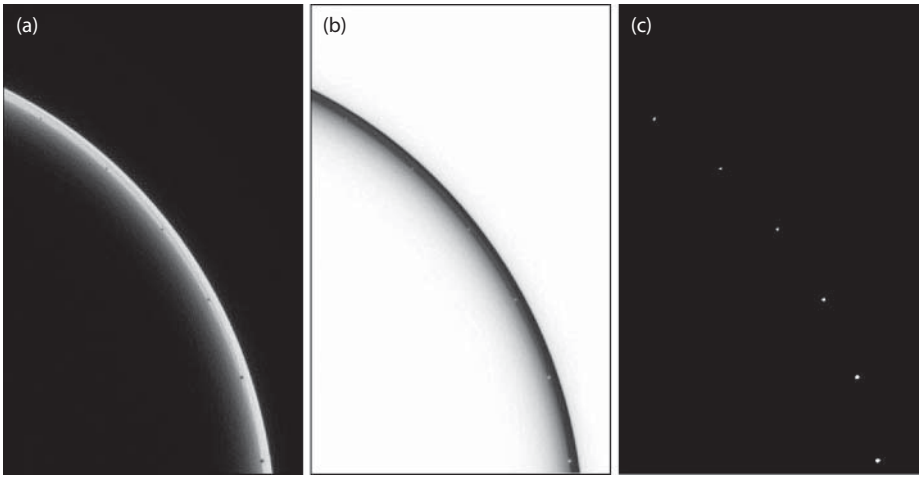

Figure 3. MM/CT processing of tungsten ring. (a) Individual reconstructed CT image slice containing holes #8 through #13 (ranging from 508 µm to 305 µm diameter). (b) Result of applying MM alternating sequential filter and complementing the image. (c) Result of highlighting the voids after 3-D MM white tophat reconstruction and thresholding steps.

Nanobarometers: *In-Situ* Diagnostics for High-Pressure Experiments

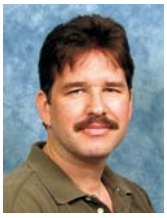

James S. Stölken
(925) 423-2234
stölken1@llnl.gov

The mechanistic understanding of high-pressure phenomena requires the capability to probe the local material response at high spatial resolution using experiments with complex loading history. Such experiments rely heavily on computational simulations for the interpretation of local conditions such as temperature and pressure history. The development of an *in-situ* nanoscaled pressure sensor provides a means to assess the quality of these simulations through the direct measurement of local peak pressure and comparison with simulation.

The diagnostic developed under this project consists of nanoscale sensors that are imbedded within, or in contact with, the medium to be measured. They record the local peak pressure and may be read-out following the experiment using a variety of micro-spectroscopy techniques. The small size of the nanosensors, combined with low volume fractions, limits the influence of the sensors on the high-pressure phenomena being studied while allowing for high spatial resolution of the peak local pressure. Preliminary work indicates that the fabrication, deployment, and read-out of the nanoscale pressure sensors are possible. We are executing a comprehensive plan to explore the scale dependence, concentration limits, and pressure sensitivity of nanoscale pressure sensors. The final product shall be an *in-situ* nanoscale pressure sensing capability that has been calibrated over a wide range of pressures (from 30 to 300 kbar) and a range of deformation conditions from quasi-static to weak shocks. The development of an *in-situ*, nanoscale pressure sensor will provide both a valuable tool for many existing high-pressure applications and an enabling technology for new uses and novel experiments; thus complementing many existing Laboratory programs in nanoscale modeling, material failure and fracture, and laser-driven experiments. A natural extension would be to design new materials to extend the useful pressure range of the proposed sensors to both lower and higher pressures.

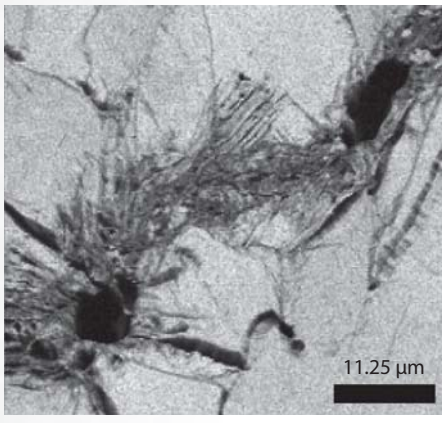

Figure 1. Micrograph of incipiently spalled and recompressed copper sample.

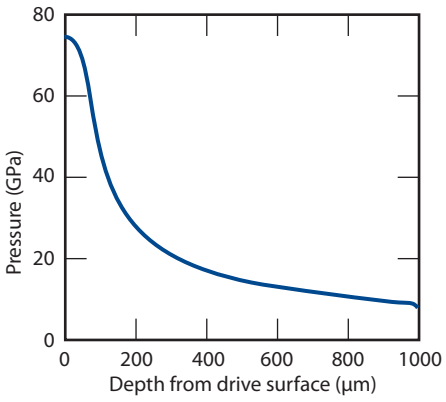

Figure 2. Computed peak pressure profile due to a laser-driven shock.

Project Goals

The project goal is to develop an *in-situ* diagnostic for high-pressure experiments capable of providing local peak pressure information at high resolution (<1 μm) and over a broad range of pressure (30 to 300 kbar). Key issues to be addressed shall include calibration and sensitivity analysis of the nanosensors to quasi-static conditions. Major goals of the proposed research are to quantify the extent of pressure induced changes in the sensor material, determine their dependence on sensor size, and establish the sensitivity of pressure induced structural changes to static loading.

Relevance to LLNL Mission

The study of high-pressure phenomena is at the core of many DNT and NIF related programs, with many important applications in the range of a few hundred kilobars, such as fragmentation and spall. Such experiments rely heavily on computational simulations for the interpretation of local conditions such as temperature and pressure history. The development of an *in-situ* nanoscaled pressure sensor provides a means to assess the quality of these simulations through the direct measurement of local peak pressure and comparison with simulation. Such a capability is especially useful in laser-driven experiments with complex wave profiles and non-steady loading. The proposed nanosensors complement many existing Laboratory programs in multi-scale modeling, material failure and fracture, and laser-driven experiments. Potential application to three classes of experiments is envisioned: Quasi-Static Experiments in Bulk Materials, Unsteady Shocks in Bulk Materials, and High Explosives. From gas-gun and laser-driven experiments to Site 300 and NTS U1a test shots, there is a need for an accurate, local measure of material peak pressure.

FY2006 Accomplishments and Results

Figures 1-4 illustrate our results. A key question regarding the existence and nature of the densification mechanism in silica nanoparticles has been explored. The issue was whether or not the densification phenomena observed in bulk silica occurred in nanoparticles. Since the success of the entire project is predicated upon this, it was crucial to experimentally verify this assertion. The results of a series of Raman spectroscopy and diamond anvil experiments on silica nanoparticles are quite intriguing. The permanent shift in the Raman spectra is clearly visible, consistent with the published results in bulk silica glass. To the best of our knowledge, this is the first such measurement in nanoparticles as a function of particle size. Not unexpected is the dependence of the Raman shift upon the particle size, a key research question to be addressed by this project. Results obtained this last year show, as suspected, a clear change in the size dependence for the smallest particles (< 80 nm in Fig. 3). Note that each experimental point represents an entire sequence of spectra taken upon loading and unloading of each sample. As a consequence of the success of this year's experiments a record of invention has been filed and a preliminary patent is being pursued.

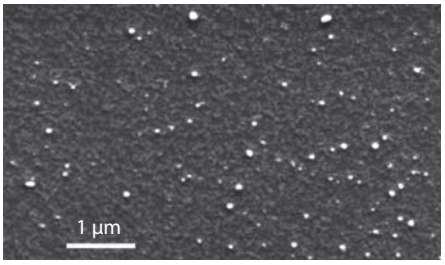

Figure 4. Micrograph of sub-micron silica sensors embedded in a copper matrix.

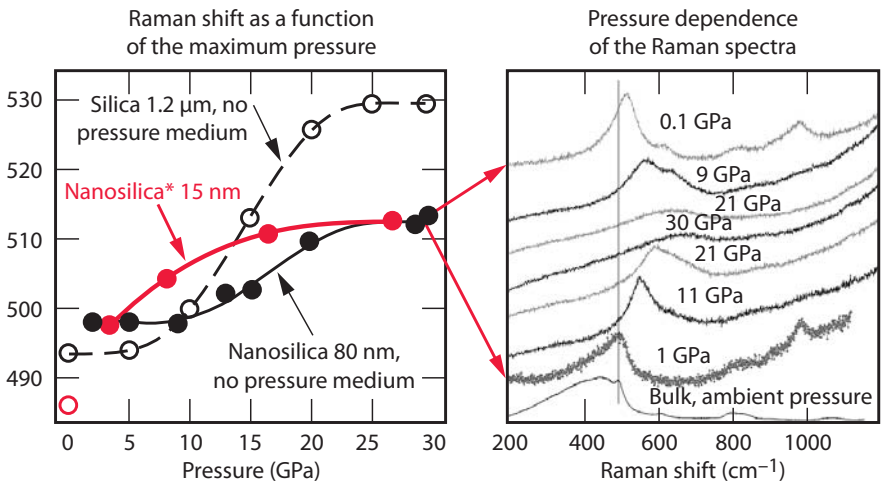

Figure 3. Permanent shift in Raman spectra as function of peak pressure and particle size (15, 80, and 1200 nm). 15 nm particles show distinctly different pressure dependence.

Related References

1. Brazhkin, V. V., and A. G. Lyapin, "High-Pressure Phase Transformations in Liquids and Amorphous Solids," *J. Phys. Condens. Matter,* **15,** 36, pp. 6059–6084, September 17, 2003.

2. Cowley, J. M., "Applications of Electron Nanodiffraction," *Micron,* **35,** 5, pp. 345-360, 2004.

3. Garvie, L. A. J., and P. R. Buseck, "Bonding in Silicates: Investigation of the Si L-2, L-3 Edge By Parallel Electron Energy-Loss Spectroscopy," *Amer. Mineralogist,* **84,** 5-6, pp. 946-964, May-June 1999.

4. Kubota, A., M. J. Caturla, J. S. Stölken, and M. D. Feit, "Densification of Fused Silica Due to Shock Waves and Its Implications for 351 nm Laser Induced Damage," *Optics Express,* **8,** 11, pp. 611-616, May 21, 2001.

5. Sugiura, H., R. Ikeda, K. Kondo, and T. Yamadaya, "Densified Silica Glass After Shock Compression," *J. Appl. Phys.*, **81,** 4, pp. 1651-1656, February 15, 1997.

Micro/ Nano-Devices and Structures

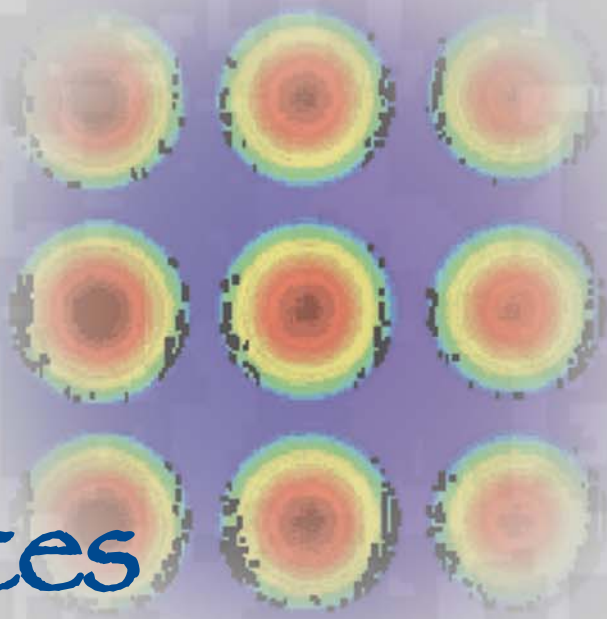

FY 06 Engineering Research and Technology Report

Rapid Defense Against the Next-Generation Biothreat

Raymond P. Mariella, Jr.
(925) 422-8905
mariella1@llnl.gov

Bioengineered and emerging pathogens represent a significant threat to human health. The best defense against a rapidly expanding pandemic is to isolate the pathogen quickly from biological samples so that it may be identified, characterized, and have treatments developed against it. The one persistent technology gap in the process of identifying and quantifying the presence of pathogenic agents has been sample handling and preparation that must precede any assay. Also, we need higher-performance, multiplex assays for families of rapidly-mutating RNA viruses.

Project Goals

The objective of this project is to replace burdensome, manual techniques for sample handling and preparation with new automated technologies. We use microfluidics with ultrasonics, electrophoretics, and dielectrophoretics to separate and purify viruses from biological and environmental samples. We will also create less costly, but more general multiplex assays for viruses, using multiplex, ligation-dependent probe amplification (MLPA).

Relevance to LLNL Mission

By making it possible to rapidly isolate and detect engineered and naturally emerging biothreats, this project contributes to the nation's defense against bioterrorism, which is central to LLNL's homeland security mission. In addition, this project supports LLNL's mission in bioscience to improve human health.

FY2006 Accomplishments and Results

In FY2006, we established a Bio-Safety Level 1 (BSL-1) lab in which we propagate the virus MS2 using the host bacterium *E. coli*. We developed harvesting and clean-up procedures of the MS2, as well as fluorescent staining techniques for this virus. Using microfluidic systems, we determined that the "gold standard" solution for handling

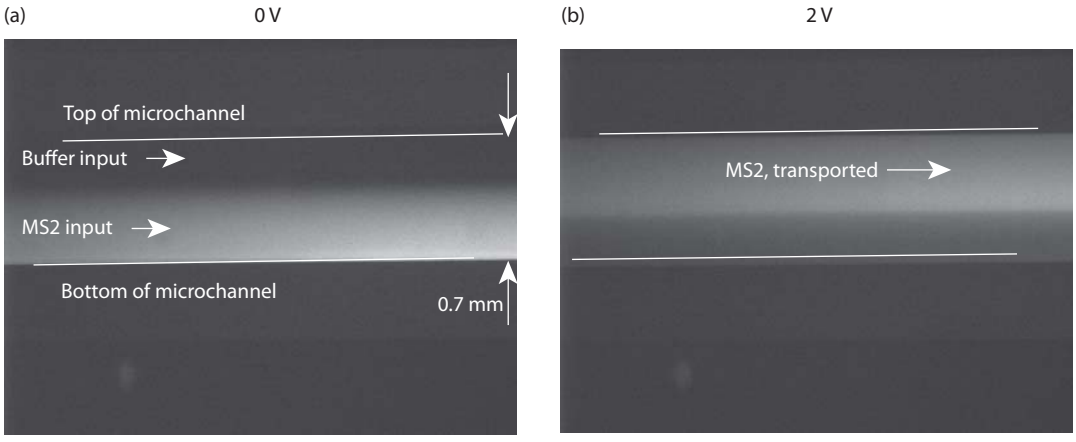

Figure 1. Monochrome photographs of a low-conductivity solution of fluorescently-labeled virus MS2, flowing in a microchannel with top and bottom electrodes (not seen). There are two solutions being introduced from the left of the channel: the upper solution is a clean buffer and the lower solution contains the labeled MS2. In the left-hand photograph, there is no voltage applied and the laminar flow and relatively low diffusivity of the MS2 confine the MS2 to the bottom half of the flow. In the right-hand photograph, with 2 V applied perpendicular to the flow, the MS2 has been almost entirely transported up into the buffer solution, as desired.

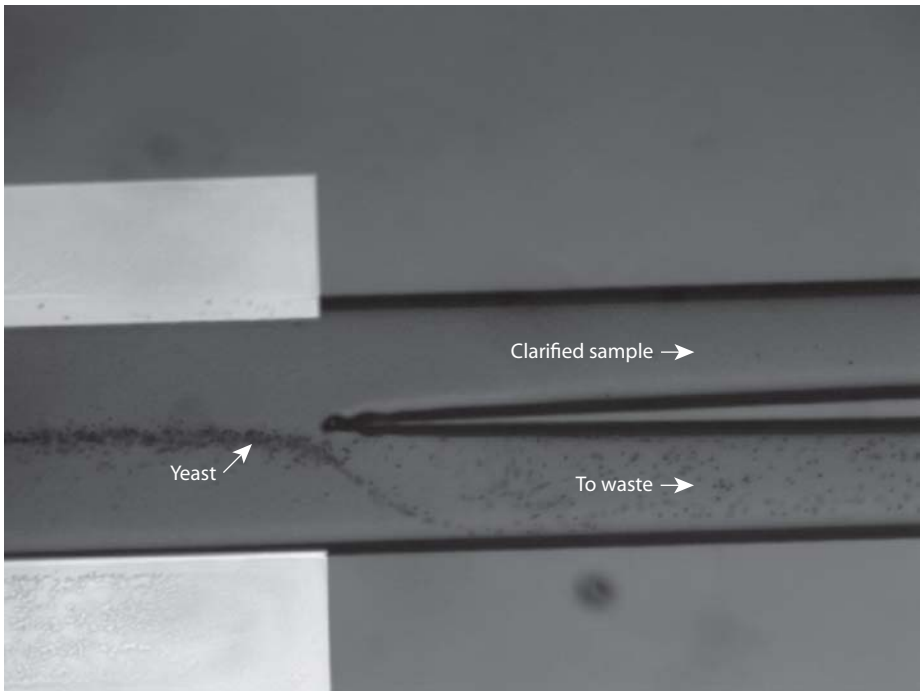

Figure 2. Photograph of yeast flowing in a 0.5-mm microchannel that has an ultrasonic standing wave, perpendicular to the image plane and running along the center of the flow channel. Ultrasonic transducer is outside of viewing area.

viruses, Viral Transport Medium, is incompatible with electrophoretic manipulations of particles, due to its high electrical conductivity. We developed a buffer exchange process that produced MS2 in solutions with conductivities below 0.1 mS. With this, we successfully transported MS2 in the manner desired (Fig. 1).

We also investigated the manipulation of baker's yeast (*S. cerevisiae*) as a model for human cells. In accordance with theory, the use of acoustic radiation pressure from an ultrasonic standing wave was easily able to transport suspended yeast cells, flowing in a microfluidic channel, in a matter of seconds over a distances of 100's of µm. Using an ultrasonic standing wave in a microchannel, we moved and confined the flowing yeast cells to the bottom half of the channel, so that it could be directed to the waste reservoir and not to the collection reservoir (Fig. 2).

Since receiving funding for this project, an MLPA protocol for rapid detection of viruses was successfully designed and tested using a combination of multiplex ligase-dependent PCR and suspension microarray (Luminex platform) detection of signal. Eight probe sets were tested in MLPA multiplex reaction with DNA target. Six of the eight probes were multiplexed with minimal effort. The assay was also able to detect target DNA despite the presence of mismatches in the probe sequences, indicating that the assay will tolerate the diversity characteristic of viral genomes. Conserved regions for all vertebrate-infecting viral families have been identified and will be used for subgroup-specific MLPA probe design. The protocol and probe design parameters are currently being optimized to increase multiplex depth and assay sensitivity.

We have also established collaborations with two of the world's leaders in virus discovery, Prof. Forest Rohwer at SDSU and Prof. Joe Derisi at UCSF.

FY2007 Proposed Work

A 40-plex assay for detection of known viruses and viral families is now under development. Quantified viral RNA and DNA have been purchased so the assay sensitivity can be accurately determined.

A multiplex assay will be designed for detection of respiratory pathogens. This assay will include the pathogens previously tested so the different assay formats can be compared for sensitivity, specificity, and ease of development and automation.

We will work with Dr. Aaron Brault a highly regarded UC Davis arbovirologist, to design and test an MLPA assay for detection of arboviruses circulating in the Western U.S. This assay will be used to identify arboviruses present in mosquito pools and human clinical samples.

As multiplex assays are developed, probes will be pooled within a single assay to determine the number of probes that may be multiplexed using this technique and the speed of assay development.

Prior to using human nasopharyngeal samples, we will use prepared mixtures of viruses with bacteria and eukaryotic cells in our research on microfluidic separation techniques. Some examples of these mixtures are the bacteriophage MS2 with its host bacteria, *E. coli,* and BSL-1, Risk-Group-1 virus such as fowlpox virus vaccine with its host cell, DF-1, derived from chickens.

Thermal-Fluidic System for Manipulation of Biomolecules and Viruses

Kevin D. Ness
(925) 423-1856
ness5@llnl.gov

We are developing a reconfigurable fluidic system that demonstrates the ability to *simultaneously* perform separations, concentrations, and purifications of biomolecules and viruses using temperature gradient focusing (TGF). Many projects throughout LLNL, particularly those related to pathogen detection, mitigation and protection, require the manipulation of biomolecules or viruses to accurately quantify the presence of a particular substance or to accurately synthesize and investigate the function of a molecule.

TGF, a novel microfluidic technology, is an equilibrium gradient version of capillary electrophoresis (CE) that allows for the stationary fractionation and concentration (up to 10,000 x) of target analytes on the dimension of bulk or free-solution electrophoretic mobility. In this technique, a delicate balance is achieved in a microchannel between a net fluid flow and an opposing electrophoretic velocity gradient to capture charged analytes at a specific location (Fig. 1). TGF then separates the analyte based on the physicochemical property of bulk or free-solution electrophoretic mobility, which is related to the analytes surface charge (zeta potential) and hydrodynamic drag (shape and size).

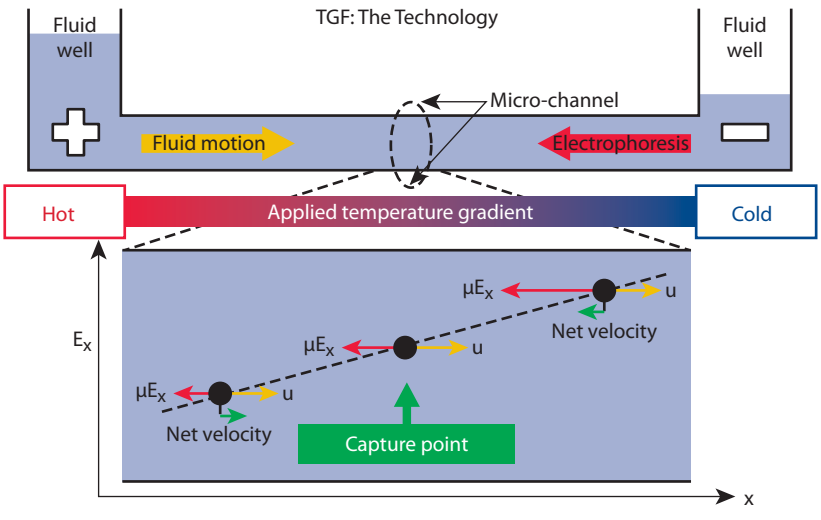

Figure 1. Schematic of TGF. Bulk fluid motion (yellow arrow) is balanced by an opposing electrophoretic velocity (red arrow) to capture analytes at a unique spatial location within a specific electrophoretic mobility range.

Project Goals

The project goal in the first year was to develop an automated TGF instrument to improve the separation resolution and throughput when applied to front-end processing of biological samples. Goals for years two and three are to identify two specific application areas to demonstrate the novel sample manipulation capabilities inherent to TGF: 1) the purification and separation of different virus strains in complex samples (Fig. 2); and 2) to perform protein concentration and separations for *in vitro* transcription/translation (IVT) protein expressions.

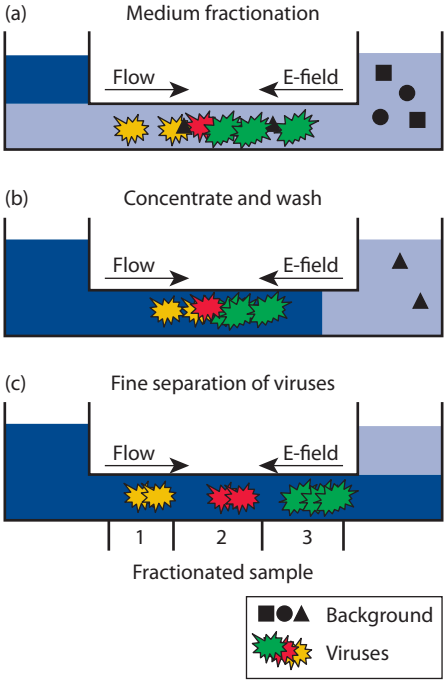

Figure 2. Schematic of TGF as applied to viral front-end sample preparation. (a) Viral samples are loaded and captured using TGF. Capture conditions are set to capture the viruses of interest (focusing), allowing some background contaminates to flow through to waste (purification). (b) Potential second buffer is flushed through system to perform further sample clean-up (buffer exchange). (c) The TGF separation resolution is adjusted in real-time to fractionate the sample into viral groupings (separation) to further simplify downstream detection and identification.

To accomplish this, precise control over temperature (<1 ˚C), voltage (<10 V) or current (<1 μA) and flow rate (1 nL/min) is required, and in-house equipment and procedures must be developed to address these needs.

Relevance to LLNL Mission

TGF specifically addresses LLNL's need for the detection of biomolecules, viruses or cells at low concentrations through enhanced collection, separation, and purification strategies. This is facilitated by performing the necessary front-end sample preparation through concentration procedures, and removing noisy background signals/contaminants. This project supplies LLNL's engineering programs with a novel capability to perform biomolecular, viral, and cellular control in a flexible format to address a wide range of programmatic assay conditions. In addition, this aligns LLNL capabilities with the requirements of a major new DOE program, Genomics: Genomes to Life for protein production and characterization.

FY2006 Accomplishments and Results

In FY2006, we accomplished the following:

1. purchased equipment for two TGF test stations, secured laboratory space, submitted IWS and received approval;
2. surveyed current state of microbial electrophoresis;
3. developed an in-house microfluidics stable flow (nL/min) and pressure source (0.1 Pa) (Fig. 3);
4. performed flow experiments leading to stable valve switching and steady flow at the nL/min range;
5. developed glass chip fabrication protocols for microchannel fabrication and port holes;
6. developed a fluorescently labeled protein electrophoretic mobility marker set (Fig. 4);
7. characterized labeled proteins using processes such as SDS-PAGE, native gel, absorbance, and the limit of detection (Fig. 5); and
8. established external collaborations with industry and academia.

FY2007 Proposed Work

Future work is to modify the static TGF instrument to operate in a dynamic "sweeping" mode to adjust capture conditions in real-time to increase the dynamic range of captured analytes. Work will also begin to transition from separations in "clean" buffered samples to separations in "complex" real-world environmental samples and the purification of specific analytes from these "dirty" samples.

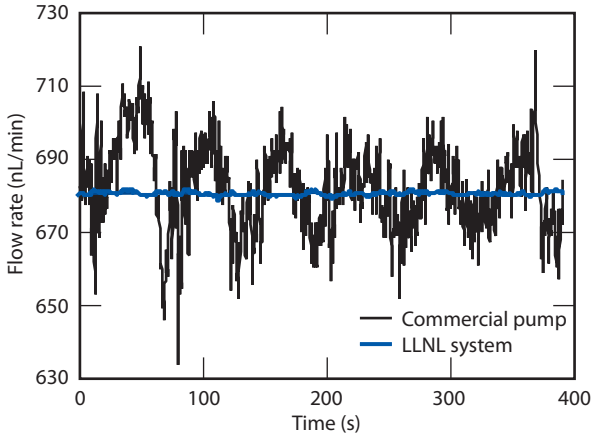

Figure 3. Flow rate stability comparison of commercially available pump versus LLNL flow control system developed for precision sample manipulation.

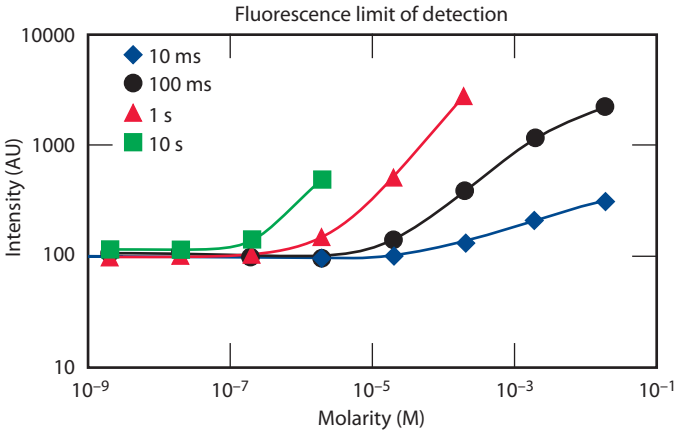

Figure 5. Data showing the TMR probe detection limit using the TGF microscopy equipment with varying fluorophore concentrations and exposure times.

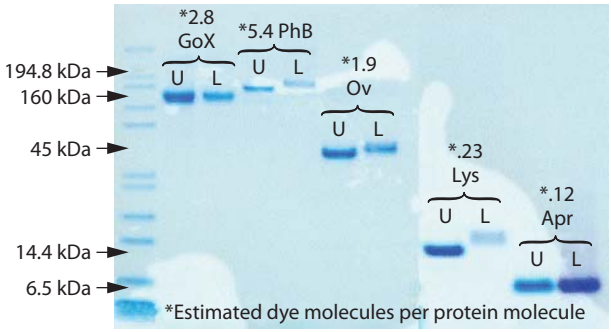

Figure 4. Image of a denaturing PAGE protein separation experiment showing the molecular weight shift observed between fluorescently labeled (L) and unlabeled (U) proteins.

Precision Sample Control and Extraction Component

Klint A. Rose
(925) 423-1926
rose38@llnl.gov

Incorporating microfluidic-based technologies into bio-analytical instruments has many benefits, including reduced sample consumption, faster response times, and improved sensitivity. To achieve these benefits, microfluidic analysis often requires sample concentration and separation techniques to isolate and detect an analyte of interest. Complex or scarce samples may also require an orthogonal separation and detection method or off-chip analysis for confirmation of results. To perform these additional steps, the concentrated sample plug must be extracted from the primary microfluidic channel with minimal loss of sample and with minimal dilution. Extracting these samples requires precise metering and control of nanoliter volumes of fluid.

Extraction of concentrated samples has been demonstrated, requiring constant control of complex electrode structures. This project reduces to practice sample extraction using droplet and bubble generation techniques. These methods are integrated with the equipment and software necessary to improve sample exchange among LLNL microfluidic technologies and improve their functionality. This technology will enable LLNL to supply the next generation biothreat detection instrumentation by improving microfluidic device performance.

Project Goals

The overall goal of this project is to deliver a universal ability to manipulate and extract small volumes of fluid (pico- to microliters) from micron-scale channels. The desired system functions include precise and reproducible control of small volumes of fluid within a microchannel, and the extraction of these sample volumes with minimal effect on the main microfluidic module's performance.

An illustration of this concept is shown in Fig. 1. These functions should be achieved in platforms with fabrication protocols that are standard in the LLNL cleanroom.

Relevance to LLNL Mission

This project addresses needs identified in LLNL's Engineering roadmaps for the detection of biomolecules (DNA, RNA and proteins) and viruses at low concentrations (10 to 1000 copies/ml). Specifically, this project addresses the necessary (and often neglected) front-end sample preparation through precise control and high-yield sample extraction of targeted analytes from upstream concentration, purification and/or separation-based microfluidic devices. This new functionality will enable additional off-chip postprocessing procedures such as DNA/RNA microarray analysis, RT-PCR, and culture growth to validate chip performance. Many LLNL programs will benefit from the improved front-end preparation offered by the precision fluidic control and sample extraction capabilities created by this project.

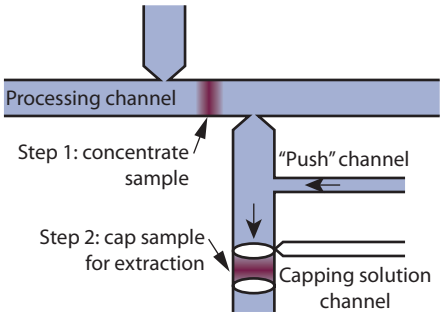

Figure 1. Flow-rate stability comparison of commercially available pump versus flow-control system created for precision sample extraction.

FY2006 Accomplishments and Results

We have accomplished our overall goal by delivering the protocols and microfluidic architecture necessary for manipulating and extracting small volumes of fluid from micron-scale channels. Specific results and accomplishments include the following:

1. Used a system for precise sample control, which includes a flow-rate sensor as feedback for a pressure unit. This system reduced the standard deviation in flow rate to 5% of that for a commercially available precision pump.
2. Created protocols for fabricating microfluidic chips for extraction. This protocol includes the hydrophobic coating necessary for capping aqueous samples. An example is shown in Fig. 2.
3. Demonstrated the capping of samples in a microfluidic channel using air bubbles and fluorinert droplets, as shown in Fig. 3. Capping with incompressible fluorinert droplets provided the most reproducible results compared to air.
4. Verified effectiveness of capping samples to eliminate loss of solute. Fluorinert-capped fluorescent samples were analyzed over thirty minutes and demonstrated no diffusion or detectable loss in concentration.
5. Demonstrated through modeling and experimental flow measurements that proposed injection of samples into fluorinert or air (inverse of capping technique) results in sample loss greater than 20% and dilution of original concentration by greater than 50% (Fig. 4). This result shows capping to be a more effective technique for partitioning samples.

Related References

1. Lin, R., D.T. Burke, and M. A. Burns, "Addressable Electric Fields for Size-Fractioned Sample Extraction in Microfluidic Devices," *Analytical Chemistry,* **77,** pp. 4338-4347, 2005.
2. Hung, L.-H., *et al.*, "Alternating Droplet Generation and Controlled Dynamic Droplet Fusion in Microfluidic Device for CdS Nanoparticle Synthesis," *Lab on a Chip,* **6,** pp. 174-178, 2006.
3. Tan, Y.-C., V. Christini, and A. P. Lee, "Monodispersed Microfluidic Droplet Generation by Shear Focusing Microfluidic Device," *Sensors and Actuators B,* **114,** 1, pp. 350-356, 2006.
4. Gartecki, P., *et al.*, "Formation of Droplets and Bubbles in a Microfluidic T-Junction—Scaling and Mechanism of Break-Up," *Lab on a Chip,* **6,** pp. 437-446, 2006.

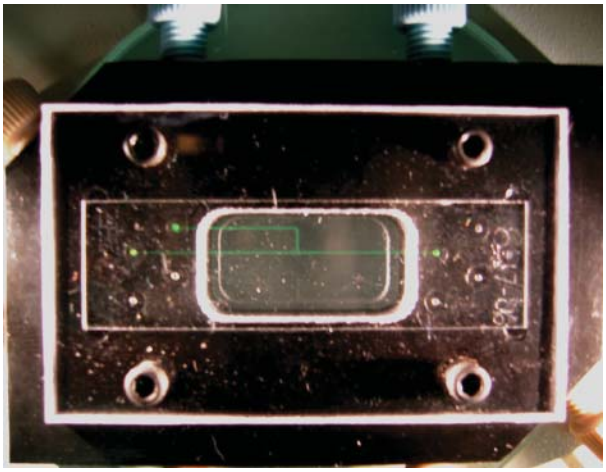

Figure 2. Microfluidic chip and mesoscale package for sample extraction. The extraction protocol can be integrated into existing microfluidic devices with the addition of a single input channel.

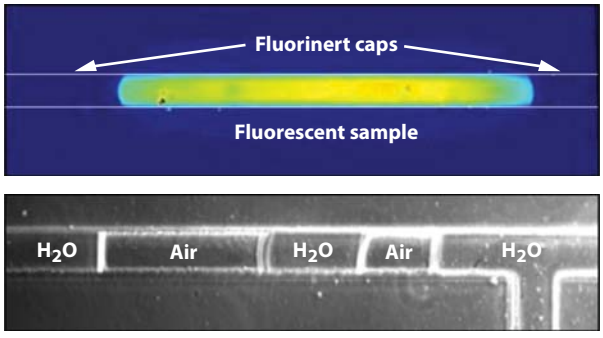

Figure 3. Demonstration of sample capping technique in which air bubbles or fluorinert droplets are injected around a sample. These techniques segregate the sample and enable extraction with minimal loss and dilution.

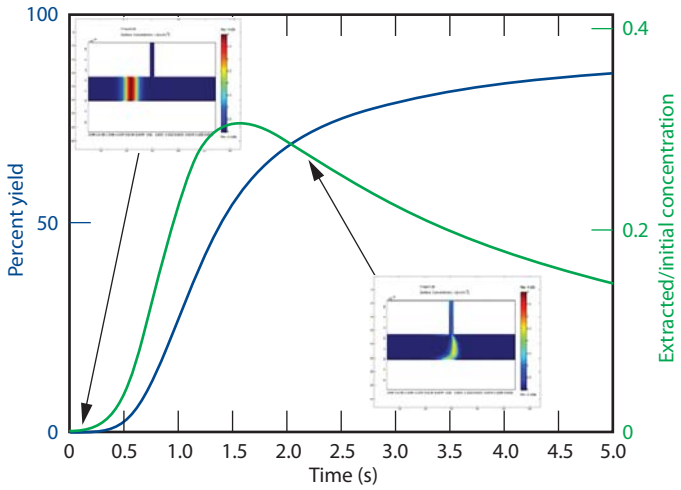

Figure 4. Results from finite element models predicting the extraction yield (blue, left axis) and dilution (green, right axis) for a sample injected into the carrier solution as a function of time. The insets depict the concentration profile of a concentrated plug at times t = 0 s (upper left) and t = 2 s (lower right) as the plug is injected from the primary channel into the side channel with pressure-driven flow. As expected, the percentage of sample extracted increases with time (blue plot) but the concentration (green plot) peaks at ~50% of the sample.

Single-Molecule Assay of DNA Integrity

George Dougherty
(925) 423-3088
dougherty9@llnl.gov

DNA molecules are susceptible to damage resulting from flow through microchannels in microfluidic devices and systems. This damage, which can take the form of either single- or double-strand breaks, is dependent on the size of the channels, fluid flow speeds, and the size of the DNA molecules that flow through the device. This damage can make it difficult to analyze the DNA using processes such as DNA sequencing, polymerase chain reaction (PCR), and labeling of specific sequences with fluorescent probes to search for specific DNA molecules.

An assay to characterize the degree of damage is important because it allows one to optimize microfluidic device parameters such as flow speed, aperture size, and geometry. A single molecule assay to characterize damage is particularly useful for microfluidic devices where the concentration of DNA is low, such as low copy number DNA analysis. In these cases, bulk assays, such as electrophoresis, are not sensitive enough to characterize the damage to the DNA.

In this project we measured the elasticity of single lambda-phage DNA molecules (contour length = 16.4 µm) before and after flow through microfluidic devices. Optical traps were used to stretch single DNA molecules attached to 1-µm beads as shown in Fig. 1. The displacement of the bead in each optical trap varied linearly with applied force, much like a bead on a spring, and the image of the bead on a quadrant photodiode detector was used to accurately measure the elastic tension the DNA molecule experienced as the distance between the traps increased. Figure 2 shows the difference in elasticity between

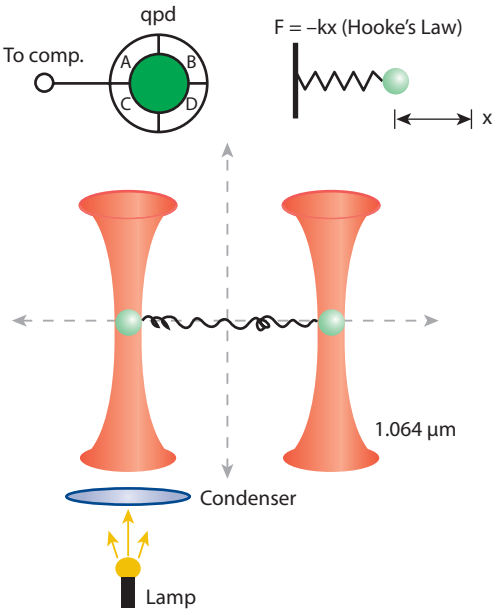

Figure 1. Two optical traps (orange laser beams) are used to hold, stretch, and measure the elasticity of a single lambda-phage DNA molecule via 1-µm beads attached to the ends.

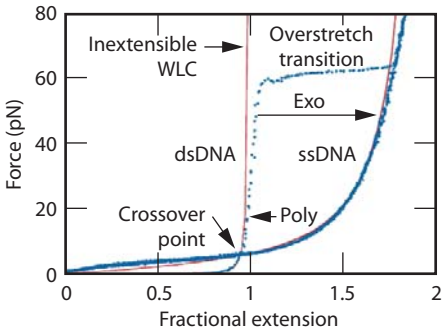

Figure 2. Differences in the elasticity of double-stranded DNA (dsDNA) and single-stranded DNA (ssDNA).

double-stranded DNA and single-stranded DNA that forms the basis of this assay. It takes much greater force to stretch double-stranded DNA than it does single-stranded DNA, and this fact can be used to detect DNA molecules that contain single-stranded portions, due to single-strand nicks, or where strands have been pulled apart due to shearing forces.

Project Goals

The project goals were to 1) identify a DNA biosensor for testing; 2) perform control measurements on DNA at very low flow speeds; 3) test DNA integrity using both gel electrophoretic and DNA single-molecule elasticity measurements to determine the degree of both double- and single-strand breaks; and 4) optimize the flow speed and geometry of the microfluidic device to minimize DNA damage.

Relevance to LLNL Mission

The expertise gained from this project will enable LLNL to develop microfluidic devices for DNA biosensors with a higher efficiency of detection. The increased efficiency of DNA detection will be the direct result of assessing the damage to DNA samples after they pass through microfluidic biosensors, and then optimizing flow speed and biosensor geometry to minimize this damage.

FY2006 Accomplishments and Results

First we performed control measurements on lambda-phage DNA during flow through microfluidic devices using both bulk- and single-molecule techniques. We flowed lambda-phage DNA through a "packed bed reactor" at flow speeds between 0 and 10 µL/s. Gel electrophoresis of the resultant DNA revealed no double-strand breaks. This is shown in Fig. 3. A 1-kb sizing standard run in the left-most lane gives an idea what fragmentation of the original DNA would have looked like.

Next, we stretched individual lambda-phage DNA molecules that flowed through a multichannel cell at very low speeds (0.3 µL/s). Figure 4 shows the characteristic "overstretching transition" and is very similar to the graph shown in Fig. 2. However, at higher flow rates damage to the DNA was evidenced by a dip in the overstretching transition shown in Fig. 5. The dip is indicative of damage to the molecule and results from a portion of the molecule becoming single-stranded. This data is supported by Fig. 2, which indicates that there is a large difference in the elasticity of single- and double-stranded DNA at forces close to 65 pN.

This technique represents a sensitive way to measure damage to single DNA molecules that occurs when DNA flows through small channels at high flow rates. Further work will be required to obtain more quantitative information about the extent of the damage to the DNA.

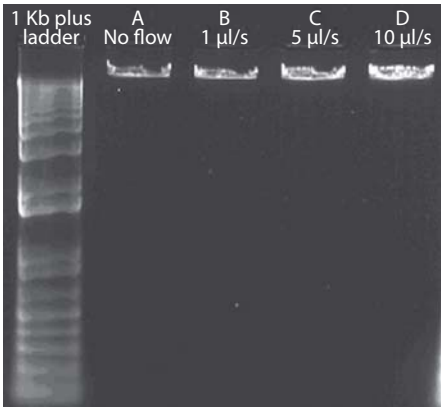

Figure 3. Gel electrophoresis of lambda-phage DNA molecules that have been run through a "packed bed reactor" (courtesy E. Wheeler) at flow rates of A) 0 µL/s, B) 1 µL/s, C) 5 µL/s, and D) 10 µL/s. No double-strand breaks were observed. The leftmost lane contains a 1-kb sizing ladder.

Related References

1. Bustamante, C., Z. Bryant, and S. B. Smith, "Ten Years of Tension: Single-Molecule DNA Mechanics," *Nature* **421**, pp. 423-427, 2003.
2. Brewer, L. R., M. Corzett, and R. Balhorn, "Protamine-Induced Condensation and Decondensation of the Same DNA Molecule," *Science* **286**, pp. 120-123, 1999.
3. Bianco, P. R., *et al.*, "Processive Translocation and DNA Unwinding by Individual Recbcd Enzyme Molecules," *Nature* **409**, pp. 374-378, 2001.
4. Brewer, L., M. Corzett, E. Y. Lau, and R. Balhorn, "Dynamics of Protamine 1 Binding to Single DNA Molecules," *J. Biol. Chem.*, **278**, pp. 42403-42408, 2003.

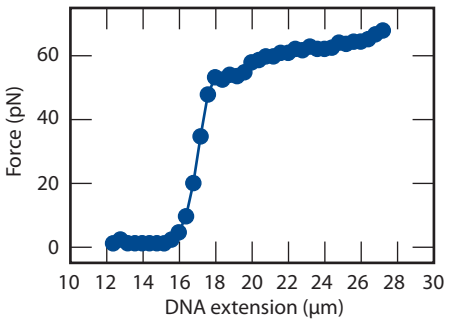

Figure 4. Elasticity of a single lambda-phage DNA molecule taken after an initial flow rate of 0.3 µL/s through a microchannel flow cell.

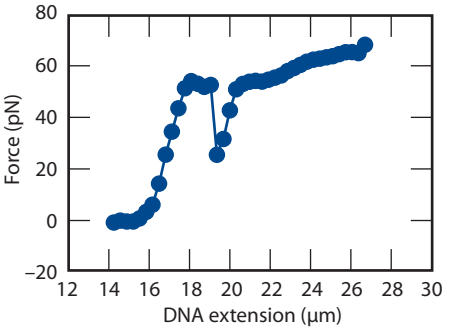

Figure 5. Elasticity of a single lambda-phage DNA molecule taken after an initial flow rate greater than 1 µL/s through a microchannel flow cell, showing a strong dip in the middle of the overstretching transition. This dip shows that a portion of the molecule is single-stranded, possibly due to fluid shear forces.

Colocation of MEMS and Electronics

Satinderpall Pannu
(925) 422-5095
pannu1@llnl.gov

This project bridges the gap between micro-electro-mechanical systems (MEMS) sensors and the necessary integrated circuits to communicate with and control/manipulate the MEMS. Since the advent of MEMS, electrical interconnections have been made using macroscopic wires to electrically bond the MEMS devices to integrated circuits for control and sensing. For a growing number of applications, the associated parasitic resistance and capacitance, as well as the large number of wires required, are not acceptable as an interconnect strategy. Several groups have produced MEMS devices and integrated circuits monolithically by fabricating the electronics next to the MEMS or using low temperature materials that can be deposited without exceeding the thermal budget of the integrated circuits. However, these strategies severely limit the types of MEMS devices that can be fabricated monolithically with integrated circuits. Further, for applications that require dense arrays of MEMS devices such as spatial light modulators (SLMs), packaging density is a vital metric. The area increase incurred by placing MEMS devices next to integrated circuits is not acceptable.

The technology to bond MEMS and integrated circuit dies together with microfabricated metal bumps will enable MEMS devices to be fabricated in conventional processes and then bonded to an integrated circuit.

Project Goals

This project established an enabling technology to colocate MEMS devices with integrated circuits. SLMs were used as the demonstration system since these systems benefit from both the scalability and the increased sensitivity of colocated integrated circuits. Arrays of micro-mirrors (for the SLM), as well as the corresponding high-voltage drivers were fabricated. The two dies were colocated by metal compression bonding. The resulting system was tested for mechanical and electrical functionality. An array of 25 micro-mirrors bonded to high-voltage drivers was assembled and tested.

Relevance to LLNL Mission

This project has relevance to a variety of LLNL interest areas. The ability to integrate MEMS devices and integrated circuits is an enabling technology within LLNL. This technology enables a new generation of devices for a wide variety of applications: chemical and biological sensors; targeting and tracking and location; biomedical devices; high-speed optical processing;

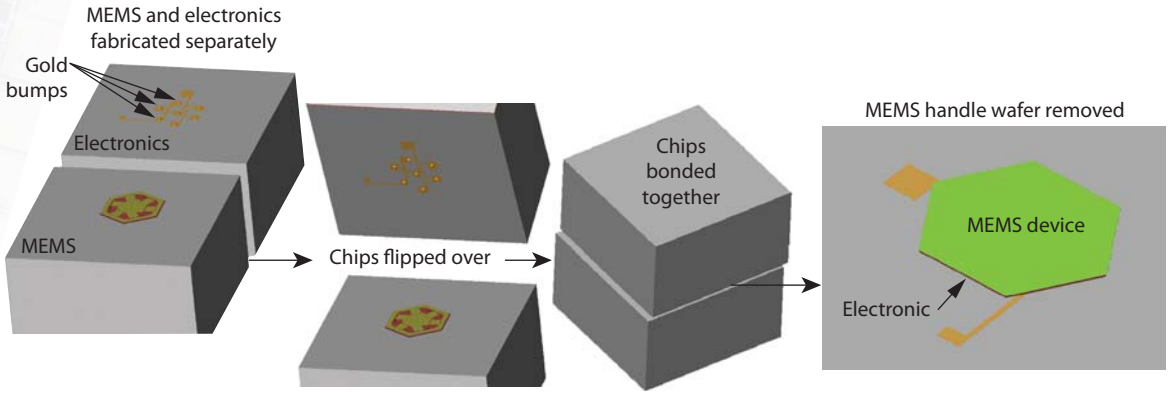

Figure 1. Schematic of overall process flow for the assembly of MEMS and integrated circuits.

and NIF target fabrication. This project has resulted in technology needed for the creation of meso- to microscale devices with nanoscale precision.

FY2006 Accomplishments and Results

In FY2006, the array of micro-mirrors and the high-voltage integrated circuits were fabricated and tested. Further, the micro-mirrors and integrated circuits were assembled and tested. Figures 1 to 3 illustrate our results. The details for each subtask are given below.

MEMS fabrication. The MEMS micro-mirrors were fabricated in the first quarter of FY2006. A large fraction of the fabrication process was carried out in LLNL's cleanroom. However, LPCVD deposition of polysilicon and silicon dioxide, which required well-characterized tools, was carried out at the UC Berkeley microfabrication facility. In the second quarter of FY2006, mechanical substitutes for the integrated circuit device were fabricated so the micro-mirror could be released and tested. The MEMS were released and tested in the third quarter of FY2006.

CMOS fabrication. We outsourced two integrated circuit fabrication runs in FY2006 based on plans completed in FY2005. The first two integrated circuit runs were shown to perform as predicted and work as expected, and a third CMOS run, which would have provided a backup in case one of the first two runs failed, was cancelled.

Assembly. A fabrication process for forming gold bumps for metal compression bonding was created with an external vendor. The MEMS micro-mirrors were then assembled to the integrated circuits by compression bonding the gold bumps against the corresponding metal pads on the integrated circuit die. The MEMS micro-mirrors were then separated from their substrate by breaking small silicon tethers.

Testing. The MEMS micro-mirrors were demonstrated to respond to electrostatic actuation on mechanical models of the integrated circuit die. The testing of the assembled device is ongoing.

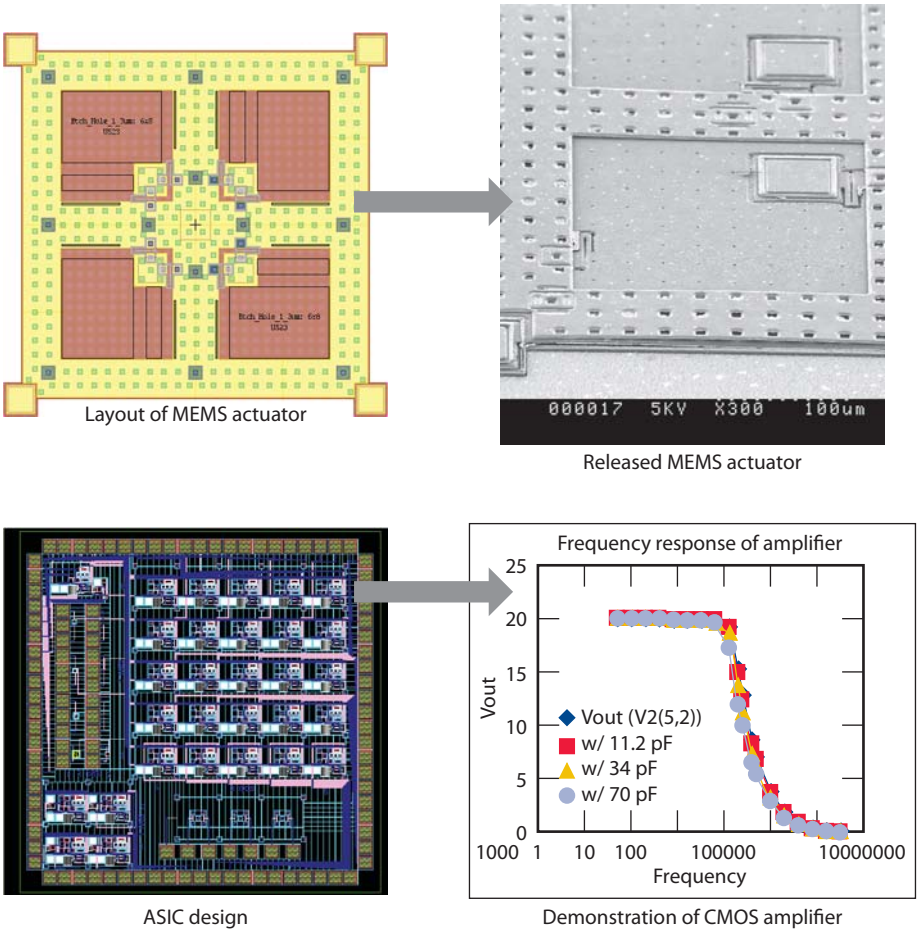

Figure 2. The schematics on the left side depict the layout of the MEMS micro-mirror and the integrated circuit. the images on the right side depict the fabricated micro-mirror and the measured frequency response of the integrated circuit.

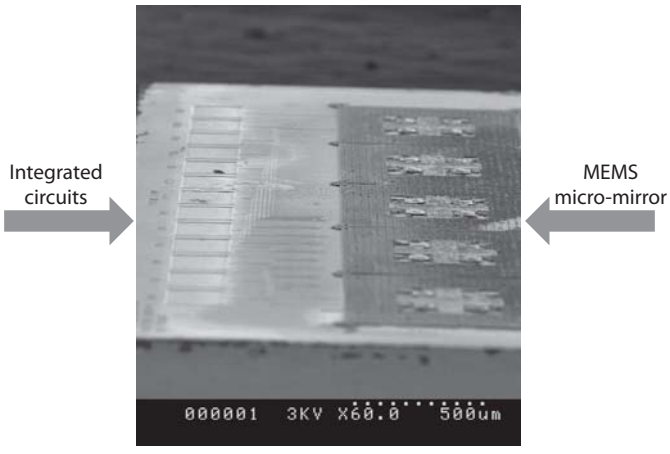

Figure 3. MEMs micro-mirrors colocated with integrated circuits.

Related References

1. Stappaerts E., "Differentially-Driven MEMS Spatial Light Modulator," U. S. Patent Number 6,791,735.

2. Singh, A., D. A. Horsley, M. B. Cohn, A. P. Pisano, and R. T. Howe, "Batch Transfer of Microstructures Using Flip-Chip Solder Bonding," *Journal of Microelectromechanical Systems*, **8,** 1, pp. 27-33, March 1999.

3. Humpston, G., and S. J. Baker, "Diffusion Bonding of Gold," *Gold Bulletin*, **31,** 4, 1998.

Optoelectronic Device Fabrication

Rebecca J. Nikolić
(925) 423-7389
nikolic1@llnl.gov

Optoelectronic devices are a core technology at LLNL. In order to fabricate many of the desired optoelectronic devices, plasma etching is frequently required to construct structures with 3-D shapes. Additionally, plasma etching is required to connect multiple devices within a semiconductor wafer. The plasma etching that is needed requires vertical and smooth sidewalls to allow for such integration and also for device performance.

In this project we have addressed the device integration requirements by determining methods to fabricate turning mirrors. We also have a large effort in the area of pillar fabrication, which is being considered for thermal neutron detectors. In this area we have made advances in terms of fill factor and aspect ratio, as well as the determination of process recipes to fabricate a demonstration device. This is a two-year project and the signal routing component was addressed in the first year of the project (FY2005), while the second year of the project is primarily concerned with the pillar fabrication methods and the required techniques to fabricate a demonstration device for thermal neutron detection.

Project Goals

For data routing we will create turning mirrors, splitters and combiners. The fabrication processes studied satisfy requirements of specific ongoing projects as well as increase our technology toolbox. Pillar structures are demonstrated with a geometry of at least 100 x 100 pillars with a fill factor of 50 %, (where the fill factor is the percent of semiconductor used for pillars). Additional microfabrication tasks will be carried out in order to demonstrate a pillar-structured neutron detector.

Relevance to LLNL Mission

This work is supporting both internally- and externally-funded projects that require advanced InP-, GaAs- and Si-based process technology. There are many different devices having broad applications that share the same fabrication hurdles. Having this technology will allow deployable microfabricated systems for several applications that are at the core of LLNL's national security missions, such as: high-speed radiation diagnostic devices for NIF, single-transient recording technologies, devices for encryption applications, and radiation detection.

FY2006 Accomplishments and Results

The work focusing on data routing elements for inverters was carried out in FY2005. The scope of work for FY2006 is focused on building a technology toolbox required to fabricate a pillar-structured neutron detector. Two major areas were enhanced: 1) high-aspect-ratio etching, and 2) fabrication methods for a demonstration detector (see figure).

Within the high-aspect-ratio etching work, we have increased our aspect ratio to 10. This yields 2-µm-diameter pillar geometry, with a 2-µm separation and 20-µm pillar etch depth. The fill factor for this pillar area is 50 % for our 1-cm-x-1-cm chip.

Within the area of demonstration detector fabrication, we implemented processing recipes for our pillar-structured neutron detector. This included the specification and procurement of lithographic masks, the evaluation of methods to deposit the boron materials, which is the neutron-converting material for this particular device, as well as lapping, polishing and etching techniques of boron. Processes to fabricate low-resistance contacts to silicon were demonstrated. This included ohmic contact formation to both p+ and n+ silicon: for p+ Si a platinum/titanium/gold multi-layer stack, (400/400/2000 Å), and for the n+ side, a titanium single layer (2000 Å). Both of these metallization schemes form a silicide upon annealing, yielding a low-resistance metal contact of $R_C < 10^{-5}$ Ω-cm^2.

Related References

1. Nikolic, R. J., C. L. Cheung, C. E. Reinhardt, and T. F. Wang, "Roadmap for High Efficiency Solid-State Neutron Detectors," *SPIE - International Symposium on Integrated Optoelectronic Devices, Photonics West,* Boston, Massachusetts, October 2005.
2. Suligoj, T., and K. L. Wang, "A Novel Isolation of Pillarlike Structures by CMP and Etchback Processes," *Electrochemical and Solid-State Letters,* **8,** 5, pp. G125-7, May 2005.
3. Cheung, C. L., R. J. Nikolic, C. E. Reinhardt, and T. F. Wang, "Fabrication of Nanopillars by Nanosphere Lithography," *Nanotechnology,* **17,** pp. 1339-1343, March 2006.
4. Shultis, J. K. and D. S. McGregor, "Efficiencies of Coated and Perforated Semiconductor Neutron Detectors," *IEEE Transactions on Nuclear Science,* **53,** 3, pp. 1659-1665, June 2006.

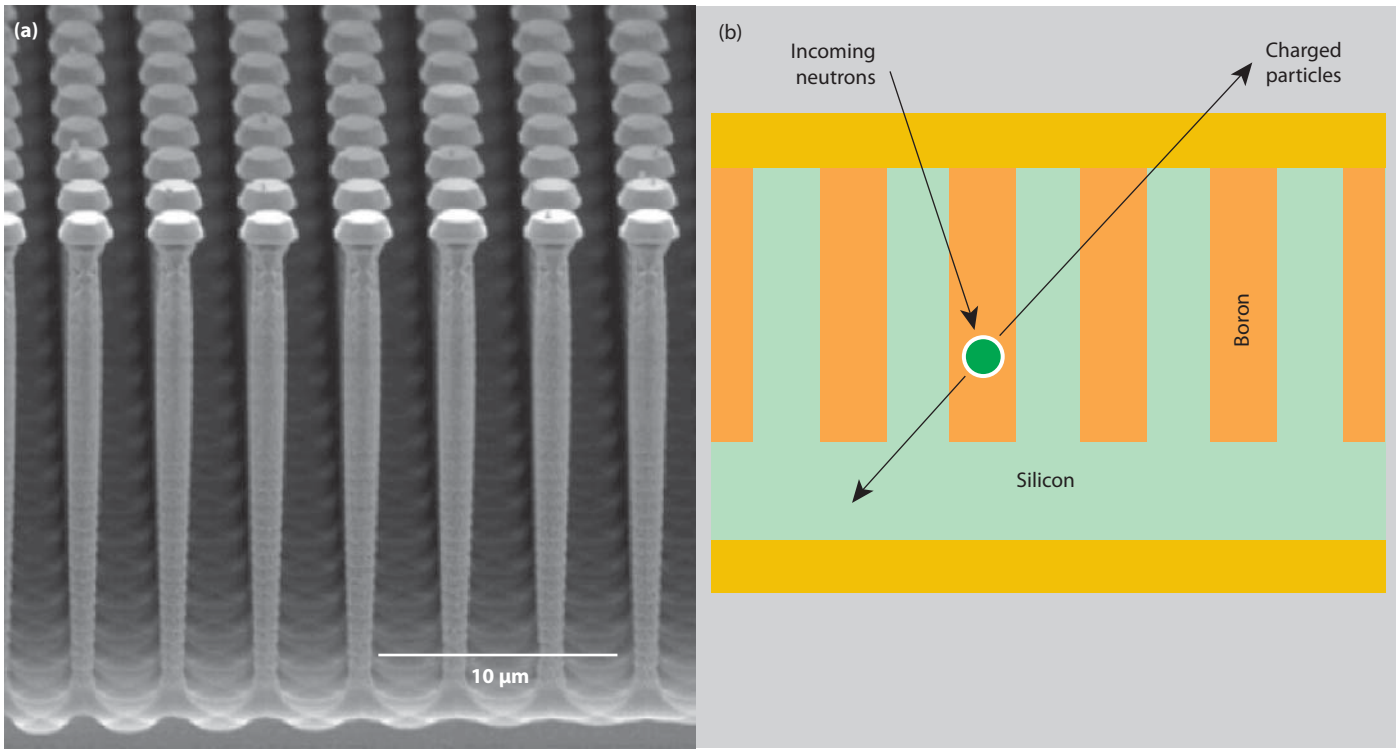

(a) Micrograph, showing the etched silicon pillars used in the Pillar Detector. Pillars are 20 µm in height and spaced about 2 µm apart. (b) Thermal neutron detector: incoming neutrons interact with the pillars within a semiconductor matrix.

Block Copolymer Nanolithography

James Courtney Davidson
(925) 423-7168
davidson4@llnl.gov

Block copolymer technology has been used increasingly for patterning nanoscale features in polymers, silicon and metals. Highly-ordered nanoscale features are produced in thin (nanometer-thick) self-assembled films. In diblock copolymer systems these films consist of two covalently bonded polymer chains. These systems form distinct domain structures due to phase separation of the chemically dissimilar polymers during solidification. Depending on the relative volume fraction, domains can form as spheres, cylinders, or lamellae oriented either perpendicular to or parallel to the surface with a period on the order of 10 to 100 nm.

Recently, advanced directed block copolymer self-assembly is showing great promise for controlled nanolithography techniques for achieving advanced SEMI lithography nodes and high-density periodic pore arrays and gratings. Still others have demonstrated the potential of nanofeature masks for fabricating components for micro- and optoelectronics, magnetic storage devices, nanopore membranes and nanotemplates for ordered detector arrays.

Project Goals

Our interest in block copolymers has been to leverage existing efforts in order to establish a core nanolithography capability. First year goals were to form a collaboration to assist in the definition and stand-up of a diblock copolymer process within LLNL. This process was based on the polystyrene (PS) and polymethylmethacrylate (PMMA) diblock copolymer. A second goal was the dimensional characterization of these nanostructures using existing analytical tools including SEM, AFM, and TEM. An additional goal of this effort was to incorporate findings from an associated modeling effort to prescribe block copolymer specifications for dimensional characterization and parametric studies. Second year goals include a continued use and refinement of predictive modeling for the 2-D process and extension toward 3-D nanolithography.

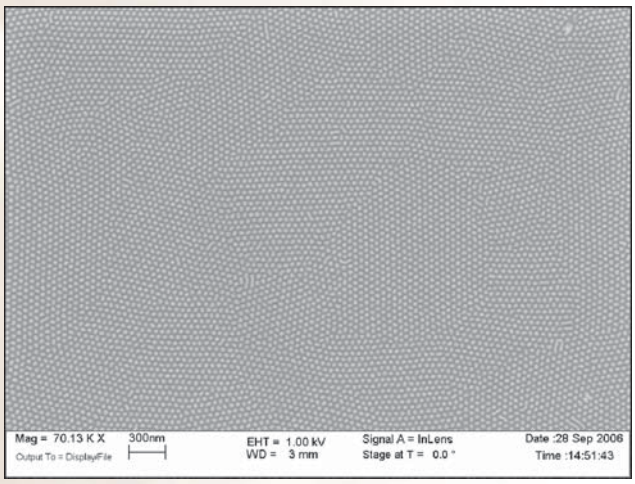

Figure 1. SEM of self-assembled DiBCP thin film with ~ 60 nm period. The hex pack PS (light gray) cylinders are vertically oriented and ~ 30 to 35 nm in diameter.

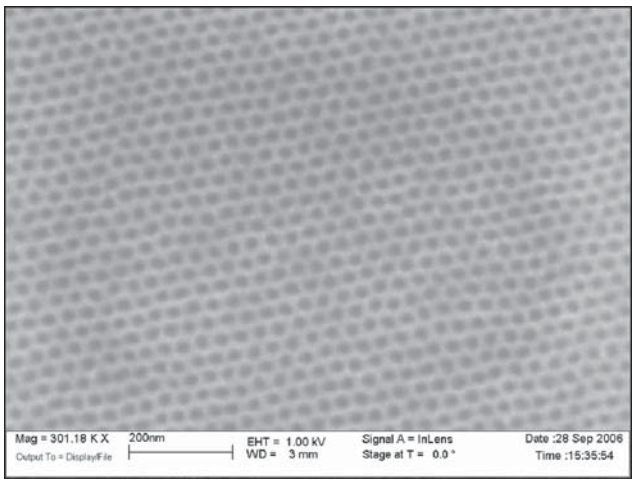

Figure 2. SEM of a 40-nm period thin film produced by etching out the spherical PMMA domain, leaving a PS (light gray) mask.

Relevance to LLNL Mission

Reducing a block copolymer nanolithography process technology to practice maps directly onto LLNL's Micro/Nano-Devices and Structures roadmap initiative. This is an enabling technology that will initially provide a capability of nanoscale mask lithography with applications to NIF targets and sensor systems integration for NHI and DNT. Example applications include x-ray gratings, nanobridge wires, nano-dimension antennas and resonators, high surface area for high-energy-density storage capacitors and batteries, novel radiation detectors, and graded density targets.

FY2006 Accomplishments and Results

First year efforts resulted in the demonstration of a 2-D self-assembled block copolymer process. We worked with staff at LBNL and UCB to define and establish a well-characterized PS/PMMA process at LLNL. Requisite polymers and solvents were specified and materials were procured. An experimental plan with process controls was put in place to work with solvents at high temperature to obtain monolayer films.

Cylindrical and spherical block copolymer structures were fabricated as shown in Figs. 1 and 2. These films were characterized using SEM, and AFM to determine feature sizes as small as 25 nm (Fig. 3).

An initial wet etch process was demonstrated to remove the PMMA component in the film. This proved to be prerequisite for increasing the topology and thus contrast in the SEM observation. We worked with various volume fractions of the PS/PMMA system to demonstrate the different domain formations, including lamellae, although these were observed only in the parallel configuration. These efforts were repeated on both silicon and oxide substrates in keeping with our intent to demonstrate the utility of the process for increased surface area. These parametric studies also served to validate predictive modeling efforts. These results are providing insight to polymer system selection for proposed predictive graded-density film fabrication next year.

We also began to define and establish a dry etch process for the removal of the PMMA polymer. Process steps have been identified to pursue parametric definition of a dry process in order to fabricate robust etch masks.

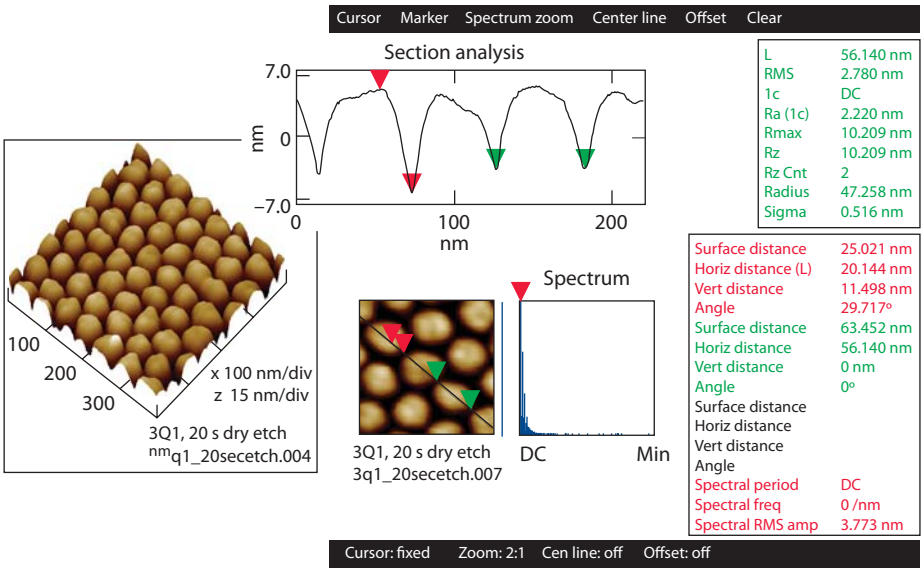

Figure 3. AFM scan of vertically-oriented cylindrical block copolymer. Cylinders are in close-pack hexagonal formation and are approximately 30 nm in diameter with a 63-nm period.

Related References

1. Segalman, R. A., "Patterning with Block Copolymer Thin Films," *Materials Science and Engineering* **R 48**, pp. 191-226, 2005.
2. Black, C.T., *et. al.*, "Integration of Self-Assembled Diblock Copolymers for Semiconductor Capacitor Fabrication," *Applied Physics Letters*, **79**, pp. 409-411, 2001.
3. Adamson, D.H., *et. al.*, "Large Area Dense Nanoscale Patterning of Arbitrary Surfaces," *Applied Physics Letters*, **79**, 2, pp. 257-259, 2001.
4. Kim, S. O., H. H. Solak, M. P. Stoykovich, N. J. Ferrier, J. J. de Pablo, and P. F. Nealey, "Epitaxial Self-Assembly of Block Copolymers on Lithographically Defined Nanopatterned Substrates," *Nature*, **424**, pp. 411-414, 2003.
5. Weilun, C., C. Harteneck, J. A. Liddle, E. H. Anderson, and D. T. Atwood, "Soft X-Ray Microscopoy at a Spatial Resolution Better than 15 nm," *Nature*, **435**, pp. 1210-1213, 2005.

FY2007 Proposed Work

Our next efforts will focus on extension of existing processes to demonstrate 3-D nanolithography. First we plan to enhance our block copolymer fabrication capability by expanding the base process to allow for extended long range ordering. This will require control of interfaces and substrate etching for enhanced domain alignment. A parallel computational modeling effort to predict best polymer systems for extended order is also planned. This builds on FY2006 modeling efforts.

A primary FY2007 focus will be to evaluate triblock copolymers. Such films are less surface-dependent and have been shown to allow subsequent removal for building laminated structures. This, coupled with variation of block copolymer systems, will lead to varied density of films. Additionally our current process is to be expanded to permit lift-off of arbitrary thin films, such as metals. This will enable fabrication of nanometer features for surface-enhanced Raman scattering and templated carbon nanotube-based chemical sensors.

Characterization of Deep Reactive Ion Etching of Dielectric Materials

Satinderpall Pannu
(925) 422-5095
pannu1@llnl.gov

High-aspect-ratio microstructures in silicon have been available for almost a decade due to the advent of the Bosch process. Similar high-aspect-ratio microstructures in dielectric materials such as silicon dioxide have not been available until recently. This project established base recipes for the reactive ion etching of dielectrics using a new deep reactive ion etcher (DRIE). The dielectrics of interest are silicon dioxide and silicone elastomers. There exists no commercially available high-aspect-ratio etching of silicone. With this project, LLNL now has a unique capability in advanced dielectric definition and etching. This new fabrication capability enables the generation of advanced devices for a wide variety of applications. This project involved the optimization and characterization of recipes for the deep reactive ion etching of dielectrics.

Project Goals

This project established a new LLNL capability to etch high aspect ratio structures in silicon dioxide and silicone. Basic recipes were tested to etch both materials using etch rate, mask selectivity (ratio of etch rate of substrate to the etch rate of the mask), aspect ratio (ratio of width of feature being etched to the final depth of etched feature), and sidewall profile angle as the figures of merit. These basic recipes can then be tailored to etch program-specific microdevices.

Relevance to LLNL Mission

This project has relevance to a variety of LLNL interest areas. The ability to etch dielectric materials with high-aspect ratios brings a unique fabrication technique to areas in meso-, micro-, and nanotechnology. This fabrication capability enables a new generation of devices for a wide variety of applications: chemical and biological sensors; targeting, tracking, and location; biomedical devices; high-speed optical processing; and NIF target fabrication. This project has resulted in fabrication capabilities needed for the development of meso- to microscale devices with nanoscale precision.

FY2006 Accomplishments and Results

Experiments were formulated to characterize the etch performance of silicon dioxide and silicone in a Surface Technologies Systems Advanced Oxide Etch platform. The figures of merit were

Table 1. Performance of optimized recipe for silicon dioxide (quartz).

Feature size	Aspect ratio	Etch rate	Selectivity	Profile angle
50 µm	4:1	1.25 µm/min	4.5	89°
100 µm	2:1	1.3 µm/min	4.6	89°
200 µm	1:1	1.4 µm/min	5	89°
400 µm	1:2	1.5 µm/min	5.2	90°

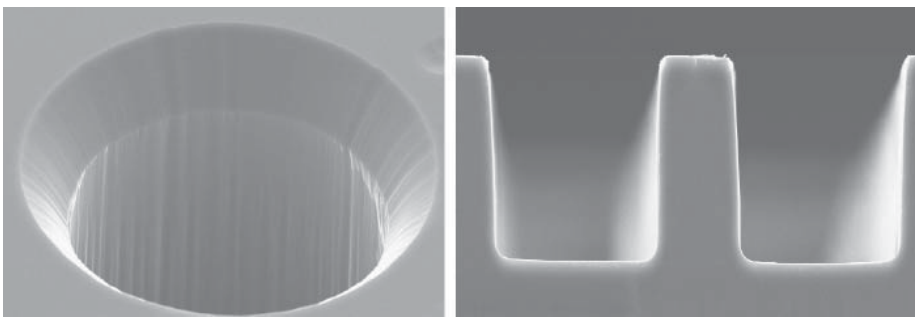

Figure 1. 100-µm holes and trenches etched 200 µm deep in a quartz (silicon dioxide) substrate using silicon shadow mask.

etch rate, sidewall profile, aspect ratio, and mask selectivity. A photolithography mask was produced which had holes and stripes which varied in feature size from 50 µm to 500 µm. Several masking materials were evaluated including silicon, chromium, and photoresist. The silicon shadow mask gave the highest selectivity to both silicon dioxide and silicone.

Several recipes were tested to optimize the figures of merit listed above using a silicon shadow mask. A summary of the results for holes etched in the silicon dioxide (quartz) substrate is given in Table 1.

Figure 1 shows the etch of 100-µm holes and trench to a depth of 200 µm in quartz (crystalline silicon dioxide). In typical high-aspect-ratio etching, trench-like features are not limited by diffusion-based processes and hence these features do not demonstrate the performance of the system. Hole-like features are diffusion-limited and provide a more difficult challenge for high-aspect-ratio etching. Hence the etch rate and the selectivity decreases as the aspect ratio increases. Overall, the figures of merit are all in desirable ranges for all the feature sizes and are similar to high-aspect-ratio silicon etch systems. Figure 2 shows an array of 200-µm holes etched 200 µm deep in quartz.

Similar experiments were conducted on silicone. Recipes were tested to optimize the figures of merit listed above using a silicon shadow mask. A summary of the results for holes etched in the silicone on a silicon substrate is given in Table 2.

Figure 3 shows the etch of 100-µm holes to a depth of 200 µm in silicone on a silicon substrate. Again, as with the quartz etch recipes, the etch rate and the selectivity decreases as the aspect ratio increases. Overall, the figures of merit are all in desirable ranges for all the feature sizes and are similar to high-aspect-ratio silicon etch systems. A wafer-to-wafer uniformity study was conducted on 15 silicone wafers to determine the repeatability of the process. The etch rate was used as the figure of merit. The results are summarized in Table 3.

In summary, base recipes for high-aspect-ratio etching of silicon dioxide and silicone were tested using a silicon shadow mask. The figures of merit are similar to the values obtained on high-aspect-ratio silicon etch systems.

Related References

1. Garra, J., T. Long, J. Currie, T. Schneider, R. White, and M. Paranjape , "Dry Etching of Polydimethylsiloxane for Microfluidic Systems," *Journal of Vacuum Science and Technology A: Vacuum, Surfaces, and Films,* **30**, 3, pp. 975-982, May 2002.

2. Tserepi, A., G. Cordoyiannis, G. Patsis, V. Constantoudis, E. Gogolides, E. Valamontes, D. Eon, M. Peignon, G. Carty, C. Cardinaud, and G. Turban, "Etching Behavior of Si-Containing Polymers as Resist Materials for Bilayer Lithography: The Case of Poly-Dimethyl Siloxane," *Journal of Vacuum Science and Technology B: Microelectronics and Nanometer Structures,* **21**, 1, pp. 174-182, January 2003.

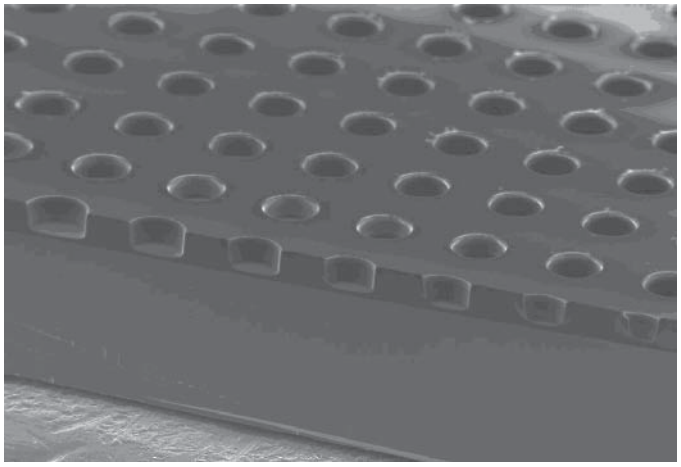

Figure 2. Array of 200-µm holes etched 200 µm deep in a quartz (silicon dioxide) substrate using silicon shadow mask.

Table 2. Performance of optimized recipe for silicone-on-silicon substrate.

Feature size	Aspect ratio	Etch rate	Selectivity	Profile angle
50 µm	4:1	1.0 µm/min	2.5	89°
100 µm	2:1	1.15 µm/min	2.6	89°
200 µm	1:1	1.2 µm/min	2.9	89°
400 µm	1:2	1.25 µm/min	3.0	89°

Table 3. Results of wafer-to-wafer uniformity study conducted on 15 silicone wafers.

Figure of merit	50 µm	100 µm	200 µm	400 µm
Mean etch rate	1.05 µm/min	1.12 µm/min	1.20 µm/min	1.32 µm/min
Run to run uniformity	5.2%	3.8%	2.9%	2.2%

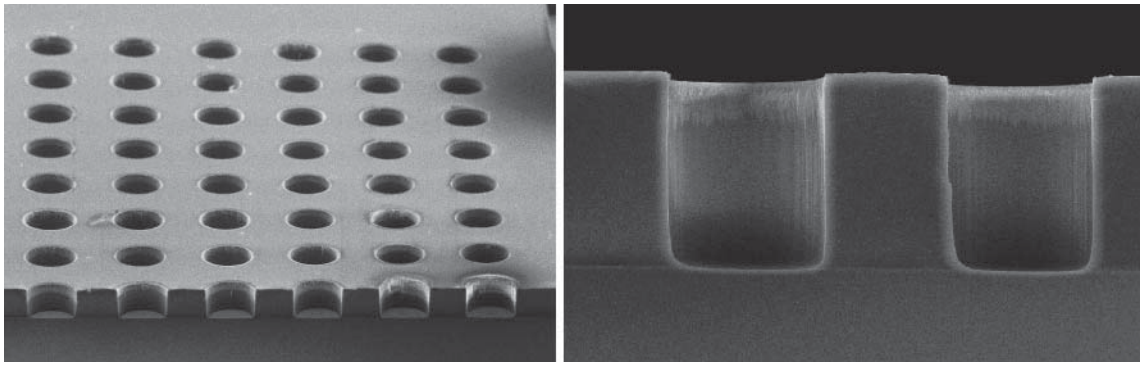

Figure 3. 100-µm holes etched 200 µm deep in silicone on a silicon substrate using silicon shadow mask.

Gray-Scale Lithography for Sloped-Surface 3-D MEMS Structures

Christopher M. Spadaccini
(925) 423-3185
spadaccini2@llnl.gov

Microfabrication techniques that originated from the IC community typically yield 2-D extruded geometries or structures with limited angles due to crystallographic orientation. Gray-scale lithography in MEMS is capable of generating a gradient height profile in photoresist, and subsequently in silicon, after deep reactive ion etching (DRIE) or other dry etching techniques. Our work has sought to establish this 3-D microfabrication capability at LLNL. Gray-scale lithographic techniques previously reported in the literature were used to baseline and calibrate arbitrary sloped-surface, 3-D microstructures at LLNL.

Typically, photolithographic processes involve a photomask with only an opaque "dark field" and a transparent "clear field," resulting in 2-D features with relatively straight sidewalls in the photoresist. The gray-scale technique is performed by using a photomask with multiple, discreet "gray-levels" or with pixilated features to locally modulate the intensity of UV light used in the standard photoresist exposure process. This results in locally varied photoresist exposure and correspondingly varied depth/thickness upon wet chemical development. After DRIE, the 3-D depth profile is transferred to the silicon substrate and altered, based on the etch selectivity to silicon versus photoresist. By varying the optical density and spacing of the gray levels on the photomask, an arbitrary angle in the silicon microstructure can be achieved. This capability will enable a whole new class of microstructures not previously considered manufacturable at LLNL.

Project Goals

The result of this work will be the capability to fabricate arbitrary angle, sloped-surface, 3-D microstructures. Deliverables include:

1. a well-defined process for fabricating 3-D MEMS structures (sloped surfaces) of arbitrary angle based on a combination of parameters such as photomask optical density, spacing of

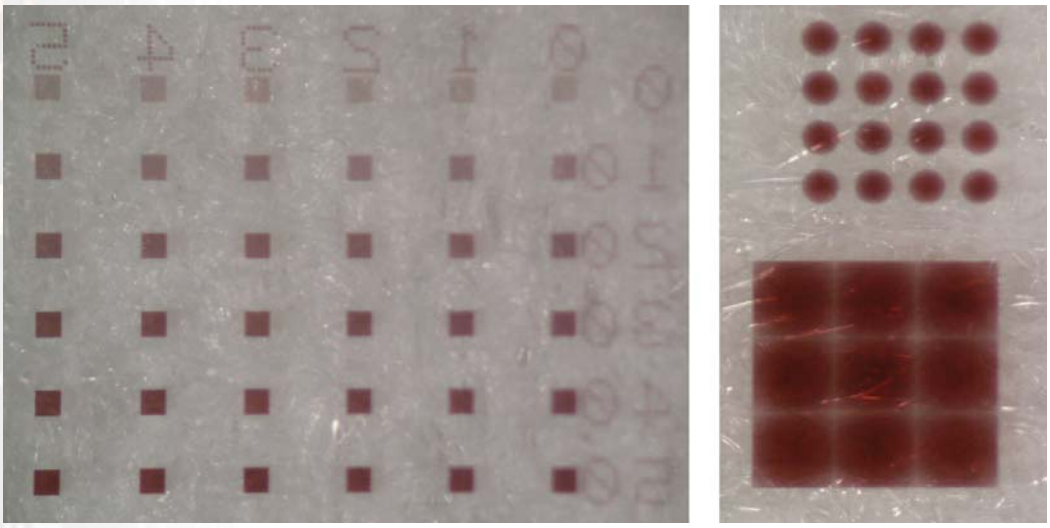

Figure 1. Calibration squares of varying optical density and micro-lens arrays on the HEBS glass gray-scale photomask.

gray levels, photoresist thickness, and photoresist development time; and
2. documentation of the process and parametric study for general use so that the LLNL microfabrication community at large can easily fabricate a microstructure with an arbitrary sloped surface.

Relevance to LLNL Mission

The ability to fabricate sloped surfaces at an arbitrary angle in silicon microsystems allows for a host of new geometries not previously considered, and will shift the overarching microfabrication paradigm away from 2-D structures. The availability of this technique will advance the core microfabrication competencies at LLNL, which provides vital support to both internal and external customers.

FY2006 Accomplishments and Results

High-energy beam-sensitive (HEBS) glass from Canyon Materials, Inc. was selected as the material for the photomask. HEBS glass is doped with a photoinhibitor that changes opacity when exposed to an electron beam. The change in optical density of the glass varies with the intensity of the beam, thus controlling the gray levels. The theoretical minimum feature size for a gray level is the thickness of the beam, and ~1000 discreet gray levels of varying optical density are possible. The photomask used in this work contained a variety of features intended to calibrate the gray-scale process in LLNL's cleanroom, and show some of the capabilities of the technique. Features included micro-lens arrays, grating structures, tapered structures of varying height, and calibration squares of varying height to correlate photoresist thickness to mask optical density. Figure 1 shows some of the features on the photomask.

Two types of photoresist were calibrated with the gray-scale mask. These included AZ4620 thick resist and AZ1518 thin resist. A range of thicknesses (~1 to 10 µm) of each of these photoresist types were spun onto silicon wafers, exposed to UV light, and developed. The photoresist profiles were then characterized using a SEM and an optical interferometer. Figure 2 shows interferometer measurements of photoresist profiles for the micro-lens features. By careful measurement of the remaining photoresist height, a calibration curve of resist thickness versus photomask optical density for a given set of process conditions was generated. These curves can then be used by engineers to design gray-scale photomasks for custom applications.

Finally, DRIE of the photoresist profiles was performed and 3-D features in the silicon substrates were obtained. Figures 3 and 4 show SEMs of the micro-lens arrays and the varying height calibration squares in silicon. The overall etch depths for these features were ~120 µm and the AZ4620 thick photoresist was used.

As a result of this work LLNL now has the capability to produce arbitrary, 3-D, sloped-surface microstructures for a variety of applications.

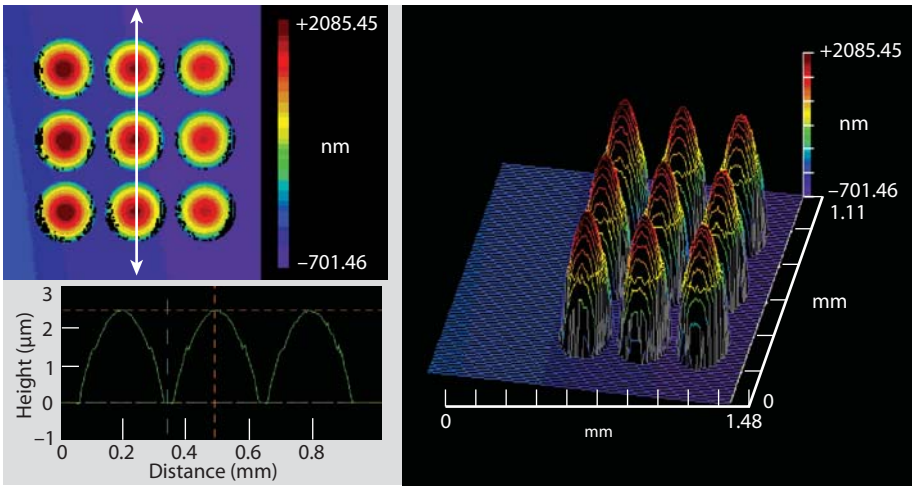

Figure 2. Optical interferometer measurement of micro-lens photoresist profiles.

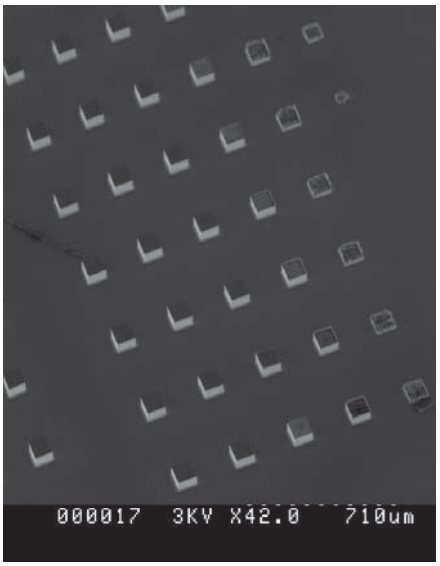

Figure 3. SEM of varying height calibration squares after DRIE in silicon.

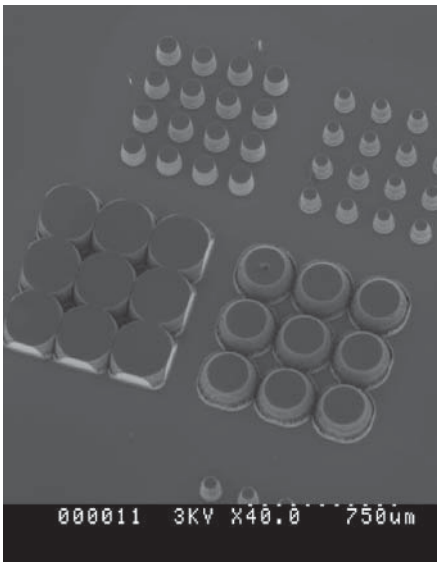

Figure 4. SEM of micro-lens arrays after DRIE in silicon.

Absolute Conditioner for Fabry-Perot Microsensors

Michael D. Pocha
(925) 422-8664
pocha1@llnl.gov

High-fidelity flight tests are required by the weapons stockpile stewardship mission to assure weapon viability without underground testing. Additionally, embedded sensors in future reliable replacement warheads (RRWs) will monitor state-of-health and ageing. These applications require miniature, minimally invasive sensors and readout systems. Sensors also need to be optically read out to reduce exposure of sensitive components to electrical energy. Several different sensors are available to measure parameters such as acceleration, strain, displacement, pressure, and temperature, at various locations within test assemblies. This effort is focusing on two important new sensors, an optical gap gauge (OGG) and an optical force probe (OFP). While a variety of miniature sensors (commercial and custom made) are available, current signal conditioners (readout systems) are big and bulky (usually rack mounted), and unacceptable for LLNL applications.

Project Goals

This is the first year of a two-year project to reduce to practice several concepts for miniature OGG and OFP sensors, as well as techniques for implementing the necessary absolute measurement signal conditioners for these and similar sensors. The sensor fabrication was begun in this first year and will conclude with demonstration of working devices in the second year. Our goal for the absolute conditioner was to demonstrate, in the laboratory, our concept for the miniaturizable conditioner, for the first year, and to explore miniaturization techniques in the second year.

Relevance to LLNL Mission

High-fidelity flight tests to assure weapon viability without underground testing and implementation of future RRWs are central to the LLNL weapons stockpile stewardship mission.

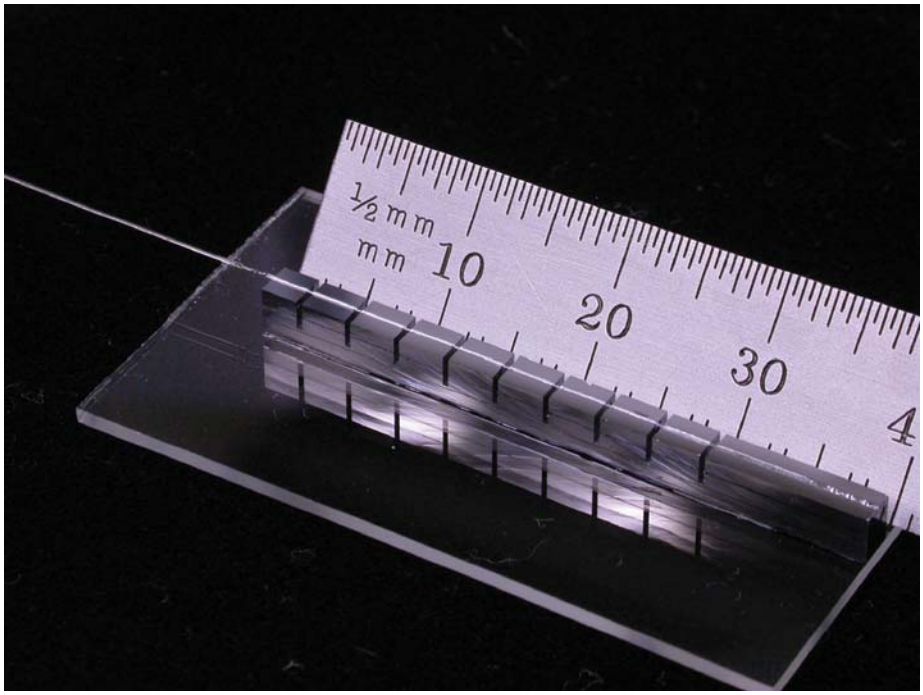

Figure 1. Optical gap gauge spacers for enhanced sensitivity.

FY2006 Accomplishments and Results

Fabrication of the OFP, as part of this effort, requires several new methods of silicon processing, sensor assembly, and packaging. Accomplishments were made in all these areas. A commercial readout system has also been specified and purchased to help the testing of the new OFPs.

A major concern is joining of the optical fiber to two silicon halves that form the transducer. Specifically, anisotropic plasma etching of silicon has been defined to form grooves to assist with fiber mounting. Brazing of the sensor components has also been defined to improve joints used to date. Assembly jigs and methods have been created to assist handling of silicon parts and sensor assembly. Finally, packaging methods have been defined to encapsulate the OFP. The new OFP will have a total thickness of 140 µm, is thermally compensated, can be multiplexed with multiple devices on a single fiber, and is resistant to particulate or other contamination.

The OGG fabrication has been modified to scale its sensitivity. Used as a Fabry-Perot (FP) sensor, the OGG requires the separation between the fiber's core and the sensor's beam to increase to achieve greater displacement sensitivity. Processing to accomplish this has been demonstrated.

The absolute conditioner effort included fringe visibility experiments; fiber preparation; a gap movement linearity study; full conditioner modeling for simulation of light sources and predictive understanding of practical limitations imposed by several optical components; and finally, testing the effectiveness of various computational algorithms for extracting the sensor gap (the key measurement parameter) from the raw fringe data. A key result is that a preliminary model, which can be implemented with commercial components, reduces the conditioner volume to approximately 3 in^3. We estimate that a further order of magnitude in volume reduction is possible when several custom MEMS components are fully implemented.

Figures 1 to 3 illustrate our results.

FY2007 Proposed Work

New OGGs of varying displacement sensitivities will be fabricated. The fabrication and testing of the new OFP will continue. Implementing a fully miniaturized version of the absolute conditioner is an extensive task beyond the scope of this project. But, we will explore miniaturization technology, and attempt to fabricate the reduced-size functional model that was created in FY2006.

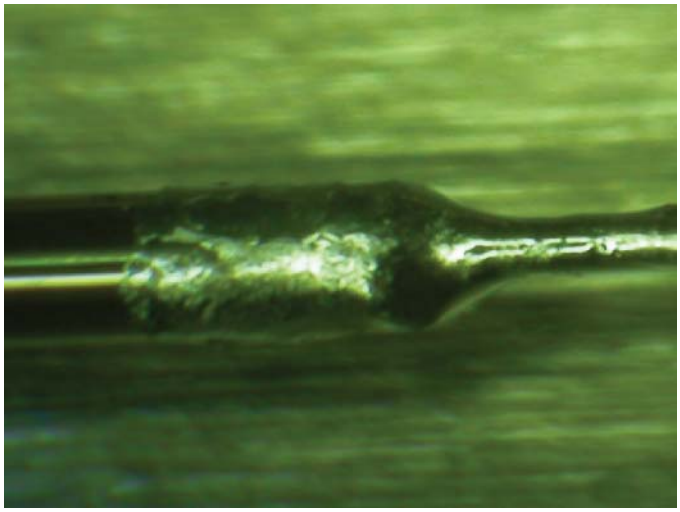

Figure 2. Fiber braze joint, bonding fiber to capillary for use in FP-based microsensors. Brazed and bonded joints offer long-term sensor stability and hermetic sealing.

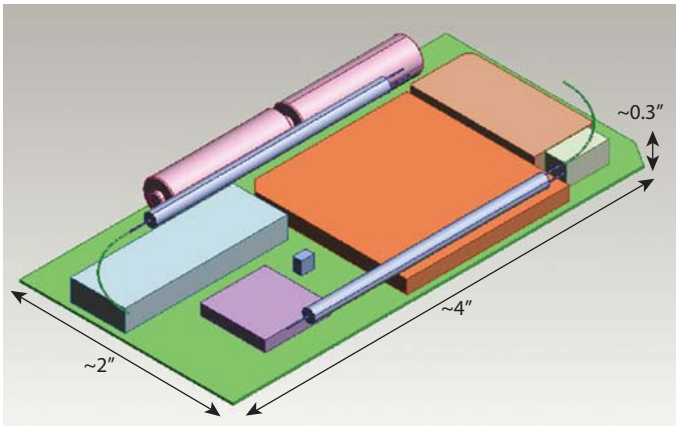

Figure 3. Representation of repackaging of commercial components, which can lead to a readout system that fits within a 3- $in.^3$ volume.

Implementing Nano-Imprint Capability

Robin Miles
(925) 422-8872
miles7@llnl.gov

Photolithography is a common technique for patterning features on planar substrates. Photosensitive polymer coated on the substrate is illuminated through a mask and upon development of the polymer, the pattern of the mask is transferred to the substrate. These techniques are used at LLNL to make MEMS sensors, microfluidic devices, and photonic components. While micron-sized features are common, sub-micron, achieving nanoscale features, typically require expensive equipment.

Nano-imprinting is a new method of "lithography" wherein sub-micron features are stamped into the polymer coating using a 3-D mask rather than illuminating through the traditional planar glass mask. The advantages of nano-imprinting are low cost and reduced capital equipment complexity for producing nanoscale features. Many commercial semiconductor companies are considering using this technique in their fabrication lines.

Competing sub-micron lithographic techniques such as e-beam lithography are expensive. Focused Ion Beam (FIB) fabrication is both expensive and practical for use over only a limited area of the material. A number of current and potential future projects can benefit from nano-imprinting methods. In particular, projects such as graded density targets where low densities (on the order of 1% of a 1.2 gm/cc material) are desired, structures for block-copolymers, nano-electrodes for dielectrophoresis, and new optical devices such as ring-resonators for sensors will require nanostructures that can be produced using this technique.

Project Goals

The current EV aligner in the microfabrication facility is capable of performing nano-imprint lithography. The goal of this project was to characterize this process so that this technique could be applied to future program needs.

Relevance to LLNL Mission

Several future projects may rely on the ability to produce devices with sub-micron features. Among the potential applications of this capability are the graded density reservoirs for equation-of-state targets. Other program applications include next-generation sensors for weapons surveillance, radiation detection, and bio-security where nanoscale devices and structures will lead to significantly improved performance.

FY2006 Accomplishments and Results

We received training on nano-imprinting. The equipment uses UV curable resists as opposed to the majority of nano-imprinting techniques, which use thermal processing methods. Polydimethylsiloxane (PDMS) secondary masks made from molds of a master silicon or quartz mask are used to define features across a 100-mm wafer. We purchased a quartz master mask with sub-micron features. We have used this technique to produce patterns on both glass and silicon substrates. A sample test pattern is shown on a glass substrate in the figure. Line widths of 100-500 nm are possible.

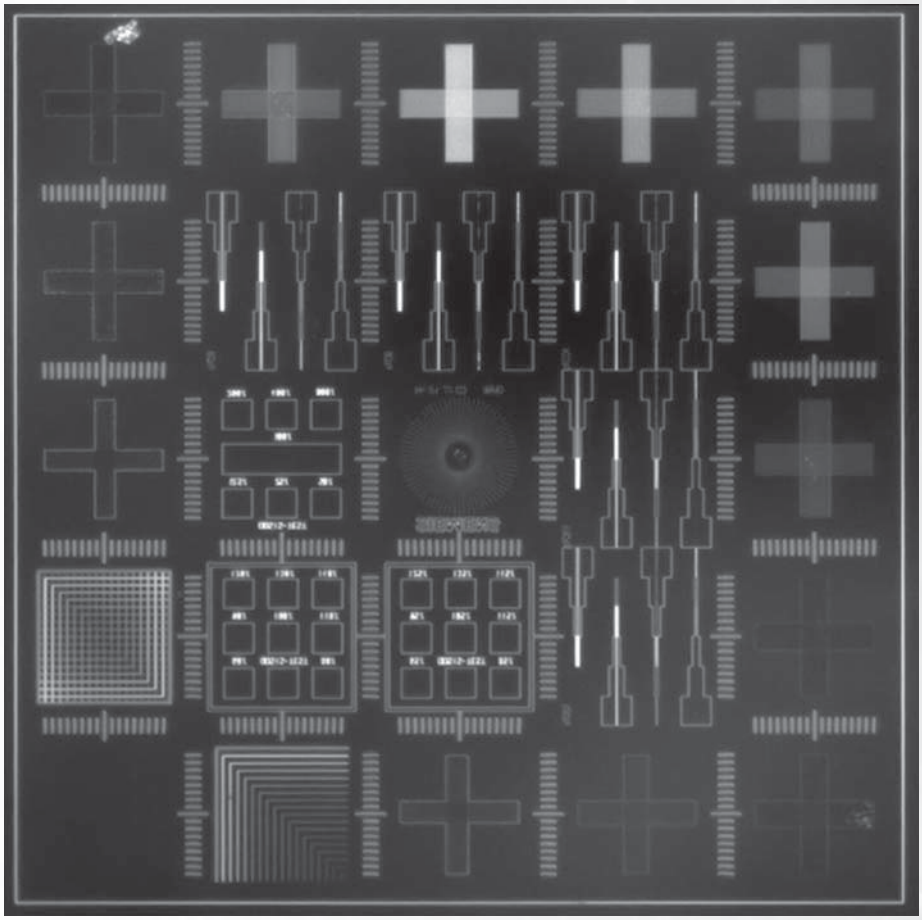

Test pattern nano-imprinted on a glass substrate.

Silicon Nitride Furnace Installation

Robin Miles
(925) 422-8872
miles7@llnl.gov

Low-stress silicon nitride windows are used as a component of targets for many high-energy physics experiments. These are thin (50 to 500 nm thick) substrates upon which materials of interest are applied such as metal films or occasionally biological materials. The windows have been used in targets for OMEGA, Jasper, ALS at LBNL and at the Center for Accelerator Mass Spectrometry (CAMS). A window fabricated for CAMS is depicted in Fig. 1.

These windows are fabricated in LLNL's cleanroom facilities. Often, many hundreds of windows are fabricated for a particular target application. A new silicon nitride furnace was installed under this project and is a great improvement over the former system. The former system was a multi-user system in which a variety of materials were processed including carbon. Occasionally, the former system would become contaminated with particulates, possibly from organics, which adversely affected the quality of the silicon nitride films. Further, the former system was very variable in its output, exhibiting very non-uniform films across a wafer and from wafer to wafer. These attributes made producing acceptable films slow, tedious work. The new silicon nitride system will greatly improve the quality of the films processed in this facility.

Project Goals

The goal of this project was to install a new low-stress silicon nitride furnace that would provide uniformly thick nitride films across a set of 25 wafers. The furnace would be used for particular non-organic substrates to maintain cleanliness.

Relevance to LLNL Mission

Several programs at LLNL use targets in accelerator or laser systems to measure material properties such as opacity, to conduct warm dense matter experiments, or to serve as a gas barrier

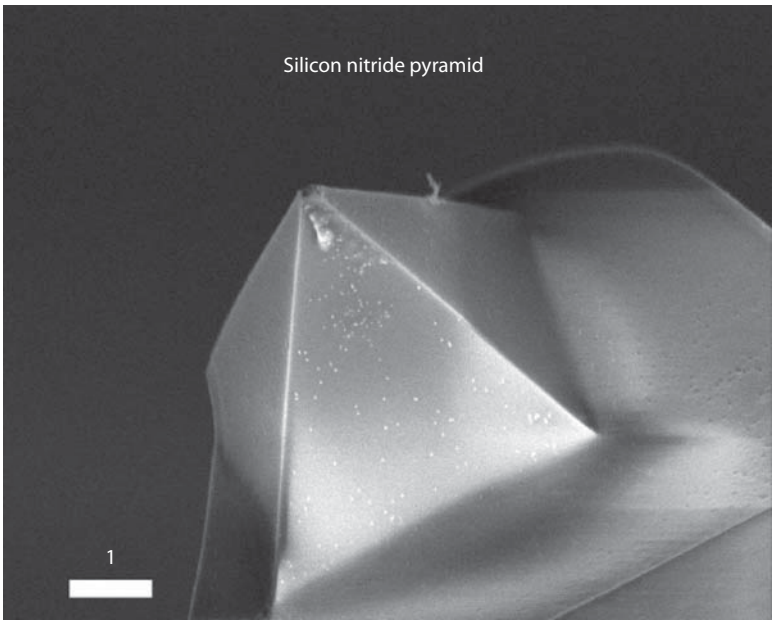

Figure 1. Silicon nitride window fabricated for CAMS.

for the measurements of gas properties. Silicon nitride windows can be an important component of those targets. Silicon nitride windows are also used to produce photocathodes for streak cameras for these experiments.

FY2006 Accomplishments and Results

Low-stress nitride is a non-stoichiometric film produced in a reaction between ammonia and dichlorosilane at about 800 ºC at 300 mTorr. We completed the installation process, which involved tasks such as 1) installing and testing gas lines, manifolds, and gas sensors with special consideration given to the toxic nature of the gas; 2) installing custom thermocouples, interlocks, and brackets; 3) installing a vacuum capability; and 4) installing a controller. The completed system is shown in Fig. 2.

Figure 2. Silicon nitride deposition furnace.

High-Density Plasma Source

Steven L. Hunter
(925) 423-2219
hunter5@llnl.gov

We acquired and evaluated a new type of high-density plasma source for sputter deposition. The plasma "beam" used for sputtering is generated remotely, and its path to the target is defined by the orthogonal locations of two electromagnets: one at the orifice of the plasma tube and the other just beneath the target plane. An example configuration of a vacuum chamber with the plasma source for sputter deposition is shown in Fig. 1.

One advantage of this source is that the high plasma density lends itself to higher deposition rates, an important parameter in the production of metal oxides. Another, more subtle advantage is the ability to independently control the deposition rate and the target bias voltage. This adds another means to control oxide properties that are not available in typical magnetron sputter sources. The electromagnets enhance the electron mean free path in the space between the plasma orifice and the target. When the RF power is applied to the coils around the plasma source, the argon atoms in this region are ionized. The current to the orifice electromagnet is kept constant, while the current to the steering electromagnet is adjusted to steer the high-density plasma beam onto the target. The target bias potential accelerates the argon atoms across the dark-space sheath and sputters the target material.

Project Goals

We performed a study to determine the deposition rate dependency of the high-density plasma source on deviations from the optimal geometric configuration. The study was performed during the reactive deposition of niobium oxide. The effect on deposition rate was determined by moving the plasma source away from the target in one direction, and by moving the target assembly away in an orthogonal direction. Deposition parameters were established to produce nonabsorbing niobium oxide films of about 100-nm and 350-nm thicknesses. The quality of the niobium oxide films was studied spectroscopically, ellipsometrically, and stoichiometrically.

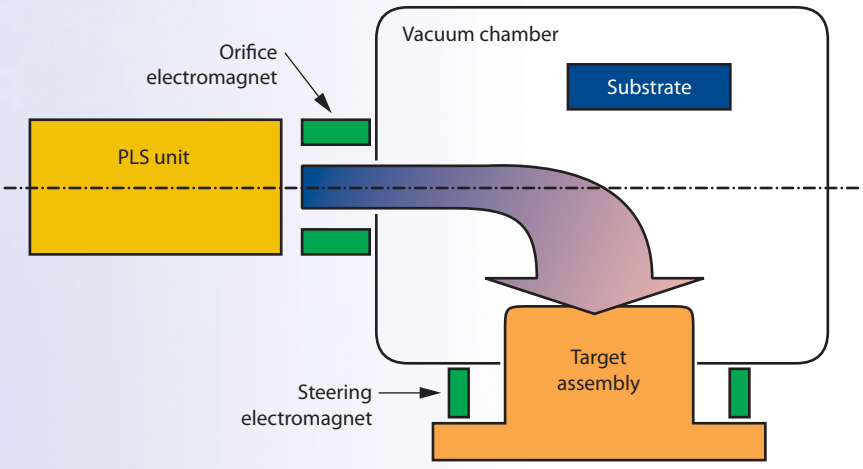

Figure 1. High-density plasma source configuration for sputter deposition.

Relevance to LLNL Mission

Over the last several years, LLNL has been working towards miniaturization and survivability of fireset components for integration onto a single substrate for weapons applications. Nanostructure multilayer technology (NML) is a key factor in the component work. Improvements have been made toward increasing the capacitance, energy density, and dielectric strength of our NML capacitors by testing different materials and sputtering processes.

FY2006 Accomplishments and Results

The high-density plasma source was acquired, installed in the Vacuum Test Lab, and its performance was evaluated. Figure 2 is an image of the source in operation. The deposition rate characteristics of the high-density plasma source were evaluated. Reactive sputtering with a high-density plasma source of niobium in the presence of an oxygen partial pressure produced stoichiometric niobium pentoxide, which is an important material for programmatic missions.

Related References

1. Vopsaroiu, M., M. J. Thwaites, S. Rand, P. J. Grundy, and K. O'Grady, "Novel Sputtering Technology for Grain-Size Control," *IEEE Transaction on Magnetics,* **40**, 4, pp. 2443–2445, July 2004.
2. Hockley, P. J., M. J. Thwaites, and G. Dion, "High Density Plasma Deposition," *Society of Vacuum Coaters 48th Annual Technical Conference Proceedings,* 2005.
3. Moulder, J. F., W. F. Stickles, P. E. Sobol, and K. D. Bomben, Handbook of X-Ray Photoelectron Spectroscopy, J. Chastin and R. C. King, Jr., Eds., Physical Electronics USA, Eden Prairie, Minnesota, p. 111, 1995.
4. Venkataraj, S., R. Drese, O. Kappertz, R. Jayavel, and M. Wuttig, "Characterization of Niobium Oxide Films Prepared by Reactive DC Magnetron Sputtering," *Phys. Stat. Sol. A,* **188**, 3, pp. 1047–1058, 2001.

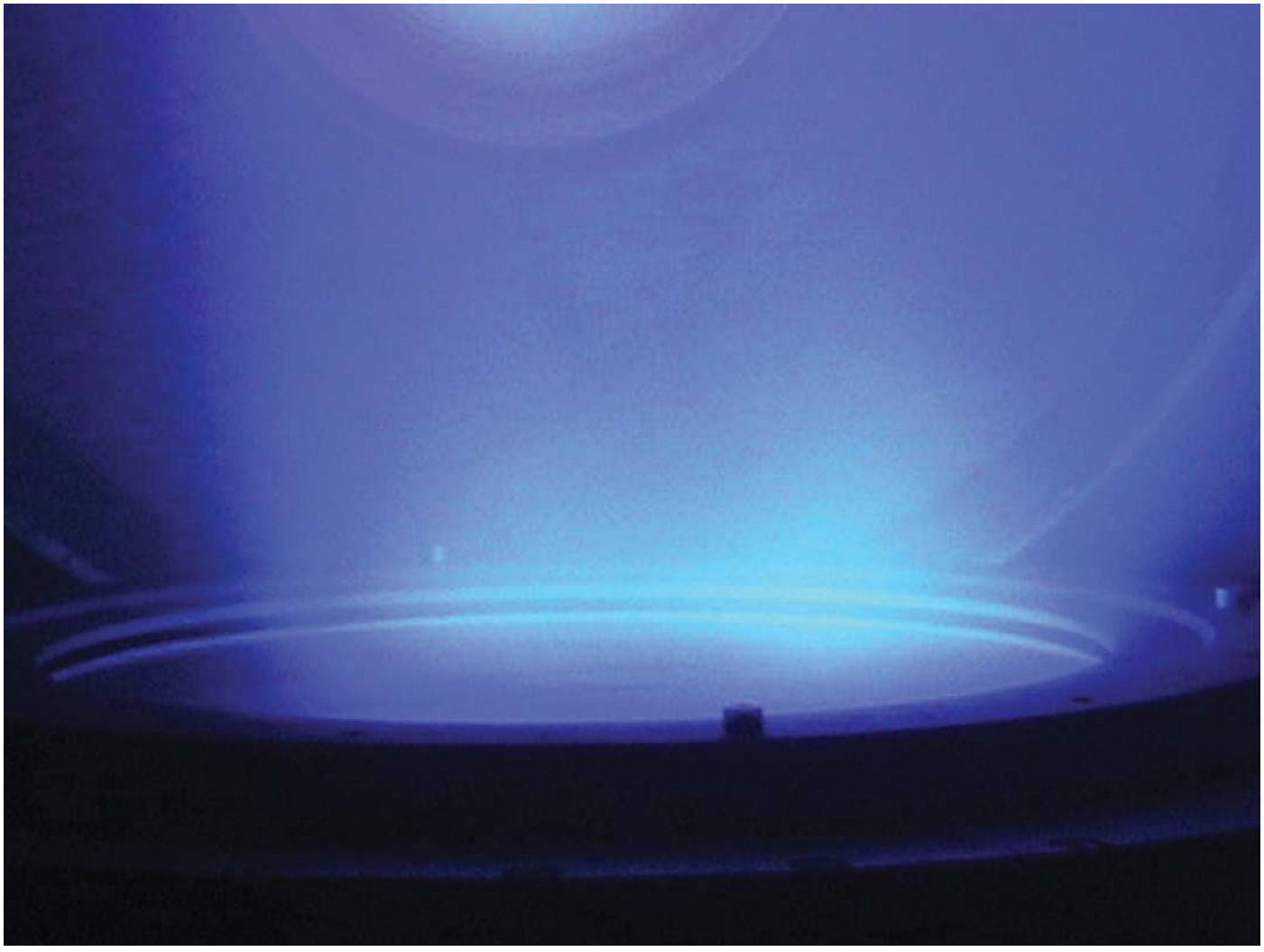

Figure 2. High-density plasma source in operation.

Precision Engineering

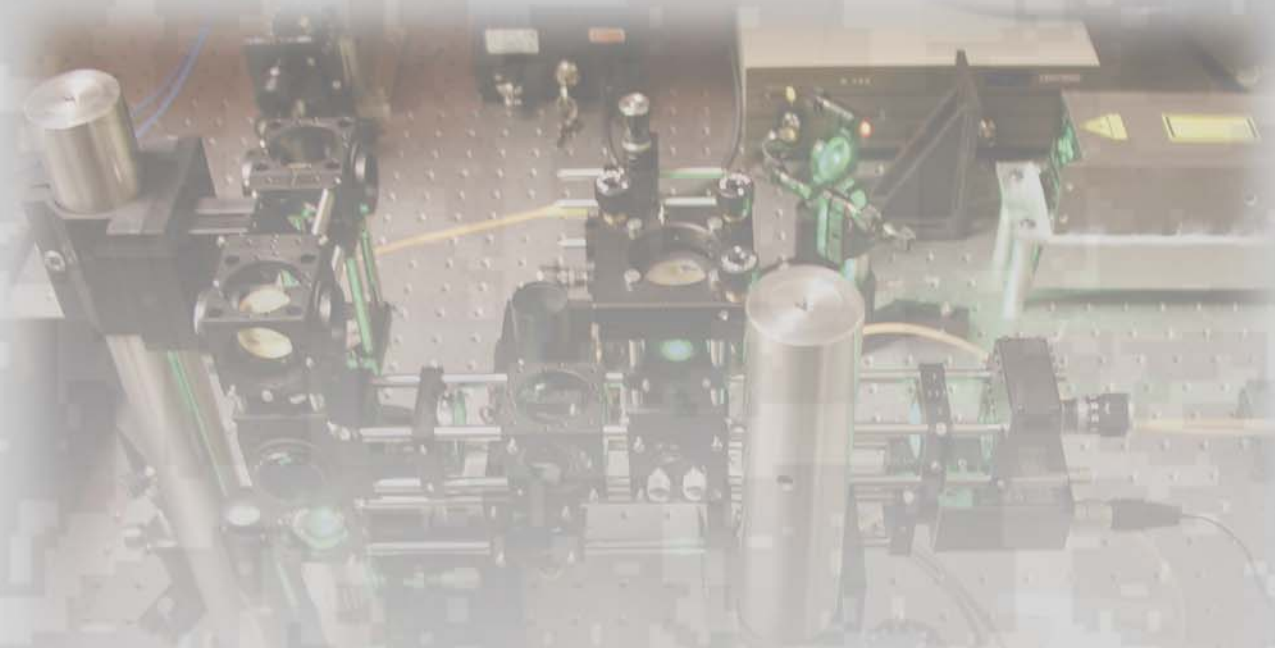

Error Budgeting and Certification of Dimensional Metrology Tools

Jeremy J. Kroll
(925) 422-6437
kroll4@llnl.gov

The creation of radiographic and ultrasonic measurement tools has progressed from providing qualitative information to providing quantitative information. There has not been a quantitative error budget prepared for these tools, in the same manner that error budgets have traditionally been created for coordinate measuring machines, *e.g.*, the Atomic Thickness Measuring Machine (ATMM). In this effort, we formulate an error budget for nondestructive evaluation (NDE) tools such as the Xradia CT (computed tomography) microscope, and the Laser UT (ultrasonic testing) system shown in Fig. 1

These conclusions are compared with error analyses from traditional Coordinate Measuring Machines (CMM) tools such as ATMM. In addition, one to three characteristic artifact parts are fabricated and measured among the various instruments. The differences in the measurements are compared within the context of the formulated error budgets.

By validating error budgets for non-traditional metrology tools, we are applying a known engineering technique to both scientific and technical problems.

Project Goals

The goal is to produce validated quantitative error budgets for the Xradia CT microscope and the Laser UT system, which will enable a structured approach for improving the capabilities of these machines as well as provide insight into the effect of individual error sources.

Relevance to LLNL Mission

The advantage to LLNL is a broader view of dimensional metrology that

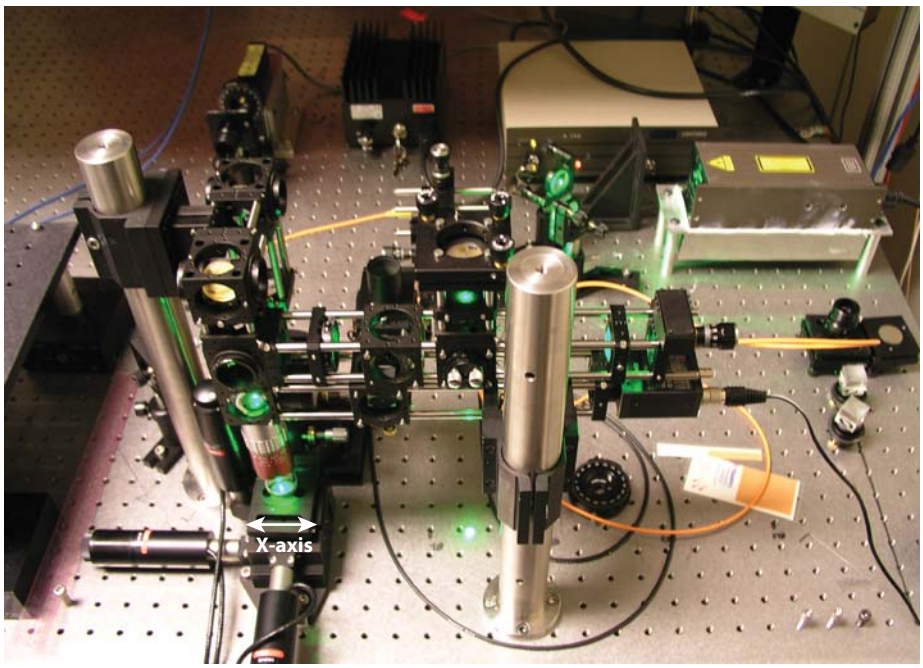

Figure 1. Tabletop GHz laser-acoustic measurement system (Laser UT).

extends beyond the traditional tools. LLNL programs obtain improved quantification of the uncertainties in the fabrication of targets or other components and new synergy among various projects. Initial testing will be performed on workpieces that are relevant to LLNL's mesoscale investigations.

FY2006 Accomplishments and Results

Initial parameterization of error sources within the Xradia CT microscope and the Laser UT system has been completed. Using these error sources, an error budget framework, consisting of three major components—source, object, and detector—was created for each system. Work has begun to describe how these errors propagate through the subsequent object retrieval algorithms to determine system sensitivity.

To produce 3-D measurements, both NDE systems rely on mechanical stages to move the object under investigation. The object motion, as defined by the stages, is a significant portion of the error budget framework. Using accepted stage characterization techniques, these stage motion errors can be measured and the results can be integrated into the error budgets. Each linear or rotational axis has six degrees of freedom. To characterize an axis we measure each degree of freedom individually and then combine the results to obtain an uncertainty in the position of the object.

The Laser UT system, which consists of three linear stacked axes, has been fully characterized. Initial data analysis has begun. Figure 2 shows the linear displacement accuracy (LDA) of the x-axis slide. The LDA is the difference between a calibrated distance along a straight line and the distance indicated by the axis feedback. This linear position data indicates that, excluding the first point, the slide has an accuracy of 11 µm. The first point disparity was determined to be a preloading issue and had been observed by the Laser UT operator, but had not been diagnosed. The measurements completed include six error measurements on each axis, as well as three measurements to characterize the orthogonality between axes.

Fixturing for the metrology of the rotary axis of the Xradia CT machine has been completed.

Related References

1. Huber, R. H., D. J. Chinn, O. O. Balogun, and T. W. Murray, "High Frequency Laser-Based Ultrasound," *Review of Progress in Quantitative Nondestructive Evaluation*, August 2005.

2. Martz, H. E., Jr., and G. F. Albrecht, "Nondestructive Characterization Technologies for Metrology of Micro/Mesoscale Assemblies," *Proceedings of Machines and Processes for Microscale and Mesoscale Fabrication, Metrology, and Assembly*, ASPE Winter Topical Meeting, Gainesville, Florida, pp. 131-141, January 22-23, 2003.

FY2007 Proposed Work

For FY2007, we will fully characterize the Xradia CT mechanical stages. The stage error data for both NDE machines will be analyzed and used to populate the error budgets. Characteristic artifact parts will be fabricated. These artifacts will be measured on both CMM and NDE tools to validate the error budgets. Finally, validated quantitative error budgets will be delivered for the Xradia CT and Laser UT machines.

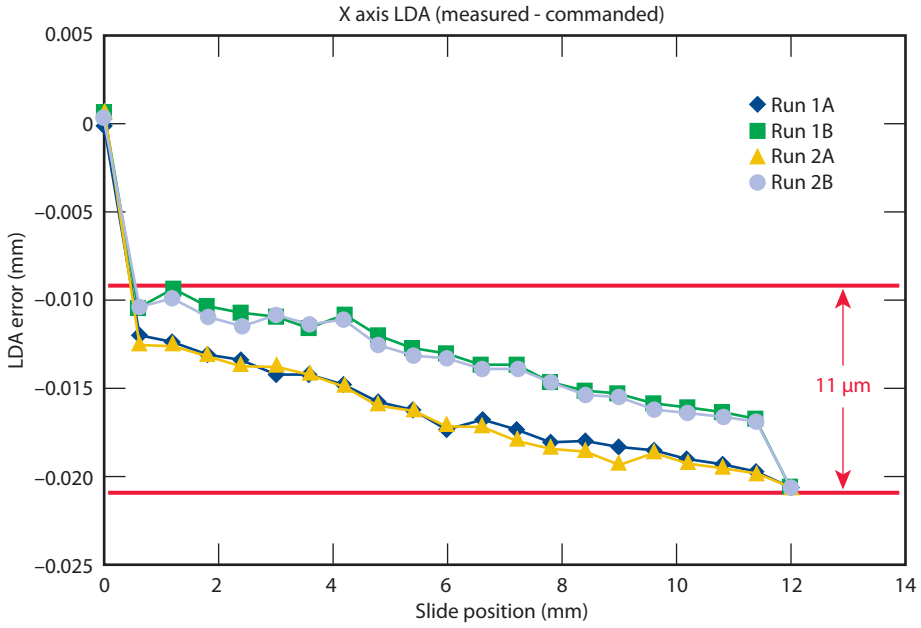

Figure 2. Linear displacement accuracy of the x axis for the Laser UT.

Uncertainty Analysis for Inspection Shop Measurements

Walter W. Nederbragt
(925) 424-2807
nederbragt1@llnl.gov

The LLNL inspection shop is chartered to make dimensional measurements of components for critical programmatic experiments. These measurements ensure that components are within tolerance, and provide geometric details that can be used to further refine simulations. For these measurements to be useful, they must be significantly more accurate than the tolerances that are being checked. For example, if a part has a specified dimension of 100 mm and a tolerance of 1 mm, then the precision and/or accuracy of the measurement should be less than 1 mm. Using the "10-to-1 gaugemaker's rule of thumb," the desired precision of the measurement should be less than 100 µm. Currently, the process for associating measurement uncertainty with data is not standardized, nor is the uncertainty based on a thorough analysis. This project aims to augment the efforts within the LLNL inspection shop with a standardized and commensurately rigorous approach to determining and reporting uncertainty.

Project Goals

The goal of this project is to begin providing measurement uncertainty statements with critical measurements performed in the inspection shop. To accomplish this task, we need comprehensive and quantitative knowledge about the underlying sources of uncertainty for measurement instruments. Moreover, measurements of elemental uncertainties for each physical source need to be combined in a meaningful way to obtain an overall measurement uncertainty.

Relevance to LLNL Mission

The measurements made by the inspection shop are used to make decisions about accepting or rejecting critical parts. The inspection shop is widely used within LLNL's engineering programs, and the measurements are typically accepted as being "sufficiently" accurate. This assumption should be verified by a measurement uncertainty analysis, which is the accepted practice at all of the other NNSA sites. There is a

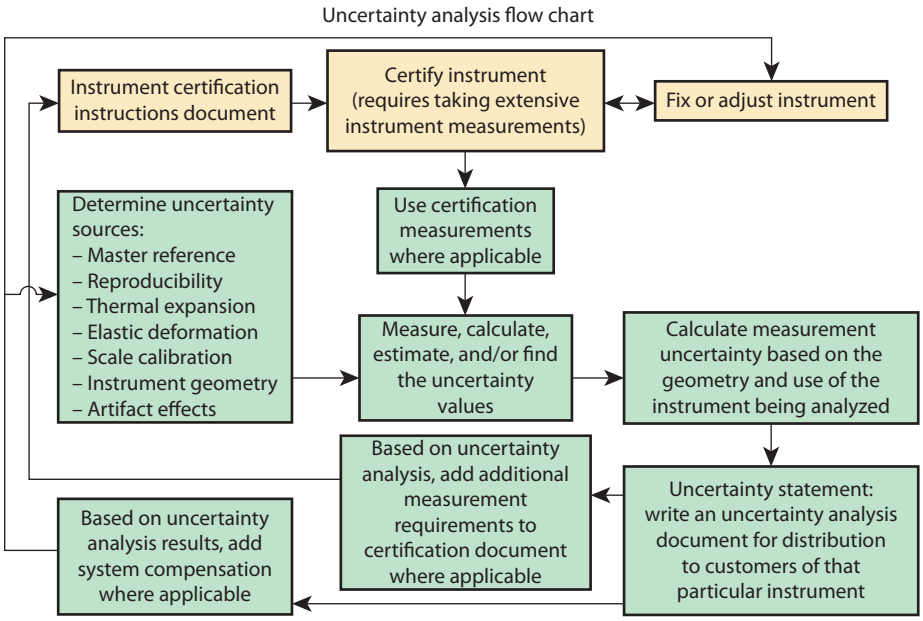

Figure 1. Analysis flowchart for determining the measurement uncertainty of a particular measurement tool. The yellow boxes represent tasks that are already performed; the green boxes represent new tasks to be implemented in FY2007.

significant risk to programs if measurement data is in error, which could lead to the use of components that are outside of specifications.

FY2006 Accomplishments and Results

During the year, six tasks were completed:

1. The role of the inspection shop, as defined in various DOE/NNSA documents, was reviewed and analyzed.
2. The critical equipment in the inspection shop was investigated to understand uses and limitations.
3. The relationship between the Primary Standards Lab (PSL) at Sandia National Laboratories and the LLNL inspection shop was examined.
4. A plan was created to perform uncertainty analysis on the critical measurement equipment in the inspection shop. Figure 1 shows an uncertainty analysis flowchart.
5. Uncertainty analysis methods and tools used by the National Institute of Standards and Technology (NIST) and PSL were studied.
6. The uncertainty analysis of the Precision Inspection Shell Measuring Machine (PrISMM) was initiated (Fig. 2).

Two reports were written to document this work. One report covers the current operation of the inspection shop, including descriptions of the critical measurement machines; the other report describes a plan for implementing uncertainty analysis in the inspection shop

Related References

1. Doiron, T., and J. Stoup, "Uncertainty and Dimensional Calibrations," *Journal of Research of the National Institute of Standards and Technology*, **120**, 6, pp. 647-676, 1997.

2. Taylor B. N., and C. E. Kuyatt, "Guidelines for Evaluating and Expressing the Uncertainty of NIST Measurement Results," *National Institute of Standards and Technology*, Technical Note 1297, 1994 Edition.

FY2007 Proposed Work

There are over a dozen instruments on the critical inspection equipment list that need to have their measurement uncertainties determined. These machines will be divided into groups: Coordinate Measurement Machines (CMMs, of which there are six in the inspection shop); shell measurement instruments (PrISMM and the rotary contour gauge); and other measurement instruments, such as Moore measurement machines and the Y/Z machine. In the first quarter, the rotary contour gauge and PrISMM will be analyzed to determine their measurement uncertainties because there is a higher level of programmatic interest in completing analysis of these machines. Using this information, in the second quarter, the CMMs will be analyzed. In the third and fourth quarter, the remaining machines will be analyzed. At the end of the fourth quarter, preliminary measurement uncertainty data sheets for each instrument will be available to customers. Moreover, our understanding of the measurement machines will be greatly enhanced. This knowledge will be applied to improve the certification and accuracy of the existing machines.

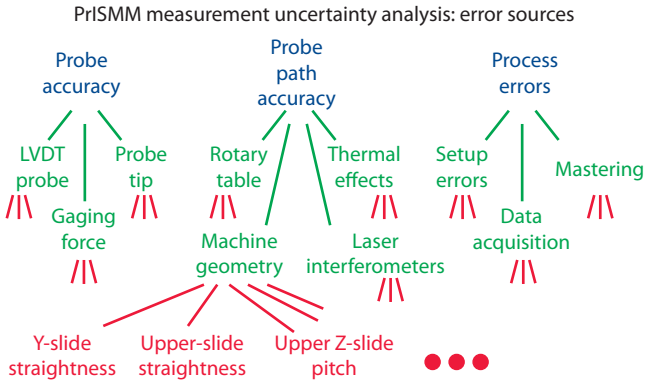

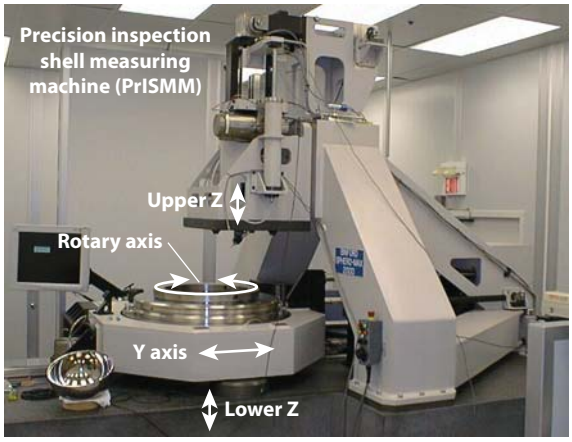

Figure 2. Hierarchical error source breakdown for PrISMM. The error sources at the top (blue) are general error categories. The errors at the bottom (red) are specific error sources (only three are shown). The low level errors need to be determined, by measurement, calculation, estimation, and/or specification, to create an error budget.

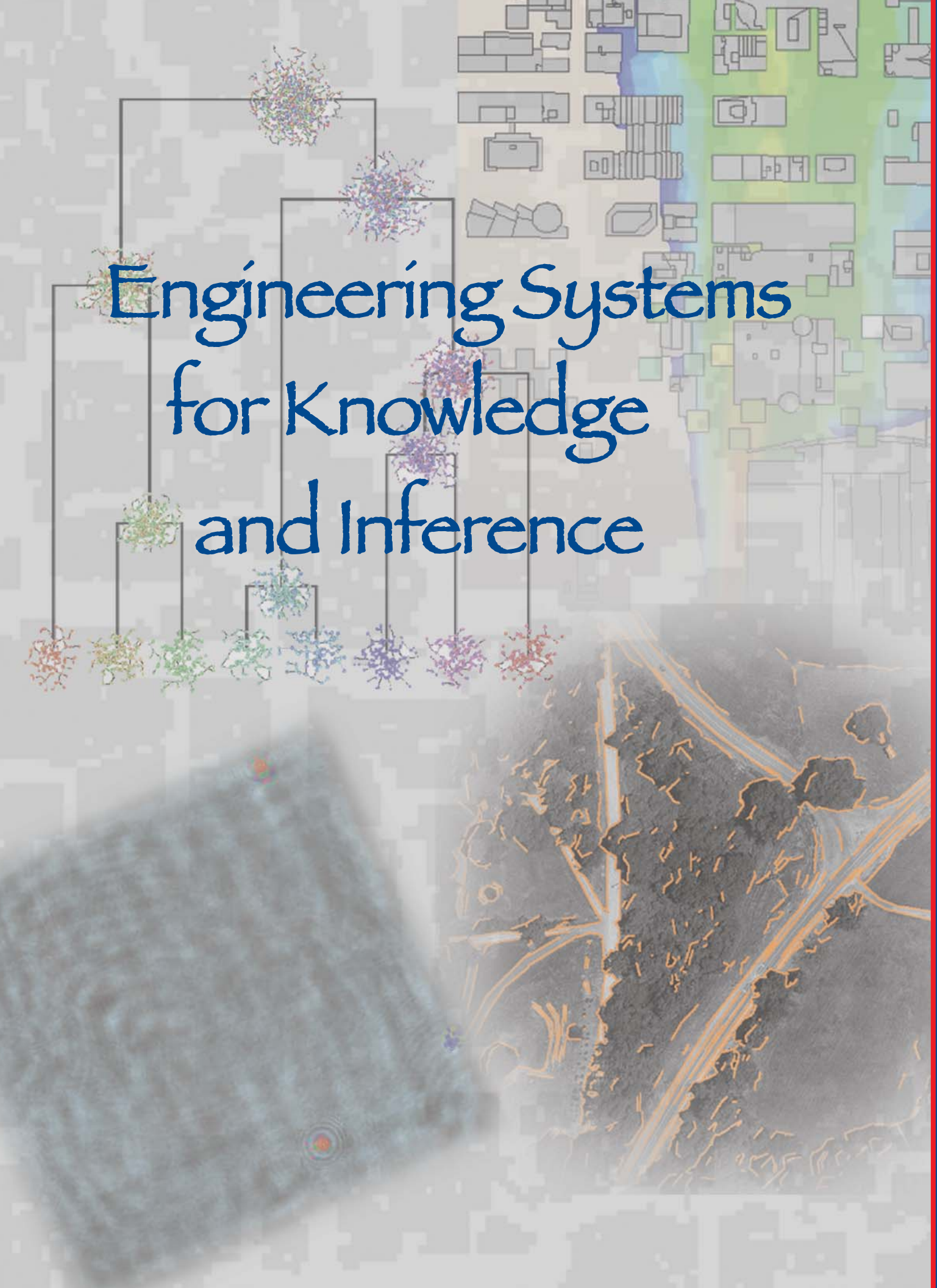

Engineering Systems for Knowledge and Inference

FY 06 Engineering Research and Technology Report

Image Relational Search Engine

David Paglieroni
(925) 423-9295
paglieroni1@llnl.gov

Information science is concerned with extracting knowledge from raw data sources. In surveillance and site monitoring applications, data from *in situ* radiation, biological, chemical or motion sensor networks can be used to construct dynamic measurement fields from which anomalies can be detected. Passive and active remote sensing systems are now capable of producing still image coverage over broad area landmasses, and video for persistent surveillance of designated sites.

One overarching goal of information science is to develop a multi-step process for transforming raw data into knowledge. Unformatted raw data must first be transformed into formatted tables or semantic graphs containing items of interest extracted from the data. Patterns of interest must then be extracted from these tables or graphs, or naturally occurring patterns must be discovered. By creating statistical models for dynamic activities of interest, whose components are tied to such patterns, one can evaluate a set of observed patterns against the hypothesis that a particular activity of interest is occurring or is about to occur. Alternatively, one can discover correlations between patterns in historical data so that anomalies can be detected and predictions can be made from incoming data.

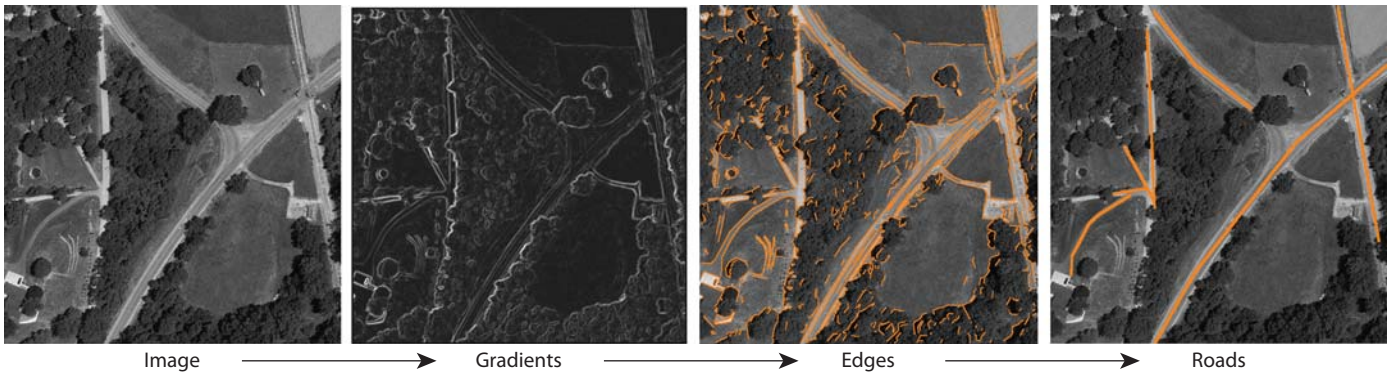

Figure 1. Example of road extraction.

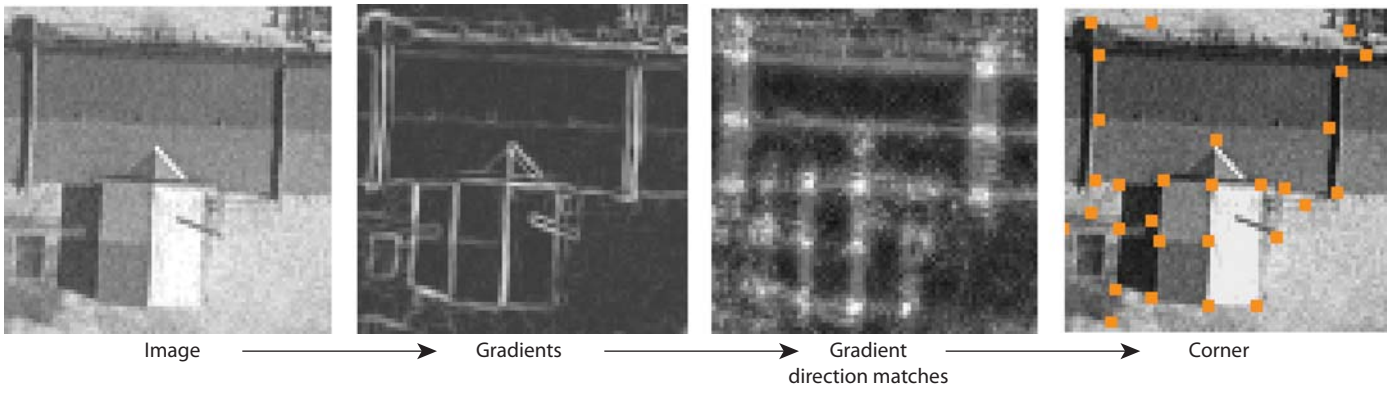

Figure 2. Example of corner extraction.

The Image Relational Search Engine (IRSE) Project focuses on specific aspects of the overall problem described. It addresses only one voluminous raw data source—imagery from remote sensors. The focus of IRSE is limited to extracting items of interest such as roads, buildings, and vehicles from images, and then searching for patterns that contain combinations of items that relate to each other in a prescribed way.

Project Goals

The goals of the IRSE project are: 1) develop algorithms that advance the state of the art in extracting roads and buildings from images; and 2) develop a customized code layer on top of a commercial search engine code that leverages novel algorithms for finding matches to multi-component Probabilistic Relational Models (PRMs) in databases and graphs. The databases and graphs contain items extracted from images. PRMs constructed by experts specify spatial and temporal relationships between these items precisely or with uncertainty.

Relevance to LLNL Mission

IRSE addresses needs in knowledge extraction from overhead images related to LLNL's mission. IRSE is relevant to national security problems involving broad area image search, and database/graph evolution, query, and prediction.

FY2006 Accomplishments and Results

Our linear consolidation algorithm produces road extraction results from images (Fig.1) that go beyond the state of the art. Gradient Direction Matching algorithms developed for matching 3-D objects to images have been modified to extract corners of buildings (Fig.2). We have developed algorithms that quickly extract buildings from images, independent of position, size and orientation, by finding groups of corners that satisfy rectangular shape constraints (Fig.3).

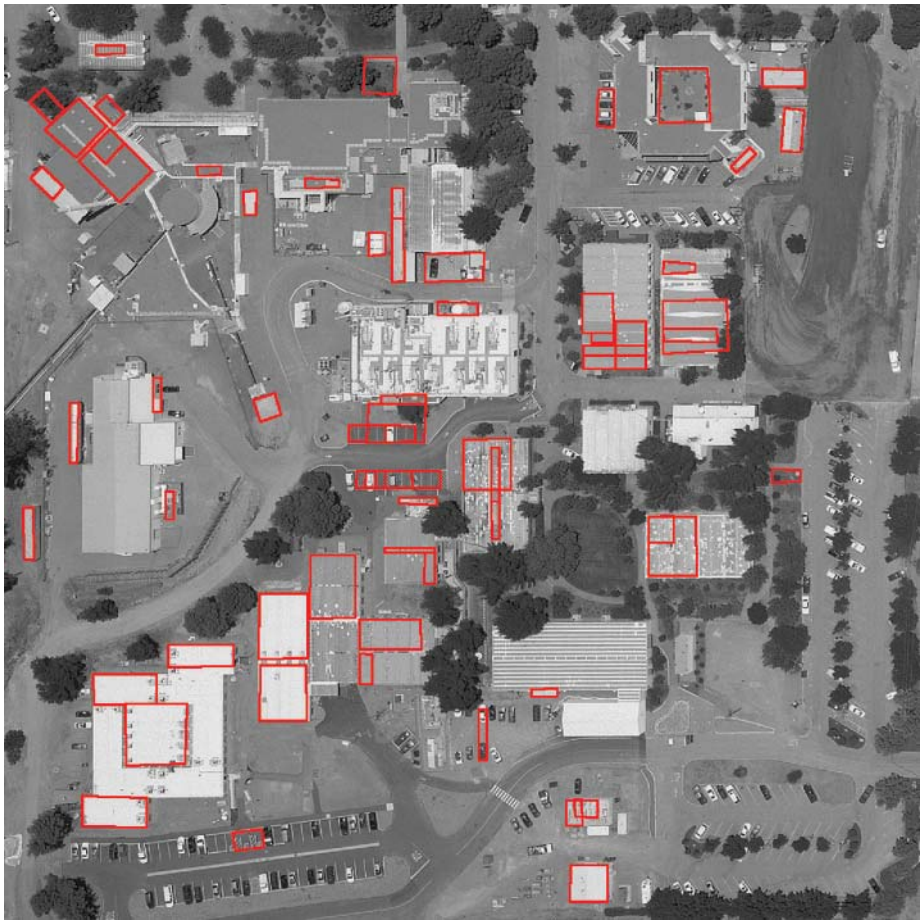

Figure 3. Example of rectangle extraction (dimensions from 25 to 75 pixels).

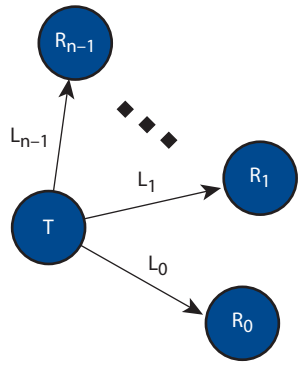

Figure 4. Graphical depiction of Single Transmitter Model with one transmitter item, T, *n* links, L, and *n* receiver items, R.

An algorithm for matching Single Transmitter Models (a type of PRM) to databases and graphs has also been developed (Fig.4). Matching is posed as a minimum cost assignment problem in which candidate items are assigned to model links in an optimal way.

Our method is unique in that it accounts for the following factors simultaneously:

1. the relative significance (importance) of each concept in the pattern model;
2. the similarity between corresponding concepts in the pattern match and the pattern model;
3. the degree of relational consistency between the pattern match and the pattern model;
4. probabilistic uncertainty associated with the pattern model; and
5. links missing from the pattern match.

Related References

1. Chen, B., and D. Paglieroni, "Using Gradients, Alignment and Proximity to Extract Curves and Connect Roads in Overhead Images," *Proc. SPIE D&SS*, pp. 17-21, April 2006.

2. Paglieroni, D., *et al*, "Phase Sensitive Cueing for 3D Objects in Overhead Images," *Proc. SPIE D&SS*, **5809**, pp. 28-30, March 2005.

3. Kuhn, H., "The Hungarian Method for the Assignment Problem," *Naval Research Logistics Quarterly*, **2**, pp. 83-97, 1955.

Dynamic Data-Driven Event Reconstruction for Atmospheric Releases

Branko Kosovic
(925) 424-4573
kosovic1@llnl.gov

The release of aerosols and chemical species into the atmosphere creates a downstream plume. Our effort has been to sample the plume and then estimate the location of its source. We attempt to answer the critical questions: How much material was released? When? Where? What are the potential consequences?

Accurate estimation of the source term is essential to accurately predict plume dispersion, effectively manage the emergency response, and mitigate consequences in a case of a release of hazardous material. We have developed a capability that seamlessly integrates observational data streams with predictive models to provide probabilistic estimates of unknown source term parameters consistent with both data and model predictions. Our approach uses Bayesian inference with stochastic sampling based on Markov Chain Monte Carlo (MCMC) and Sequential Monte Carlo (SMC) methodologies. The inverse dispersion problem is effectively addressed by reformulating it as an efficient sampling of an ensemble of predictive simulations, guided by statistical comparisons with data.

Project Goals

Our goal was to develop a flexible and adaptable data-driven event-reconstruction capability for atmospheric releases that provides:

1. quantitative probabilistic estimates of the principal source-term parameters (*e.g.*, the time-varying release rate and location);
2. predictions of increasing fidelity as an event progresses and additional data become available;
3. analysis tools for sensor network design and uncertainty studies; and
4. a model for quantification of dispersion model errors.

Our computational framework incorporates multiple stochastic algorithms, operates with a range and variety of atmospheric models, and runs on multiple computer platforms, from laptops and workstations to large-scale computing resources. We developed a multi-resolution capability for both real-time operational response and high-fidelity multi-scale applications.

Relevance to LLNL Mission

This project directly aligns with LLNL's homeland and national security missions by addressing a critical need for atmospheric release event reconstruction tools. Our efforts support the rapidly growing number of operational detection, warning, and incident characterization systems being developed and deployed by the Department of Homeland Security and the Department of Energy. The event reconstruction

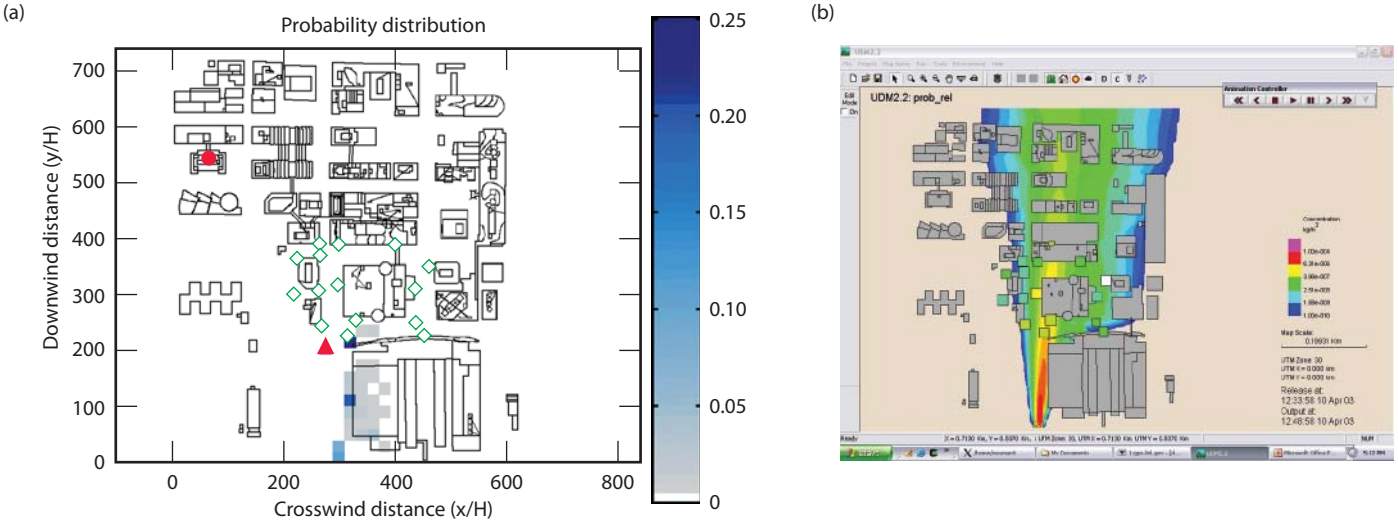

Figure 1. Example of event reconstruction for a release in an urban environment using an operational puff-dispersion model and concentration measurements from the field tracer experiment Joint Urban 2003 in Oklahoma City. (a) Color contours (blue) represent probability distribution of source location; the actual source is denoted with a triangle. (b) Color contours represent the plume from one of three likely locations (the probability distribution mode on the far South of (a)) that most closely corresponds to the actual release rate. Sensors are denoted with squares and color-coded according to measured concentrations.

capability developed by this project is targeted for integration into the next-generation National Atmospheric Release Advisory Center and a new Interagency Modeling and Atmospheric Analysis Center, based at LLNL.

FY2006 Accomplishments and Results

In FY2006 we accomplished the following:

1. implemented an operational Gaussian puff dispersion model for the simulation of urban dispersion into the MCMC capability, and tested it using data from the Joint Urban 2003 experiment in Oklahoma City (Fig. 1);
2. extended the event reconstruction capability to handle complex continental scale atmospheric releases;
3. successfully demonstrated the continental scale MCMC capability using a real world example of accidental release of radioactive material at Algeciras, Spain, in 1998 (Fig. 2);
4. developed an error quantification model for data, input parameters, and internal model output error;
5. continued developing and testing efficient stochastic sampling and convergence algorithms;
6. implemented components of a multi-resolution capability for more efficient sampling for source characterization;
7. tested a computational framework including hybrid MCMC-SMC algorithms on massively parallel platforms; and
8. continued performance enhancement of the computational framework on the range of platforms for efficient event reconstruction of complex atmospheric releases.

Related References

1. Chow, T., B. Kosovic, and S. Chan "Source Inversion for Contaminant Plume Dispersion in Urban Environments Using Building-Resolving Simulations," *Sixth Symposium on Urban Environment at Eighty-Sixth Annual American Meteorological Society Meeting*, Atlanta, Georgia, January 30 – February 2, 2006.

2. Delle Monache, L., K. Dyer, W. Hanley, G. Johannesson, B. Kosovic, S. Larsen, G. Loosmore, J. K. Lundquist, A. Mirin, and G. Sugiyama, "Event Reconstruction for Atmospheric Releases at the Continental Scale: A Case Study: Algeciras, Spain, May 1998," *Tenth Annual George Mason University Conference on Atmospheric Transport and Dispersion Modeling*, Fairfax, Virginia, August 1-3, 2006.

3. Kosovic, B., G. Sugiyama, S. Chan, F. Chow, K. Dyer, R. Glaser, W. Hanley, G. Johannesson, S. Larsen, G. Loosmore, J. K. Lundquist, A. Mirin, J. Nitao, R. Serban, and C. Tong, "Stochastic Source Inversion Methodology and Optimal Sensor Network Design," *Ninth Annual George Mason University Conference on Atmospheric Transport and Dispersion Modeling*, Fairfax, Virginia, July 18-20, 2005.

4. Johannesson, G., *et al.*, "Sequential Monte-Carlo Approach for Dynamic Data-Driven Event Reconstruction for Atmospheric Release," *Proceedings of the Nonlinear Statistical Signal Processing Workshop*, Cambridge, UK, September 13-15, 2006.

5. Neuman, S., L. Glascoe, B. Kosovic, K. Dyer, W. Hanley, and J. Nitao, "Event Reconstruction with the Urban Dispersion Model," *Sixth Symposium on Urban Environment at Eighty-Sixth Annual American Meteorological Society Meeting*, Atlanta, Georgia, January 30–February 2, 2006.

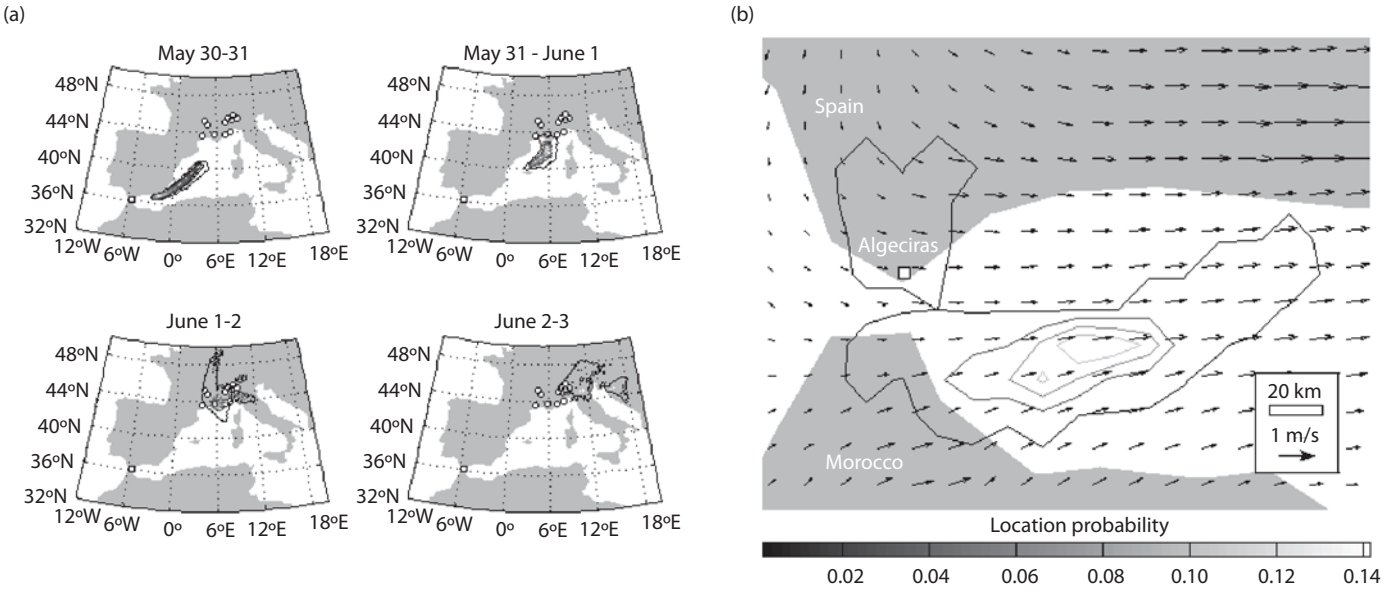

Figure 2. Example of continental scale event reconstruction using operational 3-D Lagrangian particle dispersion model and data from accidental release of Cs-137 at Algeciras, Spain, in 1998. (a) Contours represent simulated plume dispersion from the actual source over a period of four days; circles represent sensor locations. The actual source is denoted with a square. (b) Contours represent probability distribution of source location superimposed on the wind field obtained from a mesoscale model.

Decomposition of Large-Scale Semantic Graphs

Yiming Yao
(925) 422-1922
yao3@llnl.gov

Graphs are frequently used to analyze many types of complex systems such as the World Wide Web and biological and social networks. "Communities," or densely connected clusters, tend to form naturally in these graphs, where there are strong underlying relationships, such as protein modules in biological networks or autonomous systems on the Internet. The identification of these communities, particularly in very large graphs, can enable us to more effectively and efficiently analyze their underlying structure. To this end, we are developing a new, two-stage hierarchical approach for identifying communities.

The crux of our technique is its first stage, in which the graph is efficiently transformed into a tree of bi-connected components (BCCs) (Fig. 1). This transformation facilitates the parallel identification of communities within the BCCs during the second stage of the algorithm, greatly increasing computational efficiency.

Project Goals

Existing hierarchical algorithms for community identification, such as the high quality algorithm developed by Girvan and Newman, are capable of processing only graphs with up to approximately ten thousand nodes, due to their prohibitively high computational complexity. We expect our two-stage approach to eventually process graphs with up to a billion nodes. During the course of our research, we will make significant contributions to path counting and graph transformation algorithms in the field of graph theory. However, from a practical standpoint, we expect the outcome of this project to help resolve a variety of outstanding operational issues encountered by various LLNL programs that leverage semantic graph technologies.

Relevance to LLNL Mission

LLNL has been developing semantic graph technologies in recent years in an

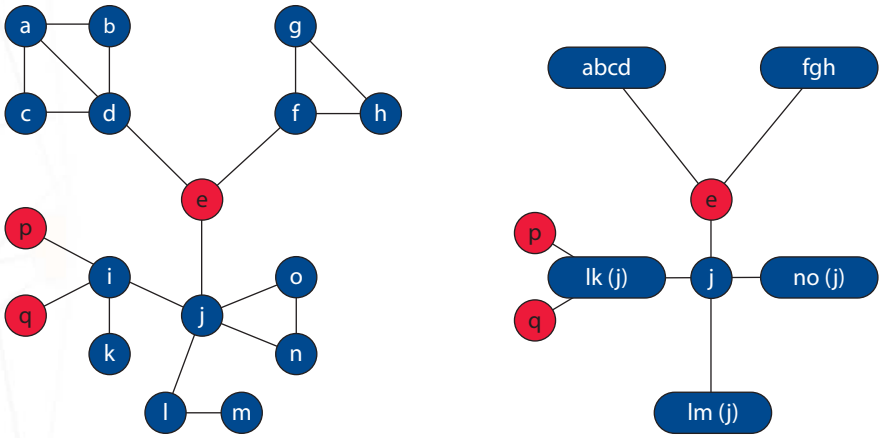

Figure 1. A graph and its tree of BCCs.

effort to enable large-scale data mining and information discovery through the fusion of knowledge from numerous and disparate information sources into massive semantic graphs. We now face a new and critical challenge, however, to decompose these massive graphs into meaningful sub-graphs that analysts can efficiently interrogate, to discover behaviors and relationships of interest. Community decomposition techniques divide semantic graphs into manageable, semantically homogeneous sub-graphs and thus provide the foundation for building information analysis environments vital to various LLNL activities.

FY2006 Accomplishments and Results

During FY2006, we have completed the algorithms that identify BCCs within a semantic graph, and we have designed and implemented the BCC-based algorithms for applying Girvan and Newman's community identification technique. We have also created the first integer linear programming (ILP) model for maximizing Newman's modularity, which is a significant improvement on White and Smyth's integer quadratic programming (IQP) model. We have used our ILP model to find the optimal community structures in several well-studied graphs found in the published literature (*e.g.*, Fig. 2). We intend to submit two journal papers based upon these accomplishments.

During our research, we have also found an efficient solution to a query problem that had arisen from LLNL's semantic graph technology efforts. The transformation of a semantic graph into a tree of BCCs has led to a simple solution for identifying all simple paths of up to a user-specified path length between two vertices of interest (Fig. 3). We presented these findings at the Risk Analysis for Homeland Security and Defense conference in March, 2006.

Related References

1. Girvan M., and M. E. J. Newman, "Community Structure in Social and Biological Networks," *Proc. Natl. Acad. Sci. USA* **99**, pp. 7821-7826, 2002.

2. Newman, M. E. J., and M. Girvan, "Finding and Evaluating Community Structure in Networks," *Phys. Rev. E*, **69**, 026113, 2004.

3. White, S. and P. Smyth, "A Spectral Clustering Approach to Finding Communities in Graphs," *Proceedings of the 5th SIAM International Conference on Data Mining*, 2005.

4. Zachary W., "An Information Flow Model for Conflict and Fission in Small Groups," *Journal of Anthropological Research*, **33**, pp. 452-473, 1977.

FY2007 Proposed Work

In the coming year, we intend to focus our efforts on developing the parallel implementation of the two-stage community partitioning approach, as well as on enhancing the individual algorithms in both stages. We will continue to seek new application areas where the BCC transformation can lead to significant enhancement of computational performance.

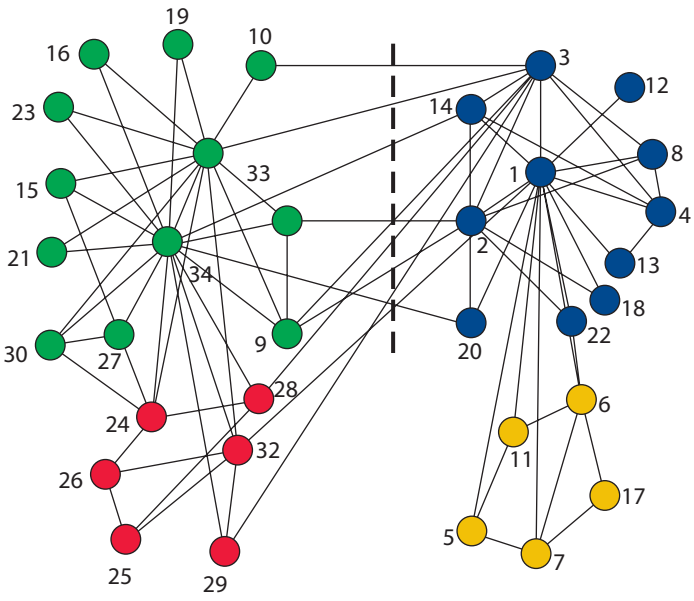

Figure 2. Optimal community structure for Zachary's "karate club."

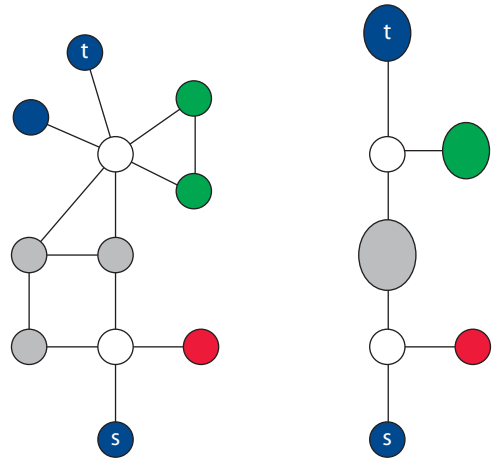

Figure 3. All simple paths between nodes *s* and *t* (left) are transformed into the sole path linking them in the BCC isomorphic transformation (right).

Semantic Graph Hierarchical Clustering and Analysis Testbed

Tracy Hickling
(925) 422-0219
hickling1@llnl.gov

LLNL has invested more than a decade on semantic graph-based information representation in an effort to improve the efficiency of data storage and analysis, and therefore facilitate knowledge discovery. Effective use of graph data frequently requires the modification and application of a variety of inference techniques. Knowledge discovery systems based upon semantic graphs, however, are rarely optimal for enabling the construction and testing of these algorithms.

We are addressing this deficiency by building a testbed to serve as a companion to analysts and the information systems they use. Its fundamental purpose will be to permit rapid prototyping of graph-based algorithms in an environment equipped to evaluate and compare efficiency and performance. Due to the unique needs of LLNL in regard to massive graphs, we chose an environment that emphasizes hierarchical clustering methodologies as the foundation of the analysis process, together with other algorithms that may be applied within this framework.

Project Goals

The testbed will provide a suite of modular algorithm components, categorized according to their typical function in graph analysis algorithms, which may be combined and sequenced to create distinct algorithms for evaluation and comparison.

Algorithm evaluation will take place within a testing framework suitable for the evaluation of numerical algorithm results as well as for the visualization of non-numerical algorithm output, such as the dendrogram in Fig. 1. Particularly in the case of hierarchical clustering techniques, performance evaluation frequently requires significantly subjective assessment and therefore, extensive analyst interaction. We will provide tools to help guide analysts in evaluating many aspects of algorithm performance, such as estimating the strength of cluster relationships, or the optimality of a graph partition. In addition, we will enhance the interpretability of algorithm outcomes by providing use cases for a selection of desirable algorithms together with a manual for advanced operation of the testbed.

Relevance to LLNL Mission

Semantic graphs provide an exciting glimpse into the future of knowledge extraction and inference in support of LLNL's intelligence/security mission and other science and technology applications. Large knowledge discovery systems have the potential

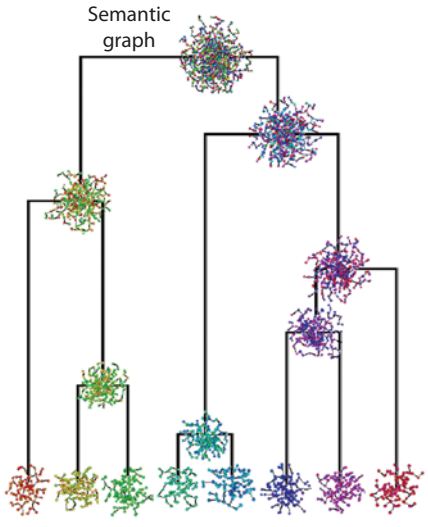

Figure 1. Example of a dendrogram representation of a hierarchical graph clustering algorithm.

to revolutionize our ability to perform real-time inference activities, since massive graphs are capable of fusing terabytes of multisource data that conceal complex relationships. This testbed will make further work on analysis techniques more efficient and cost-effective, leading to more productive use of semantic graphs and the knowledge discovery systems that exploit them.

FY2006 Accomplishments and Results

Our testbed is being built as a plug-in to Everest, a relatively mature graph visualization environment at LLNL, and has been modified to run either independently or within a larger system. We invested a significant amount of time analyzing Everest's current architecture, an immense, constantly evolving body of program code. The testbed environment has been reconciled with Everest to be compliant with its restrictions while taking maximal advantage of its many features, such as the graph-based maintenance of panel states, and the ability to group nodes interactively. We have completed an I/O plug-in that will allow the testbed to ingest semantic graphs of an XML-based default format together with a commensurate ontology, as shown in Fig. 2.

The base architecture operates in such a way that each of the various components of the testbed will reside in a visualization panel that can be operated and maintained independently. These panels, though not yet functional, have been built, and we have made significant progress on the underlying implementation for the algorithm sequencer.

We have successfully built an algorithm template that approximates the general structure with regard to functionality of most hierarchical decomposition algorithms. The template is general enough to accurately describe a large number of algorithms, but detailed enough to suggest a modularized collection of graph metrics and operations that can be wrapped and interchangeably inserted into algorithm prototypes (Fig. 3).

Related References

1. Bollobás, B., Random Graphs, Cambridge University Press, 2001.
2. Duch, J., and A. Arenas, "Community Detection in Complex Networks Using Extremal Optimization," *Phys. Rev. E*, **72**, 027104, 2005.
3. Newman, M. E. J., and M. Girvan, "Finding and Evaluating Community Structure in Networks," *Phys. Rev. E*, **69**, 026113, 2004.
4. Gross, J. L., and J. Yellen, Handbook of Graph Theory, CRC Press, 2004.
5. Guimerà, R., and L. A. N. Amaral, "Cartography of Complex Networks: Modules and Universal Roles," *J. Stat. Mech.*, P02001, 2005.

FY2007 Proposed Work

We will complete a beta version of the testbed by the conclusion of the third quarter in FY2007. The tasks remaining for completion involve building the visualization plug-ins necessary for performing benchmarking and non-numerical results analysis, as well as implementing the algorithm sequencer. We will implement a suite of commonly used metrics in graph theory and will finalize the testbed with the implementation of a number of use cases to verify and validate the final software product. A manual for proper use will be provided.

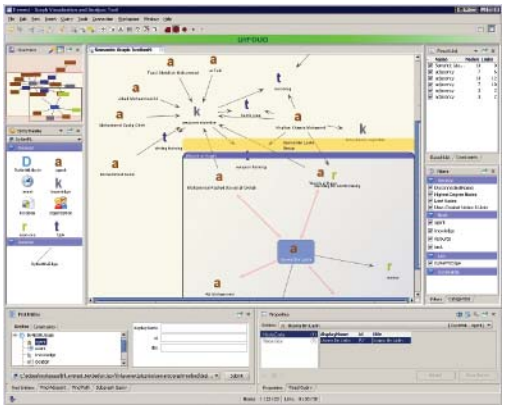

Figure 2. Screenshot of the testbed with data of the default format, DyNetML, loaded.

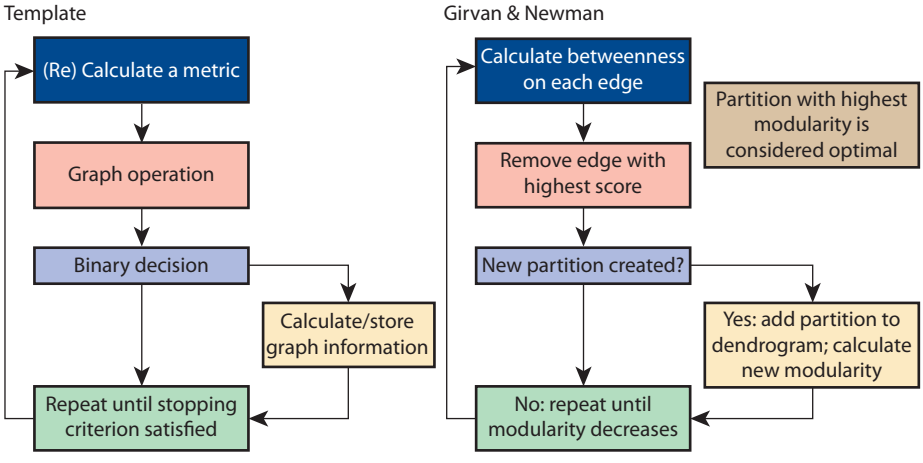

Figure 3. Example algorithm (Girvan and Newman) expressed in template form.

Image Content Engine for Finding Rings of Defects on Optics

Laura M. Kegelmeyer
(925) 422-0924
kegelmeyer1@llnl.gov

In prior years, LLNL's Image Content Engine (ICE) project produced a fast, robust technique for finding patterns in images, called GDM (Gradient Direction Matching). This algorithm differs from other template matching algorithms in that it correlates a template with an image after both are first transformed into images containing only gradient direction information (Fig. 1).

Project Goals

Our goal was to customize and apply the GDM technique from ICE to support one of the optics inspection requirements for the National Ignition Facility (NIF): finding rings of defects on optics (FRODO).

Our objective was to augment the NIF Optics Inspection analysis capabilities (which finds in-focus defects in images of the NIF optics) by finding indirect evidence of defects for which we cannot physically focus the cameras. The indirect evidence we want to find is the diffraction ring pattern that is formed downstream of the interaction between a plane wave of the illuminating laser light and the spherical wave of the obscuring defect (Fig. 2).

The resulting ring pattern will match with the custom luminance disk template when both are transformed into gradient space and correlated with the GDM technique. Once diffraction rings are found, we can incorporate our knowledge of the ring location with predictions about defects that are not in focus and we can also improve our confidence metrics for defects that we can detect directly.

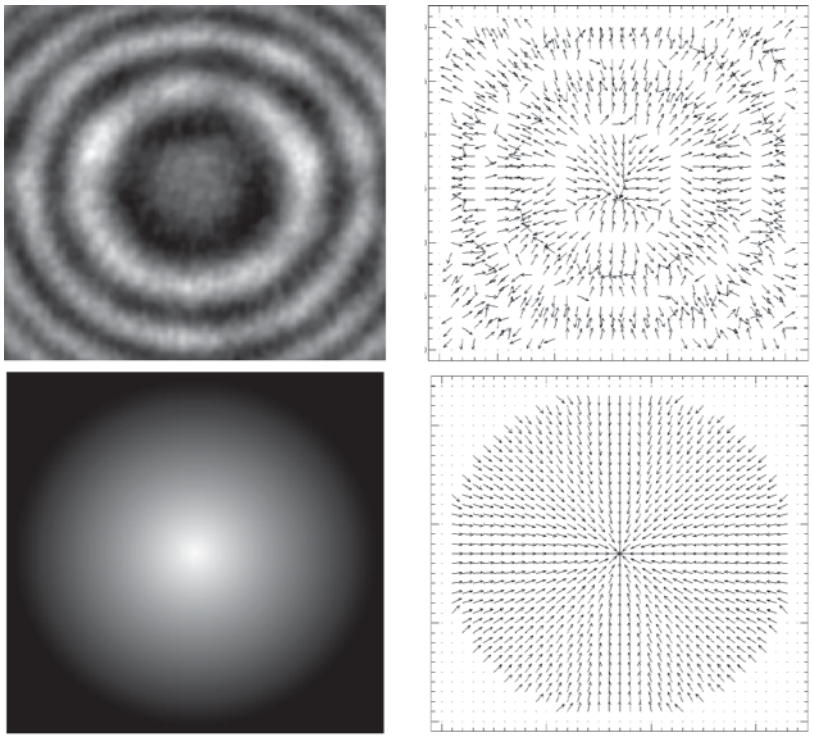

Figure 1. Luminance disk matching. Top: diffraction ring pattern (left) and corresponding direction flow field (right). Bottom: luminance disk model image (left) and corresponding gradient direction flow field (right). Arrows point in direction from dark to light.

Relevance to LLNL Mission

The GDM technique has already been beneficial to several areas within the NIF directorate. One is to find diffraction rings, as planned. Another, unexpected benefit is that it also robustly and effectively finds halos in off-beam-line laboratory images needed to verify the quality of optic coatings. BioSciences, NDE, and Chemistry are other areas where the FRODO results can be usefully applied to find circular features in complex images.

FY2006 Accomplishments and Results

This year saw successful completion of the project milestones, from the initial concept to the final characterization of FRODO for NIF Optics Inspection. We produced tools to create a training set and to generate Receiver Operating Characteristic (ROC) curves in order to evaluate algorithm performance. Then, we used an optimization program, APPSPACK, to optimize parameters used in the FRODO codes. Optimized parameters were incorporated into FRODO and used to analyze the training set. An image showing detected rings is shown in Fig. 3.

The fringe contrast level ratio is $R = (I_{max} - I_{min})/(I_{max} + I_{min})$, where I_{max} and I_{min} are the maximum and minimum intensities, respectively.

A ROC curve showing performance with different parameter settings is shown in Fig. 4, demonstrating the final success of the FRODO project. An additional effort is underway to incorporate these results into the NIF Optics Inspection Analysis process.

Related References

1. Paglieroni, D.W., W. G. Eppler, and D. N. Poland, "Phase Sensitive Cueing for 3D Objects in Overhead Images," *Defense & Security Symposium, Proc. SPIE*, **5809**, Orlando, Florida, March 2005.
2. Chen, B. Y., L. M. Kegelmeyer, J. A. Liebman, J. T. Salmon, J. Tzeng, and D. W. Paglieroni, "Detection of Laser Optic Defects Using Gradient Direction Matching," *SPIE Photonics West LASE Symposium: 8th International Workshop on Laser Beam and Optics Characterization, Proc. SPIE*, **6101**, January 21-26, San Jose, California, 2006.
3. Kolda, T., and G. Gray, *et al.*, Asynchronous Parallel Pattern Search, Sandia National Laboratories, http://software.sandia.gov/appspack.

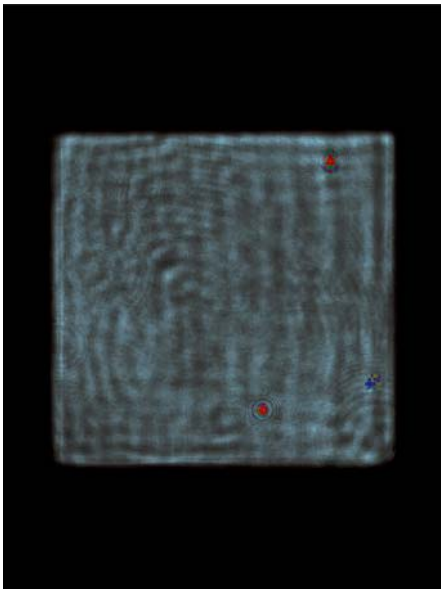

Figure 3. Image from a camera focused on a main laser power amplifier, with diffraction rings labeled with colored circles: blue circle indicates a ring with fringe contrast level ratio irradiance above a value of 0.15; red circles have fringe contrast level ratio irradiance below 0.15.

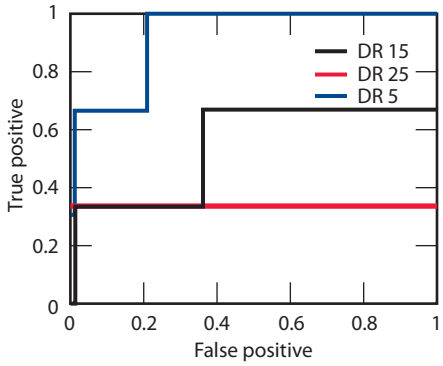

Figure 4. ROC curve for the results of FRODO analysis for an image of a main laser power amplifier. The three separate curves were obtained using three different radii for the luminance disk radius (DR) in the GDM algorithm. A y-axis value of 1 indicates that all labeled rings in the image were identified, whereas a value less than 1 indicates that FRODO did not find all the labeled rings. The graphs show that FRODO finds large, clear rings easily, but has trouble with fainter rings when using a larger disk radius size.

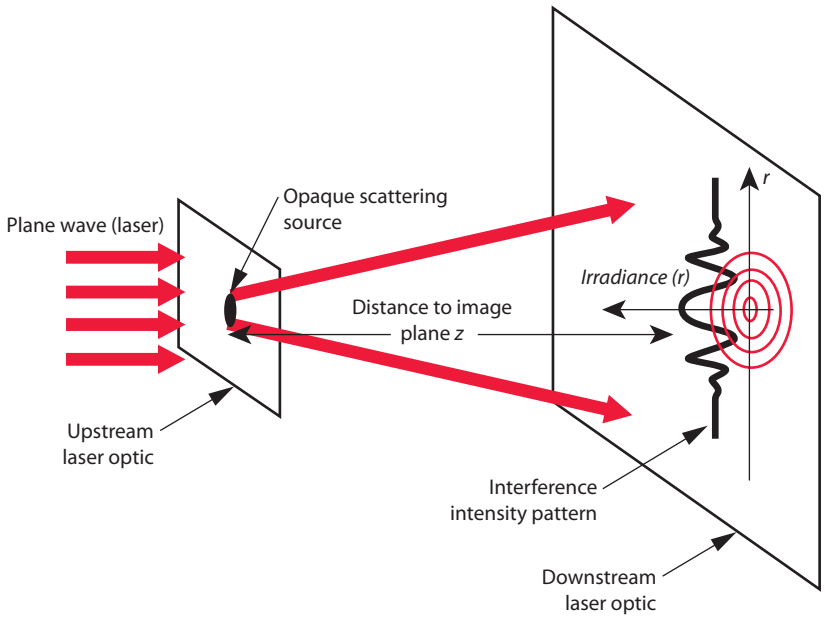

Figure 2. Diffraction ring patterns arising from the interference between a plane wave and an opaque scattering source, *e.g.*, a defect scattering site.

Energy Manipulation

FY 06 Engineering Research and Technology Report

Improving the Vacuum Surface Flashover Performance of Insulators for Microsecond Pulses

Jay Javedani
(925) 422-8569
javedani1@llnl.gov

One of the main areas of pulsed-power R&D is high-voltage insulation and dielectric breakdown, which is very often the limiting factor in attaining the highest possible performance in pulsed-power devices. The surface of an insulator exposed to vacuum can fail electrically at an applied field more than an order of magnitude below the bulk dielectric strength of the insulator. This mode of breakdown, called surface flashover, imposes serious limitations on the power flow into a vacuum region. While many researchers have studied this problem over several decades, there is still no consensus of opinion about the underlying mechanisms that fully explain this phenomenon.

A detailed understanding of the breakdown mechanism must be achieved so that improvements in the insulator performance can be made. This understanding is achieved by staging key computational models and supporting experimental configurations to induce flashover by introducing plasma or geometry effects to the insulator.

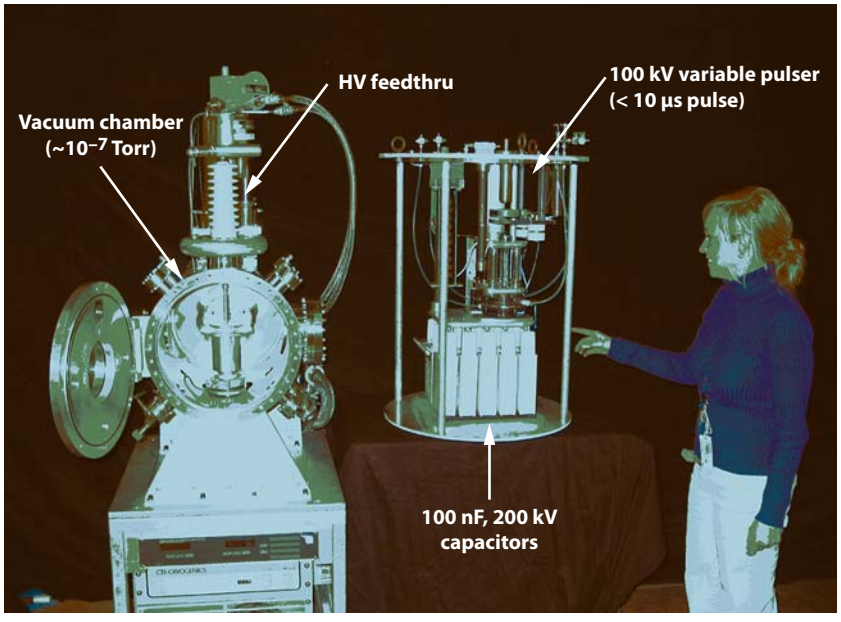

Figure 1. Operational testbed.

Project Goals

The objective of this investigation has been to address outstanding issues and establish a sound understanding of the mechanisms that lead to surface flashover, and evaluate the most promising techniques to improve vacuum insulators that enable high-voltage operation at stress levels near the intrinsic bulk-breakdown limits of the material. The high-voltage vacuum insulators for DARHT-II at LANL, for ZR at SNL, and for Phoenix at LLNL would directly benefit from this work. These results will also be very useful to other electrically stressful systems in the pulse power community.

Relevance to LLNL Mission

For many systems the delivery of pulsed power into a vacuum region is the most critical factor impacting performance and reliability, and the past two decades have seen a sustained growth in the diversity and complexity of device applications where vacuum is required to support high voltages and high electric fields. The applicability of our investigation in flashover performance spans scientific apparatus such as high-current particle-beam accelerators, high-power radio frequency and microwave sources, high-power laser sources, pulsed neutron sources, nuclear weapons effects simulators, lightning and electromagnetic pulse effects simulators, x-ray and proton radiography machines, inertial fusion drivers, directed energy weapons, and electromagnetic launchers. As such, the results have a significant impact on the LLNL national security mission.

FY2006 Accomplishments and Results

Computational and circuit modeling was used to design an experimental testbed (Figs. 1 and 2) to study the insulator breakdown mechanism. The testbed was fabricated and assembled and is operational at LLNL.

The testbed is comprised of a vacuum chamber (70 l, 10^{-7} Torr) with several access ports; a variable 100-kV pulser with 200-ns rise-time and up to 10-µs flat-top pulses that is connected to the anode electrode disk by a HV cable through a vacuum feedthru; a spring-loaded cathode electrode disk that is set at 1.0-cm gap distance from the anode; a liquid voltage resistive divider (VRD) monitoring the output of the pulser; and a Pearson 110 current transformer measuring current on the cathode support stalk.

To investigate surface flashover in the widely used 45˚ conical insulator configuration, we installed a 45˚ conventional HD polyethylene insulator in the gap (visible in Fig. 2). With applied +100-kV pulses of 5 µs duration, the insulator held off the applied voltage, but experienced flashover if a source of plasma/electrons in the form of a small piece of velvet (1.0-mm diameter) was introduced in the vicinity of the insulator on either of the electrode's surfaces. Figure 3 shows the voltage collapse and drawn current for the cases when the velvet is placed on the surface of the cathode insulator at discrete distances away from the cathode triple junction (CTJ) for an applied voltage of +80 kV. Plasma expansion velocities of 1.4 to 2.7 cm/µs are inferred from these signals. The actual flashover occurs when the plasma that is launched from the cathode reaches either the insulator or the anode electrode, whichever happens first. The insulator, however, provides a much quicker conduit to the anode electrode at ns time scales that cannot be resolved by present 20-MHz bandwidth-limited voltage and current probes.

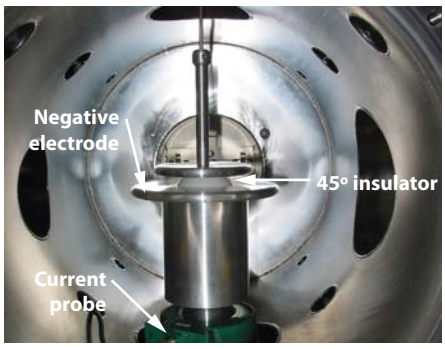

Figure 2. Test chamber with a HD polyethylene insulator installed between electrodes.

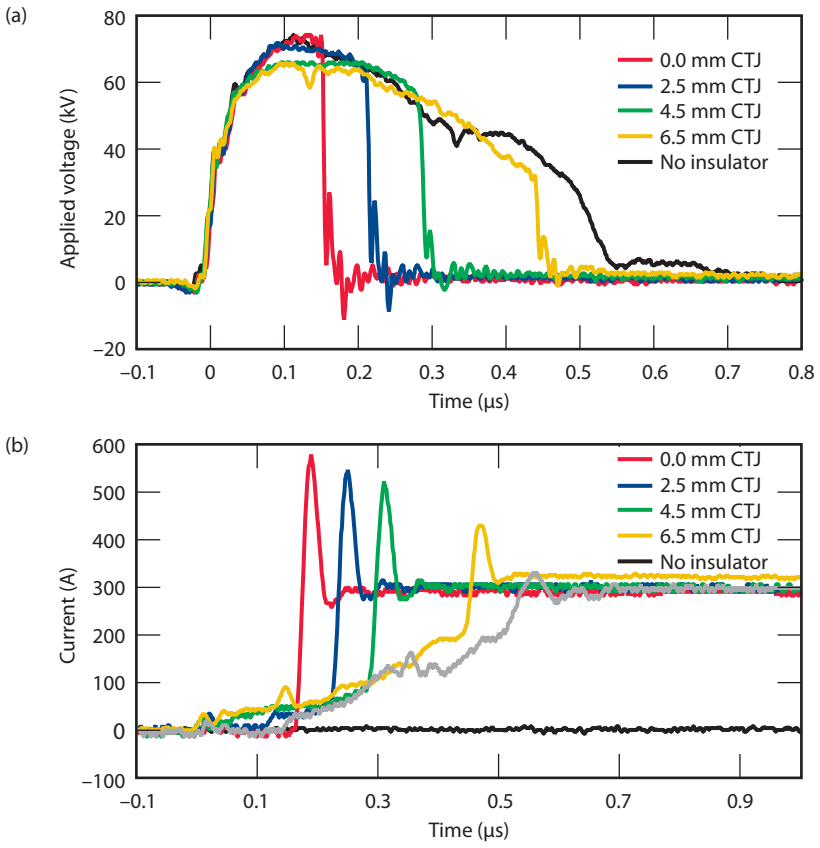

Figure 3. (a) Voltage waveform, and (b) current waveform, for +80 kV-discharge for velvet at different positions of CTJ.

Related References

1. Anderson, R. A., "Surface Flashover: Three Decades of Controversy," *Fourteenth International Symposium on Discharges and Electrical Insulation in Vacuum*, Santa Fe, New Mexico, September 1990.
2. Stygar, W. A., *et al.*, "Improved Design of a High-Voltage Vacuum Interface," *Phys. Rev. ST Accel. Beams*, **8050401**, 2005.
3. Houck, T. H., *et al.*, "Study of Vacuum Insulator Flashover for Pulse Lengths of Multi-Microseconds," *LINAC*, Knoxville, Tennessee, August 2006.

FY2007 Proposed Work

The detailed electron dynamics prior to and including flashover are not yet fully understood and an investigation has been limited by the temporal and spatial resolution of our experimental and analytical tools. To overcome these limitations and enable the investigation, we will:

1. emplace faster diagnostic probes (D-dots with 3-GHz bandwidth) to resolve the details of the insulator flashover;
2. replace the solid-anode electrode with a thin aluminum foil backed with BC422 scintillator to facilitate pictures of the expanding plasma from its initiation point with a fast intensified camera; and
3. introduce a secondary electron avalanche physics capability into a 2-D/3-D programmable intelligent computer (PIC) code and verify its accuracy for our application.

During FY2007 we will complete these tasks and execute a detailed investigation of the phenomenology prior to completing a physics description and extracting the engineering guidelines that are critical to our support of programs.

Improving Switching Performance of Power MOSFETs

Edward G. Cook
(925) 422-7871
cook5@llnl.gov

As their switching and power handling characteristics improve, solid-state devices are finding new applications in pulsed power. This is particularly true of applications that require fast trains of short-duration pulses. High-voltage (600 to 1200 V) metal-oxide-semiconductor field-effect transistors (MOSFETs) are especially well suited for use in these systems, as they can switch at significant peak power levels and are easily gated on and off very quickly. MOSFET operation at the shortest pulse durations is not constrained by the intrinsic capabilities of the MOSFET, but rather by the capabilities of the gate drive circuit and the system physical layout. This project sought to improve MOSFET operation in a pulsed power context by addressing these issues.

Project Goals

The primary goal of this project is to improve the switching performance of power MOSFETs for use in high rep-rate, short-pulse, high-power applications by improving the configuration of the gate-drive circuits and the circuit layouts used in these systems. This requires evaluation of new commercial gate-drive circuits and upgrading LLNL-created circuits. In addition, these circuits must be tested with the fastest available high-voltage power MOSFETs.

Relevance to LLNL Mission

Solid-state pulsed-power circuits are replacing older technology devices such as vacuum tubes and thyratrons, which have availability and reliability issues. This is especially true in a number of

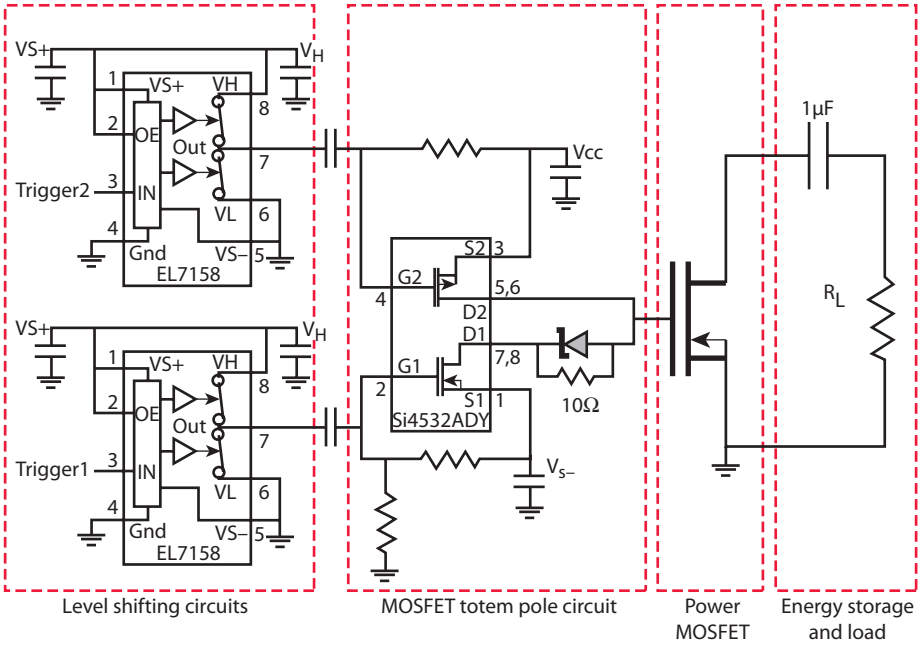

Figure 1. MOSFET gate-drive test circuit.

LLNL programs, such as the accelerator and laser efforts, where MOSFET-switched inductive adder circuits allow detailed control of voltage waveforms that would be impossible with the previous technology. Fast solid-state pulsed power is therefore an enabling technology that finds applications in both new and existing programs at LLNL, which frequently push the limits of switching speeds and short-duration pulses.

FY2006 Accomplishments and Results

We have identified several commercial gate-drive devices that exhibit excellent stability and are capable of generating pulses with fast rise and fall times and at high burst frequencies. These devices are very useful for many pulsed-power applications. However, these commercial circuits are inherently incapable of generating pulses of very short pulse duration. Their internal structure limits the minimum pulse width to a value that maintains stable operation and prevents the production of oscillating gate-drive pulses.

In an effort to generate shorter duration pulses, we have turned to an LLNL circuit composed of discrete components, as shown in Fig. 1. This circuit uses commercially available level shifting components and discrete MOSFETs arranged in a totem-pole configuration. To achieve the best control, multiple independent trigger pulses are used to overcome the limitations of turn-on and turn-off delays, shoot-through, and the MOSFET Miller capacitance.

The best of the commercial gate-drive circuits are capable of generating pulses having a minimum pulse duration (measured at the base of the pulse) of 12 to 16 ns. With the LLNL gate-drive circuit layout, we have been able to reduce the minimum pulse width to 5 ns with rise and fall times (10 to 90%) of less than 2 ns. Results are shown in Fig. 2. The switching speeds of this circuit, as measured by rise and fall times, are approximately twice as fast as those achieved with the commercial circuits. Additionally, we have operated this circuit at burst frequencies of 3 MHz for 50 pulse bursts with no degradation in the measured waveforms. This level of gate-drive circuit performance can only be realized when operated with MOSFETs that are optimized for high-frequency or pulse applications. In this respect, the gate-drive circuit and the power MOSFET should be considered to be an integrated system.

The ultimate result of this project has been that the gate-drive circuit and its associated knowledge base have entered the arsenal of LLNL capabilities that are available, as needed, to its programs. For example, the circuit is presently being refined prior to final implementation in the Kicker Pulser of the International Linear Collider so that it can provide 3- to 4-ns pulses with rise and fall times of 1 ns over a wide operating range.

Related References

1. Hickman, B. C., and E. G. Cook, "Evaluation of MOSFETs and IGBTs for Pulsed Power Applications," *International Pulsed Power Conference*, Hollywood, California, June 2001.

2 Cook, E. G., B. C. Hickman, B. S. Lee, S. A. Hawkins, E. J. Gower, and F. V. Allen, "Solid-State Modulator R&D at LLNL," *International Workshop on Recent Progress in Induction Accelerators*, Tsukuba, Japan, October 2002.

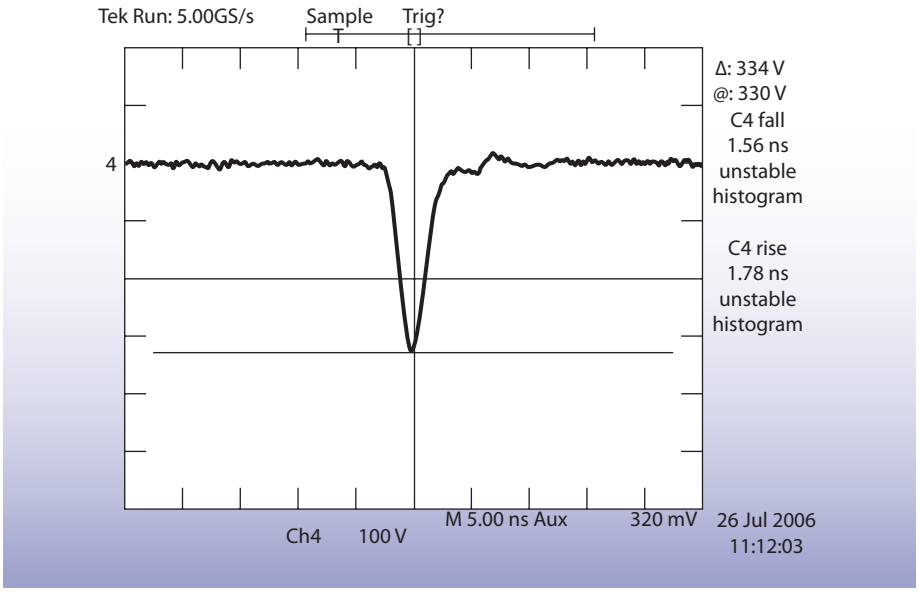

Figure 2. Pulse width results with gate-drive circuit layout.

Solid-State Switch Replacements for Ignitrons

Edward S. Fulkerson, Jr.
(925) 423-5978
fulkerson1@llnl.gov

Ignitron-type power-pulsed switches, often used for high-current handling, pose problems associated with mercury hazards, auxiliary cooling, shock limits, and reliability in field deployments. Transitioning to solid-state technology offers advantages in many applications, but demonstration of performance is needed for acceptance. The goal of this project is to evaluate the newest commercially available solid-state switches beyond manufacturers' ratings, to determine limits of high current and high dI/dt for short pulse durations, and to evaluate suitability for LLNL's pulsed power applications.

Project Goals

The goals of this project included 1) the demonstration of a 10-kV, 20-kA solid-state replacement for the ignitron used at LLNL's Big Experimental Explosive Facility (BEEF); and 2) providing a basis for a 30-kV, 500-kA series/parallel solid-state switch for BEEF, NIF, and the Environmental Measurements Laboratory (EML).

Relevance to LLNL Mission

Among the many applications at LLNL for high current/energy capacitive discharge units (CDUs) are: magnetic flux compression generators (DNT); flashlamp banks (Lasers/NIF); pulsed high-field magnets (Sustained Spheromak Physics Experiment (SSPX)); EM Launchers/Rail Guns (NAVY); and compact electric power conversion.

FY2006 Accomplishments and Results

Six state-of-the-art commercial thyristors (8 kV, 90 kA) were procured for evaluation. A general purpose high-current (>100 kA) testbed has been

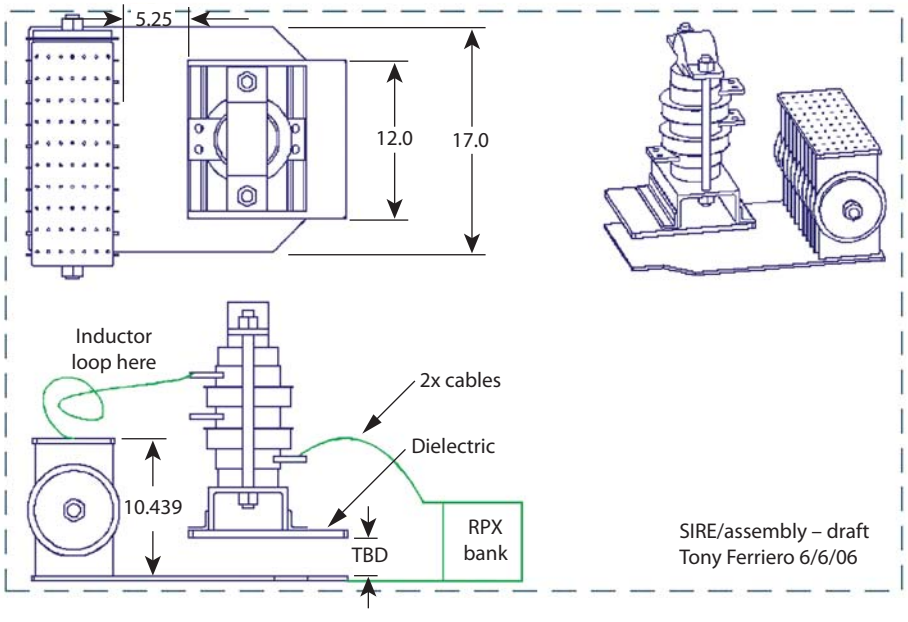

Figure 1. Mechanical drawing of testbed.

constructed that is capable of testing a wide range of solid-state switch components. Initial high-voltage/low-current "leakage" testing has been completed. Figures 1 to 3 illustrate our system and set-up.

Related References

1. Arnold, P. A., "Solid-State Replacements for Hydrogen Thyratrons," http://www-eng.llnl.gov/pdfs/lsr_sys_opt-3.pdf
2. Erickson, R. W., and D. Maksimovic, Fundamentals of Power Electronics, Kluwer, Academic Publishers, United Kingdom, 2001.
3. Williams, B.W., Power Electronics: Devices, Drivers, Applications and Passive Components, McGraw-Hill, New York, New York, 1992.
4. Kassakian, J., M. Schlecht, and G. Verghese, Principles of Power Electronics, Addison-Wesley, Reading, Massachusetts, 1991.

FY2007 Proposed Work

We plan to conduct tests on a unit procured in FY2006 and create a reliable "operational envelope" for pulse power applications by operating the units beyond the manufacturer's specifications for peak current and dI/dt. We will investigate both series and parallel operation of the devices to extend both peak voltage and current capabilities.

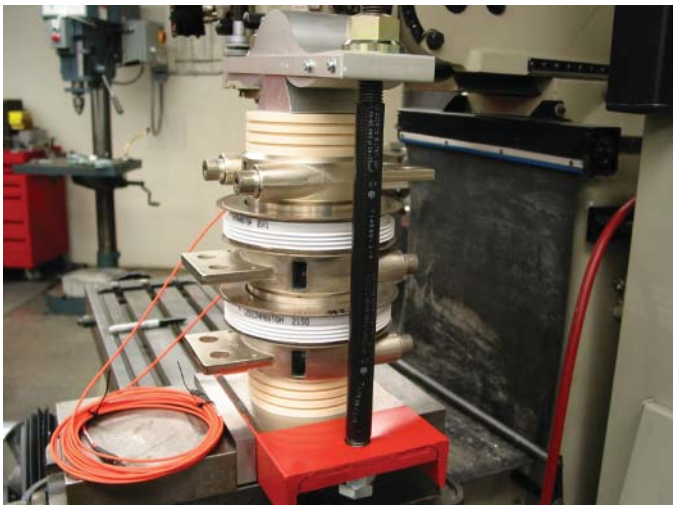

Figure 2. Assembled 2-thyristor stack.

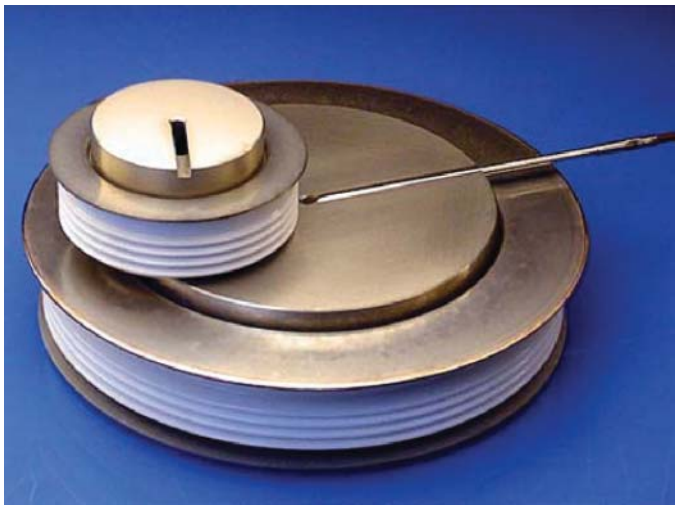

Figure 3. Light-triggered thyristors.

Author Index

Manuscript Date April 2007
Distribution Category UC-42

This work was performed under the auspices of the U.S. Department of Energy by the University of California, Lawrence Livermore National Laboratory under Contract W-7405-Eng-48.
ENG-06-0061-AD

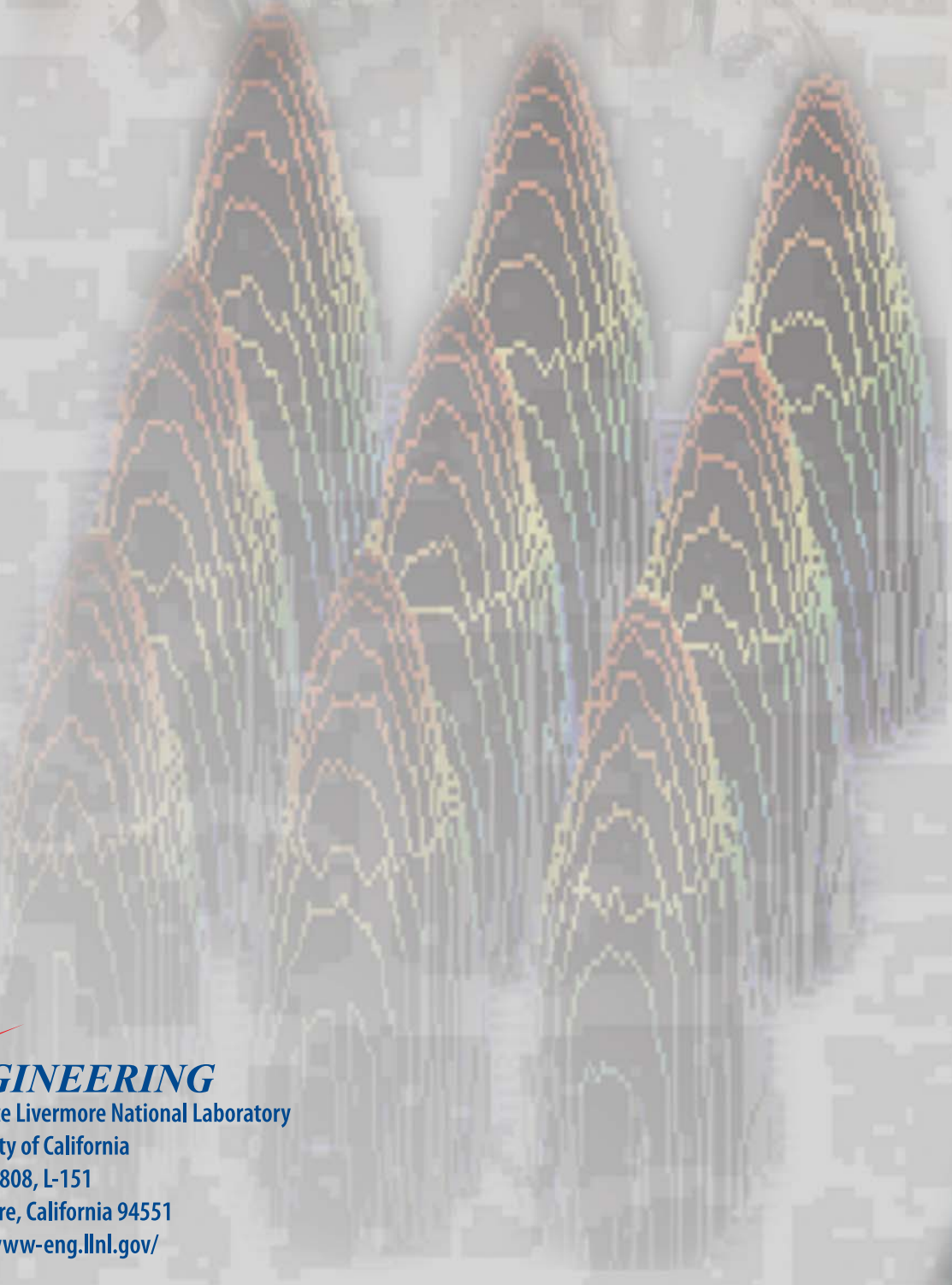

ENGINEERING

Lawrence Livermore National Laboratory
University of California
P.O. Box 808, L-151
Livermore, California 94551
http://www-eng.llnl.gov/